Conference Proceedings of the Society for Experimental Mechanics Series

Tom Proulx *Editor*

Engineering Applications of Residual Stress, Volume 8

Proceedings of the 2011 Annual Conference on Experimental and Applied Mechanics

SEM Springer

Conference Proceedings of the Society for Experimental Mechanics Series

For other titles published in this series, go to
www.springer.com/series/8922

Tom Proulx
Editor

Engineering Applications of Residual Stress, Volume 8

Proceedings of the 2011 Annual Conference on Experimental and Applied Mechanics

Springer

Editor
Tom Proulx
Society for Experimental Mechanics, Inc.
7 School Street
Bethel, CT 06801-1405
USA
tom@sem1.com

ISSN 2191-5644 e-ISSN 2191-5652
ISBN 978-1-4614-0224-4 e-ISBN 978-1-4614-0225-1
DOI 10.1007/978-1-4614-0225-1
Springer New York Dordrecht Heidelberg London

Library of Congress Control Number: 2011929872

Preface

Engineering Applications of Residual Stress represents one of eight volumes of technical papers presented at the Society for Experimental Mechanics Annual Conference & Exposition on Experimental and Applied Mechanics, held at Uncasville, Connecticut, June 13-16, 2011. The full set of proceedings also includes volumes on Dynamic Behavior of Materials, Mechanics of Biological Systems and Materials, Mechanics of Time-Dependent Materials and Processes in Conventional and Multifunctional Materials, MEMS and Nanotechnology; Optical Measurements, Modeling and, Metrology; Experimental and Applied Mechanics, Thermomechanics and Infra-Red Imaging, and Engineering Applications of Residual Stress.

Each collection presents early findings from experimental and computational investigations on an important area within Experimental Mechanics. The Engineering Applications of Residual Stress conference track was organized by: Gary S. Schajer, University of British Columbia and Gavin Horn, University of Illinois at Urbana-Champaign.

The work presented in this volume reflects the practical importance of residual stresses in engineering systems and design. The hidden character of residual stresses often causes them to be underrated or overlooked. However, they profoundly influence structural design and substantially affect strength, fatigue life and dimensional stability. Since residual stresses are induced during almost all materials processing procedures, for example, welding/joining, casting, thermal conditioning and forming, they must be taken seriously and included in practical applications.

This volume highlights the wide range of research relating to residual stresses, including stress development, control, modeling, measurement, and physical responses of engineering components. These topics are organized into five major areas:

Destructive (Relaxation) Residual Stress Measurements
Non-Destructive Residual Stress Measurements
Residual Stress and Reliability on the Micro- and Nano-scale
Industrial Residual Stress Measurements
Modeling and Experimental Validation of Residual Stresses

The Residual Stress Technical Division sincerely thanks all the speakers for carefully preparing their presentations and thanks the authors, presenters, organizers and session chairs for their participation and contribution to this volume.

Bethel, Connecticut

Dr. Thomas Proulx
Society for Experimental Mechanics, Inc

Contents

Residual Stresses Measurement and Inner Geometry Inspection of Pipelines by Optical Methods

Armando Albertazzi Jr*, Matias R. Viotti, Pedro Buschinelli, Allan Hoffmann, Walter Kapp

Universidade Federal de Santa Catarina, Mechanical Eng. Department,

Florianopolis, SC, CEP 88.040-970, Brazil, *e-mail: albertazzi@labmetro.ufsc.br

ABSTRACT

This paper describes three different optical systems designed to be used outside the lab for pipeline inspections. The first one is a robust and portable ESPI based hole-drilling unit with radial sensitivity used for residual stresses measurement. The device has a special diffractive optical element that produces an achromatic interferometer. The displacement component around the hole drilled is measured by ESPI with radial in-plane sensitivity and is fitted by least square methods to evaluate residual stresses. An infield application for analyzing the integrity of a gas pipeline is presented as an application example. The second system is a conical laser triangulation device to measure the geometry of the inner surface of pipes. A laser beam is deflected by the tip of a 45° conical mirror and produces a radial light plane that intercepts the inner surface of the pipe producing a bright ring all way around 360°. The image of the light ring is used to compute the radius of about 1400 points in each section while the device is moved along the pipe axis. Finally, the third system uses active photogrammetry to measure in cylindrical coordinates the details of the inner geometry of pipe junctions and welding seams. It was designed to inspect welded joints, to check weld seam quality as well as to identify transverse and angular misalignment between adjacent sections.

1. Introduction

Light is a very rich and powerful information carrier. Intensity, trajectory, wavelength/color, polarization state, speed and coherence state are light properties that can carry information. The ability to manipulate light to change one or more property as a function of a quantity of interest is the basic principle behind any optical measurement principle. Mechanical, chemical, electrical, thermal, temporal quantities can be measured by optical methods. It is possible to measure quantities in the nanoworld as well to measure distances of remote galaxies over 10^{25} m far away from earth.

From the engineering point of view, optical measurement methods are very attractive for two main reasons: high speed and non-invasiveness. The ability to measure at the light speed makes it possible to handle highly dynamic events and to acquire a large amount of data in a very short time. Light usually does not scratch, deform, wear or damage most engineering surfaces

T. Proulx (ed.), *Engineering Applications of Residual Stress, Volume 8*, Conference Proceedings of the Society for Experimental Mechanics Series 999, DOI 10.1007/978-1-4614-0225-1_1,

or materials. However, light behavior can be influenced by environmental disturbances like temperature, moisture, vibration, dust or pressure, what make the design of an optical measurement system a careful task. That task is even more challenging if the system has to operate in harsh environments.[1]

This paper presents three optical measurement systems designed to operate out of the laboratory environment. The first one is an optical digital speckle patter interferometer (DSPI or ESPI) with a special configuration to reach radial in-plane sensitivity.[2-6] It is integrated with a high speed drilling unit to measure residual stresses using the incremental hole drilling technique. This paper reports an application of this system that uses the residual stresses values to access the external loading applied to a gas pipeline exposed to surrounding soil movement. The second optical system is an optical profilometer that uses a special laser triangulation configuration with a conical mirror to measure the internal geometry of pipes.[9] It was designed to inspect the inner surface of pipes for corrosion. Finally, the third system is another optical profilometer that uses a special optical configuration to measure in high resolution the inner geometry of pipes using active photogrammetry.[10, 11] It was designed to inspect welded pipe joints for misalignments and to verify weld seams quality.

Cartesian coordinate systems are frequently used for most engineering applications. They are appropriate when the quantity has a rectangular domain. However, there is a class of engineering problems where polar or cylindrical coordinate systems are the natural choice. The radial digital speckle pattern interferometer measures the displacement field around the hole drilled in polar coordinates. The two profilometers do the measurement and process the results in cylindrical coordinates. Those characteristics make the systems very appropriate for the target applications.

2. Radial in-plane ESPI interferometer

There are two basic ways to illuminate the measured surface in digital speckle pattern interferometry (DSPI or ESPI): single illumination or double illumination.[8] In the first case, only one light source is directed to the surface. The interference is produced with the aid of another reference illumination, which can be directed to the camera sensor or to an auxiliary surface. Single illumination is mostly used to perform out-of-plane displacement measurements. In double illumination, coherent light coming from two different directions illuminates the surface. The interference is produced by the mutual interaction between the two light components. This configuration is preferable for in-plane displacement measurements. The sensitivity direction in a given point P is defined by the vector difference between two unitary vectors pointing from P to each illumination source. If the illumination directions are symmetrical to the surface normal, the resulting sensitivity vector is parallel to the measured surface, what is the ideal configuration of measuring in-plane displacements. In order to measure the complete in-plane 2D displacement field, two double illumination configurations are needed and their data combined.

2.1 The interferometer

The author's group developed a double illumination digital speckle pattern interferometer with in-plane sensitivity in polar coordinates.[2-7] In order to obtain in-plane sensitivity in the radial direction a special diffractive optical element was developed. This configuration is very suitable for engineering applications since it is possible to measure the stress state from a unique illumination scheme.

Figure 1 shows a sketch of the special diffractive optical element (DOE). It is a binary phase diffraction grid with about 1000 concentric circles per millimeter. Its shape is like the disk shown in the left part of the figure with about 30 mm diameter. The diffractive area is represented in gray. A central clear window is left for viewing proposes. The middle of the figure shows a cross section along a diametric line of the DOE displaying four particularly chosen light rays from a collimated illumination source, which are diffracted by the DOE. Only the first diffraction order is shown in the figure, what bends the light rays toward the center of the circular region. If a point P is particularly considered, diffracted rays illuminate it symmetrically along the illumination directions indicated by the unitary vectors $\mathbf{k_1}$ and $\mathbf{k_2}$. Sensitivity direction is given by the vector $\mathbf{k}$ obtained from the subtraction of the two unitary ones. Since the angles are symmetrical for both light rays, in-plane sensitivity is reached at point P in the radial direction. The same conclusion is valid for any other point on a diametral line, producing radial in-plane sensitivity in the central circular area. The only exception is the center of the circular region that receives light from all directions and is a singular point.

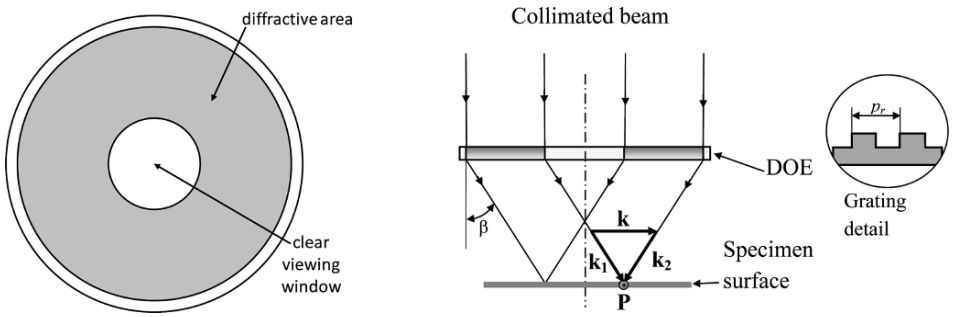

Figure 1: Cross section of the diffractive optical element showing the principle of radial in-plane sensitivity.

2.2 Achromaticity

It can be verified that the configuration described in Figure 1 is achromatic, i.e., the measurement sensitivity does not depends on the laser wavelength. A monochromatic light ray that goes through an ordinary diffraction grating is split in several diffraction orders. The angle β between the incident ray and the first diffraction order is given by equation (1):

$$\sin\beta = \frac{\lambda}{p} \tag{1}$$

where λ is the light wavelength and p is the diffraction grating period. A small variation in the wavelength will change the diffraction angle β. The relationship between the radial in-plane displacement component $u_r(r,\theta)$ and the optical phase distribution $\varphi(r,\theta)$ for the radial in-plane interferometer presented in Figure 1 is given by:

$$u_r(r,\theta) = \frac{\lambda}{4\pi\sin\beta}\ \varphi(r,\theta) \tag{2}$$

where r and θ are the polar coordinates and β the first order diffraction angle. Since the diffraction angle is given by equation (1), the value of $\sin\beta$ can be replaced in equation (2):

$$u_r(r,\theta) = \frac{\lambda}{4\pi\dfrac{\lambda}{p}}\ \varphi(r,\theta) = \frac{p}{4\pi}\ \varphi(r,\theta) \tag{3}$$

According to equation (3), the relationship between the displacement field and the optical phase distribution only depends on p, the period of the grating, and not on laser wavelength. This configuration allows the use of non-wavelength stabilized diode lasers, which are compact, robust and a lot less expensive. The sensitivity of the interferometer is only a function of the stability of the pitch of the diffractive optical element, which in a silicon substrate typically changes only about 0.0004% for temperature variations of 1 kelvin.

2.3 Equipment for residual stresses measurement

Figure 2 shows a practical realization of the achromatic radial in-plane interferometer. Expanded light from a diode laser (L) passes through a central hole of mirror M_1 and illuminates mirrors M_2 and M_3. The laser is reflected back to mirror M_1 being directed to the lens (CL) to obtain an annular collimated beam. Finally, the light is diffracted by the first order of the diffractive optical element is symmetrically directed from both sides towards the specimen surface. Mirror M_2 is attached to a

piezo translator (*PZT*) to introduce a constant phase shift between both illuminations in order to calculate wrapped phase maps using phase shifting algorithms.

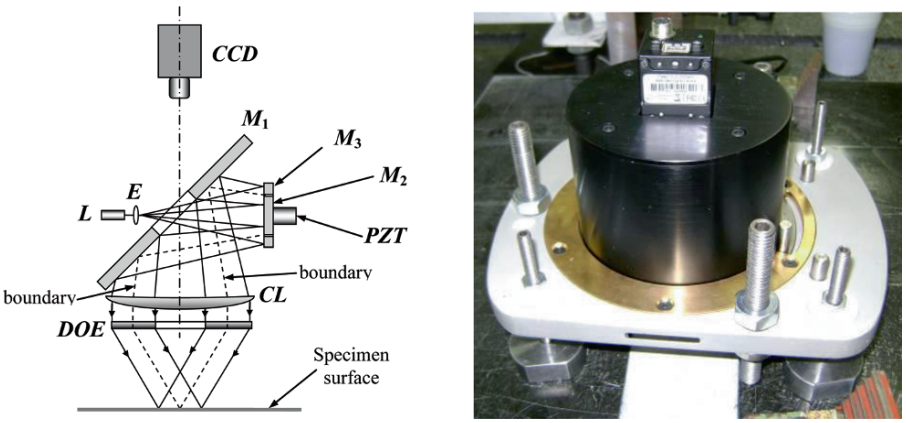

Figure 2: Practical realization of the radial in-plane interferometer.

Figure 3 shows the complete set used for residual stresses measurement. A universal base is rigidly attached to the specimen surface by four rare earth magnets combined with three rods with sharp conical tips. The optical head is shown in the right part. The left part shows the hole drilling unit equipped with a high speed pneumatic turbine. A kinematic mounting scheme makes the positioning and replacement of both modules to the universal base very repeatable. After attaching the universal base to the surface where the residual stresses have to be measured, the optical measurement module (OMM) is positioned in the universal base and an initial phase pattern is acquired and digitally stored. After that, the OMM is removed and replaced by the high speed drilling module (HSDM). The drilling is done until a predefined depth is reached. Air is continuously blown during the drilling to remove metal chips from the measurement area. The HSDM is removed and the OMM positioned again and another phase pattern is acquired. The process is sequentially repeated until the predefined number of drilling increments is reached. After that, the phase differences are calculated, digitally processed and the residual stresses computed. The total measurement time depends on the number of increments. However it is typically only 25% of the time required to do the same measurement with hole drilling and strain gauges.

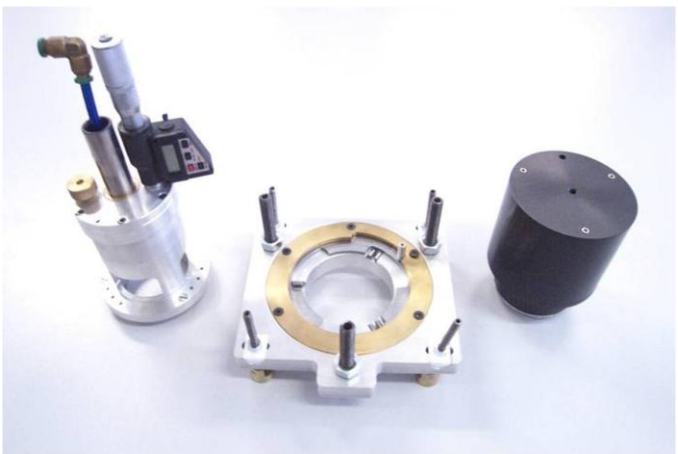

Figure 3: The set used for in-field residual stresses measurement. Left: hole drilling unit; central: universal base and right: optical measurement module.

3. Residual stresses measurement in a gas pipeline

The optical residual stresses measurement system was used in a risky area of a gas pipeline located in a steep hill near to a small river. The soil moves constantly at that region. A contention structure was built in order to minimize soil movements

and interactions between it and the pipeline. The measurements were used to estimate the amount of soil loading as a way to investigate the effectiveness of the contention structure. The quantity already measured by the hole drilling technique is the total amount of stresses acting on the material. This amount is a combination of real residual stresses coming from the pipe manufacturing process plus mechanical service stresses due to the internal pressure and soil/pipeline interaction. In order to estimate the effect of the soil/pipeline interaction, an additional measurement must be done in a reference section with known loading. Figure 4 shows the interferometer installed in a section of the gas pipeline.

The measurements were made in five different cross sections, located in different places along a very sloppy area. For each section, the measurements were made in four points in order to have enough data to compute the axial loads as well as bending moments. Three reference sections were measured in a sample of the pipe, kept free from external loading. The amount of axial load and bending moments were computed for five different cross sections. The estimated amount of longitudinal loading for the five sections is shown in Figure 5.

Figure 4: Measurement of loading components in a gas pipeline using the radial in-plane interferometer and the hole drilling method.

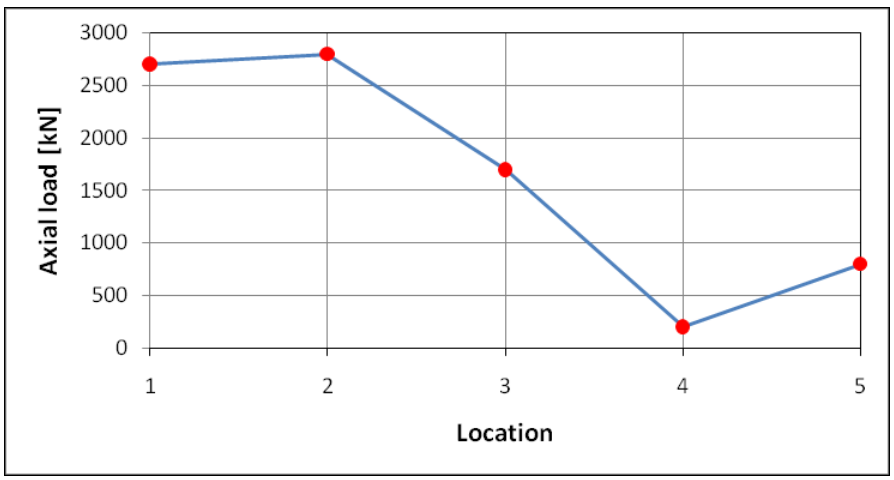

Figure 5: Amount of longitudinal load estimated for five sections along the pipeline. The values are in kN.

4. Optical profilometer with conical triangulation

The first optical profilometer presented in this paper uses a radial light sheet and conical triangulation to measure the inner geometry of pipes in cylindrical coordinates.

4.1 Measurement principle

A collimated laser beam is directed to the nose of a 45° conical mirror to form a radial light sheet. The reflected laser light propagates radially all way around 360° and perpendicularly to the conical mirror axis, as shows Figure 6. The light sheet intercepts the inner surface of the pipe producing a light ring. If the inner geometry of the pipe is perfectly circular, and the alignment of the optical components is ideal, the light ring is seen as a perfect circle by a camera through a wide angle lens. As the inner geometry of the pipe departures from perfectly circular, the camera image of the light ring becomes distorted.

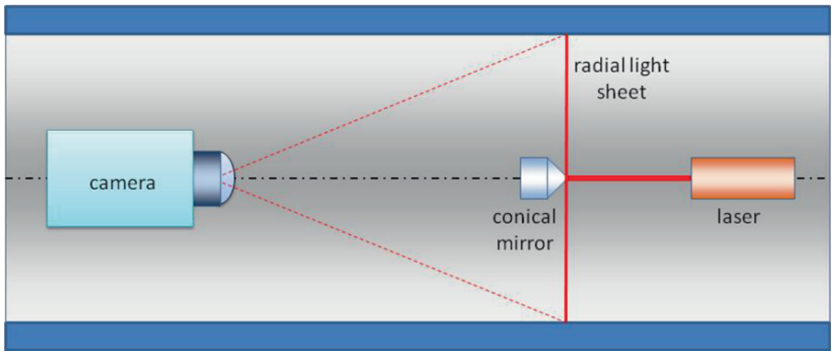

Figure 6 – Measurement principle of the optical profilometer.

The theoretical relationship between the camera image of the light ring and the geometry of the actual light ring in the internal pipe surface can be determined by using a simple pinhole camera model. A calibration is done to correct the ideal relationship due to misalignments and lens aberrations. The left part of Figure 7 shows the profilometer in an optical bench measuring a test profile with known geometry. The laser ring image is processed in order to extract a regular array of points with the radius values as a function of the polar angle θ. Since the laser ring is much brighter than the rest of the image, it is easy to locate the radial position of the laser line for any given polar angle θ. The image is scanned along a virtual radial line. The laser line location is related to the intensity peak. The right part of Figure 7 shows the negative of the light ring image its sampling with a constant $\Delta\theta$ increment. The actual increment is of 0.25°, what produces 1440 discrete points. The image processing is done in high speed and in a parallel way in a graphical board using NVIDIA's parallel computing architecture (CUDA). Up to 50 images are acquired and processed every second.

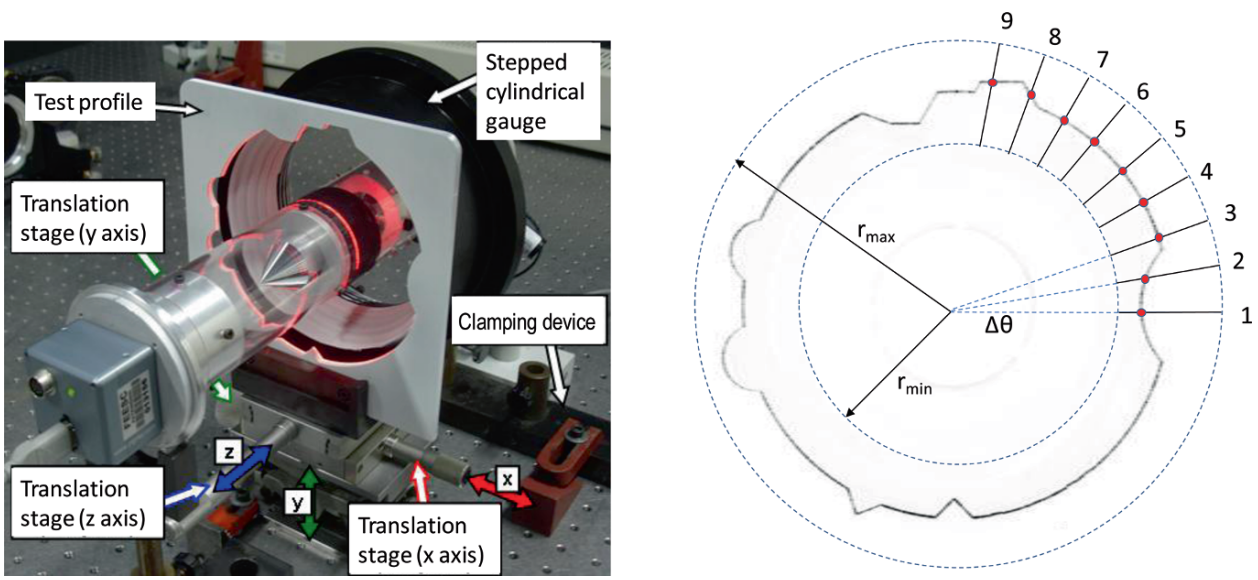

Figure 7 – Left: the profilometer measuring the inner geometry of a test profile. Right: negative of the light ring image of the test profile and the sampling scheme.

To measure the inner geometry of the pipe, the whole device is continuously moved along the pipe axis. The laser ring image is acquired every time the device is moved by a predefined displacement step ΔZ, forming a regular mesh of measured sessions, as shows Figure 8. In the actual device typically one image is acquired for, for example, each 1.0 mm displacement step. After processing, a regular cloud of points in cylindrical coordinates of the inner geometry of the pipe is formed. The lateral resolution of the cloud achieved in these conditions is about 1.0 mm in both directions, resulting in about 1.4 millions of data point per meter.

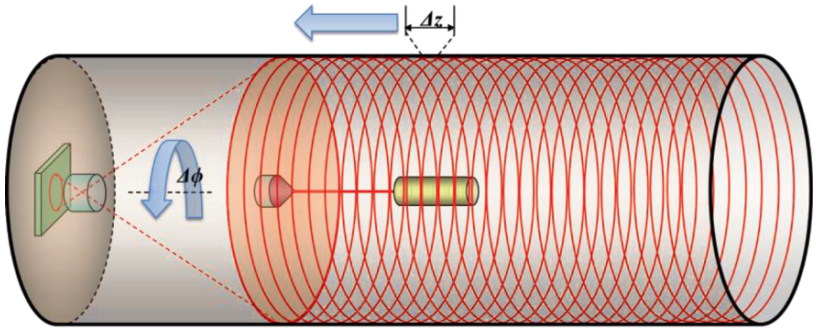

Figure 8 – Inner surface measurement while the device is moved along the pipe axis.

Considering that undesired rotation toward the pipe axis can happens ($\Delta\phi$ in Figure 8), an inclinometer was added to the optical profilometer to detect the amount rotation, so it can be compensated by the mearurement software. This procedure is necessary to keep the sections of the cloud of points properly oriented.

4.2 Constructive aspects

Figure 9 shows some constructive aspects of the developed optical profilometer. The laser and the conical mirror are fixed to a transparent tube by flanges. Both laser and conical mirror are carefully aligned to the axis of the transparent tube. The camera and imaging lens are inside of the housing in the left part of the transparent tube, as well as some electronics. Two sets of self-centering wheel trains are used to keep the profilometer approximately aligned to the axis of the measured pipe. The device has also a seventh wheel, which is connected to an odometer. The odometer is used to measure the profilometer position along the pipe axis as well to trigger the camera every time a given displacement increment (usually 1.0, 2.0, 5.0 or 10.0 mm) is achieved. That defines the lateral resolution along the pipe axis dimension. Since the triggering is defined by position increments, and not by time increments, the uniformity of the velocity of the profilometer is not a critical issue.

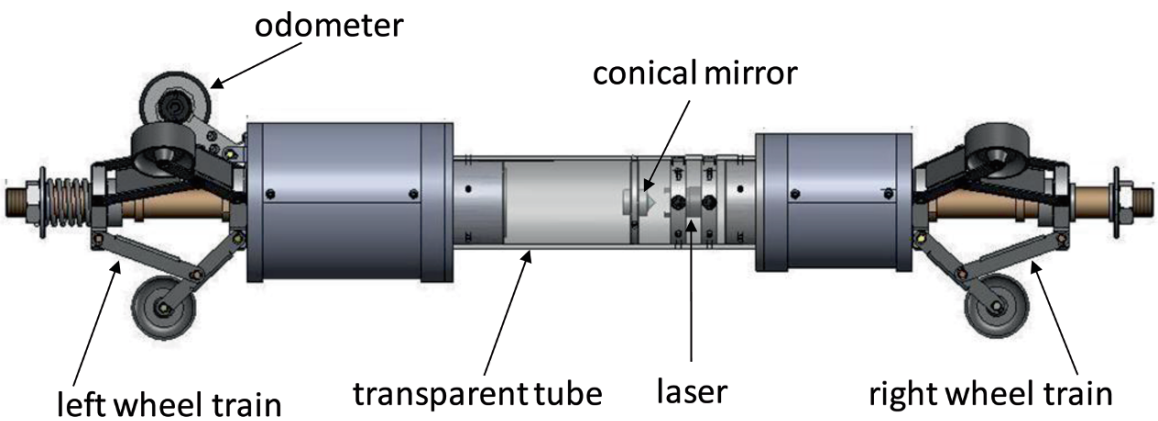

Figure 9 - Constructive aspects of the optical profilometer

4.3 Measurement results

In order to evaluate the performance of the profilometer a test bench was built. It consists of a 2.5 long pipe where the profilometer is pulled by a flexible steel cable with controlled velocity. The pipe has three removable gutters that can accommodate surfaces with artificial and known artifacts. The profilometer was used to measure the inner geometry of the test bench in the region of a gutter with 36 artifacts. The system was adjusted to acquire one section each 1.0 mm, moving about 30 mm per second. The resulting cloud of points is shown in Figures 11 and 12. Although the measurement was made from the inside, Figure 10 shows an external view of the inner surface of the pipe to emphasize the geometry of the cavities. The artificial artifacts are also visible in the upper part of this figure. Figure 11 shows an internal view of the measured surface. Both uses color scales to quantify the measured values. The dimensions are indicated in millimeters. Note that all the 36 artifacts are clearly present in the clouds of points.

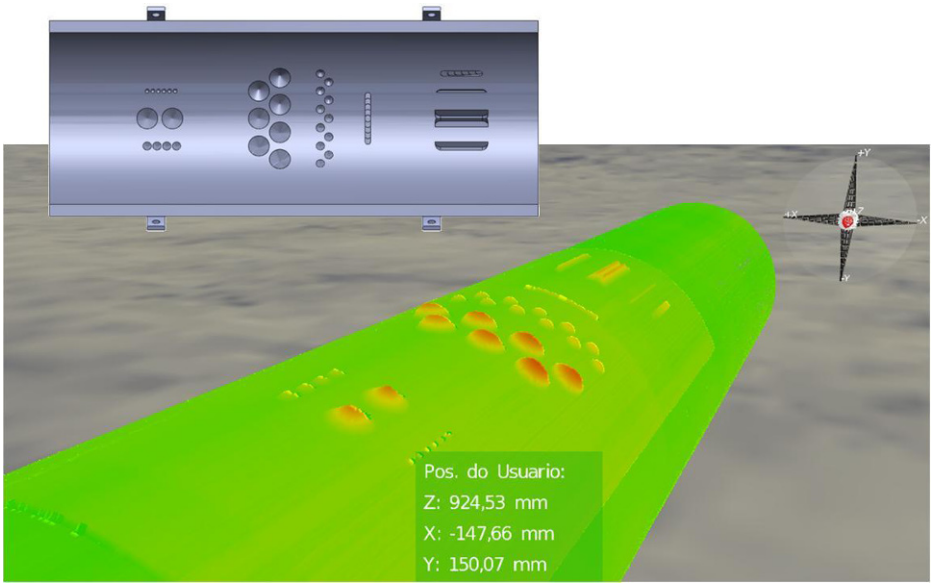

Figure 10 - Cloud of points from the test surface. External view.

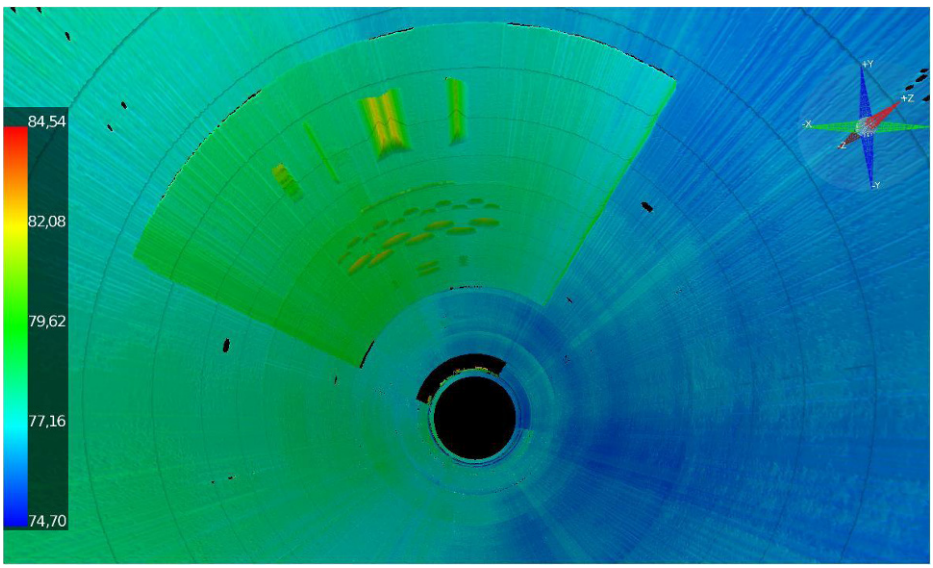

Figure 11 - Cloud of points from the test surface. Internal view.

Up to this moment the profilometer has been tested in laboratory conditions. Its uncertainty with 95% confidence level was estimated to be better than 0.3 mm. The profilometer is currently been prepared to run inside a real oven pipe with diameter of 152 mm (6") and about 50 m long. The goal is to inspect the pipe to find corrosion cavities. The measurement time is expected to be around 25 min and the amount of measurement data in the order of 70 millions points.

5. Optical profilometer with active photogrammetry

The second optical profilometer was developed to inspect and measure inner surfaces of welded pipe joints. The main application is to verify the weld seam geometry and to check for misalignments between two adjacent welded sections. In this case, measurement time is not a limitation. However, a much higher lateral resolution is required. A completely different optical measurement principle is used.[10,11]

5.1 Measurement principle

Photogrammetry is an optical measurement technique where 3D information about physical objects is obtained combining data extracted from two or more images acquired from different viewing angles.[12-14] Since the camera position, orientation and lens parameters can be determined by calibration, the 3D coordinates of a given point is space can be computed since its location on the acquired images can be determined. The accurate and efficient determination of corresponding points in multiple images is the most challenging task in photogrammetry. It becomes particularly difficult if the scene has a monotonous texture. In those cases, a very good approach is the use of active photogrammetry[15,16].

In active photogrammetry a sequence of light structures is projected in the scene. It can be done with a completely random texture or with a sequence of regular fringes[15, 16]. The idea is to encode phase information into the projected fringe pattern and use phase information to efficiently and accurately locate corresponding points. Usually a sequence of 3 or 4 phase shifted images are projected and acquired as well additional images to obtain the absolute phase values.

5.2 Constructive aspects

A special configuration of active photogrammetry is used to build the profilometer[10, 11]. The main elements are visible in Figure 12. Cameras A and B are two identical cameras aligned with the symmetry axis of the device and facing each other. The camera positions and lens parameters are chosen in such way that both cameras can see the central surface of the inner cylinder, delimited by dashed lines in the figure. A specially designed helical fringe projector is installed in the central part and is able to appropriately illuminate the central area of the inner cylinder all way around 360°. It is formed by a lamp and another transparent tube where a set of sinusoidal helical lines are printed. A halogen lamp projects the shadows of the helical lines producing a set of 360° helical fringes on the central part of the inner surface of the cylinder to be measured. The surface of the transparent tube, where the helical fringes are printed, is rotated by a calibrated amount through a step motor, represented in the right part of the figure. Since the fringes are helical, they can be phase shifted when the step motor is rotated. An external transparent tube is used to keep all those elements fixed and aligned to each other.

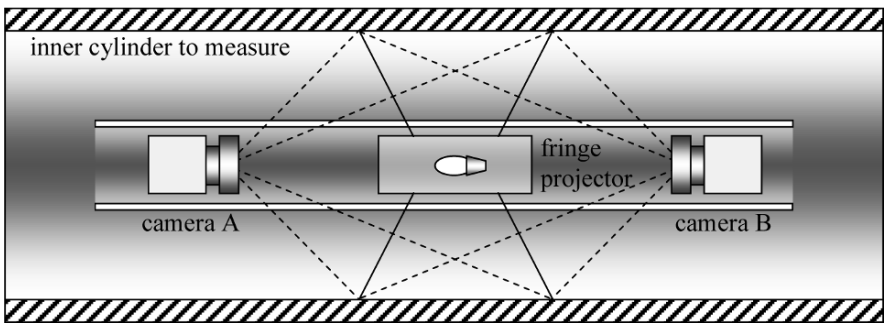

Figure 12 - Basic configuration of the photogrammetric profilometer.

Also here, a self centering mechanical device with two sets of three wheels is used to keep the endoscope approximately aligned to the cylinder axis. Figure 13 shows some constructive aspects of the built prototype. It was optimized to measure welded joints of 6” pipes (152 mm).

Figure 13 – Actual view of the photogrammetric profilometer.

5.3 Application

The target application for the profilometer was inspection of inner surface of weld seams during a pipeline manufacturing process. The idea is to insert the profilometer just after welding a joint since one end of the pipe will be open. After positioning, a sequence of images is acquired for each camera. The data is combined and processed in order to obtain the absolute phase pattern for each camera.

A 13 m long testing tube was built from 152 mm (6”) diameter pipes. A weld joint was prepared and inspected by the profilometer. The welded joint was intentionally prepared with welding defects. Two regions were welded with an unusual shallow welding seam and two regions with very deep welding seams. These defects will produce different welding seams geometries. Additionally, the welded pieces were intentionally misaligned producing a transverse translation of about 2 mm.

After phase unwrapping the images looks like the ones in Figure 14. The left phase image is for camera A and the right one is for camera B. Since each camera is in a different side, the image of one of the cameras was horizontally mirrored in such way that the left side becomes the right one and vice versa. Therefore, corresponding points are always located along radial lines with the same angular position. Note that the phase values decreases along a radial line coming from the center in the left image. In the right one the phase values increases. That is more clearly seen in the lower part of the figure. The “bumps” along the phase lines were produced by a welding seam located inside of a measured pipe.

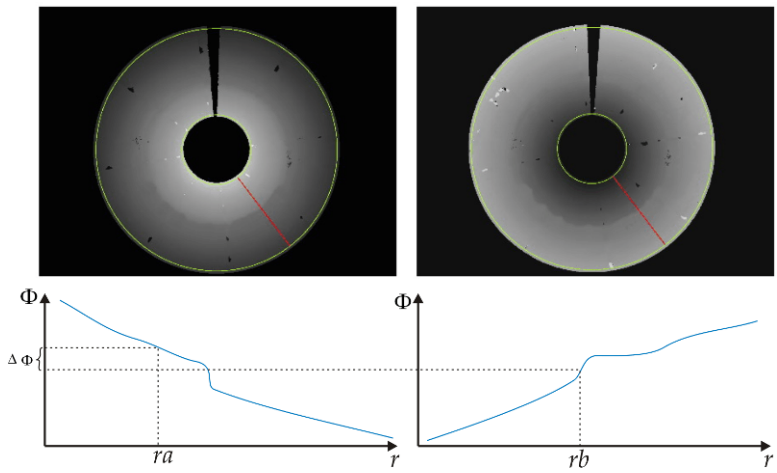

Figure 14 – Finding corresponding points using unwrapped phase information.

The region of the welded joint was measured. The obtained cloud of points is shown in Figure 15. The left part represents the measured surface using a continuous false color scale related to radial values. The lighter/darker areas in the upper left part of the left figure make clear the presence of a transversal misalignment between the jointed parts that is in the order of 2 mm. The welding seam is visible all way around 360°. In some areas it is like a deep grove. In others, it is like a protuberance. The right part of the figure shows another color scale that emphasizes only regions with too deep or too shallow welding seams.

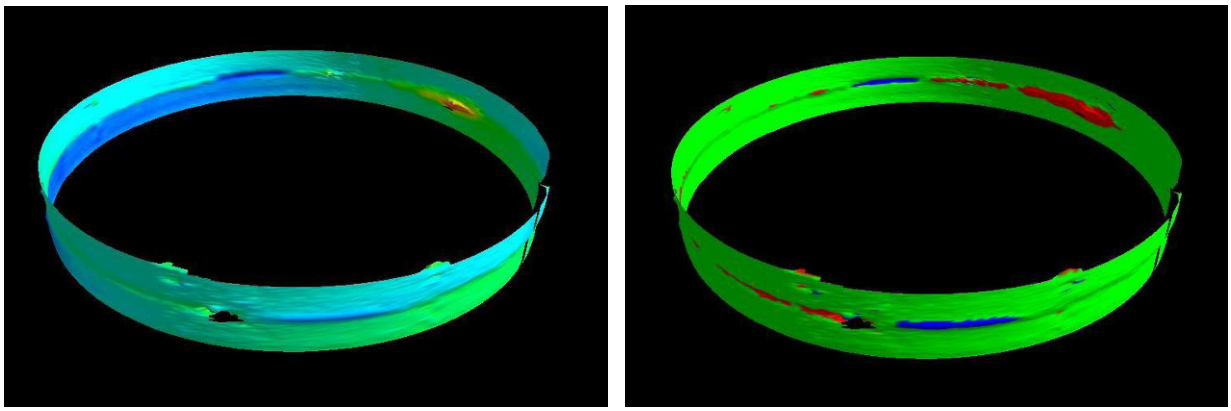

Figure 15 – Left: cloud of points acquired in the region of a welded joint represented in a false color scale. Right: the same cloud of points with a different color scale to emphasize regions with shallow or deep welding seam.

The measurement was repeated five times after removing and replacing the profilometer. The repeatability of the system for measuring both transverse misalignment and angular misalignment was very good. The sample standard deviation was below 0.04 mm for the transverse misalignment and 0.2° for the angular measurement, what is very good for the target application.

6. Conclusions

This paper presents three different optical measurement systems used for in-field measurements in pipelines. They were developed and optimized to meet specific demands. The radial in-plane DSPI interferometer has been commercially used along the last three years for gas or oil pipeline inspections in risky areas. The measurement uncertainty of this system is comparable to hole drilling technique with strain gauges. However, the measurement time is typically only 25% of the time required for strain gauge measurement. The profilometer with laser triangulation is in the final stage of development. Its measurement uncertainty is about 0.3 mm for the radius of any point. Its lateral resolution is of 1.0 mm in each direction. The maximum measurement speed range from 50 to 500 mm/s, depending on the lateral resolution selection. The profilometer will be used soon for inspection of 50 m long oven pipes, from where about 70 million points will be acquired. Finally, the photogrammetric perfilometer is used only in a static mode. The system is able to acquire a dense cloud of points with up to 0.05 lateral resolution, what is good enough for the target application. The standard deviations in misalignment measurement are about 0.04 for transverse misalignment measurement and 0.2° for angular misalignments.

7. Acknowledgements

The authors would like to acknowledge the valuable contributions of João Márcio Santos, Claudio Camerini, Cesar Kanda, Marcelo Moya, João Freitas, Danilo Santos, Darlan Becker, Fábio Silva, Guilherme Bencke, Luan Volpato, Prof. Wolffgang Osten, Eduardo Valim, Ricardo Gondo, Thiago Freitas, Wagner, Sunada, Dionísio, Fernando and Fabrício Broering and the financial support of Petrobrás/CENPES, ANP/PRH-034, FINEP, SEBRAE, CNPq, CTPetro, CEnerg, and Photonita.

References

[1] Viotti, M. R ; Albertazzi Jr, A. . Industrial inspections by speckle interferometry: general requirements and a case study. In: SPIE 2009 - Optical Metrology 2009, 2009, Munich, Alemanha. SPIE 2009 - Optical Metrology 2009, 2009. v. 7389. p. 73890G-1-73890G-15.

[2] Viotti, M. R. ; Kapp, W. ; Albertazzi Jr., A.; "Achromatic digital speckle pattern interferometer with constant radial in-plane sensitivity by using a diffractive optical element". Applied Optics, v. 48, p. 2275, 2009.

[3] Viotti, M ; Albertazzi Jr, A. ; Kapp, W . "Experimental comparison between a portable DSPI device with diffractive optical element and a hole drilling strain gage combined system". Optics and Lasers in Engineering, v. 46, p. 835-841, 2008.

[4] Albertazzi Jr, A. ; Viotti, M. R . "Radial speckle interferometry and applications. In: Guillermo H. Kaufmann. (Org.). Advances in speckle metrology and related techniques". Weinherim/Estados Unidos: John Wiley & Sons, 2009, v. 1.

[5] Kaufmann, G. H ; Albertazzi Jr, A. . Speckle interferometry for the measurement of residual stresses. In: H. John Caulfield; Chandra S. Vikram. (Org.). New Direction in Holography and Speckle. Valencia, California: American Scientific Publishers, 2008, v. , p. 1-22.

[6] Albertazzi Jr, A. ; Viotti, M. R ; Kapp, W. A. . Performance evaluation of a radial in-plane digital speckle pattern interferometer using a diffractive optical element for residual stress measurement. In: SPIE Optics + Photonics 2010: Interferometry XV: Applications, 2010, San Diego. SPIE Optics + Photonics 2010: Interferometry XV: Applications, 2010. v. 7791. p. 1-6.

[7] Albertazzi Jr, A. ; Viotti, M. R . In-field loading analysis of pipelines using a radial digital speckle pattern interferometer combined with the hole drilling method. In: OPTIMESS 2009 - 4th International Conference on Optical Measurement Techniques for Structure & Systems, 2009, Antwerp. OPTIMESS 2009 - 4th International Conference on Optical Measurement Techniques for Structure & Systems, 2009. v. 1. p. 1-6.

[8] Leendertz, J. A., "Interferometric displacement measurement on scattering surfaces utilizing speckle effect", J. Phys. E. Sci. Instrum., 3, 214-218 (1970).

[9] Buschinelli, P., "Development of an optical system with conical triangulation for inspection of inner profile of pipes", Universidade Federal de Santa Catarina, PosMCI program, Master of Science Dissertation, 2007 (in Portuguese)

[10] Albertazzi Jr, A. ; Hoffmann, A. C. H. ; Fantin, A. V. ; Santos, J. M. C. "Photogrammetric endoscope for measurement of inner cylindrical surfaces using fringe projection". Applied Optics, v. 47, p. 3868-3876, 2008.

[11] Albertazzi Jr, A. ; Hoffmann, A. C. H.; Pezzotta, A. V. F. ; Santos, J. M. C. . Development and application of a photogrammetric endoscopic system for measurment of misalignment and internal profile of welded joints in pipelines. In: SPIE 2009 - Optical Metrology 2009, 2009, Munich, Alemanha. SPIE 2009 - Optical Metrology 2009, 2009. v. 7389. p. 73891W-1-73891W-12

[12] Faugeras, O. D., [Three Dimensional Computer Vision], The MIT Press, (1993).

[13] Hartley, R.; Zisserman, A., [Multiple View Geometry], Cambrige University Press, (2003).

[14] Longet-Higgins, H. C., "A Computer Algorithm for Reconstructing a Scene from Two Projections", Nature, vol. 293, 133-135 (1981).

[15] Zumbrunn, R., "Automated Fast Shape Determination of Diffuse Reflecting Objects at Close Range by Means of Structured Light and Digital Phase Measurement", in Proceedings of ISPRS Intermission Conference on Fast Processing of Photogrammetric Data, 363–379 (1987).

[16] Carsten, R.; Ritter, R.; Thesing, J., "3-D Shape Measurement of Complex Objects by Combining Photogrammetry and Fringe Projection", Op. Eng. 39(01), 224-231 (2000).

[17] Fantin, A. V.; Pinto, T. L. F. C.; Albertazzi, A. "An Efficient Mesh Oriented Algorithm for 3D Measurement in Multiple Camera Fringe Projection". In: Optical Metrology 2007, 2007. Munique-Alemanha. Proceedings of SPIE, 2007. v.6616.

Contour Method Advanced Applications: Hoop Stresses in Cylinders and Discontinuities

Michael B. Prime (prime@lanl.gov)
Los Alamos National Laboratory, Los Alamos, NM 87545

ABSTRACT

The traditional contour method measures a cross-sectional map of residual stress by cutting a body carefully in two and measuring the surface contour. This talk will present two new advances, both motivated by the measurement of a single challenging part. The first advance is a two-step process for measuring hoop stresses in cylinders. In the first step, a cut is made to split the cylinder (from an “o” cross-section to a “c”). That cut releases a bending moment which would otherwise causes errors in the contour measurement. The amount the cylinder springs open or closed is measured and used to determine the bending moment stresses. In the second step, the traditional contour method is applied: a cut is made to measure the remaining hoop stresses on a cross section normal to the hoop direction. The total residual stresses are given by superimposing the bending stresses and the remaining stresses. In this paper, the two-step process is applied to measuring the stresses in a circumferential welded cylinder of depleted uranium and is compared to neutron diffraction results. The welded cylinder also contains a further measurement complication. The weld was only partial penetration, leaving part of the joint unwelded. The measured surface contour therefore had a discontinuity across the joint. Proper handling of the surface discontinuity is presented.

INTRODUCTION

The contour method is a relatively new method for measuring residual stress [1-3]. In the contour method, a part is carefully cut in two along a flat plane causing the residual stress normal to the cut plane to relax. The contour of each of the opposing surfaces created by the cut is then measured. The deviation of the surface contours from planarity is assumed to be caused by elastic relaxation of residual stresses and is therefore used to calculate the original residual stresses. One of the unique strengths of this method is that it provides a full cross-sectional map of the residual stress component normal to the cross section. The contour method is useful for studying various manufacturing processes such as laser peening [4-9], friction welding [5,10,6,11,12] and fusion welding [13-24].

The contour method has been extensively validated and applied for relatively simple geometries such as rectangular (or nearly rectangular) cross section bars and plates (examples above and [25-28]). Other applications involve more complicated cross sections but still prismatic extrusions [29,7,30] such as a railroad rails [31]. Occasionally, the contour method is applied to slightly more complicated geometries but ones that do not require much special effort [32-34].

This paper details a contour method application that involves two geometrical complications that require special attention. The first is the measurement of hoop stresses in a cylinder. The second is a discontinuity in the measured surface contour because of an unbonded butt joint.

Hoop Stresses in Cylinders

Pipes and cylinders are important geometries for residual stress measurement. A notable example is girth (circumferential) welds on piping and pressure vessels. Cracks cause concern for rupture in nuclear power plants [35,36]. To remain in service, such defected components must be demonstrated to be safe against rupture. Residual stresses are a main driver for the growth of cracks and must be known for crack growth and leak-before-break analyses [37-39]. Measurement of those stresses is difficult. Neutron diffraction is the most commonly published technique for measuring internal stresses. However, some components are too thick for neutron

T. Proulx (ed.), *Engineering Applications of Residual Stress, Volume 8*, Conference Proceedings of the Society for Experimental Mechanics Series 999, DOI 10.1007/978-1-4614-0225-1_2, © The Society for Experimental Mechanics, Inc. 2011

measurement and welds are often problematic because of spatial variations in the reference lattice constant caused by chemistry changes in and around the weld [40-42] or the presence of microstresses [42]. The deep hole method [43] has had the most success on very thick components but measures only a 1D stress profile. For all of the reasons, the ability of the contour method to measure a cross-sectional map of hoop stress in a cylinder is important.

Measuring hoop stresses in a cylindrical geometry requires special attention with the contour method. In simply-connected geometries, residual stresses must satisfy force and moment equilibrium over any cross section. Because the cylinder is a multiply-connected geometry, the residual hoop stresses can have a net bending moment through the thickness of a ring, see Fig. 1. Even for axisymmetric stresses, the moment is balanced by the opposite moment at any other cross section. For a contour method measurement of hoop stress, a radial cut is used. During cutting, because of the bending moment, excessive stresses build up at the cut tip and can cause plasticity. Since the contour method assumes elastic stress relaxation, errors can result and have been observed with the contour method [3] and similarly with the crack compliance method [44].

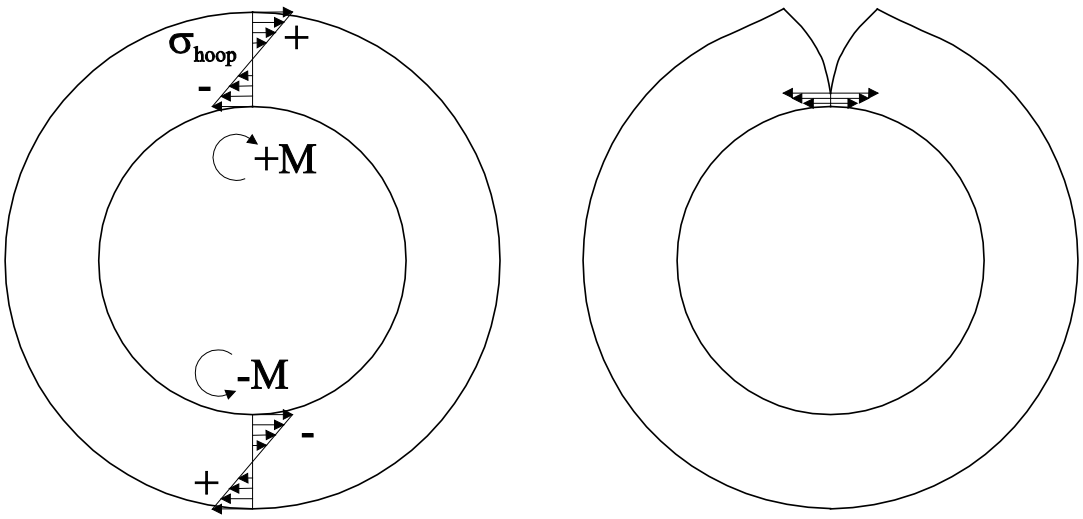

Fig. 1 Residual hoop stresses in cylinders can have a net bending moment (left), which can cause excessive stresses at the cut tip (right) when making a contour method measurement of hoop stress.

Discontinuity

Butt joints are often joined using only a partial penetration weld for several reasons. A partial penetration joint is often used for cost and simplicity reasons when the strength of a full penetration weld is not required. Other times, especially in pipes in cylinders, partial penetration is used to protect more delicate inner layers from heating or to maintain geometric tolerances inside the structure.

When a weld joint that includes an unfused portion is cut for a contour method stress measurement, the two sides of the unfused joints may deform such that there is a discontinuity in surface height on the cut surface. A conventional analysis of contour method data would involve smoothing and not allow a discontinuity. To achieve accurate results, the discontinuity must be properly preserved during data processing.

EXPERIMENTAL

Residual hoop stresses were measured in a cylinder with a partial-penetration weld butt-joint. The stresses measured with the contour method were recently compared with neutron diffraction measurements [45]. Space limitations in that paper prevented the presentation of details regarding the contour method measurements, which are detailed in this paper. The neutron measurement details are not repeated here.

Specimen

Fig. 2 shows a schematic, drawn approximately to scale, of the welded uranium sample studied in this work. The individual cylinders were as-cast depleted uranium. The sample had the form of a tube 131 mm in axial length with an inner diameter (ID) of 122 mm. At one end, termed the “A” end the outer diameter (OD) was 149 mm but at the opposite end, the “B” end, the outside surface was chamfered down to an OD of 137 mm, resulting in a wall thickness of 14 mm at the “A” end and 8 mm at the “B” end. In this paper, the axial coordinate *y* is measured relative to the “A” end and the radial or *x* component is zero at the rotation axis.

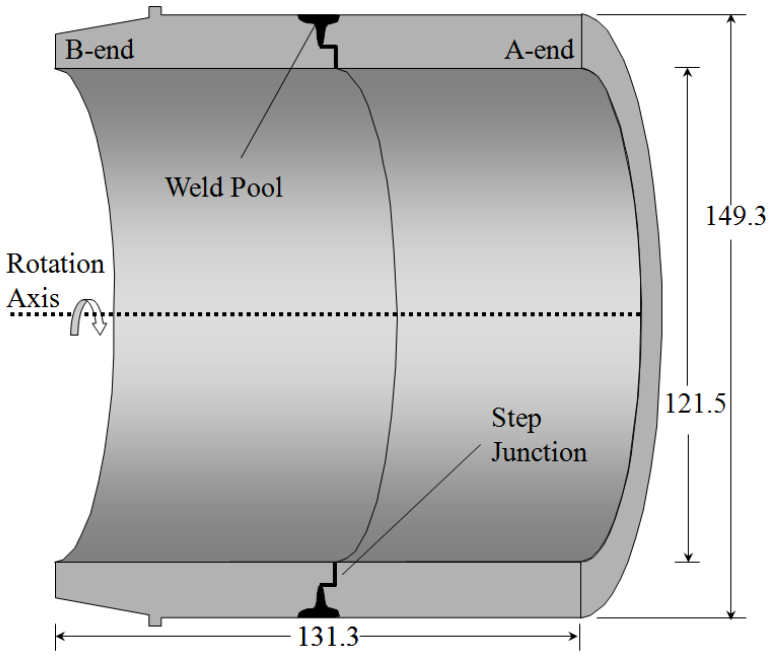

Fig. 2. Schematic of the electron beam welded uranium tube. Dimensions are approximately to scale. From [45].

The cast cylinders were machine fit at a step joint, as shown schematically in Fig. 2. The weld was a two-pass partial-penetration, autogenous electron beam weld centered at 64.8mm from the “A” end. The first pass, with the e- beam focused, penetrated roughly half of the thickness, bonding the two cast cylinders. The e- beam was then defocused for the second, cosmetic weld pass. The microstructure of the weld is detailed elsewhere [45].

Contour method procedure

In order to avoid plasticity at the cut tip, a novel, multiple-step variation of the contour method was used to measure hoop stresses over a radial-axial cross-section of the cylinder, see Fig. 3. The first cut severed the cylinder, which relaxed the bending moment. The resulting opening is measured and used to calculate the bending moment stresses. A subsequent cut is used to measure the remaining the remaining hoop stresses with the contour method. Because the bending moment is relaxed prior to the contour cut, plasticity issues are avoided.

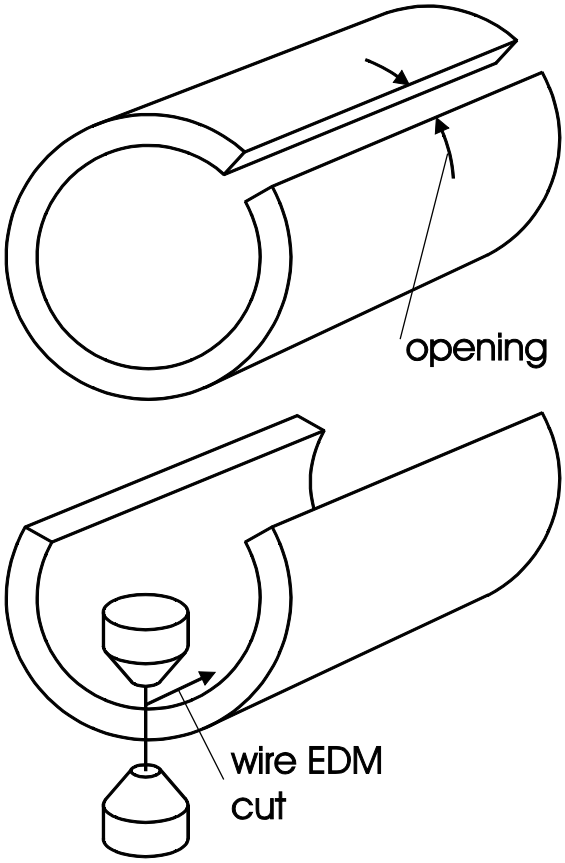

Fig. 3. Multi-cut process for measuring cylinders. The amount of opening, measured after the first cut, is used to determine the released bending moment prior to the final EDM cut used for the contour method. From [46].

A total of three EDM cuts were made on the uranium tube. Each cut operation used a 100 μm diameter brass wire and "skim cut" settings to reduce the introduction of new stresses [47]. Pairs of scribe lines, separated by about 6mm, were made along the length of the cylinder on the OD. The first EDM cut was made between the scribe lines with the wire oriented axially and translated radially. After unclamping, the relative displacements of the scribe lines were optically measured at 25 mm increments along the length of the tube. The second cut, taken at ~120° counter-clockwise from the first radial cut direction, was used to provide access for the third cut, but has no significant effect on the stresses measured by the third cut. The larger remaining section of the specimen was then measured with the contour method. A stainless steel fixture was machined to securely clamp the part along the ID and OD surfaces. To achieve better cut quality, the wire was now oriented in the radial direction and translated axially to make the cut.

After the final cut, the contours of the opposing surfaces were measured in a temperature controlled environment using a Coordinate Measuring Machine (CMM) with a 0.5 mm diameter ruby touch probe. The surfaces were scanned on a 0.5 mm grid giving about 6800 points per surface.

DATA

As a result of the first cut, the cylinder sprung open by 1.27 ± 0.01 mm uniformly along the length of the cut.

Fig. 4 shows the contours measured by the CMM on the two surfaces created by the third cut. One of the surfaces has been flipped to match the orientation of the other. The peak-to-valley range of the contours exceeds 40 μm. The close agreement between the two contours indicates that the part was clamped well during the cut and the experimental conditions were symmetric [48]. The contours are low in the weld region (right edge, mid height in this figure, see Fig. 2 for weld geometry) as would be expected if tensile stresses were relieved. A height

discontinuity is evident cross the joint near the ID, which is mechanically admissible because of the un-joined material associated with the partial penetration weld.

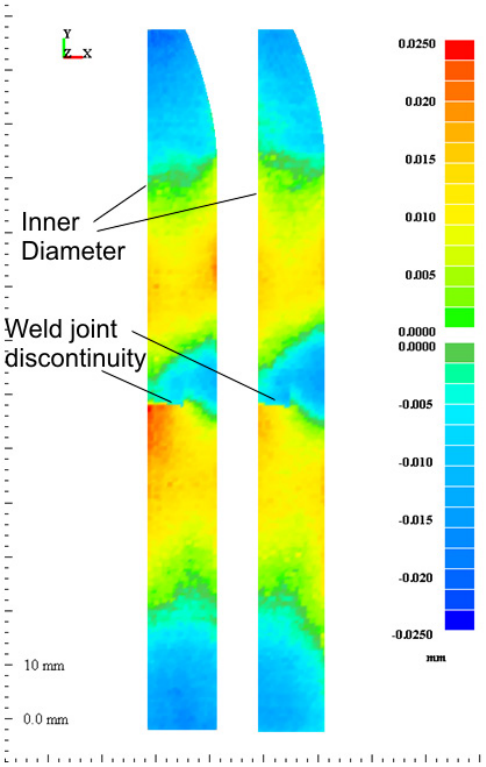

Fig. 4. Surface height contours measured on the two opposing surfaces created by the cut show the expected low region near the weld and also a discontinuity at the unwelded portion of the joint, near the ID.

ANALYSIS

The contour method analysis assumed isotropic elasticity with E=195 GPa, ν = 0.21.

A 3D elastic finite element (FE) model was used to calculate the stresses from the contour data. The perimeter of the cross-section was modeled based on the CMM data, and then the surface was meshed with 2D elements. The elements were not joined across the un-joined portion of the step joint. The 2D surface mesh was extruded circumferentially to produce 3D meshes 180 degrees and 120 degrees in extent to analyze the first and third cut data, respectively. The elements were approximately cubes 1.4 mm on a side near the cut surface and graded to be coarser in the circumferential direction farther away. The 180 degree mesh had almost 90,000 bi-quadratic (20 node) reduced integration hexahedral elements. No contact surfaces were used in the un-joined portion of the joint. Observation of the joint after cutting indicated that the gaps between the surfaces were sufficient to prevent contact.

First cut – bending moment

The first FE analysis, using the 180 degree mesh, was used to calculate the bending moment stresses released in the first cut. A symmetry plane was used to constrain one surface and concentrated forces were used to apply a bending moment on the opposite surface, see Fig. 5. The force magnitude was scaled until the surface in the half-symmetry model deformed the opposite amount of the opening observed experimentally.

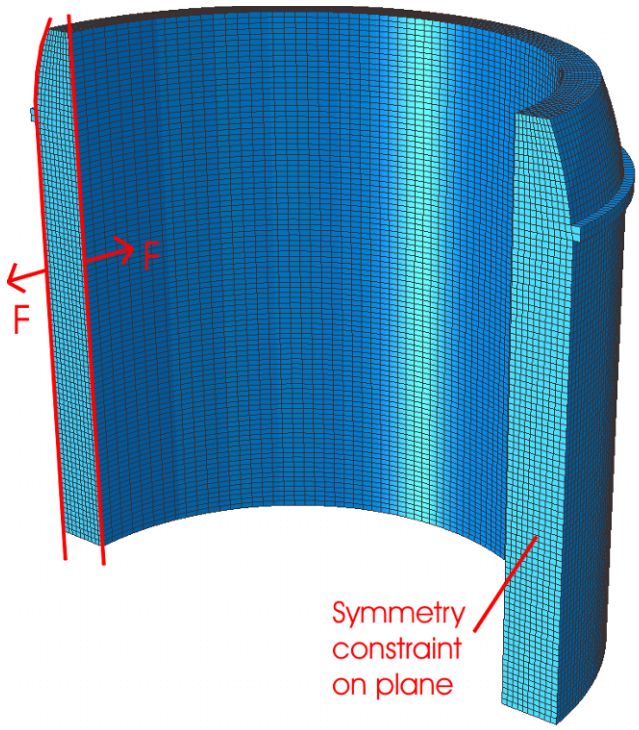

Fig. 5. Finite element calculation of bending moment stresses.

Contour method cut and discontinuity

In the contour method, the stresses are calculated in a finite element model by forcing the cut surface into the opposite shape of the measured contour [1]. For this experiment, converting the raw data into a form suitable for stress calculation generally followed standard procedure [3,2], except for some special care because of the discontinuity in the surface contours across the un-welded portion of the joint, see Fig. 4. The two opposing surfaces created by the cut were aligned with each other and then the data was interpolated onto a common grid and averaged. To handle the discontinuity, the surface was divided into two regions on either side of the weld joint with a few mm of overlap only in the part joined by the weld, see Fig. 6. Each region was then smoothed using quadratic bivariate spline fits with an optimal knot spacing determined to be about 5 mm. The two smooth surfaces were then joined together which resulted in discontinuities matching the data but a continuous joint in the weld region where the two regions overlapped.

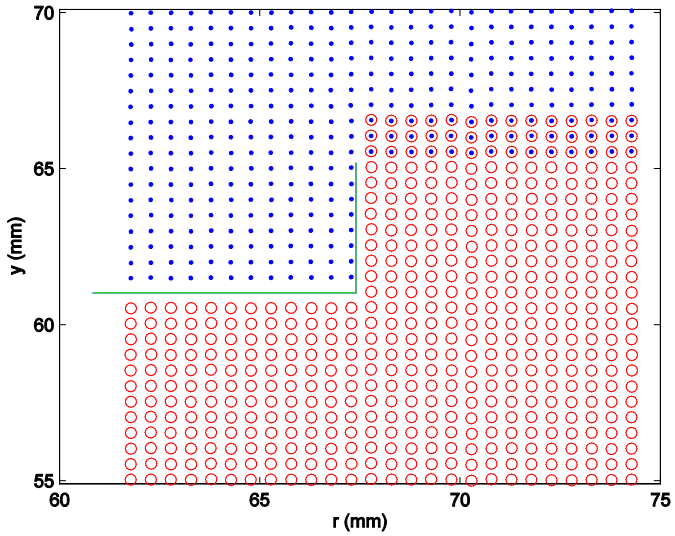

Fig. 6. Grid points used for fitting surface, zoomed in near weld region of Fig. 4. The green line indicates the unwelded portion of the joint and hence the discontinuity. The red and blue points are the grid points for the two fitting regions, which overlap in the weld region to ensure continuity.

The joined surface was evaluated at nodal coordinates in order to apply displacement boundary conditions to the FE model. Fig. 7 shows the FE model after the displacements were applied to the cut surface to calculate the stresses from the third cut. In this analysis, the other surfaces are unconstrained. The discontinuity across the joint is evident in Fig. 7. For the calculated stresses, a one standard deviation uncertainty of ± 25 MPa was estimated considering random errors in measured contours and uncertainty in the amount of data smoothing [2] but not any systematic errors.

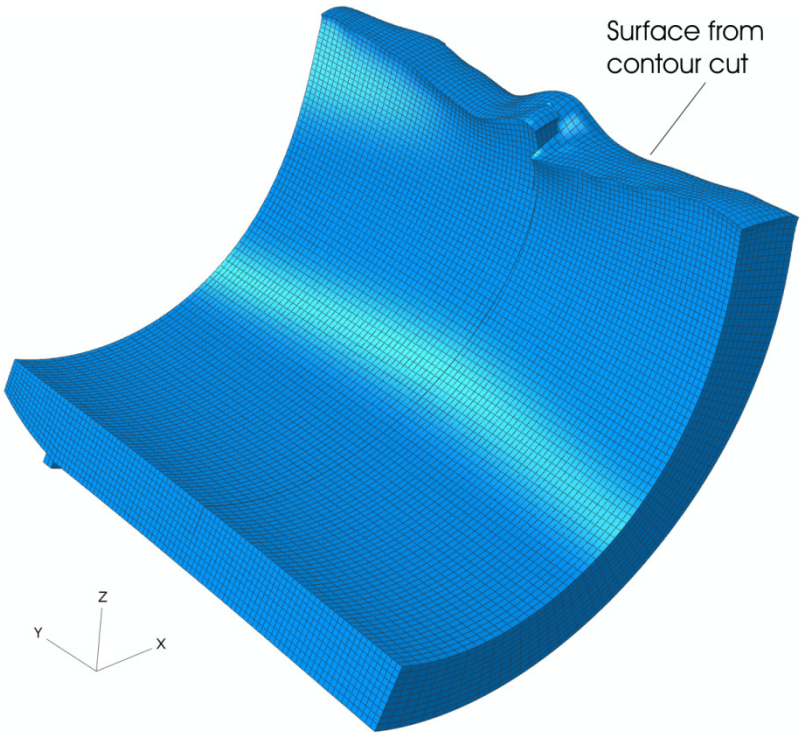

Fig. 7. The finite element model of a section of the cylinder with the cut surface deformed into the opposite of the measured contour. Displacements magnified by a factor of 300.

The stresses calculated from the contour analysis (Fig. 7) were added to the bending moment stresses calculated from the first cut (Fig. 5) to determine the total residual stress.

RESULTS

Bending moment stresses

The bending moment stresses given by the analysis of Fig. 5 are shown in Fig. 8. The stresses varied nearly linearly from about -60 MPa on the inner surface to about 50 MPa on the outer surface.

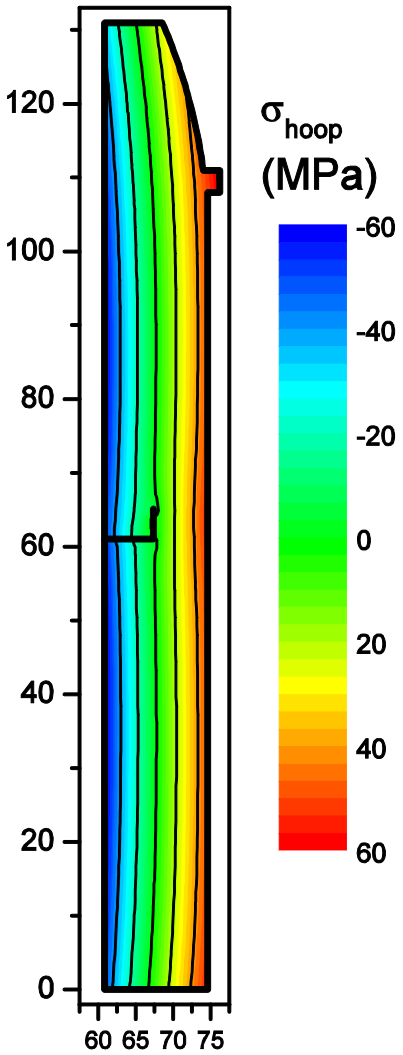

Fig. 8. Bending moment stresses calculated from the amount the cylinder sprung open (see Fig. 3) after the first cut.

In order to validate the bending moment stresses measured by the first cut, the results are compared with the neutron diffraction measurements [45]. The neutron diffraction measurements were taken before the cylinder was cut and, therefore, give the total stresses. Fig. 9 shows the comparison, with stresses plotted through the thickness of the cylinder. The neutron results are plotted for all of the measurement points, taken at multiple axial positions along the cylinder. The bending moment stresses measured by the first cut agree well with the linear trend in the neutron stresses, as they should. Since the non-bending stresses must satisfy equilibrium, an average of the total stress over the axial length of the cylinder should give only the bending stresses. In order to compare, such an average of the neutron stresses was calculated. Because the neutron sampling volumes were not equally spaced, the averaged was weighted in order to approximate a true spatial average. Also, the average

was only taken at the three radial locations where the neutron measurements spanned the full length of the cylinder (the same data is potted later in Fig. 11, Fig. 12, and Fig. 13). The average of the neutron stresses is plotted in Fig. 9 and agrees quite well with the bending stresses measured by the first cut.

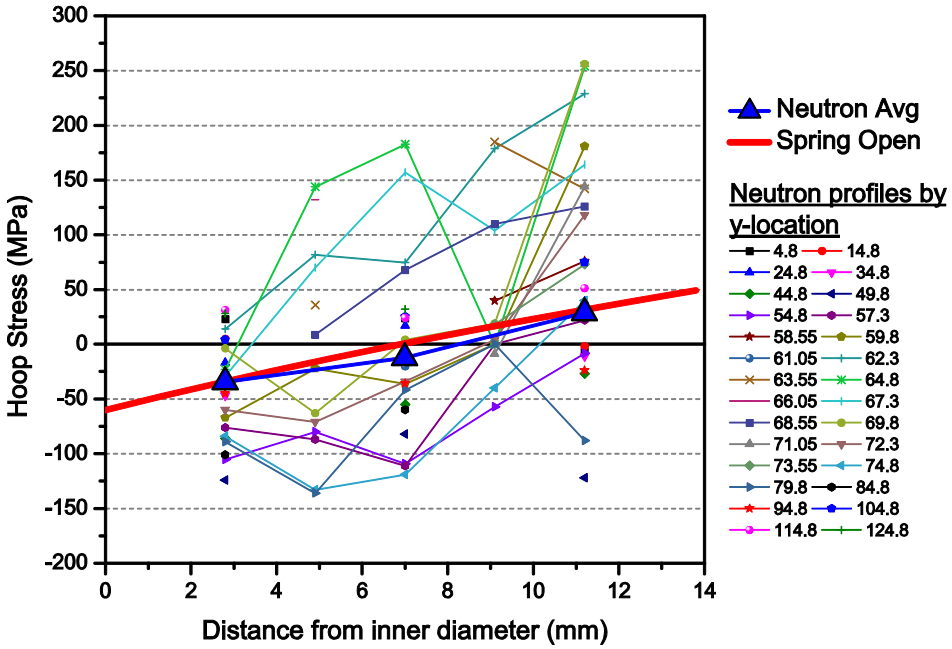

Fig. 9. Bending moment hoop stresses calculated from the "spring open" measured in the first cut compared with neutron diffraction measurements of *total stress*. The bending stresses agree well with the trend in the neutron data and with the average neutron stress.

Total stresses

Fig. 10 shows the hoop stresses measured in the welded cylinder. Fig. 10a shows the stresses calculated by the contour method analysis of Fig. 7. Fig. 10b shows the total stresses measured by the contour method, from adding the bending moment stresses of Fig. 8 to the stresses in Fig. 10a. Since the peak bending stresses are only about 15% of the peak total stress magnitudes, the correction is relatively minor. Fig. 10c shows the hoop stresses measured by neutron diffraction. The stress distribution is qualitatively similar, but the neutron-measured stresses are much lower in magnitude.

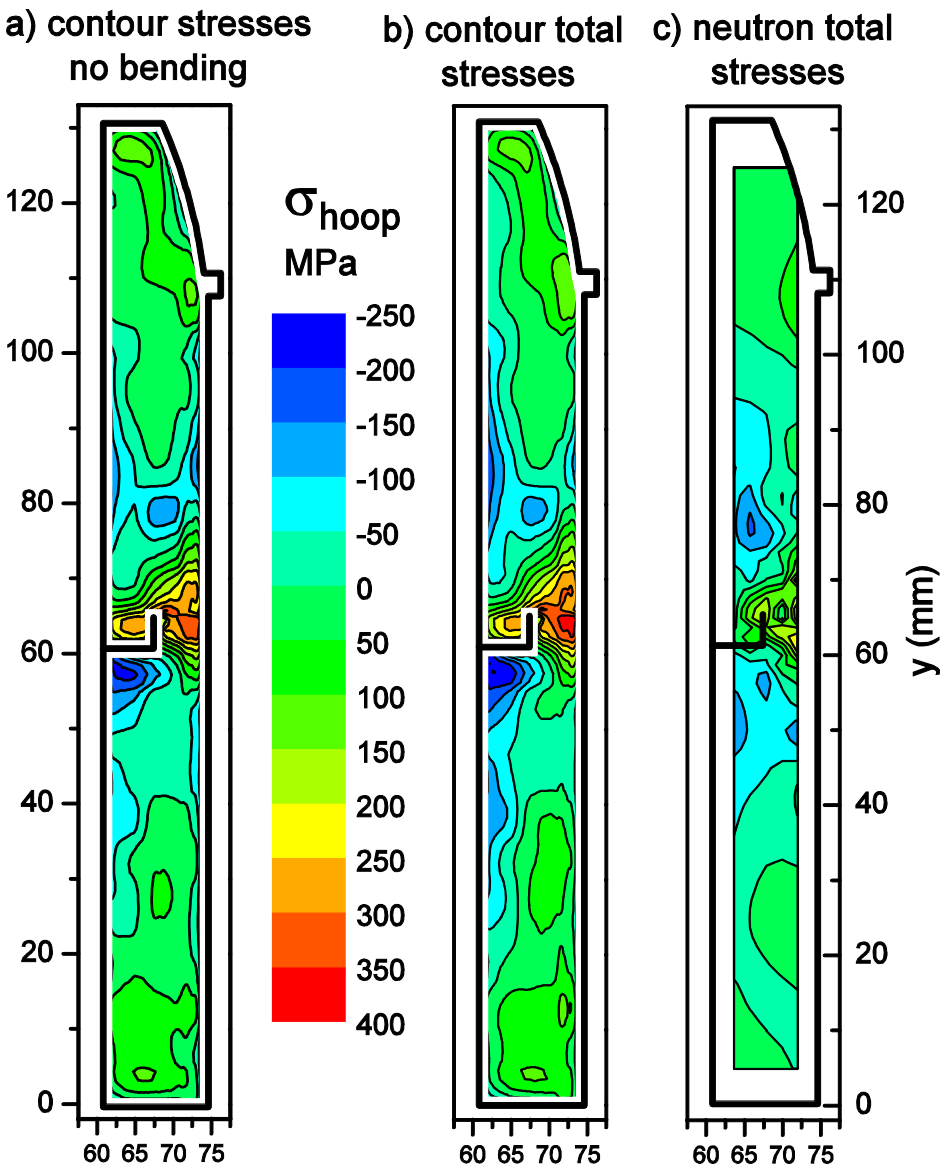

Fig. 10. Measured hoop stresses.

To further illustrate the issues, the results (Fig. 10 b and c) are compared along three neutron scan lines located at different locations through the thickness of the cylinder wall. Fig. 11 shows the comparison along the scan line near the cylinder inner diameter, which is the only scan line to cross the unfused portion of the joint. The contour and neutron results agree quite well away from the joint but not near the joint. Fig. 12 shows the comparison near the mid-thickness of the cylinder wall. Outside the weld region, results generally agree, with stresses differing nearly by a constant offset of ~40 MPa. One possible source for such an error can be the unstressed lattice spacing, also known as d_0, used in calculating strains and then stresses from the neutron diffraction measurements [41,42]. The weld stresses differ by more like 100 MPa. Fig. 13 shows the comparison along the scan line near the cylinder outer diameter. A shift of ~40 MPa would bring the comparison in better agreement away from the weld, but the contour stresses are again about 100 MPa higher in the high tensile stress region of the weld. For reference, note that the contour method FE stress calculation automatically enforces the constraint that the stresses satisfy force equilibrium. Because the neutron measurements do not cover the entire cross section, it is difficult to make conclusions about equilibrium.

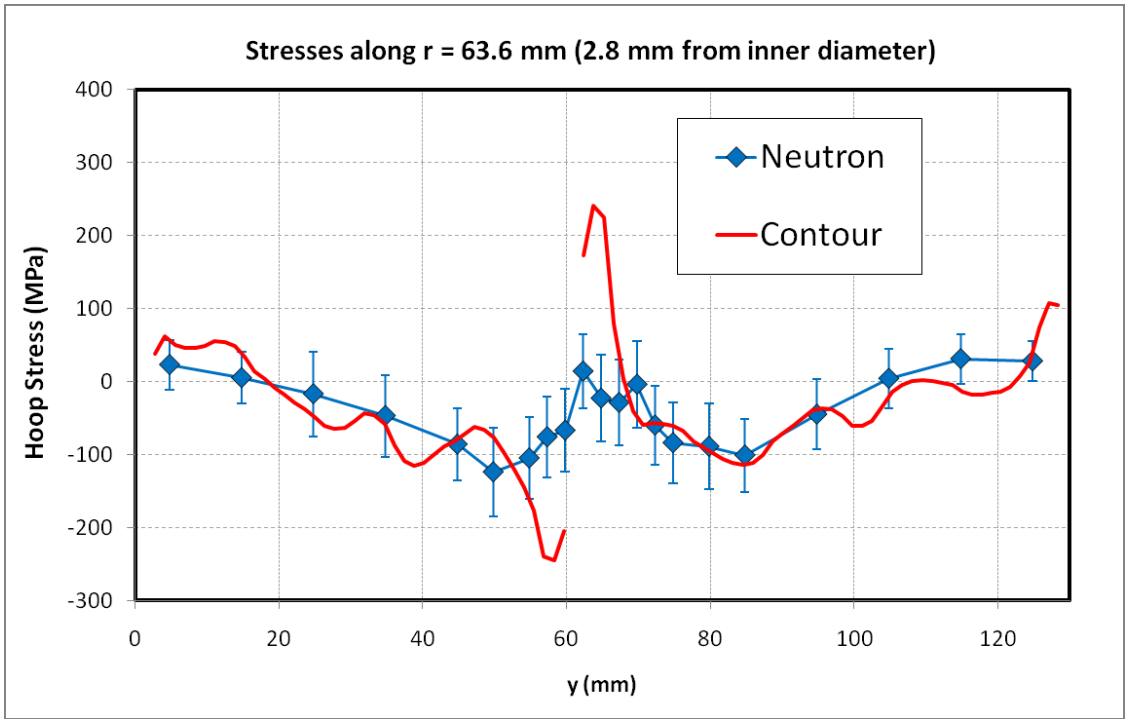

Fig. 11. Stresses along neutron scan line located about 2.8 mm from the cylinder inner diameter. This path crosses he unwelded joint at y=61

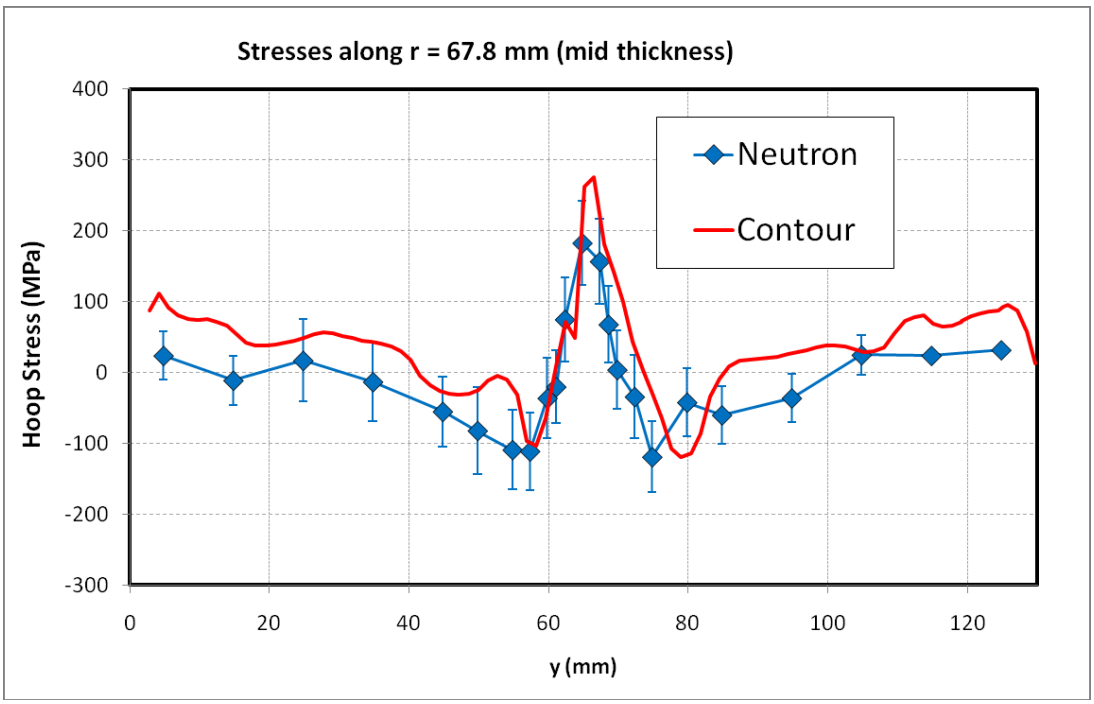

Fig. 12. Stresses along neutron scan line centered about mid-thickness in the cylinder.

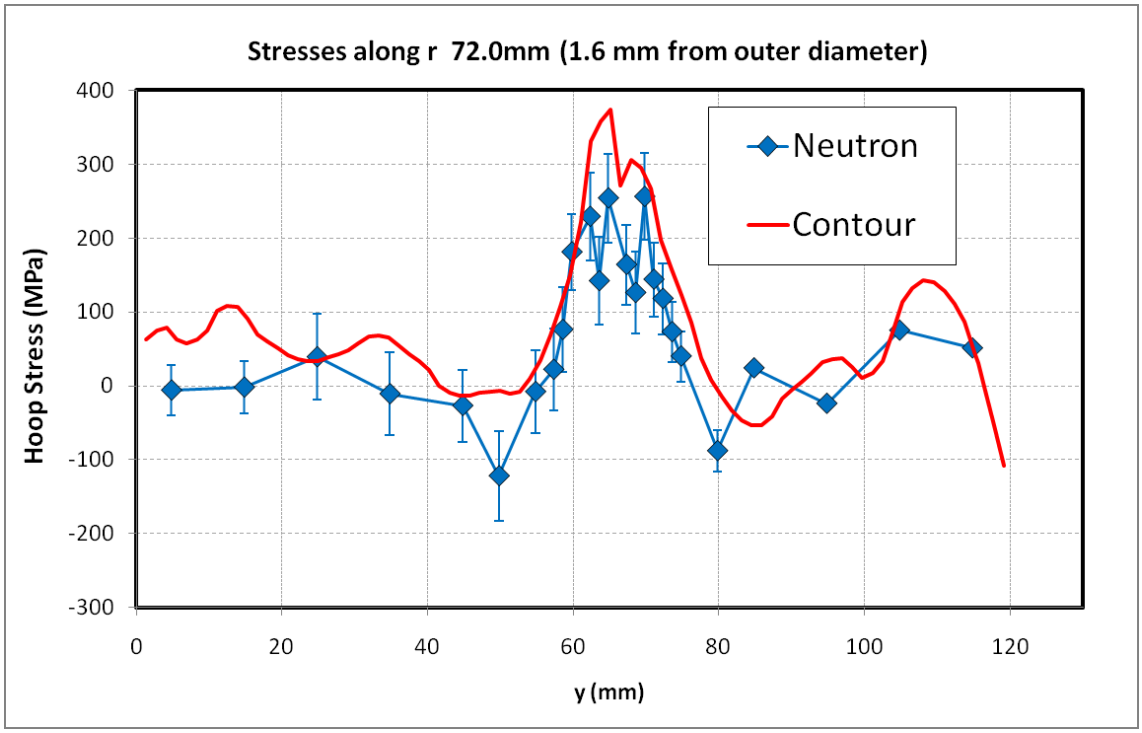

Fig. 13. Stresses along neutron scan line located about 1.6 mm from the cylinder outer diameter.

DISCUSSION

The contour method stresses are in reasonable agreement with the neutron results away from the weld region. The minor trend in the disagreement of the neutron stresses being lower by about 40 MPa might be explained by errors in the unstressed lattice spacing in the neutron measurements.

The contour method stresses are significantly higher than the neutron stresses in the tensile region of the weld. As will be discussed in the following paragraphs, there are many possible explanations for the difference. Some explanations are that the comparison does not fairly compare stresses at the same location. Other explanations include possible errors in both the neutron and contour measurements.

The neutron and contour measurements were not made over spatially identical regions. The neutron sampling volumes were 2×2×2 mm cubes. Because of issues with large grains, the neutron measurements were averaged around the circumference of the cylinder by rotating the cylinder during the measurements, effectively sweeping the sampling volume around the entire cylinder. There are two issues with the circumferential averaging. First, tolerances for both the part itself and the alignment and rotation during neutron measurements would make it likely that sharp discontinuities and gradients, such as in Fig. 11, would be smeared out in the neutron results. Second, the circumferential averaging would average in any changes near the start and stop of the weld, which can have significantly different stresses [22]. The contour results, by contrast, are taken only at the circumferential location of the cut. Unfortunately, the start-stop location of the weld was not known, so it is possible although unlikely that the contour results reflect localized stresses near the start or stop.

The results were challenging for neutron diffraction, which may have resulted in some errors. The uranium alloy has an orthorhombic crystal structure and had large grains, both of which made the neutron measurements more challenging and more prone to errors [45].

The two most common systematic errors associated with the contour method, plasticity and changing cut width, are unlikely to explain the difference in stress magnitudes measured by the two techniques. In tensile testing, the uranium showed yield strengths of about 200-250 MPa with strain hardening to over 400 MPa. The peak hoop stress in the cylinder exceeds the initial yield strength. (Because of the multi-axial nature of the stress and the strain hardening of the material, individual residual stress components exceeding nominal yield strength have

been observed routinely in tensile stress regions near welds [49].) Because of the large measured stress magnitudes, plasticity at the tip of the cut could have caused errors. Plasticity effects are difficult to predict because they depend on prior history, strain hardening and cyclic plasticity. Nonetheless, simulations of plasticity effects for the contour method indicate possible errors in the position and shape of the stress profile, but not significant increases in peak stress magnitudes [50,51].

The contour method also assumes that the cut removes a constant width of material relative to the undeformed part. Because material ahead of the cut deforms as stresses are released, the cut width relative to the undeformed part evolves [48]. In the experiment reported in this paper, the cut width error was reduced by securely clamping the part during cutting, but could still cause errors of 5% to 10% in magnitude and spatial misalignment of results by a small amount. These effects do not likely explain the larger differences between the stresses measured with contour and neutron diffraction techniques.

The contour method has been validated in the literature many times by comparison with other measurement methods, primarily neutron and synchrotron diffraction. For specimens other than welds, the agreement between contour and other methods is generally very good [1,25,29,52,53,46,24]. “Very good” means that the measurements should agree to within one standard deviation error bars at 68% or more of the points. In welds, the agreement is less consistent. Often the agreement is good or very good [54,2,17,11,55,3,56,57]. Other times there are significant regions of disagreement [13,15,10,16,51,12]. There is a slight trend of the diffraction results having higher stresses than the contour results, in contrast with the results in this paper. However, the trend may not be significant. Because of chemistry changes, welds can be problematic for diffraction measurements [41,42]. Round robin studies with multiple diffraction measurements on the same sample often show a large amount of scatter in the results [58-60]. Therefore, one should not read too much into a comparison with neutron diffraction measurements from a single laboratory. There has been no comparable round robin with the contour method.

The contour and neutron results agree for the bending stresses but not the total stress. Is that possible physically and can the results then still validate the -cut process for the contour method? Yes. Equilibrium considerations dictate that the net bending moment be the same at any circumferential location around the cylinder[1]. Therefore, the circumferentially averaged hoop stress measured by neutrons must have the same moment as any local relaxation by a single cut. However, the distribution of circumferentially averaged stresses (neutron) certainly need not agree with a local measurement (contour).

CONCLUSION

In order to prevent or at least minimize plasticity errors, a multiple cut procedure has been developed for measuring hoop stresses in cylinders with the contour method. A first cut is used to sever the ring, allow it to open or close, and to determine the bending-moment portion of the residual stresses. For the welded cylinder in this study, the bending moment stresses agreed well with the stresses measured by neutron diffraction, validating this portion of the procedure. The bending moment stresses were a small fraction of the total stress magnitude, but could have a big effect on plasticity errors if they are not relieved.

A discontinuity was measured in the surface contour in the cut cylinder because of an unwelded portion of the joint. A procedure was developed to smooth the contour data but retain the discontinuity. High stress gradients were determined by the contour method in the discontinuity region.

Unfortunately, the total residual hoop stresses measured by the contour method did not agree with those measured by neutron diffraction, making for an unsatisfying validation of the overall procedure. However, because the neutron diffraction measurements were averaged over the circumference compared to the contour measurements taken at a single location, the differences may be real rather than an error in either measurement.

ACKNOWLEDGEMENTS

This work was performed at Los Alamos National Laboratory, operated by the Los Alamos National Security, LLC for the National Nuclear Security Administration of the U.S. Department of Energy under contract DE-AC52-06NA25396. By acceptance of this article, the publisher recognizes that the U.S. Government retains a

[1] Consider a free body diagram for any arbitrary segment of the cylinder.

REFERENCES

1. Prime MB (2001) Cross-sectional mapping of residual stresses by measuring the surface contour after a cut. Journal of Engineering Materials and Technology 123 (2):162-168
2. Prime MB, Sebring RJ, Edwards JM, Hughes DJ, Webster PJ (2004) Laser surface-contouring and spline data-smoothing for residual stress measurement. Experimental Mechanics 44 (2):176-184
3. Johnson G (2008) Residual stress measurements using the contour method. Ph.D. Dissertation, University of Manchester,
4. DeWald AT, Rankin JE, Hill MR, Lee MJ, Chen HL (2004) Assessment of Tensile Residual Stress Mitigation in Alloy 22 Welds Due to Laser Peening. Journal of Engineering Materials and Technology 126 (4):465-473
5. Hatamleh O, Lyons J, Forman R (2007) Laser peening and shot peening effects on fatigue life and surface roughness of friction stir welded 7075-T7351 aluminum. Fatigue and Fracture of Engineering Material and Structures 30 (2):115-130
6. Hatamleh O (2008) Effects of peening on mechanical properties in friction stir welded 2195 aluminum alloy joints. Materials Science and Engineering: A 492 (1-2):168-176
7. DeWald AT, Hill MR (2009) Eigenstrain based model for prediction of laser peening residual stresses in arbitrary 3D bodies. Part 2: model verification. Journal of Strain Analysis for Engineering Design 44 (1):13-27
8. Liu KK, Hill MR (2009) The effects of laser peening and shot peening on fretting fatigue in Ti-6Al-4V coupons. Tribology International 42 (9):1250-1262
9. Hatamleh O, DeWald A (2009) An investigation of the peening effects on the residual stresses in friction stir welded 2195 and 7075 aluminum alloy joints. Journal of Materials Processing Technology 209 (10):4822-4829
10. Woo W, Choo H, Prime MB, Feng Z, Clausen B (2008) Microstructure, texture and residual stress in a friction-stir-processed AZ31B magnesium alloy. Acta materialia 56 (8):1701-1711
11. Prime MB, Gnaupel-Herold T, Baumann JA, Lederich RJ, Bowden DM, Sebring RJ (2006) Residual stress measurements in a thick, dissimilar aluminum alloy friction stir weld. Acta Materialia 54 (15):4013-4021
12. Frankel P, Preuss M, Steuwer A, Withers PJ, Bray S (2009) Comparison of residual stresses in Ti6Al4V and Ti6Al2Sn4Zr2Mo linear friction welds. Materials Science and Technology 25:640-650. doi:10.1179/174328408x332825
13. Zhang Y, Pratihar S, Fitzpatrick ME, Edwards L (2005) Residual stress mapping in welds using the contour method. Materials Science Forum 490/491:294-299
14. Edwards L, Smith M, Turski M, Fitzpatrick M, Bouchard P (2008) Advances in residual stress modeling and measurement for the structural integrity assessment of welded thermal power plant. Advanced Materials Research 41-42:391-400
15. Kartal M, Turski M, Johnson G, Fitzpatrick ME, Gungor S, Withers PJ, Edwards L (2006) Residual stress measurements in single and multi-pass groove weld specimens using neutron diffraction and the contour method. Materials Science Forum 524-525:671-676
16. Withers PJ, Turski M, Edwards L, Bouchard PJ, Buttle DJ (2008) Recent advances in residual stress measurement. The International Journal of Pressure Vessels and Piping 85 (3):118-127
17. Zhang Y, Ganguly S, Edwards L, Fitzpatrick ME (2004) Cross-sectional mapping of residual stresses in a VPPA weld using the contour method. Acta Materialia 52 (17):5225-5232
18. Thibault D, Bocher P, Thomas M (2009) Residual stress and microstructure in welds of 13%Cr-4%Ni martensitic stainless steel. Journal of Materials Processing Technology 209 (4):2195-2202
19. Hacini L, Van Lê N, Bocher P (2009) Evaluation of Residual Stresses Induced by Robotized Hammer Peening by the Contour Method. Experimental Mechanics 49 (6):775-783
20. Turski M, Edwards L (2009) Residual stress measurement of a 316L stainless steel bead-on-plate specimen utilising the contour method. International Journal of Pressure Vessels and Piping 86 (1):126-131
21. Thibault D, Bocher P, Thomas M, Gharghouri M, Côté M (2010) Residual stress characterization in low transformation temperature 13%Cr-4%Ni stainless steel weld by neutron diffraction and the contour method. Materials Science and Engineering: A 527 (23):6205-6210. doi:DOI: 10.1016/j.msea.2010.06.035
22. Dai H, Francis JA, Withers PJ (2010) Prediction of residual stress distributions for single weld beads deposited on to SA508 steel including phase transformation effects. Materials Science and Technology 26:940-949. doi:10.1179/026708309x12459430509454

23. Simoneau R, Thibault D, Fihey J-L (2009) A comparison of residual stress in hammer-peened, multi-pass steel welds – A514 (S690Q) and S4150. Welding in the World 53 (5/6):R124-R134
24. Richter-Trummer V, Tavares SMO, Moreira P, de Figueiredo MAV, de Castro P (2008) Residual stress measurement using the contour and the sectioning methods in a MIG weld: Effects on the stress intensity factor. Ciência & Tecnologia dos Materiais 20 (1-2):114-119
25. Evans A, Johnson G, King A, Withers PJ (2007) Characterization of laser peening residual stresses in Al 7075 by synchrotron diffraction and the contour method. Journal of Neutron Research 15 (2):147-154
26. Martineau RL, Prime MB, Duffey T (2004) Penetration of HSLA-100 steel with tungsten carbide spheres at striking velocities between 0.8 and 2.5 km/s. International Journal of Impact Engineering 30 (5):505-520
27. Wilson GS, Grandt Jr AF, Bucci RJ, Schultz RW (2009) Exploiting bulk residual stresses to improve fatigue crack growth performance of structures. International Journal of Fatigue 31 (8-9):1286-1299
28. DeWald AT, Hill MR (2006) Multi-axial contour method for mapping residual stresses in continuously processed bodies. Experimental Mechanics 46 (4):473-490
29. DeWald AT, Hill MR (2009) Eigenstrain based model for prediction of laser peening residual stresses in arbitrary 3D bodies. Part 1: model description. Journal of Strain Analysis for Engineering Design 44 (1):1-11
30. Murugan N, Narayanan R (2009) Finite element simulation of residual stresses and their measurement by contour method. Materials & Design 30 (6):2067-2071. doi:10.1016/j.matdes.2008.08.041
31. Kelleher J, Prime MB, Buttle D, Mummery PM, Webster PJ, Shackleton J, Withers PJ (2003) The Measurement of Residual Stress in Railway Rails by Diffraction and Other Methods. Journal of Neutron Research 11 (4):187-193
32. Lillard RS, Kolman DG, Hill MA, Prime MB, Veirs DK, Worl LA, Zapp P (2008) Assessment of corrosion based failure in stainless steel containers used for the long-term storage of plutonium base salts. Corrosion 65 (3):175-186
33. Ismonov S, Daniewicz SR, Newman JJC, Hill MR, Urban MR (2009) Three Dimensional Finite Element Analysis of a Split-Sleeve Cold Expansion Process. Journal of Engineering Materials and Technology 131 (3):031007. doi:10.1115/1.3120392
34. Zhang Y, Fitzpatrick ME, Edwards L (2002) Measurement of the residual stresses around a cold expanded hole in an EN8 steel plate using the contour method. Materials Science Forum 404-407:527-532
35. Majumdar S (1999) Failure and leakage through circumferential cracks in steam generator tubing during accident conditions. International Journal of Pressure Vessels and Piping 76 (12):839-847
36. Wang X, Reinhardt W (2003) On the Assessment of Through-Wall Circumferential Cracks in Steam Generator Tubes With Tube Supports. Journal of Pressure Vessel Technology 125 (1):85-90
37. Bush SH (1992) Failure Mechanisms in Nuclear Power Plant Piping Systems. Journal of Pressure Vessel Technology 114 (4):389-395
38. Dong P, Brust FW (2000) Welding Residual Stresses and Effects on Fracture in Pressure Vessel and Piping Components: A Millennium Review and Beyond. Journal of Pressure Vessel Technology 122 (3):329-338
39. Bouchard PJ (2007) Validated residual stress profiles for fracture assessments of stainless steel pipe girth welds. International Journal of Pressure Vessels and Piping 84 (4):195-222
40. Withers PJ, Preuss M, Steuwer A, Pang JWL (2007) Methods for obtaining the strain-free lattice parameter when using diffraction to determine residual stress. Journal of Applied Crystallography 40 (5):891-904
41. Krawitz A (1994) Use of position-dependent stress-free standards for diffraction stress measurements. Materials Science and Engineering A 185 (1-2):123-130
42. Holden TM, Suzuki H, Carr DG, Ripley MI, Clausen B (2006) Stress measurements in welds: Problem areas. Materials Science and Engineering A 437:33-37
43. Smith DJ, Bouchard PJ, George D (2000) Measurement and prediction of residual stresses in thick-section steel welds. Journal of Strain Analysis for Engineering Design 35 (4):287-305
44. de Swardt RR (2003) Finite element simulation of crack compliance experiments to measure residual stresses in thick-walled cylinders. Journal of Pressure Vessel Technology 125 (3):305-308
45. Brown DW, Holden TM, Clausen B, Prime MB, Sisneros TA, Swenson H, Vaja J (2011) Critical Comparison of Two Independent Measurements of Residual Stress in an Electron-Beam Welded Uranium Cylinder: Neutron Diffraction and the Contour Method. Acta Materialia 59 (3):864-873. doi:10.1016/j.actamat.2010.09.022
46. Pagliaro P, Prime MB, Robinson JS, Clausen B, Swenson H, Steinzig M, Zuccarello B (2010) Measuring Inaccessible Residual Stresses Using Multiple Methods and Superposition. Experimental Mechanics. doi:10.1007/s11340-010-9424-5
47. Cheng W, Finnie I, Gremaud M, Prime MB (1994) Measurement of near-surface residual-stresses using electric-discharge wire machining. Journal of Engineering Materials and Technology-Transactions of the ASME 116 (1):1-7

48. Prime MB, Kastengren AL (2009) The Contour Method Cutting Assumption: Error Minimization and Correction. In: SEM Conference & Exposition on Experimental & Applied Mechanics, Indianapolis, IN USA, 2010. Society for Experimental Mechanics, Inc.,
49. Webster GA, Ezeilo AN (2001) Residual stress distributions and their influence on fatigue lifetimes. International Journal of Fatigue 23 (SUPPL. 1):S375-S383
50. Shin SH (2005) FEM analysis of plasticity-induced error on measurement of welding residual stress by the contour method. Journal of Mechanical Science and Technology 19 (10):1885-1890
51. Dennis RJ, Bray, D.P., Leggatt, N.A., Turski, M. Assessment of the influence of plasticity and constraint on measured residual stresses using the contour method. In: 2008 ASME Pressure Vessels and Piping Division Conference, Chicago, IL, USA, 2008. ASME, pp PVP2008-61490
52. Pagliaro P, Prime MB, Clausen B, Lovato ML, Zuccarello B (2009) Known Residual Stress Specimens Using Opposed Indentation. Journal of Engineering Materials and Technology 131:031002
53. Pagliaro P, Prime MB, Swenson H, Zuccarello B (2010) Measuring Multiple Residual-Stress Components Using the Contour Method and Multiple Cuts. Experimental Mechanics 50 (2):187-194. doi:10.1007/s11340-009-9280-3
54. Zhang Y, Ganguly S, Stelmukh V, Fitzpatrick ME, Edwards L (2003) Validation of the Contour Method of Residual Stress Measurement in a MIG 2024 Weld by Neutron and Synchrotron X-ray Diffraction. Journal of Neutron Research 11 (4):181-185
55. Kartal ME, Liljedahl CDM, Gungor S, Edwards L, Fitzpatrick ME (2008) Determination of the profile of the complete residual stress tensor in a VPPA weld using the multi-axial contour method. Acta Materialia 56 (16):4417-4428
56. Smith MC, Smith AC (2009) NeT bead-on-plate round robin: Comparison of residual stress predictions and measurements. International Journal of Pressure Vessels and Piping 86 (1):79-95
57. Bouchard PJ (2009) The NeT bead-on-plate benchmark for weld residual stress simulation. International Journal of Pressure Vessels and Piping 86 (1):31-42. doi:DOI: 10.1016/j.ijpvp.2008.11.019
58. Wimpory RC, Ohms C, Hofmann M, Schneider R, Youtsos AG (2009) Statistical analysis of residual stress determinations using neutron diffraction. International Journal of Pressure Vessels and Piping 86 (1):48-62. doi:DOI: 10.1016/j.ijpvp.2008.11.003
59. Withers PJ, Webster PJ (2001) Neutron and Synchrotron X-ray Strain Scanning. Strain 37 (1):19-33. doi:10.1111/j.1475-1305.2001.tb01216.x
60. Hughes DJ, Webster PJ, Mills G (2002) Ferritic steel welds - A neutron diffraction standard. Materials Science Forum 404-407:561-566

Measurement of Bulk Residual Stress Distributions in Thick-section Components using the Contour Method

Adrian T. DeWald, Hill Engineering, LLC, 3035 Prospect Park Drive, Suite 180, Rancho Cordova, CA 95670, atdewald@hill-engineering.com

Michael R. Hill, Professor, Department of Mechanical and Aeronautical Engineering, University of California, One Shields Avenue, Davis, CA 95616, mrhill@ucdavis.edu

ABSTRACT

Residual stresses are known to play a significant role in many material failure processes (e.g., fatigue, fracture, and stress corrosion cracking). For example, pressure vessels typically contain welded joints. In many cases these welded joints are large (e.g., traveling around the entire circumference), contain significant amounts of residual stress, have reduced material properties, and contain defects. For these and other reasons, the welded joints tend to be critical locations in terms of design and performance of pressure vessels. In the aerospace industry, where large integral components are often machined from a single piece of material, bulk residual stresses can lead to significant distortion of the machined part. Thus, the ability to accurately quantify residual stresses through measurement is an important engineering tool.

The contour method is as an effective tool for generating 2D maps of residual stress normal to a plane in relatively thick components [1, 2]. The contour method consists of three basic steps. First, the specimen containing residual stress is cut in half (wire EDM typical). Cutting creates a new traction-free surface within the body, which results in deformation due to residual stress release. Second, the normal direction displacements resulting from residual stress release are measured over both cutting surfaces (opposite sides of the cut). Third, an analysis is performed to calculate the initial residual stress acting normal to the surface of the cut from the measured displacements [1, 2].

Recently, a cooperative research program was initiated between the US Nuclear Regulatory Commission (NRC) and industry to address weld residual stress issues. The NRC and the Electric Power Research Institute (EPRI) signed a memorandum of understanding that allows and encourages cooperation in nuclear safety research related to dissimilar metal weld (DMW) residual stress fields [3]. As part of the program, measurements and predictions were performed on welded components including safety and relief nozzles from the pressurizer of the canceled WNP-3 plant. One nozzle contained a section of stainless steel pipe welded to the stainless steel safe-end of the nozzle. A schematic of the nozzle configuration is shown in (Figure 1). This nozzle was 711 mm long with a 201 mm outer diameter and an inner diameter of 113 mm at the location of the DMW (44 mm wall thickness).

T. Proulx (ed.), *Engineering Applications of Residual Stress, Volume 8*, Conference Proceedings of the Society for Experimental Mechanics Series 999, DOI 10.1007/978-1-4614-0225-1_3, © The Society for Experimental Mechanics, Inc. 2011

The contour method was used to measure a two-dimensional map of the hoop residual stress at two angular locations separated by 90° and a two-dimensional map of the axial residual stress at the center of the weld in section of the nozzle between them. All measurement planes are shown in Figure 1; the contour method provides a map of the residual stress component normal to the plane versus position within the plane. The contour measurements were performed in succession with the first hoop residual stress measurement (70°) completed before the second hoop residual stress measurement (160°), and finally the axial stress measurement.

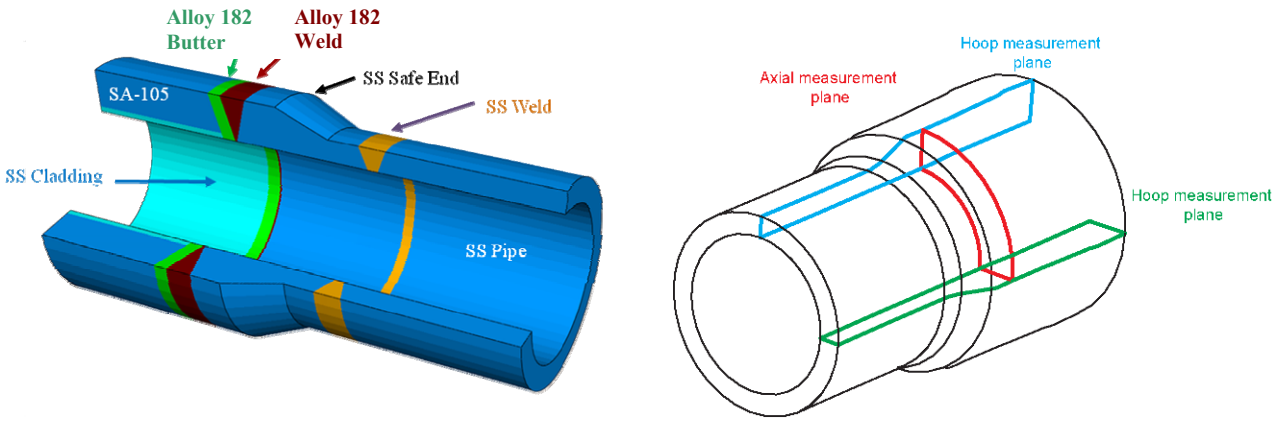

Figure 1 – Illustration of nozzle used for residual stress measurement

Due to the relative proximity of one measurement plane to another, each measurement affects the residual stress remaining in the nozzle at the locations of subsequent measurements. To account for the partial residual stress release from previous measurements, a multi-cut contour method approach was employed [4]. For example, the initial hoop residual stress residual stress at the 160° measurement plane is the sum of the residual stress released at the 160° measurement plane during the measurement performed at 70° and the stress subsequently measured (remaining) at the 160° location. Because the stress at the 70° plane was measured, it could be used to estimate the stress release at 160°. A similar approach is used for the axial measurement planes (with two previous cuts to use for the correction). Strain gage data provided measured deformation due to prior cuts, and validated use of measured stresses to account for partial stress release from prior cuts.

Contour plots of the measured hoop residual stress in the nozzle are shown in Figure 2. In general, significant compressive hoop residual stress exists on the inner diameter near the DMW. The region of compressive hoop residual stress grows larger through the butter and into the carbon steel region. Tensile hoop residual stress exists near the outer diameter, in a region that is shifted towards the stainless steel safe-end of the nozzle. A contour plot of the measured axial stress is shown in Figure 3.

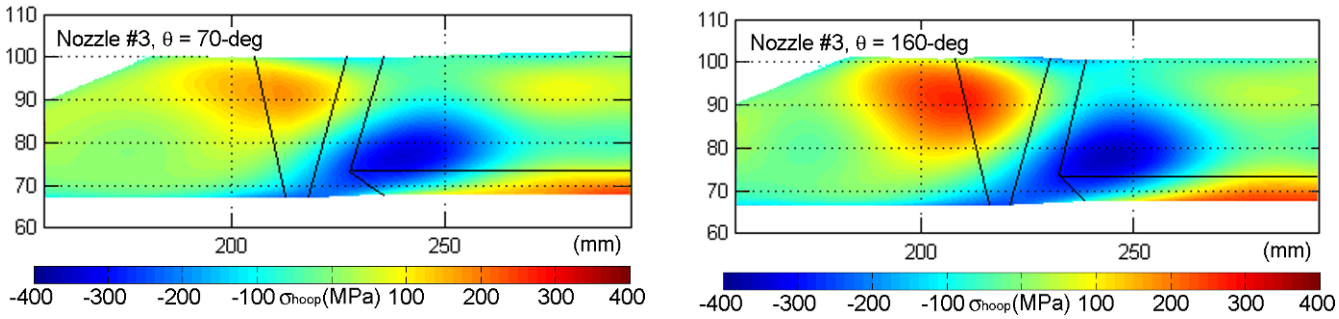

Figure 2 – Two-dimensional map of the hoop residual stress for the nozzle at the 70-deg location and 160-deg locations

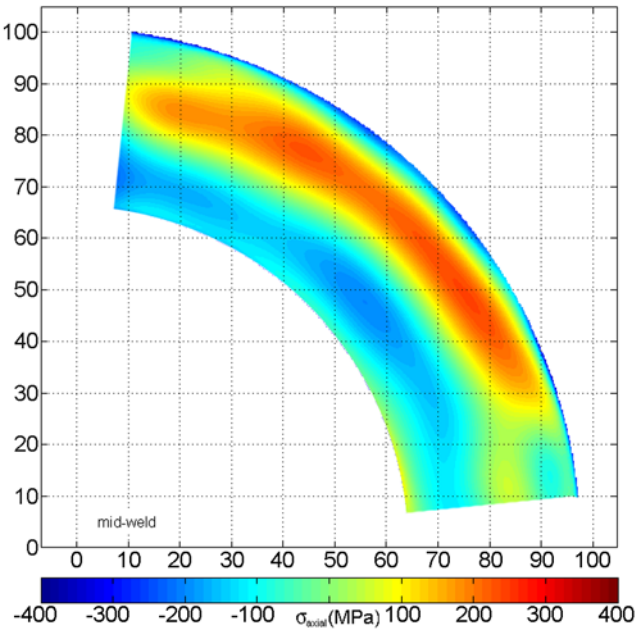

Figure 3 – Two-dimensional map of the measured axial residual stress for the nozzle (70-deg to 160-deg, counter-clockwise from x-axis)

This presentation will provide an overview of the contour method and will discuss results from recent programs where the contour method was used to quantify residual stress in thick sections. Results from the NRC/EPRI weld residual stress program will be presented. In addition, results from recent measurements on aluminum aerospace components will be shown.

References

[1] Prime, M.B., "Cross-sectional mapping of residual stresses by measuring the surface contour after a cut," *Journal of Engineering Materials and Technology*, **123**, 162-168, 2001.

[2] DeWald, A.T., J.E. Rankin, M.R. Hill, M.J. Lee, and H.-L. Chen, "Assessment of tensile residual stress mitigation in Alloy 22 welds due to laser peening," *Journal of Engineering Materials and Technology*, **126**(4), 465-473, 2004.

[3] Addendum to the Memorandum of Understanding (MOU) between NRC's Office of Nuclear Regulatory Research and Electric Power Research Institute, Inc. on Cooperative Nuclear Safety Research, NRC ADAMS Accession Number ML103490002, 2/15/2011.

[4] Pagliaro, P., M. B. Prime, H. Swenson and B. Zuccarello, "Measuring Multiple Residual-Stress Components Using the Contour Method and Multiple Cuts," *Experimental Mechanics*, **50**(2), 187-194, 2010.

Application of a Finite Strain Elastic-Plastic Self-Consistent Model to Deformation of Magnesium

Bjørn Clausen*, Donald W. Brown and Carlos N. Tomé; Los Alamos National Laboratory, USA

C. John Neil, James A. Wollmershauser and Sean R. Agnew; University Virginia, USA

EXTENDED ABSTRACT

Magnesium alloys are unique materials because tensile twinning and de-twinning can be easily activated, which leads to rapid texture and hardening evolution [1]. Here we present a study of the mechanical response of a magnesium alloy (AZ31) when deformed under twinning dominated conditions, i.e. uniaxial compression along prior extrusion axis. In-situ neutron diffraction measurements were carried out using the SMARTS (Spectrometer for Materials Research at Temperature and Stress) instrument at LANSCE (Los Alamos Neutron Science Center) [2].

The neutron diffraction measurements provide both internal strain and texture information as a function of applied strain which have previously been used to validate predictions of the elastic-plastic self-consistent (EPSC) polycrystal deformation model [3,4]. In the present case it has lead to the development of a new twinning scheme [5] into the EPSC model that incorporates; i) twin activation, ii) twin reorientation (and the associated texture evolution), and iii) the specific stress relaxation associated with twinning. Although the texture development due to twinning is included, the underlying mechanics of the model are still based upon a small strain assumption, and thus it does not include texture development due to slip. The EPSC model including the new twinning scheme was able to predict the plateau in the macroscopic stress-strain curve and the atypical internal strain development caused by the pronounced twinning as seen in Figure 1.

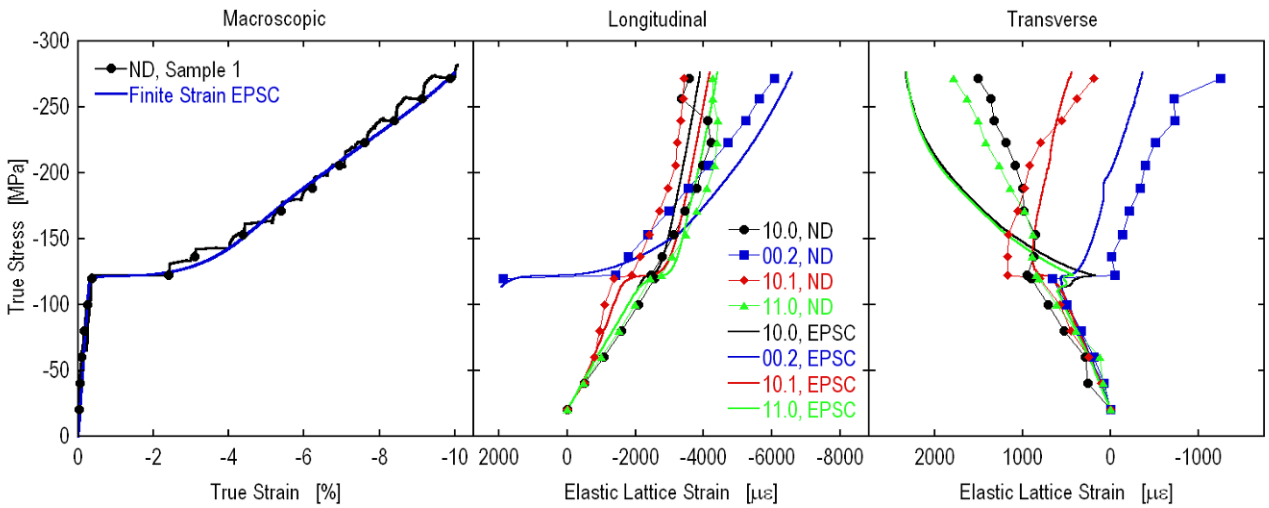

Figure 1: Measured and calculated a) macroscopic stress-strain curve, b) longitudinal lattice strains, and c) transverse lattice strains. Symbols are measured data and lines are EPSC model predictions.

The prior extrusion process produced the so-called rod texture in the magnesium alloy that drastically favored tensile twinning in the following compression cycle by aligning the basal poles perpendicular to the extrusion axis as seen in Figure 2a). Initially there are no grains with their basal pole in the longitudinal direction, i.e. the loading direction and the prior extrusion axis, positioned at the center of the pole figures. Tensile twinning in magnesium alloys is associated with at 86.6 degree reorientation of the basal pole [6], which causes the basal poles to flip from the perimeter of the pole figure to the center, as seen in Figure 2a). This means that all the grains that contribute to the basal peak in the longitudinal direction are twins, and as seen in Figure 2b), they exhibit an initially tensile lattice strain even though the polycrystal is loaded into compression. Within the model, this 'sense-reversal' is captured by assuming that the twins immediately grow to a given size

* Corresponding author: clausen@lanl.gov, P.O. Box 1663, MS H805, Los Alamos, NM 87545, USA.

T. Proulx (ed.), *Engineering Applications of Residual Stress, Volume 8*, Conference Proceedings of the Society for Experimental Mechanics Series 999, DOI 10.1007/978-1-4614-0225-1_4, © The Society for Experimental Mechanics, Inc. 2011

as they are nucleated [5]. This in turn causes a back stress in the twin and its parent grain that is responsible for the initial tensile lattice strain in the twins.
As mentioned above, almost all the grains are favorably oriented for twinning and, in fact, the twin volume fraction is approximately 70% after only 10% compression [5]. Hence, all the basal poles aligned with the compression axis after deformation as seen in Figure 2a). The rapid change in peak intensity during the deformation is shown in Figure 2b). The predicted intensity variation for the small strain EPSC model is also shown in Figure 2b). Although the model is able to predict the strong increase in the longitudinal basal pole intensity, it is clear that the decrease in the longitudinal basal pole intensity observed starting at about 8% strain is not reproduced.

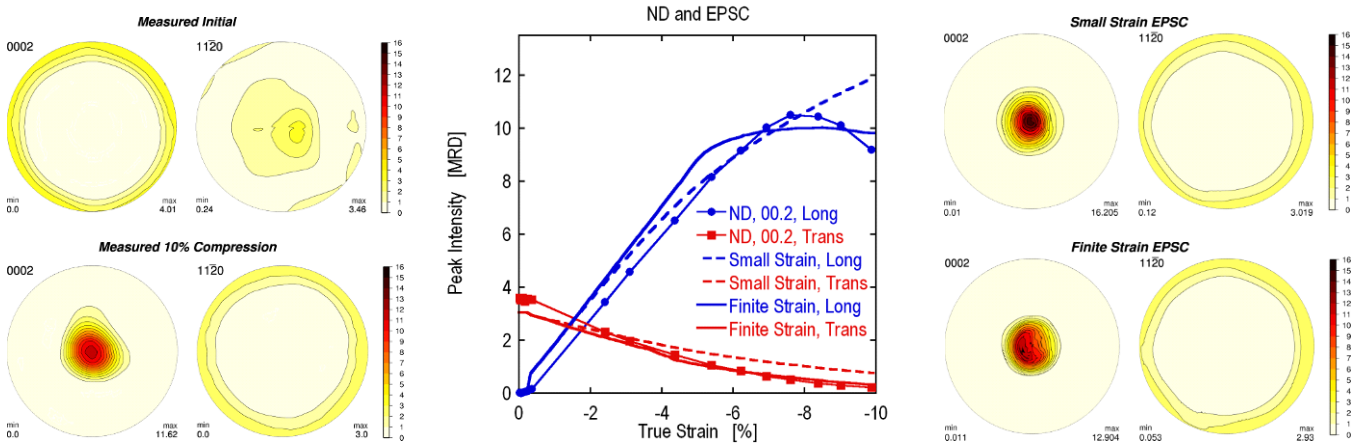

a) b) c)

Figure 2: a) measured initial and final basal and prism pole figures, b) measured and calculated basal peak intensity variation as a function of strain, and c) calculated final basal and prism pole figures.

A new finite strain EPSC model that includes the kinematics of large strains, rigid body rotations, texture evolution and grain shape evolution during deformation was introduced by Neil et al. [7]. The predictions of the finite strain EPSC model, which includes the texture development due to slip, are also shown in Figure 2b). It is clear that the finite strain EPSC model is reproducing the turn-over of the longitudinal basal pole intensity, which is caused by pyramidal slip in the twins. The pyramidal slip activity not only reduces the basal pole intensity at high strains, it also causes the spread in the center peak of the basal pole figure as evident in Figure 2c), and the maximum basal pole density predicted by the finite strain EPSC model is in better agreement with the measured data.
In conclusion, the complex internal strain state and rapid texture development during compressive loading of an extruded magnesium alloy caused by twinning has been investigated using neutron diffraction and EPSC modeling. The newly developed finite strain version of the EPSC model was able to reproduce the observed macroscopic and internal strain development as well as the texture development. It is obvious that even at modest degrees of deformation, materials with hexagonal close packed crystal structure exhibits strong texture development due to both twinning and slip activity, which significantly increases the

ACKNOWLEDGEMENTS
All authors, except DWB, were fully supported by the U.S. Department of Energy, Office of Basic Energy Sciences, Division of Materials Sciences and Engineering, Project FWP 06SCPE401 under U.S. DOE Contract No. W-7405-ENG-36. This work has benefited from the use of the Lujan Neutron Scattering Center at LANSCE, which is funded by the Office of Basic Energy Sciences (DOE). Los Alamos National Laboratory is operated by Los Alamos National Security LLC under DOE Contract DE AC52 06NA25396.

REFERENCES
[1] A. Jain and S.R. Agnew, *Magnesium Technology 2006*, Edited by TMS, pp. 219-224, 2006.
[2] M.A.M. Bourke, D.C. Dunand, and E. Üstündag, *Appl. Phys. A*, vol. 74(suppl.2), pp. S1707-S1709, 2002.
[3] B. Clausen, T. Lorentzen and T. Leffers, *Acta Mater.*, vol. 46(9), pp. 3087-3098, 1998.
[4] J.W.L. Pang, T.M. Holden, P.A. Turner and T.E. Mason, *Acta Mater.*, vol. 47(2), pp. 373-383, 1999.
[5] B. Clausen, C.N. Tomé, D.W. Brown and S.R. Agnew, *Acta Mater.*, vol. 56(11), pp. 2456-2468, 2008.
[6] M.A. Gharghouri, G.C. Weatherly, J.D. Embury and J. Root, *Phil. Mag. A*, vol. 79(7), pp. 1671-1695, 1999.
[7] C.J. Neil, J.A. Wollmershauser, B. Clausen, C.N. Tomé and S.R. Agnew, *Int. J. Plast.*, vol. 26(12), pp. 1772-1791, 2010.

Probing Strained Semiconductor Structures with Nanoscale X-ray Diffraction

Conal E. Murray
I.B.M. T.J. Watson Research Center, Yorktown Heights, NY 10598

The tailoring of strain distributions within semiconductor features represents a key method to enhance performance in current and future generations of complementary metal-oxide semiconductor (CMOS) devices. Although the impact of strain on carrier mobility in semiconductor materials was first investigated over 50 years ago [1,2], its implementation within the inversion layer of the channels in CMOS device channels has only occurred within the past decade. This includes the deposition of liner materials that possess significant values of residual stress [3]. Eigenstrained structures, deposited epitaxially within recesses on either side of the Si channel, can be used to induce either compressive strain in the channel region, by using materials that possess a larger lattice parameter than Si (e.g., SiGe)[4], or tensile strain, by using materials with a smaller lattice parameter (e.g., SiC). Because these methods generate heterogeneous strain distributions within the composite structure, it is critical to experimentally determine the distribution of strain across the current-carrying paths of the device and the surrounding environment.

Real-space x-ray microdiffraction measurements represent the optimal method to perform direct, *in-situ* characterization of strain within crystalline materials at a submicron length scale [5,6]. The diffraction facilities at the 2ID-D beamline at Argonne National Laboratory's Advanced Photon Source were used for the x-ray microdiffraction measurements [6] with a nominal beam size of approximately 0.25 μm. Samples under investigation included both CMOS devices possessing embedded stressor materials and silicon-on-insulator (SOI) structures with overlying stressor features. The embedded stressor devices, fabricated from 55 nm thick SOI layers, contained $Si_{1-x}C_x$ with a C content, x, of 1.1% in the source and drain regions, approximately 1.85 μm in length. Because C has a smaller lattice parameter than that of Si, the e-SiC structures possess in-plane tensile stress, which is transferred into the adjacent, 60 nm long SOI channel. To obtain a reference value for the unrelaxed SiC strain, square pads 200 μm in length, also consisting of heteroepitaxially deposited SiC, were characterized. Another set of SOI structures was fabricated possessing overlying stressor features, where compressively stressed Si_3N_4 films of approximately 105 nm thickness were lithographically etched to produce a matrix of rectilinear features possessing lengths of 2048 μm and widths ranging from 1 μm to 2048 μm.

X-ray microbeam measurements of the embedded stressor CMOS device revealed that the out-of-plane strains in the e-SiC were approximately -0.355% within the vicinity of the SOI channel and -0.350% 0.8 μm away from the channel [7]. Diffraction from the thin SOI layer underneath the e-SiC features indicated a small, tensile out-of-plane strain of 74×10^{-6}. The difference between the two SOI diffraction peaks measured away from and at the channel contains the depth-averaged strain information from the SOI channel, corresponding to an out-of-plane compressive strain of -0.167%. The predicted out-of-plane strains for the e-SiC feature and SOI channel are -0.355% and -0.176%, respectively, as calculated using an Eshelby inclusion model [8]. The measured strain in the e-SiC regions match well, and the out-of-plane SOI channel strain is approximately 95% of the predicted value.

A mapping of the out-of-plane SOI strain distribution under the edge of a 2048 x 2048 μm Si_3N_4 feature edge is depicted in Figure 1. Simulated out-of-strain profiles using an anisotropic, edge-force model [9] and an elastically isotropic boundary element method (BEM) model [10] are included for

T. Proulx (ed.), *Engineering Applications of Residual Stress, Volume 8*, Conference Proceedings of the Society for Experimental Mechanics Series 999, DOI 10.1007/978-1-4614-0225-1_5, © The Society for Experimental Mechanics, Inc. 2011

comparison. The BEM calculated values capture the asymmetry exhibited in the strain distribution across the Si_3N_4 feature edge location and confirm a compressive blanket film stress of -2.5 GPa in the Si_3N_4. For the edge-force model, the predicted values diverge from the measured strain in the SOI underneath the Si_3N_4 feature within 1 μm from the feature edge, or approximately 10 times the Si_3N_4 feature thickness, because peel and shear stresses at the Si_3N_4 / SOI interface cannot be captured by the edge-force model. Both experimental results and modeling clearly illustrate the extent to which strain fields can be generated in the vicinity of a free edge in a stressor material.

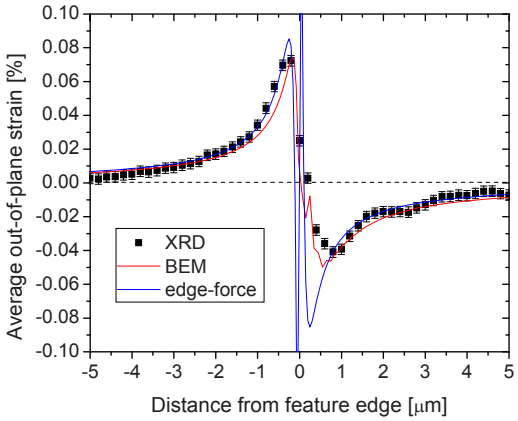

FIG. 1: Comparison of the experimentally measured and BEM calculated depth-averaged strain distribution in the SOI across the edge of an overlying 2048 x 2048 μm Si_3N_4 feature.

Figure 2 contains the measured and calculated out-of-plane SOI strain distributions under 1 μm, 1.5 μm and 2.5 μm wide Si_3N_4 features, respectively. There is a close correspondence between the BEM calculated values and the measured strain distributions outside of the immediate vicinity of the feature edges. In contrast, edge-force simulations exhibit a poor match to the measured strain values in the SOI underneath the stressor structures. The overlapping of strain fields induced by the feature edges dictates both the maxima in the depth-averaged strain observed in the SOI outside of the Si_3N_4 features as well as the shape of the distribution underneath the stressors.

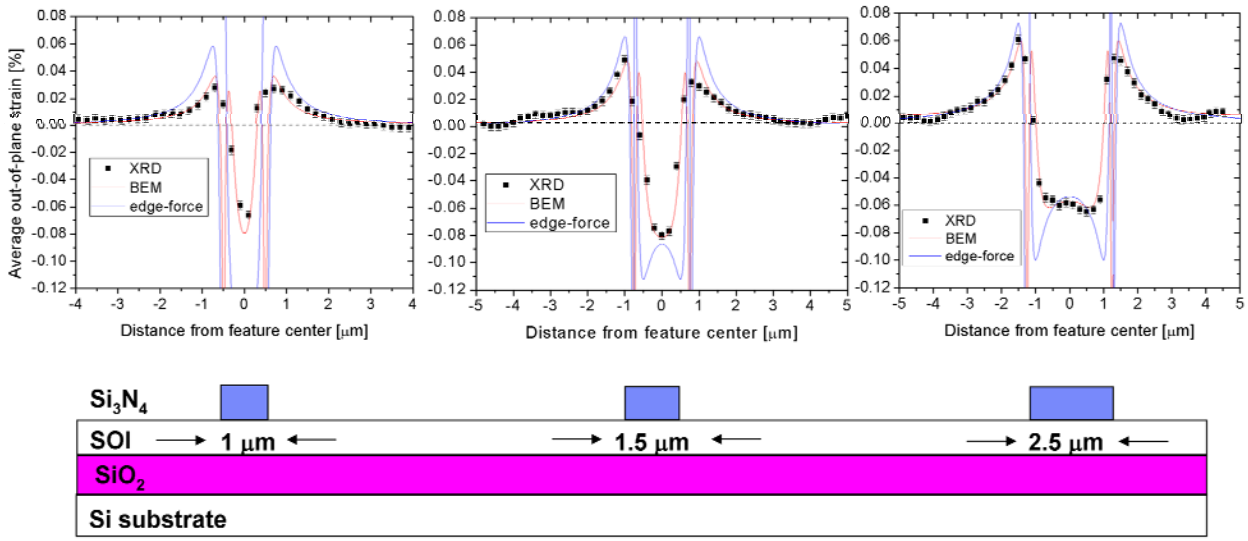

FIG. 2: Comparison of the experimentally measured and calculated SOI strain distributions across 2048 x 1 μm, 1.5 μm and 2.5 μm wide Si_3N_4 features.

[1] J. Bardeen, W. Shockley, Phys. Rev. **80**, 72 (1950).
[2] C.S. Smith, Phys. Rev. **94**, 42 (1954).
[3] S. Ito, H. Namba, T. Hirata, K. Ando, S. Koyama, N. Ikezawa, T. Suzuki, T. Saitoh, and T. Horiuchi, Microelectronics Reliability, **42**, 201 (2002).
[4] S.E. Thompson, M. Armstrong, C. Auth, S. Cea, R. Chau, G. Glass, T. Hoffman, J. Klaus, Z. Ma, B. McIntyre, A. Murthy, B. Obradovic, L. Shifren, S. Sivakumar, S. Tyagi, T. Ghani, K. Mistry, M. Bohr, Y. El-Mansy, IEEE Elect. Dev. Lett. **25**, 191 (2004).
[5] P.G. Evans, P.P. Rugheimer, M.G. Lagally, C.H. Lee, A. Lai, Y. Xiao, B. Lai, and Z. Cai, J. Appl. Phys. **97**, 103501 (2005).
[6] C.E. Murray, H.-F. Yan, I.C. Noyan, Z. Cai, and B. Lai, J. Appl. Phys. **98**, 013504 (2005).
[7] C.E. Murray, Z. Ren, A. Ying, S.M. Polvino, I.C. Noyan and Z. Cai, Appl. Phys. Lett. **94**, 063502 (2009).
[8] J.H. Davies, ASME J. Appl. Mech. **70**, 655 (2003).
[9] C.E. Murray, J. Appl. Phys. **100**, 103532 (2006).
[10] C.E. Murray, K.L. Saenger, O. Kalenci, S.M. Polvino, I.C. Noyan, B. Lai and Z. Cai, J. Appl. Phys. **104**, 013530 (2008).

Residual Stress State in Tools Used for Thermo-mechanical Metal Forming Processes

A. Gruening, M. Lebsanft, B. Scholtes
University of Kassel, Moenchebergstrasse 3, 34121 Kassel, Germany

ABSTRACT. In thermo-mechanically coupled forming processes for industrial mass production residual stresses are an unavoidable consequence of the alternating inhomogeneous fields of temperature and mechanical stress developing in tools and components dependent on the process parameters applied. Hence, a considerable interest exists to get reliable information about origin and distribution of the relevant residual stress fields and to understand the basic principles of their formation. By way of example a metal forming process based on a predefined locally and temporally differential temperature profile is described, which leads to a characteristic materials property profile and geometrical shape. The development of residual stress in tools (steel AISI H11) used for the thermo-mechanical forming operation of cylindrical flange shafts (steel SAE 6150) is outlined. To this end residual stress analyses by X-ray as well as by neutron diffraction were carried out. The loading situation of the tool was simulated by isothermal, thermal and contact fatigue tests, providing information about cyclic stress and plastic deformation during the manufacturing process.

Introduction

Thermal fatigue loading is one of the most important factors related to lifetime and damage of tools for hot metal forming processes like extrusion, die-casting or injection moulding as well as for many other hot working tools [1-4]. Thermal stresses caused by alternating temperatures in tools lead to characteristic crack formation, propagation and final failure [5,6]. A further important factor related to the lifetime of tools used for hot metal forming is the formation of harmful residual stress states. This article deals with the results of a research project entitled “Analysis and effects of residual stresses in tools and components as a consequence of thermo-mechanical processes”. The project is embedded in a large collaborative research centre “Process integrated manufacturing of functionally graded structures on the basis of thermo-mechanically coupled phenomena” established at the three German Universities of Kassel, Paderborn and Dortmund, funded by the German Research Foundation (DFG) [7]. Residual stresses are of outstanding importance during the manufacturing process as well as for strength, lifetime and reliability of the produced components. This is one of the main reasons for the establishment of the project mentioned above.

As an example of a thermo-mechanically coupled forming process Fig. 1 shows the individual production steps of a functionally graded flange shaft which is envisaged for industrial mass production. The process starts with a cylindrical bar (steel SAE 6150) which is heated up to austenitizing temperature by an induction coil. Due to pressing the bar between two tools, a flange shaft is formed. Besides the aim of an exact geometry it is of fundamental importance to realize characteristic temperature-time-courses in the individual regions of the flange shaft to achieve technologically advantageous gradients of microstructures. It is the challenge of the process to adapt the microstructures produced and, hence, the local strength of the material, at the prospected loading state of the components.

Cyclic heating and cooling of the tool as well as mechanical loading leads to cyclic plastic deformation and, as a consequence, to characteristic residual stress states in the tools used [8]. Therefore a great interest exists to understand and to quantify the basic processes of residual stress evolution in order to reliably predict the lifetime of tools under given process parameters. In this paper the development of residual stress in tools used for the thermo-mechanical forming operations of cylindrical flange shafts is outlined. Results of isothermal, thermal and contact fatigue tests, providing information about cyclic stress and plastic deformation during the manufacturing processes are presented and discussed in detail.

T. Proulx (ed.), *Engineering Applications of Residual Stress, Volume 8*, Conference Proceedings of the Society for Experimental Mechanics Series 999, DOI 10.1007/978-1-4614-0225-1_6, © The Society for Experimental Mechanics, Inc. 2011

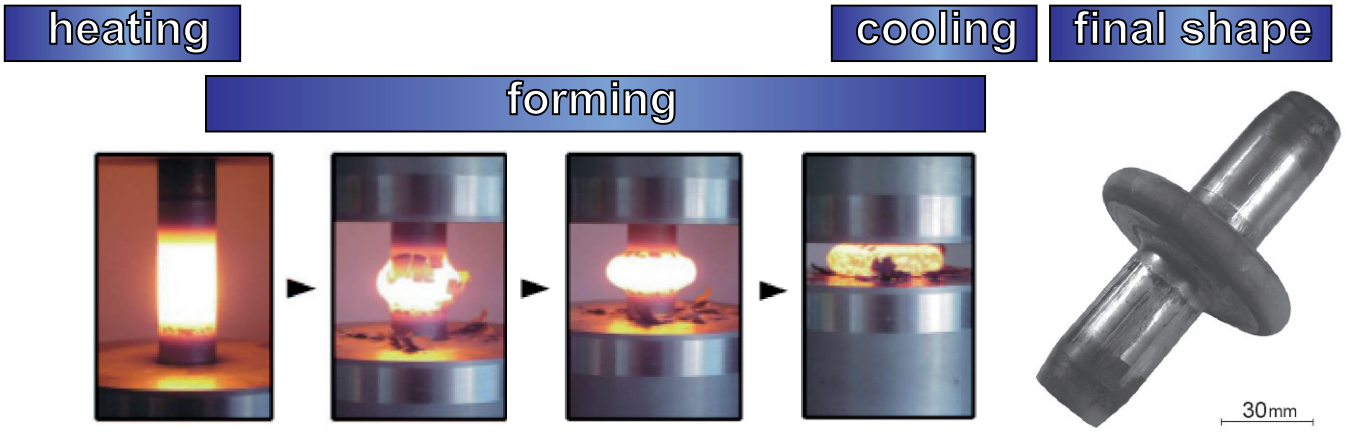

Fig. 1 Characteristic steps of the flange shaft forming process [9]

Experimental results and discussion

Residual stresses were determined by conventional X-ray diffraction technique [10] using CrKα-radiation at the {211}-planes of the annealed martensite. For stress evaluation, the $\sin^2\psi$-method was applied and the elastic constant $½s_2 = 6.09 \cdot 10^{-6}$ MPa^{-1} was used. In order to confirm the residual stress distributions determined by successive layer removal in combination with repeated application of X-ray stress measurements, additional neutron diffraction measurements were carried out at the neutron research reactor FRMII in Munich-Garching. Surface strain scans in reflection mode using a wavelength of the neutron radiation of 0.168 nm were performed. For this wavelength the {211} interference line of the annealed martensite occurs at around $2\theta \approx 91.5°$. A new method to measure near surface residual stress profiles with neutrons up to 200µm underneath the surface of steel samples without time consuming and laborious surface effect corrections was applied [11]. Aberration peak shifts caused by spurious strains, which arise due to the fact that the gauge volume is partially outside of the sample when scanning the near surface region, were minimized by using an optimized bending radius of a SI (400) monochromator. The gauge volume defined by the primary and secondary optics was 1mm³.

By way of example Fig. 2 shows a tool used for approximately 200 hot metal forming operations as described in Fig. 1. A dark ring around the inner bore hole characterizes the heat-affected zone of the tool. Residual stresses measured in radial and tangential direction at the surface are plotted along the radius of the tool. High tensile residual stresses occur in the cyclically heated and cooled area of the tool, whereas in the other regions compressive residual stresses are measured.

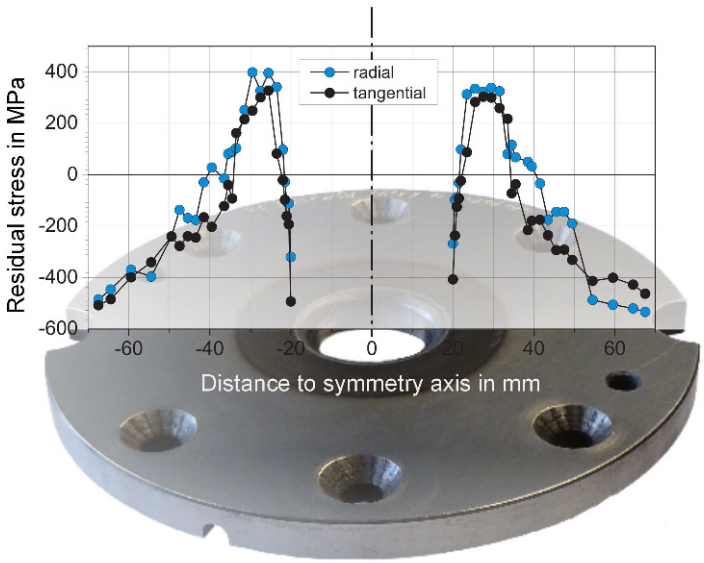

Fig. 2 Residual stress distribution at the surface of the tool after approximately 200 hot metal forming operations

To get further information about the origin of these residual stresses, depth distributions were analysed by X-ray and Neutron diffraction at two locations inside and outside the cyclically heated and cooled zone of the tool (see Fig. 3). Outside the heated zone, compressive residual stresses are only measured in a very thin surface layer (Fig. 3, right), inside the heated zone tensile residual stresses of about 450MPa at the surface decrease only gradually and decay within a depth of approximately 1.5mm of the tool. It is assumed that different reasons for these stresses exist. The compressive residual stresses outside the cyclically heated zone result from the final grinding process of the tool manufacturing process whereas the tensile residual stresses inside the cyclically heated zone are produced during the use of the tool as a consequence of cyclic plastic deformation due to the cyclic heating and cooling process [12]. Fig. 3 shows a good correlation of data gained by X-ray and neutron diffraction.

During the forming process of the flange shafts, time-temperature courses were measured at different positions of the hot forming tool to get an idea of the thermal loading situation. Fig. 4 shows three time-temperature courses. During each cycle temperatures rapidly increase and, after reaching maximum values, slowly decrease. Due to the different temperature courses at several points of the tool complex thermal stress states near the tools surface have to be expected.

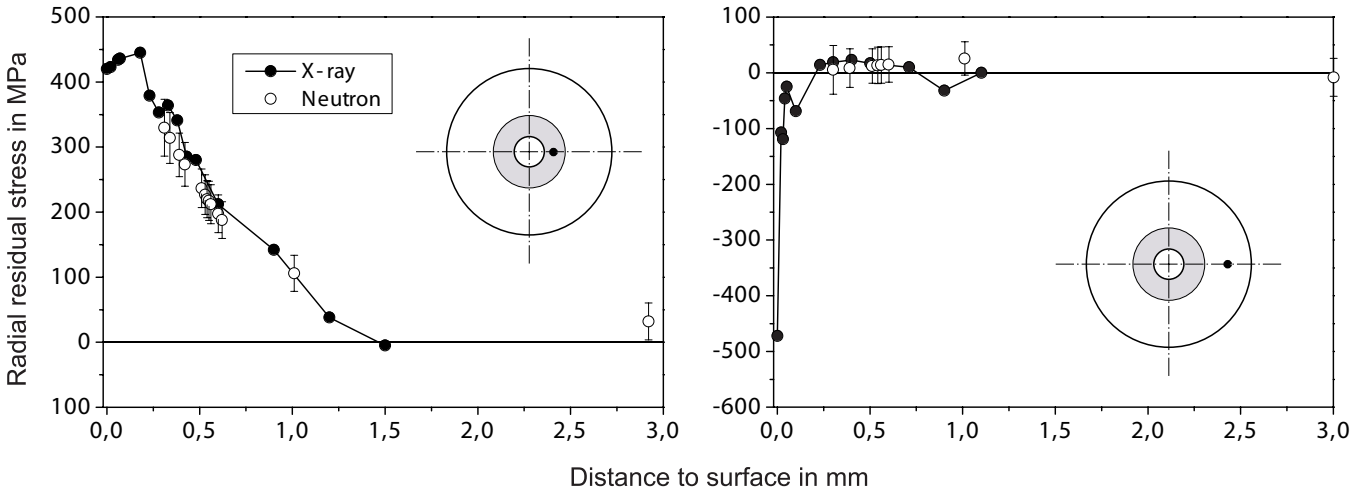

Fig. 3 Residual stress distributions measured by X-ray and neutron diffraction at different points in a thermo-mechanically loaded hot forming tool

To get further information about the materials behaviour under isothermal and thermal loading conditions, isothermal fatigue tests as well as thermal fatigue tests were carried out under axial loading states up to temperatures of 650°C. The specimens investigated have been machined from a forged ingot with the following chemical composition (wt-%.): 0.37 C, 1.2 Si, 0.23 Mn, 4.96 Cr, 1.25 Mo, 0.45 V, 0.003 P, 0.002 S, Fe balanced. Blanks of the specimens were heat treated (austenitisation for 20 min at 1025°C, quenching in oil of 60°C, two times tempering for 2 h at 625°C) to achieve a hardness of 44 HRC. The material investigated had the following mechanical properties: $R_{p0.2}$ = 1153MPa, UTS = 1384MPa. Cylindrical specimens with a diameter of 7mm and a gauge length of 10mm were machined out of the heat treated blanks. After heat treatment, all samples were hard turned to realize identical starting conditions regarding surface roughness and residual stress state.

Isothermal tests were carried out under stress control with zero mean stress and triangular stress-time paths with a frequency of 0.5Hz. Out-of-phase thermal fatigue tests were realized under complete suppression of total strain. A triangular temperature-time course with a heating and cooling rate of 10K/s was applied using a computer controlled induction system to heat up the specimens. Compressed air nozzles situated near the gauge length of the specimens were used for cooling. Cyclic heating and cooling under complete suppression of thermal expansion leads to fluctuating thermal stresses during the tests. In all cases investigated, cycling softening of AISI H11 occurs. Plastic strain amplitudes are very important indicators to assess the effects of isothermal or thermal fatigue processes. As an example for isothermal tests plastic strain amplitudes for a stress amplitude of 750MPa and different test temperatures, i.e. 20°C, 400°C and 500°C are shown in Fig. 5 (left). Decreasing total lifetimes to failure with increasing test temperature were observed. Cyclic plastic behaviour during isothermal fatigue is characteristic for quenched and tempered steels. Generally a stable microstructure can be assumed except for coarsening processes of precipitated carbides at temperatures well below the tempering temperature of 625°C. For tests at room temperature, plastic strain amplitudes are very small and a nearly macroscopic elastic behaviour is observed for

higher numbers of loading cycles. For temperatures of 400°C and 500°C plastic strain amplitudes start to increase continuously after an incubation period and very pronounced cyclic softening occurs [13]. This is attributed to rearrangements of dislocations associated with greater dislocation mobility. In addition, the formation of cracks plays a role and cyclic plastic deformation is superimposed by the consequences of crack opening and closing processes.

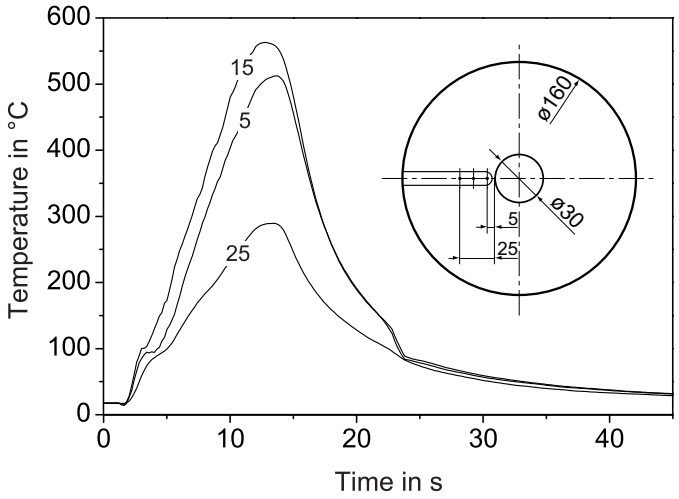

Fig. 4 Time-temperature courses during the hot metal forming process [14]

In Fig. 5 (right) plastic strain amplitudes for thermal fatigue tests using upper temperatures of 550°C, 600°C, 625°C and 650°C and base temperatures of 100°C and 200°C are shown. At first very low values of plastic strain can be observed as already shown in the isothermal case. At higher numbers of thermal cycles, the plastic strain amplitudes increase and the specimens exhibit cyclic softening behaviour. A comparison of tests carried out under identical upper temperatures shows higher plastic strain amplitudes for a base temperature of 100°C than for 200°C. Fig. 6 shows upper stresses resulting during thermal fatigue tests at a base temperature of T_{min}=100°C. Already after the first loading cycle, tensile stresses are observed which increase with increasing temperature amplitude. At the end of the lifetime, they drastically decrease due to the formation of cracks. If one assumes that specimens loaded under out-of-phase thermal fatigue conditions are representative of a small volume element in the cyclically heated and cooled zone of the tool, then results of the thermal fatigue tests presented explain the formation of tensile residual stress states in this region of the tool.

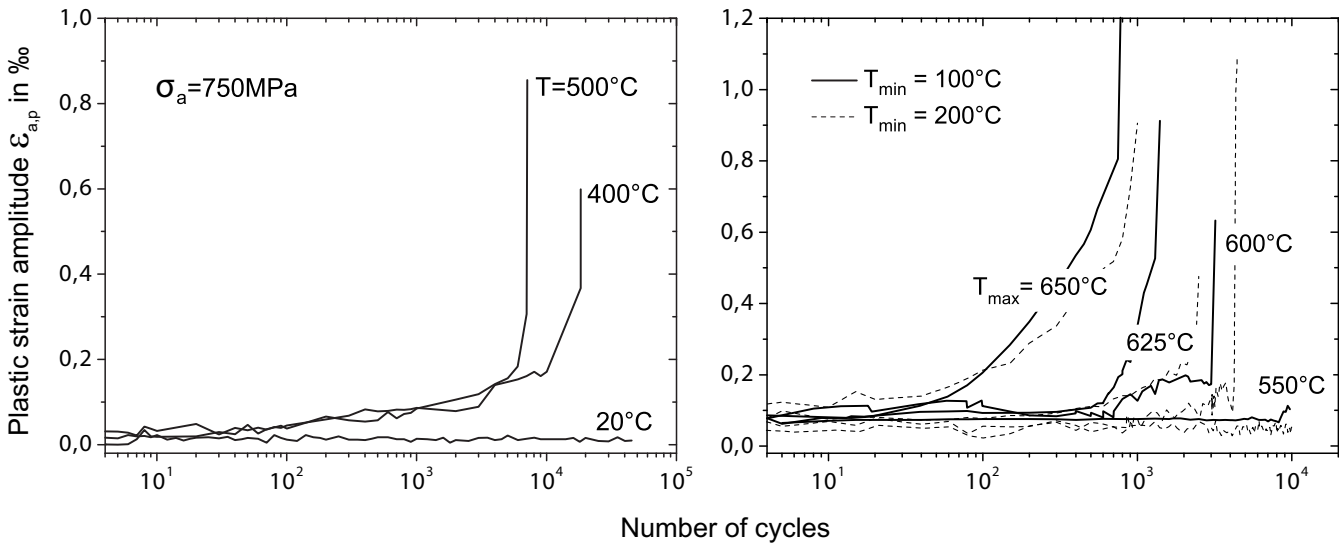

Fig. 5 Resulting plastic strain amplitudes in case of isothermal loading (left) and thermal loading (right) for different temperatures or temperature ranges

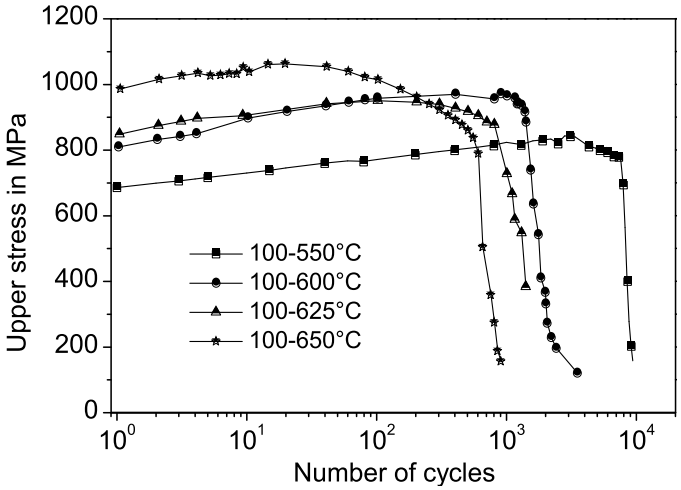

Fig. 6 Courses of upper stress for different temperature amplitudes at a base temperature of 100°C

The important role of cyclic thermal stress on residual stress formation is emphasised by the results shown in Fig. 7 Here, tangential and radial residual stress distributions are shown, measured at the surface of tool models which were only cyclically heated (without mechanical load) by an induction coil and quenched by water spraying with time-temperature courses as shown in Fig. 4. Three thermocouples were fixed 1mm beneath the tools surface at distances of 5mm, 15mm and 25mm from the inner borehole. In these tests maximum temperatures of approximately 550°C are measured [14]. As one can see, starting from manufacturing induced compressive stresses of approximately -200MPa in tangential direction and tensile residual stresses of approximately 100MPa in radial direction a tensile residual stress maximum develops close to the inner bore hole and maximum values increase with rising numbers of loading cycles. These distributions are qualitatively very similar to the distributions shown in Fig. 2. These results clearly demonstrate the significance of cyclic thermal loading for the formation of residual stress states.

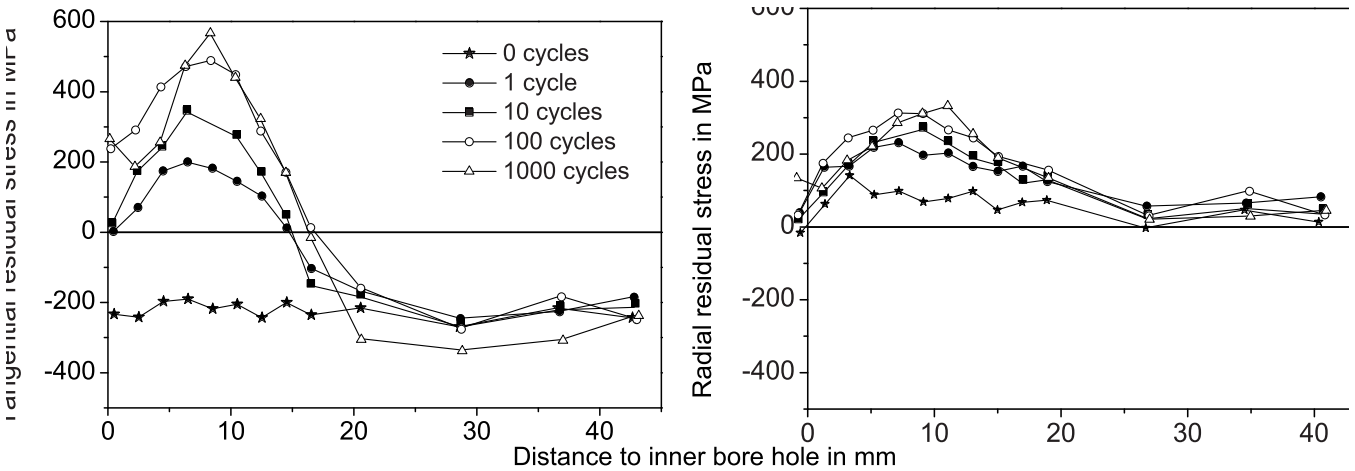

Fig. 7 Tangential (left) and radial residual stress distributions (right) at the surface of a tool which was loaded by thermal cycles only

Another focus of research is the investigation of residual stress formation induced by cyclic mechanical contact between tool and workpiece. For this purpose, flat specimens (50mm x 50mm x 20mm) of the tool steel AISI H11 were cyclically loaded under contact fatigue conditions using cylinders made of WC-Co hard metal and after that, the resulting residual stress fields were analysed using successive layer removal in combination with repeated application of X-ray stress measurements. Depth distributions of the residual stresses measured in the centre of the contact area in both directions along and perpendicular to the contact line are given in Fig. 8. Residual stresses were measured in longitudinal direction (left) and perpendicular to the contact line (right) after cyclic loading with a maximum force of 202kN for the numbers of loading cycles indicated.

Grinding induced residual stresses altered already after the first loading cycle. For stresses measured parallel to the contact line with increasing numbers of loading cycles, a thin layer of high compressive residual stresses occurs followed by a region with smaller compressive residual stresses with amounts of -50MPa to -260MPa in a depth of approximately 0.1 - 0.25mm. Then amounts of compressive residual stresses increase again, reach maximum values in a distance to surface of approximately 0.4 – 0.6mm and then decrease continuously. For higher numbers of loading cycles, amounts of compressive residual stresses increase slightly and the position of the maximum is shifted to larger distances from the surface. The stress components measured perpendicular to the contact line show a maximum of tensile residual stress about 0.1mm below the surface followed by a maximum of compressive residual stresses which becomes more pronounced and is shifted deeper below the surface with increasing numbers of loading cycles.

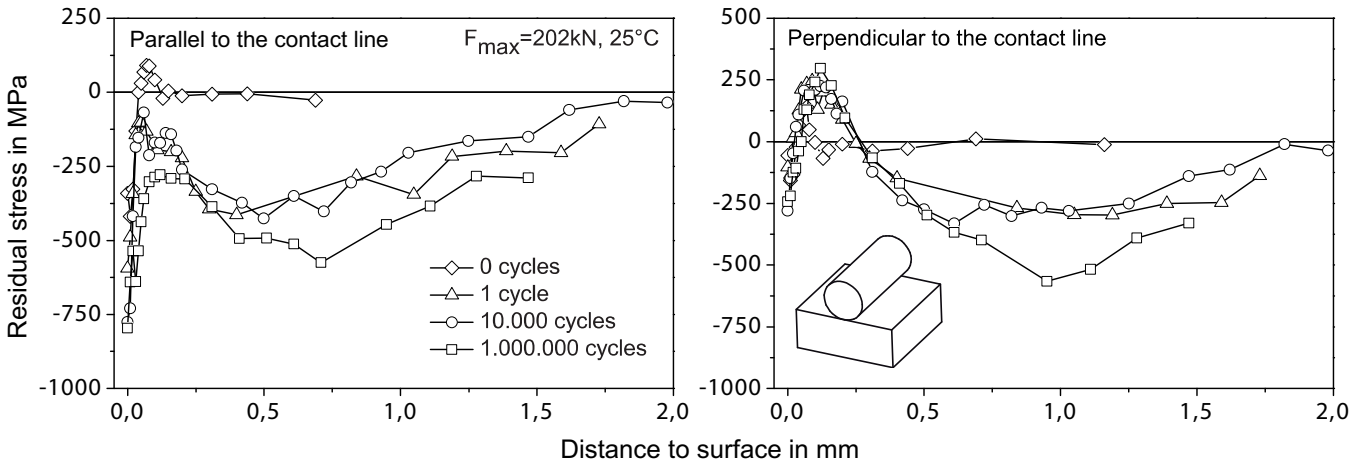

Fig. 8 Residual stress distributions as a consequence of cyclic contact loading after different numbers of loading cycles

Conclusion

The application of modern thermo-mechanically coupled hot metal forming processes allows the economic mass production of components with unique combinations of geometries and local materials microstructures or strength respectively. A characteristic feature of the new processes is that inhomogeneous thermal as well as mechanical loading states occur. Identification and assessment of basic processes responsible for the formation of characteristic residual stress states in tools and components due to thermo-mechanically coupled forming operations was the main purpose of the work carried out in this research project. The importance of thermal cycles and the associated cyclic plasticity on the residual stress state of tools used for hot metal forming of flange shafts was confirmed by the results of isothermal and thermal fatigue tests. In cyclically heated and cooled volumes tensile residual stresses have to be expected when complete suppression of thermal expansion is supposed. This effect occurs already at the beginning of the use of the tool. It has been shown that for the case investigated here, cyclic thermal loading is the most important process controlling the formation of residual stress states in the tool used and that mechanical loading plays a minor role.

Acknowledgements

Financial support of this project within the frame of the Transregional Collaborative Research Centre TRR 30 by the German Research Foundation DFG is gratefully acknowledged.

References

[1] Persson, A.; Bergström, J.; Burman, C.: Evaluation of heat checking damage in die casting. In: 5th International Conference on Tooling, p. 167-177, (1999)

[2] Muhic, M.; Tusek, J.; Kosel, F.; Klobcar, D.; Pleterski, M.: Thermal fatigue cracking of die-casting dies. Metalurgija 49 (1), p. 9-12, (2010)

[3] Wendl, F.: New materials for die casting. Journal of Heat Treatment and Materials 65 (4), p. 219-223, (2010)

[4] Krauß, M.; Scholtes, B.: Thermal Fatigue of Shot-peened or Hard Turned Hot-Work Tool Steel AISI H11. In: Wagner, L. (Edtr.): Proceed. 8th Int. Conf. on Shot Peening. Weinheim: Wiley-VCH, p. 324-330, (2004)

[5] Lacki, P.: A Study of Thermo-mechanical Load of Die Forging Dies. Int. Conf. on Metal Forming, Krakow, p. 633-639, (2000)

[6] Devi, M. U.: Damage Mechanisms in Salt Bath Nitro-carburised and Plasma Nitrided Forging Dies of H11 Tool Steel. ISIJ Int., Vol 42 (5), p. 527-533, (2002)

[7] Steinhoff, K.; Maier, H.J.; Biermann, D. (Eds.): Functionally graded materials in industrial mass production. Auerbach,Verlag Wissenschaftliche Scripten, (2009)

[8] Scholtes, B.: Assessment of Residual Stresses. In: Hauk, V.: Structural and Residual Stress Analysis by Nondestructive Methods, Elsevier, Amsterdam, 1997, p. 590-632

[9] Weidig, U.; Bergmann, K.; Scholtes, B.; Steinhoff, K.: Functionally Graded Properties by Controlled Thermo-Mechanical Interaction in Metal Forming Processes. In: Proc. 8th International Conference on Technology of Plasticity ICTP 2005, 9.-13. Oct. 2005,Verona, Italy

[10] Hauk, V.: Structural and Residual Stress Analysis by Nondestructive Methods. Elsevier, Amsterdam, Lausanne, New York, a.o., (1997)

[11] Kornmeier, R.; Gibmeier, J.; Hofmann, M.; Wimpory, R.C.: Neutron surface residual stress scanning using optimisation of a Si bend perfect crystal monochromator for minimising spurious strains. 8th European Conference on Residual Stresses (ECRS8), Riva del Garda, (2010)

[12] Grüning, A.; Lebsanft, M.; Scholtes, B.: Cyclic stress-strain behavior and damage of tool steel AISI H11 under isothermal and thermal fatigue conditions, Materials Science and Engineering A 527, p. 1979-1985, (2010)

[13] Gruening, A.; Krauss, M.; Scholtes, B.: Isothermal Fatigue of Tool Steel AISI H11. Steel Research Int. 79 (2), p. 111-115, (2008)

[14] Mahnken, R.; Sauerland, K-H.: Simulation of a Hybrid-Forming Process Considering Thermal Shock Behaviour in the Forming Tool. In: Steinhoff, K.; Maier, H.J.; Biermann, D. (Eds.): Functionally graded materials in industrial mass production. Auerbach,Verlag Wissenschaftliche Scripten, p. 185-190, (2009)

Determining Residual Stress And Young's Modulus – Can Digital Shearography Assist

D Findeis & J Gryzagoridis
Department of Mechanical Engineering, University of Cape Town
Private Bag, Rondebosch, 7700
South Africa

Abstract

Residual Stresses are inherent in most materials and structures which have been exposed to a machining or manufacturing process. They are known to have both a beneficial as well as detrimental influence on the performance of manufactured components and yet often go by undetected.

This paper presents the results of a research project aimed at determining the use of Digital Shearography as a suitable method to identify inherent material and structural properties. In order to apply the technique, 3 samples were prepared, one in its fully annealed state and the other 2 with different levels of residual stresses introduced into one of the sample surfaces. This was repeated for three different materials. Investigations were then conducted to determine the samples deflection curvatures in response to an applied load. From these deflections the investigation attempted to determine the Young's Modulus and magnitude of residual stresses present. The results are presented and compared with tensile specimen results for accuracy. From the results obtained it is apparent that Digital Shearography cannot necessarily be used to detect the presence of residual stresses, but can determine the material's Young's modulus.

Introduction

Residual stresses are present in virtually all manufactured components. They are introduced into materials and parts as a result of forming and machining processes applied, are contained within the components surface region and can vary in magnitude from part to part. The presence of residual stresses is often undesirable and in such cases heat treating procedures can be applied to remove them. In other instances the presence of residual stresses is desired[1] - compressive residual stresses are known to counteract the onset and propagation of fatigue and stress corrosion cracking.

In the challenge to reduce the weight of components without scarifying their performance, there is an increasing need to have a better knowledge of the presence and magnitude of residual stresses[2]. This can be achieved through non destructive as well as destructive testing techniques. As destructive techniques rely on some form of material removal, non destructive techniques are preferred due to the part still being intact after the test.

Optical NDT techniques such as Electronic Speckle Pattern Interferometry and Digital Shearography are non contacting inspection techniques suitable for the inspection of objects for both surface and subsurface defects and have also been used to detect the presence of residual stresses. Digital Shearography, on the face of it, appears to be particularly suited for residual stress investigations, as the technique records the rate of surface deformation in response to an applied stress. This possibility was highlighted in a pilot study, the results of which were presented at the 2010 BINDT annual conference[3]. The work focussed on using Digital Shearography to investigate the deflection characteristics of a set of mild steel cantilever beams, some with induced residual stresses, and concluded that the technique showed promise in determining both a material's Young's Modulus as well as the presence of residual stresses.

This paper extends this work by investigating the ability to detect residual stresses in three different materials using Digital Shearography and compares the calculated Young's Modulus with experimentally determined values.

T. Proulx (ed.), *Engineering Applications of Residual Stress, Volume 8*, Conference Proceedings of the Society for Experimental Mechanics Series 999, DOI 10.1007/978-1-4614-0225-1_7, © The Society for Experimental Mechanics, Inc. 2011

Theory

Digital Shearography is a laser based non-contacting interferometric technique[4]. The technique relies on an expanded monochromatic laser to illuminate the object to be inspected. The light reflected off the surface of the object is viewed through a CCD camera which in turn is connected to a PC for image processing purposes. In front of the camera a purpose built shearing device is placed. The function of the shearing device is to split the image of the object into 2 distinct images which overlap each other. In a Michelson interferometer setup this is achieved by using a 45º beamsplitter to split an incoming image into two images. For each of these images a mirror is used to reflect the images back onto the beamsplitter where they recombine and then are captured by the camera. If one of the mirrors has the ability to be manipulated in the x and y direction (the shearing mirror), the magnitude as well as position of image overlap, or shear can be controlled. A typical optical set-up is shown in figure 1 below.

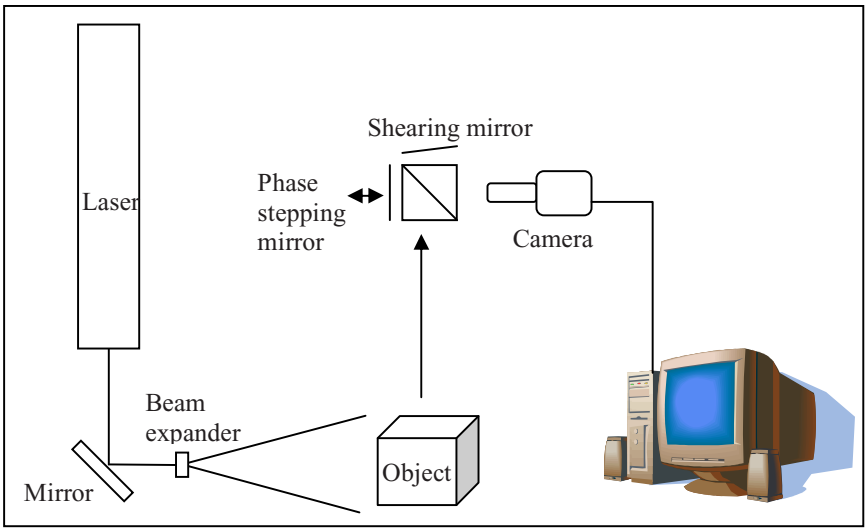

Figure 1. Typical Shearography set-up

The overlap of the two images forms a unique speckle pattern which is captured and stored in a PC. If the object is deformed due to an applied stress, and there is relative movement between the two overlapped images, a change in the speckle pattern occurs. In addition a controlled phase shift is introduced into the beam path length. Comparing the speckle images before and after for areas of correlation and decorrelation produces a saw tooth fringe pattern, where the direction of the fringe intensity gradient provides information on the direction of the displacement gradient. The mathematical formula for this process is outlined below[5].

$$I_i(x,y) = I_B(x,y) + I_{MP}(x,y)\cos(\theta(x,y) + i\cdot\pi/2) \quad (1)$$

$$\phi(x,y) = \arctan\left(\frac{I_3(x,y) - I_1(x,y)}{I_4(x,y) - I_2(x,y)}\right) \quad (2)$$

$$\beta(x,y) = \phi_a(x,y) - \phi_b(x,y) \quad (3)$$

where i = 1,2,3,4
$\phi_a(x,y)$ = phase distribution after stressing, $\phi_b(x,y)$ = phase distribution before stressing.

In order to calculate the magnitude of the displacement gradient, the following equation can be used:

$$\frac{\partial p}{\partial x} = \frac{\lambda N}{S} \quad (4)$$

where $\partial p/\partial x$ = displacement gradient in the x (or y) direction, λ = wavelength of the laser light
N = number of fringes counted, S = shear magnitude

A cantilever beam is a beam which is securely mounted at its one end and free to move at the other end. If a force is applied at the free end, perpendicular to the face of the cantilever, the force will cause the beam to bend, placing one face of the beam into tension and the other into compression, as shown in figure 2 below.

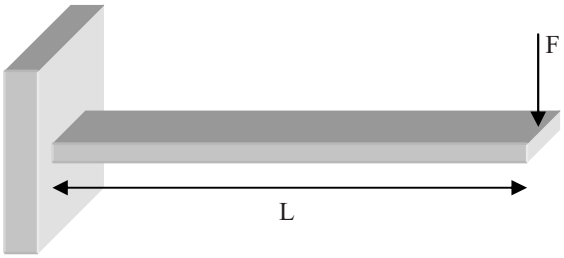

Figure 2. Schematic of a cantilever and the applied load.

With this controlled loading environment, the cantilever deflection can easily be modelled according to equation 5 below.

$$y = \frac{P}{EI}\left(-\frac{Lx^{2}}{2} + \frac{x^{3}}{6}\right) \tag{5}$$

Differentiating this equation yields the slope of the deflection.

$$y' = \frac{P}{EI}\left(-Lx + \frac{x^{2}}{2}\right) \tag{6}$$

The resultant stress produced in the surface of the cantilever is defined as:

$$\sigma = \frac{tP}{2I}(-L + x) \tag{7}$$

where: E = Young's modulus, P = Load, I = second moment of area for a rectangular beam
L = Length of the beam x = position along the beam y = beam deflection.
t = beam thickness

When a force is applied perpendicular to the cantilever, it deflects accordingly in the direction of the applied force. With the aid of Digital Shearography the rate of deflection can be determined. Using equation 4, the magnitude of the rate of deflection, can be determined without any knowledge of the material properties. The theoretical rate of displacement is defined in equation 6. All constants and dimensions, with the exception of the Young's Modulus, can be determined from the dimensions of the cantilever sample used. By selecting a suitable value for the Young's Modulus and determining the rate of displacement curve, equation 6 can be manipulated to fit the rate of displacement curve obtained experimentally in equation 4, thus determining the best suited Young's Modulus to fit the experimental data.

When considering the cantilever, residual stresses, if present, will manifest themselves in the surface layer of the cantilever. It has been suggested that these locked-in surface stresses have the ability to enhance or resist the expected deflection curve, depending on whether they are compressive or tensile stresses, when a transverse load is applied. By comparing these deflection curves with those of "stress free" cantilever beams, initial results indicate that it is possible to detect and quantify the magnitude of the residual stresses. By recording the applied force and rate of displacement in a residual stress sample, this is achieved by establishing the equivalent force required in a "stress free" sample using equation 4, which would produce the same displacement gradient as that recorded in the experiment. Equation 7 would then have to be applied to compute the stress distributions in the surfaces of the cantilevers for both the "stress free" case and the equivalent load case. The difference in surface stress levels could then be directly determined and attributed to the presence the residual stresses.

Results

Three different types of materials namely mild steel, aluminium and brass, all supplied as 6 mm rolled flat bar, were chosen to manufacture the required cantilever samples. For each material three cantilevers were machined. One of the cantilevers

was machined down to 4mm thickness by removing 2 mm of material from one side only. This was done to remove any locked–in residual stresses due to the forming process from one face of the cantilever, whilst retaining the residual stress in the other face of the cantilever. The other two cantilevers were also machined down to 4 mm by equally removing 1mm thickness from each side. In addition 4mm thick tensile specimens, two of each supplied material, were machined.

The two evenly machined cantilevers and tensile specimen of each material were then annealed in order to reduce and remove any residual stresses within the samples. One of the two cantilever samples was left in its annealed state, whilst the other sample was exposed to plastic deformation, similar to shot peening, on one side. This was achieved by using many 2mm diameter ball bearings and pressing them onto the surface of the cantilever with a hydraulic press. This process was applied to the mild steel and aluminium samples. The remaining brass sample was exposed to a second annealing process.

The cantilevers were then sequentially clamped vertically into a vice using two parallels with sharp edges to ensure uniform gripping between the vice grip faces. The force was applied normal to the rear face of the cantilever via a wire, which passed over a securely mounted pulley. Weights were used to produce the required bending force. The complete experimental configuration including the Digital Shearography setup is depicted in figure 3 and the final dimensions of the cantilevers and the applied forces are listed in table 1 below. As can be seen, the cantilevers were coated with a thin layer of matt white paint to improve visibility.

Material	Length (mm)	Breadth (mm)	Thichness (mm)	Applied Force (N)
Mild Steel	227	50	4	0.338
Aluminium	227	50.7	4.05	0.289
Brass	227	40	4	0.927

Table 1. Cantilever materials and dimensions

Figure 3. Cantilever and digital shearography setup.

Figure 4 below is the collection of results obtained for the mild steel set of cantilever beams. The leftmost image is a shot of one of the cantilevers and was used to establish the magnitude of image shear which was established to be 6.5mm, as well as the magnification factor needed to correctly locate the fringe positions. The second image is the fringe pattern obtained for the annealed cantilever, the third the result for the residual stress sample and the final image the result obtained from the inspection of the peened cantilever.

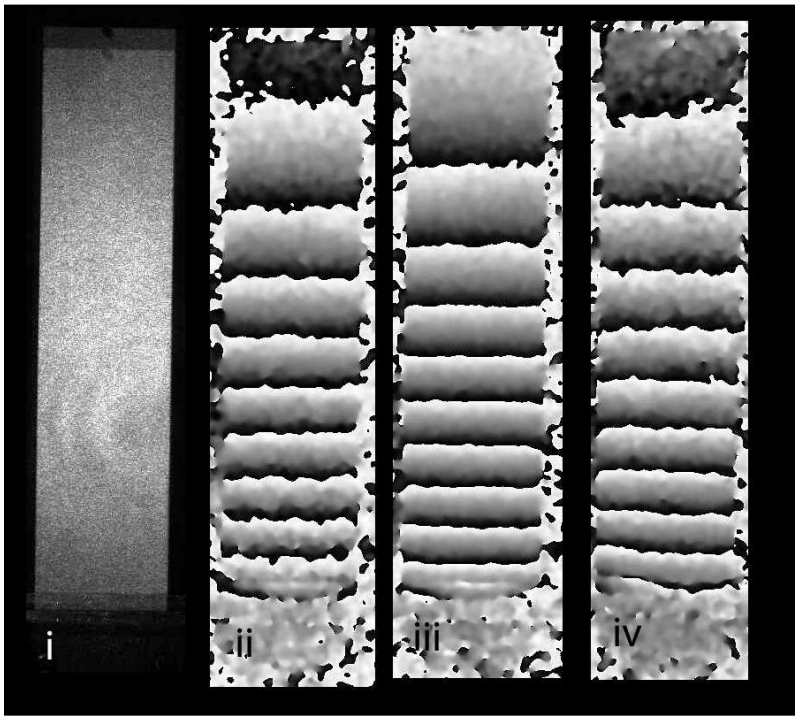

Figure 4. Mild steel cantilever fringe pattern results. i) simple image of cantilever, ii) annealed sample result, iii) residual stress result, iv) peened sample result.

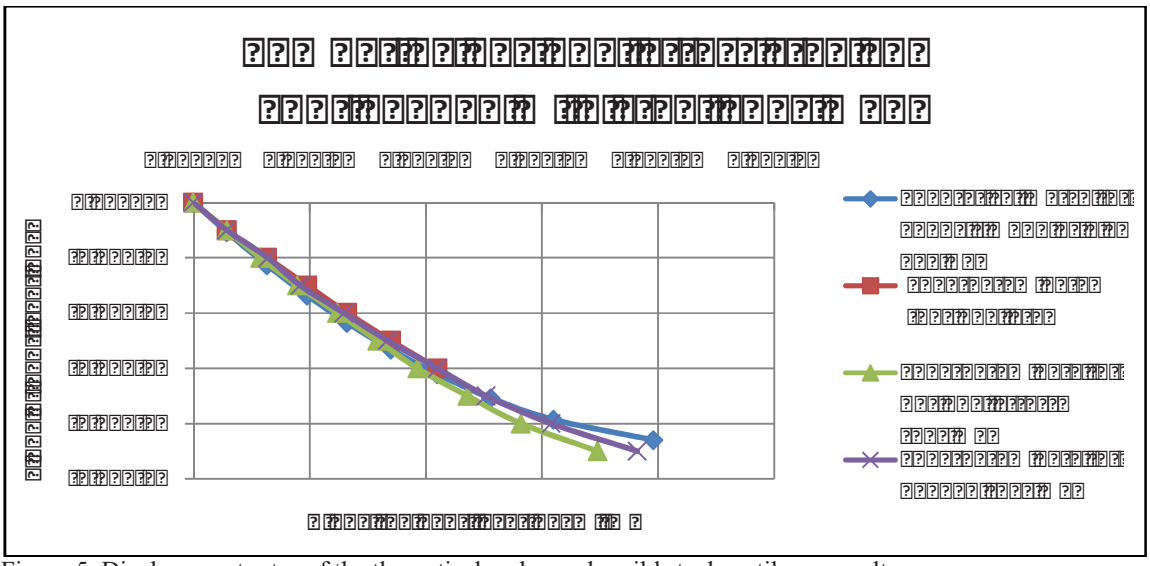

Figure 5. Displacement rates of the theoretical and sample mild steel cantilever results.

At first glance it appears that the fringe patterns are different between the individual results. Further investigation however reveals that the number of fringes produced with identical loading is roughly the same for all cantilevers, the difference between the individual results being that the location of the fringes have shifted marginally. This would indicate that the displacement curvature varies marginally from result to result, but there is no apparent significant influence of any residual stresses on the displacement rate of the prepared cantilevers.

The quantification of the displacement gradients and calculation of an appropriate Young's modulus is presented in Figure 5 above. The theoretical to experimental data curve fitting exercise revealed that a Young's modulus of 205 GPA produced a good fit to the annealed results. The Zwick/Roell tensile test on the two tensile specimens produced Young's modulus results

of 228 GPa and 200GPa resulting in an average of 214GPa. The literature lists a typical Young's Modulus value of 200 GPa and thus the experimentally determined value of 205 GPa falls within the range.

Figure 5 also indicates that there is no appreciable difference between the different displacement gradients of the specimens and there is thus no clear evidence of any residual stresses having an influence on the cantilever displacement characteristics.

The results of the inspection of the aluminium specimen are shown in Figure 6 below. Here again there are 4 images, the first a shot of the cantilever specimen and the second, third and fourth the fringe pattern results of the annealed, residual stress and peened cantilevers respectively. From the results it can be seen that the fringe patterns are similar, but do differ in that the residual and peened cantilever beams display an extra fringe for the same applied load when compared with the annealed cantilever sample. The extra fringe indicates that these samples have a slightly higher displacement rate than the annealed sample.

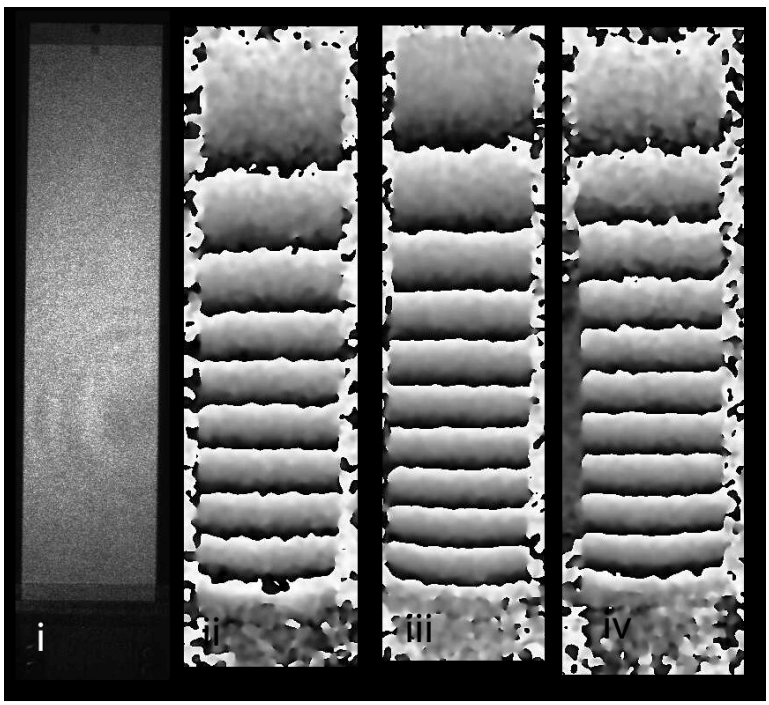

Figure 6. Aluminium cantilever fringe pattern results. i) simple image of cantilever, ii) annealed sample result, iii) residual stress result, iv) peened sample result.

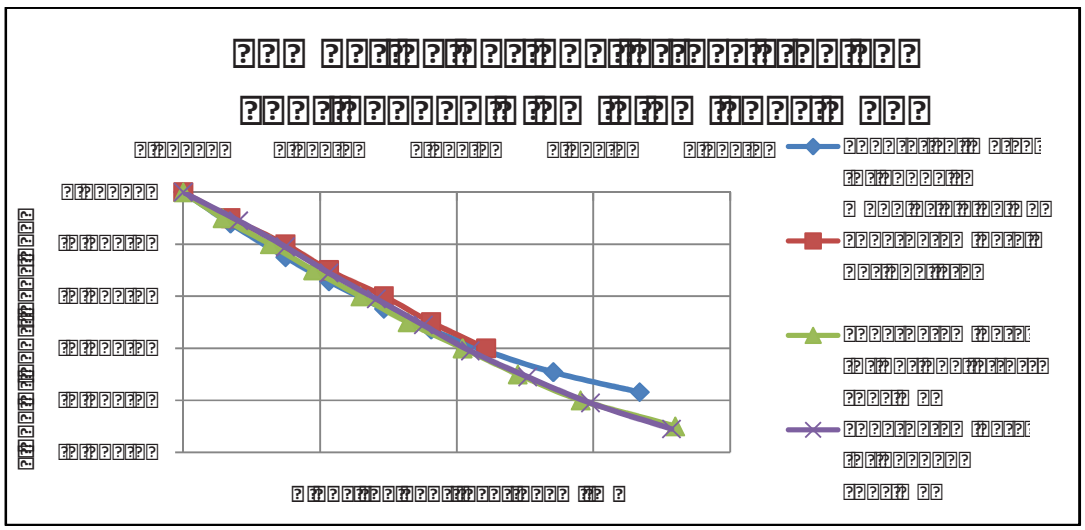

Figure 7. Displacement rates of the theoretical and sample aluminium cantilever results.

Using the annealed sample to determine the materials Young's modulus a value of 72 GPa produced a good correlation between the experimental curve and the theoretical curve. This value is slightly higher than the value reported in the literature, which is in the order of 70 GPa. Unfortunately the Zwick / Roell tensile test did not produce any usable data, as the machine appeared to not be sensitive enough, and plastic deformation was initiated before a useful stress - strain curve in the elastic region could be established. Using the displacement rate curve of the treated aluminium cantilever a Young's modulus of 70 GPa provided good theoretical correlation with the experimental data. The graph of the rate of displacement curve calculation is shown in figure 7 above.

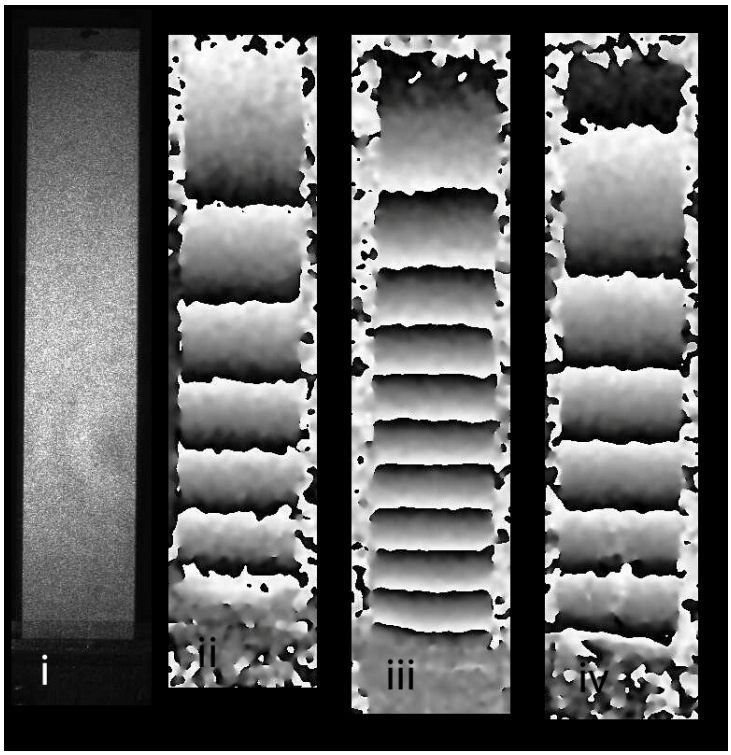

Figure 8. Brass cantilever fringe pattern results. i) simple image of cantilever, ii) annealed sample result, iii) residual stress result, iv) heat treated result.

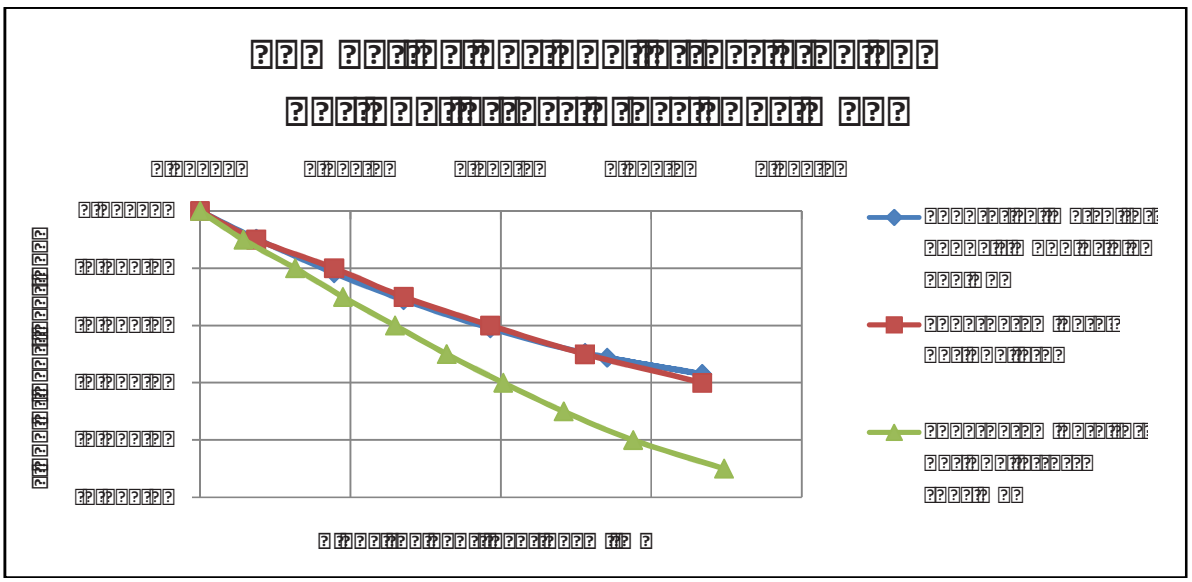

Figure 9. Displacement rates of the theoretical and sample brass cantilever results.

The results of the brass cantilever inspections are shown in figure 8 above. From the fringe patterns it is clear that there is a difference in the displacement gradients between the annealed sample and the residual stress sample. The strange aspect about this fringe patterns is that the residual stress cantilever has a greater displacement gradient and thus is less resistant to bending, which for a compressive residual stress should have had the opposite effect and resulted in a stiffer cantilever. The displacement gradient graph in figure 9 highlights this phenomenon.

The iterative process to determine the Young's Modulus yielded a value of 114 GPa, as seen in the comparative displacement gradient curves of the shearography experimental data and data derived from theory. The Zwick / Roell test of the 2 tensile specimens yielded values of 80 GPa and 114.29 GPa. The 80 GPa value appears too low, the jaws possibly could have slipped, but the second test yielding a value of 114.29 ties up very well with the data obtained from the shearography results.

Conclusions

From the above data it is clear that a cantilever setup in conjunction with Digital Shearography can be used as an effective method to determine the Young's modulus of materials. The results obtained agree well with results published in the literature as well as in house tensile tests.

The rate of displacement curves obtained for the annealed and locked in stress cantilever samples do not provide any clear evidence that the magnitude of residual stresses can be determined from the displacement curves. In particular there is no clear evidence of a decrease in the rate of the displacement curve for samples that were expected to contain compressive residual stresses, either due to the manufacturing process or peening process, which is in contrast to the results obtained and published in (3). A possible reason for this is that the samples used in the initial inspection were 15.5 mm thick, as opposed to the samples used in this investigation, which were 4 mm thick.

The results obtained from the annealed brass sample yield an acceptable Young's modulus of 114 GPa. The exact Copper and Zinc composition of the stock supplied is however not known. The displacement rate results of the machined sample however cannot be explained.

Recommendations

From the above it is clear that formulating a procedure to determine the Young's modulus using Digital Shearography is warranted. Care however needs to be taken to ensure that the prepared samples are annealed and stress free.

Further work needs to be conducted to understand why the results for the brass cantilever differ to such an extent. Investigations were undertaken to ensure that the samples are of the same thickness and that the parallels used to clamp the cantilevers were in fact flat parallels, but this did not reveal a possible cause of error.

Additional work is required to determine whether the induced residual stresses in the aluminium and mild steel samples were significant enough to influence the deflection profile, and to investigate the possible effect of the thickness of the sample on the rate of displacement profile.

References

1. C O Ruud, "A review of selected non-destructive methods for residual stress measurement", NDT International pp 15-23 Feb. (1982).
2. D L Ball, "The Influence of Residual Stress on the Design of Aircraft Primary Structure", Journal of ASTM International, p18, vol5, Apr. (2008).
3. J Gryzagoridis, D Findeis, T Chipanga, "Shearography – in identifying the presence and subsequent measurement of Residual Stress*", Proceedings 49th Annual Conference of the British Institute of Nondestructive Testing*, Cardiff, UK, 14–16 Sept. 2010.
4. Findeis D, Gryzagoridis J, Matlali M, "Phase Stepping Shearography and Electronic Speckle Pattern Interferometry", *Proceedings 3rd US-Japan Symposium on Advancing Capabilities and Applications in NDE*, Maui, 20-24 June. 2005.
5. AM Maas, PM Somers, "Two-dimensional Deconvolution Applied to Phase-stepped shearography", Optics and Lasers Engineering, 26, pp351-360, 1997.

Ultrasonic Technique and Equipment for Residual Stresses Measurement

Y. Kudryavtsev and J. Kleiman
Structural Integrity Technologies Inc., Markham, Ontario, Canada
E-mail: ykudryavtsev@sintec.ca

ABSTRACT

Different methods exist to measure the residual stresses (RS). One of the advantages of ultrasonic techniques for RS measurement is that they are non-destructive. Using such techniques, one can measure the RS in the same points many times, studying, for instance, the changes of RS under the action of service loading or effectiveness of stress-relieving techniques. An Ultrasonic Computerized Complex (UCC) for non-destructive measurement of residual and applied stresses was developed recently. The UCC includes a measurement unit with transducers and basic supporting software and an advanced database and an Expert System, housed in a laptop, for analysis of the influence of RS on the fatigue life of welded elements. In general, the ultrasonic method allows one to measure the RS in both cases: averaged through thickness or in surface layers. The advanced ultrasonic method, the equipment and some examples of RS measurement in welded elements and structures are discussed in this paper.

1. INTRODUCTION

Residual stresses (RS) can significantly affect engineering properties of materials and structural components, notably fatigue life, distortion, dimensional stability, corrosion resistance, brittle fracture [1]. Such effects usually lead to considerable expenditures in repairs and restoration of parts, equipment and structures. For that reason, the RS analysis is a compulsory stage in the design of parts and structural elements and in the estimation of their reliability under real service conditions.

Systematic studies had shown that, for instance, welding RS might lead to a drastic reduction in fatigue strength of welded elements [2]. In multi-cycle fatigue ($N>10^6$ cycles of loading), the effect of RS can be compared with the effect of stress concentration. Figure 1 illustrates one of the results of these studies. The butt joints in low-carbon steel were tested at symmetric cycle of loading (stress ratio R=-1). There were three types of welded specimens. The relatively small specimens (420x80x10 mm) were cut from a large welded plate. Measurements of RS revealed that in this case the specimens after cutting had a minimum level of RS. Additional longitudinal weld beads on both sides in specimens of second type created at the central part of these specimens tensile RS close to the yield strength of material. These beads did not change the stress concentration of the considered butt weld in the direction of loading. In the specimens of third type longitudinal beads were deposited and then the specimens were bisected and welded again. Due to the small length of this butt weld the RS in these specimens were very small and approximately the same as those within the specimens of first type [2].

Tests showed that the fatigue strength of specimens of first and third types (without RS) is practically the same with the limit stress range 240 MPa at $N=2\cdot10^6$ cycles of loading. The limit stress range of specimens with high tensile RS (second type) was only 150 MPa. In all specimens the fatigue cracks originated near the transverse butt joint. The reduction of the fatigue strength in this case can be explained only by the effect of welding RS. These experimental studies showed also that at the level of maximum cyclic stresses close to the yield strength of base material the fatigue life of specimens with and without high tensile RS was practically identical. With the decrease of the stress range there is corresponding increase of the influence of the welding RS on the fatigue life of welded joint.

T. Proulx (ed.), *Engineering Applications of Residual Stress, Volume 8*, Conference Proceedings of the Society for Experimental Mechanics Series 999, DOI 10.1007/978-1-4614-0225-1_8,

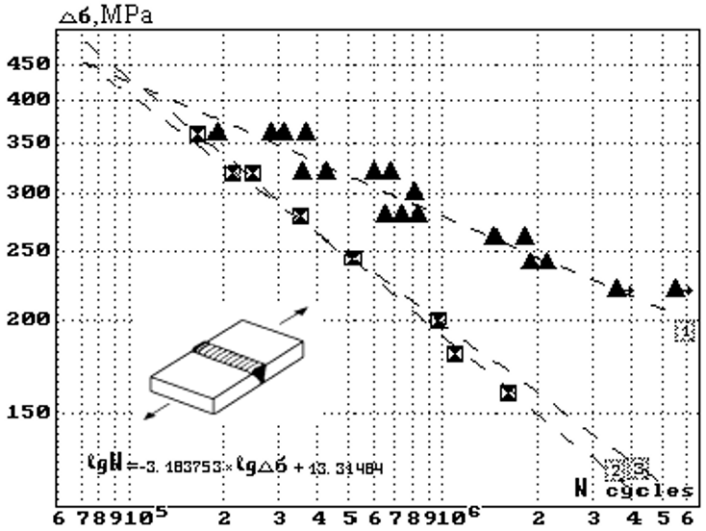

Figure 1. Fatigue curves of butt welded joint in low-carbon steel:
1 - without residual stresses; 2, 3 - with high tensile residual stresses (fatigue testing and computation)

The effect of RS on the fatigue life of welded elements is more significant in the case of relieving of harmful tensile RS and introducing of beneficial compressive RS in the weld toe zones. The beneficial compressive RS with the level close to the yield strength of material are introduced at the weld toe zones by, for instance, the ultrasonic peening (UIT/UP) [1, 3]. The results of fatigue testing of welded specimens in as-welded condition and after application of UIT/UP are presented in Figure 2. The fatigue curve of welded element in as-welded condition (with high tensile RS) was used also as initial fatigue data for computation of the effect of the UP. In case of non-load caring fillet welded joint in high strength steel (σ_y = 864 MPa, σ_u = 897 MPa), the redistribution of RS resulted in approximately two times increase in limit stress range and over 10 times increase in the fatigue life of the welded elements.

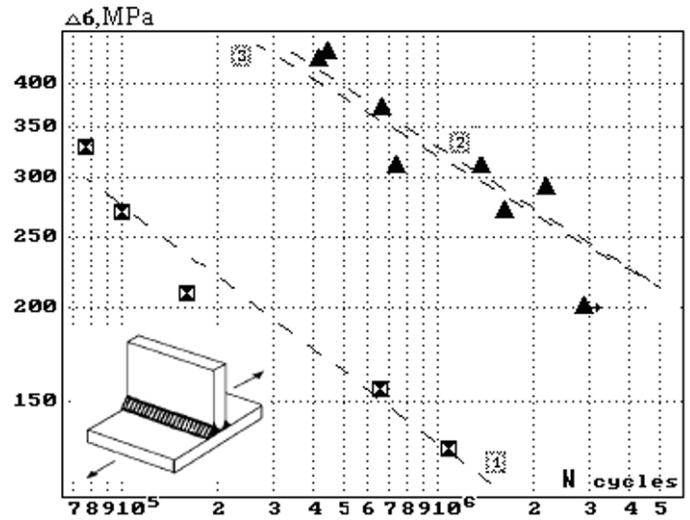

Figure 2. Fatigue curves of non-load caring fillet welded joint in high strength steel:
1 - in as-welded condition; 2, 3 - after application of ultrasonic peening (fatigue testing and computation)

The RS, therefore, are one of the main factors determining the engineering properties of materials, parts and welded elements and this factor should be taken into account during the design and manufacturing of different products. The efficient approach to the problem of RS includes, at least, stages of determination, analysis and beneficial redistribution of residual stresses. The combined consideration of the above-mentioned stages of the RS analysis and modification gives

rise to so called Residual Stress Management (RSM) concept approach [4, 5]. The RSM concept includes the following main stages:

Stage 1. Residual Stress Determination:
- Measurement: Destructive, Non-destructive,
- Computation.

Stage 2. Analysis of the Residual Stress Effects:
- Experimental Studies,
- Computation.

Stage 3. Residual Stress Modification (if required):
- Changes in Technology of Manufacturing and Assembly,
- Application of Stress-Relieving Techniques.

Over the last few decades, various quantitative and qualitative methods of RS analysis have been developed [4]. In general, a distinction is usually made between destructive and non-destructive techniques for RS measurement. The first series of methods is based on destruction of the state of equilibrium of the RS after sectioning of the specimen, machining, layer removal or hole drilling. The most common destructive methods are:

- the hole drilling method,
- the ring core technique,
- the bending deflection method,
- the sectioning method, etc.

The application of the destructive or so-called partially-destructive techniques is limited mostly to laboratory samples.

The second series of methods of RS measurement is based on the relationship between the physical and the crystallographic parameters and the RS and does not require the destruction of the part or structural elements and could be used for field measurements. The most developed non-destructive methods are:

- the X-ray and neutron diffraction methods,
- the ultrasonic techniques,
- the magnetic methods etc.

Although certain progress has been achieved in the development of different experimental techniques, a considerable effort is still required to develop efficient and cost-effective methods of residual stress analysis [4, 6]. The application of an ultrasonic non-destructive method for residual stress measurements had shown that, in many cases, this technique is very efficient and allows measuring the residual stresses both in laboratory conditions and in real structures for a wide range of materials [4-11].

2. ULTRASONIC MEASUREMENT OF RESIDUAL STRESSES

2.1. Ultrasonic Method of Residual Stress Measurement

One of the promising directions in development of non-destructive techniques for residual stress measurement is application of ultrasound. Ultrasonic stress measurement techniques are based on the acoustic-elasticity effect, according to which the velocity of elastic wave propagation in solids is dependent on the mechanical stress. The relationships between the changes of the velocities of longitudinal ultrasonic waves and shear waves of orthogonal polarization under the action of tensile and compressive external loads in steel and aluminum alloys are presented in Figure 3. As can be seen from Fig. 3, the intensity and character of such changes could be different, depending on material properties.

Different configurations of ultrasonic equipment can be used for residual stress measurements. In each case, waves are launched by a transmitting transducer, propagate through a region of the material and are detected by a receiving transducer as shown in Figure 4 [6]. The technique when the same transducer is used for excitation and receiving of ultrasonic waves is often called pulse-echo method (Figure 4a). This method is effective for analysis of residual stresses in the interior of material. In this case the through-thickness average of residual stresses is measured. In the configuration shown in Figure 4c, the residual stress in a surface/subsurface layer is determined.

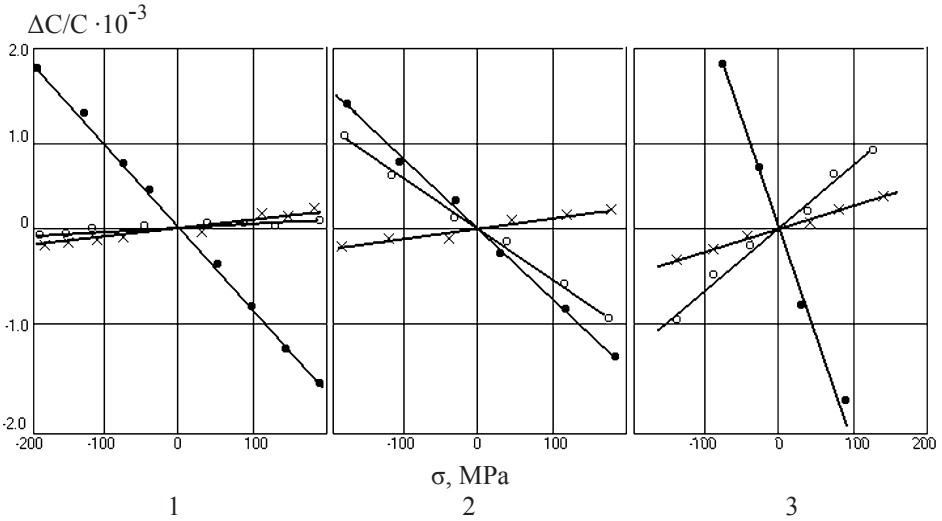

Figure 3. Change of ultrasonic longitudinal wave velocity (C_L) and shear waves velocities of orthogonal polarization (C_{SX3} ; C_{SX2}) depending on the mechanical stress σ in steel A (1), steel B (2) and aluminum alloy (3) [10]: ● - C_{SX3} ; ○ - C_{SX2} ; x - C_L

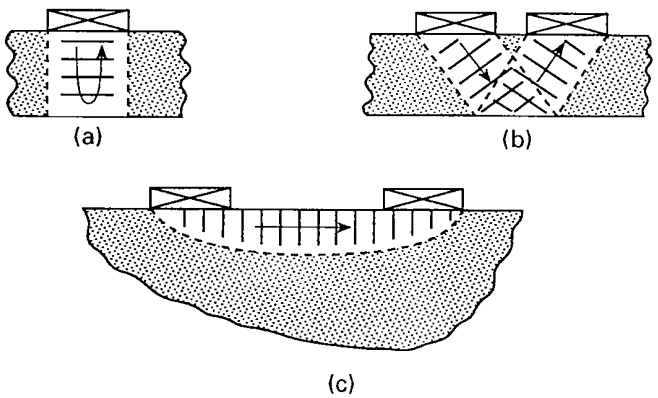

Figure 4. Schematic view of ultrasonic measurement configurations:
(a) through-thickness pulse-echo, (b) through-thickness pitch-catch and (c) surface pitch-catch

The depth of this layer is related to the ultrasonic wavelength, often exceeding a few millimeters, and hence is much greater than that obtained by X-ray method. Other advantages of the ultrasonic technique are the facts that the instrumentation is convenient to use, quickly to set up, portable, inexpensive and free of radiation hazards.

In the proposed in [7, 9, 10] technique, the velocities of longitudinal ultrasonic wave and shear waves of orthogonal polarization are measured at a considered point to determine the uni- and biaxial residual stresses. The bulk waves in this approach are used to determine the stresses averaged over the thickness of the investigated elements. Surface waves are used to determine the uni- and biaxial stresses at the surface of the material. The mechanical properties of the material are represented by the proportionality coefficients, which can be calculated or determined experimentally under an external loading of a sample of considered material.

In general, the change in the ultrasonic wave velocity in structural materials under mechanical stress amounts only to tenths of a percentage point. Therefore the equipment for practical application of ultrasonic technique for residual stress measurement should be of high resolution, reliable and fully computerized.

2.2. Ultrasonic Equipment and Software for Residual Stress Measurement

The Ultrasonic Computerized Complex (UCC) for residual stress analysis was developed recently based on an improved ultrasonic methodology [7-10]. The UCC includes a measurement unit with supporting software and a laptop with an advanced database and an Expert System (ES) for analysis of the influence of residual stresses on the fatigue life of welded components. The developed device with gages/transducers for ultrasonic residual stress measurement is presented in Figure 5. The UCC allows determining uni- and biaxial applied and residual stresses for a wide range of materials and structures. In addition, the developed ES can be used for calculation of the effect of measured residual stresses on the fatigue life of welded elements, depending on the mechanical properties of the materials, type of welded element, parameters of cyclic loading and other factors.

Figure 5. The Ultrasonic Computerized Complex for measurement of residual and applied stresses

The developed equipment allows one to determine the magnitudes and signs of uni- and biaxial residual and applied stresses for a wide range of materials as well as stress, strain and force in various size fasteners. The sensors, using quartz plates measuring from 3×3 mm to 10×10 mm as ultrasonic transducers, are attached to the object of investigation by special clamping straps (see Figure 5) and/or electromagnets.

The main technical characteristics of the measurement unit:

- stress can be measured in materials with thickness 2 - 150 mm;
- error of stress determination (from external load): 5 - 10 MPa;
- error of residual stress determination: 0.1 σ_y (yield strength) MPa;
- stress, strain and force measurement in fasteners (pins) 25-1000 mm long;
- independent power supply (accumulator battery 12 V);
- overall dimensions of measurement device: 300x200x150 mm;
- weight of unit with sensors: 7 kg.

The supporting software allows controlling the measurement process, storing the measured and other data and calculating and plotting the distribution of residual stresses. The software also allows an easy connection with standard PC's.

An example of presentation of the residual stress measurement data, using the developed software, is shown in Figure 6. The software allows comparing different data on residual stress measurement and transferring selected data for further fatigue analysis. In Figure 6, the left side of the screen displays information on the measured ultrasonic wave velocities as well as other technical information on the sample. The right side of the screen displays the distribution of calculated residual stresses.

In the example of residual stress measurement presented in Figure 6, a plate made from low carbon steel, with yield strength of 296 MPa, was heated locally, with the focal point of heating located approximately 50 mm from the left side of the plate. The distribution of both components of residual stresses in the specimen, as a result of this local heating are shown in the right side of Figure 6. As can be seen, in the heating zone, both residual stress components are tensile and reach the yield strength of the considered material. In the compression zone, located between the edge of the plate and the centre of the heating zone, the longitudinal component of residual stresses reaches minus 140 MPa.

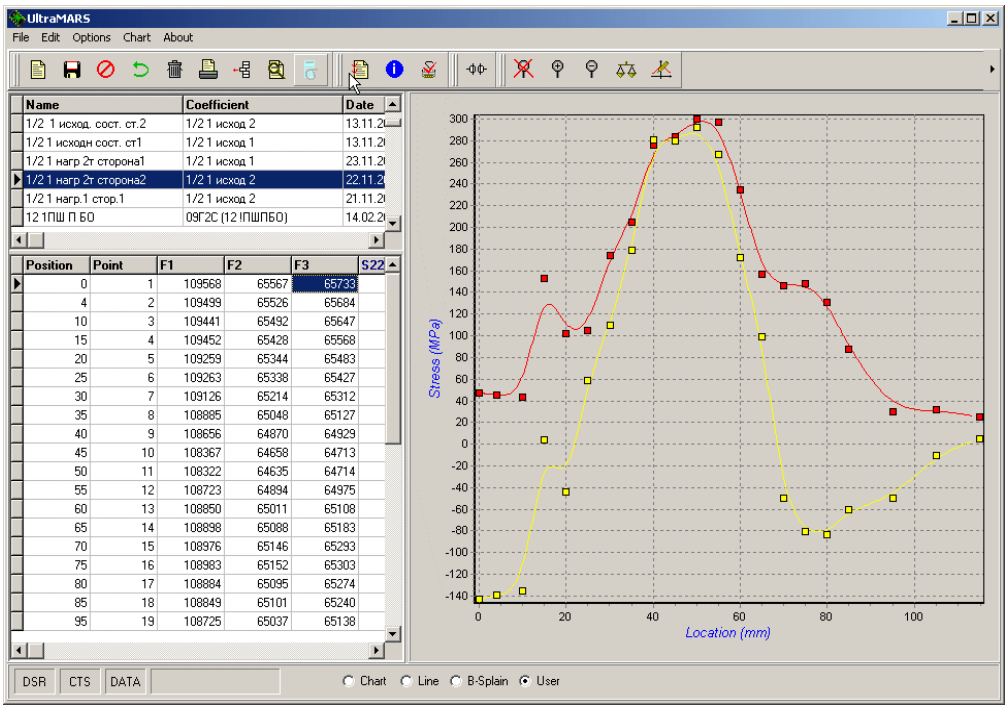

Figure 6. Distribution of residual stresses in a low carbon steel plate after local heating [10].

2.3. Examples of Residual Stress Measurements Using the Ultrasonic Method

One of the main advantages of the developed technique and equipment is the possibility to measure the residual and applied stresses in samples and real structure elements. Such measurements were performed for a wide range of materials, parts and structures. A few examples of the practical application of the developed technique and equipment for residual stress measurement based on using of the ultrasonic technique are presented below.

2.3.1. Specimen for Fatigue Testing

The residual stresses were measured in a 500x160x3 mm specimen made of an aluminum alloy (σ_y = 256 MPa, σ_u = 471 MPa) with a fatigue crack. The residual stresses were induced by local heating at a distance of 30 mm from the centre of the specimen. As can be seen from Figure 7, in the heating zone, both components of the residual stress are tensile. In the compression zones, the longitudinal component of residual stresses reaches minus 130 MPa.

2.3.2. Compound Pipes and Pipes with Surfacing

Another example of measuring the residual stresses by ultrasonic method is associated with compound pipes. Compound pipes are used in various applications and they are made by fitting under pressure one pipe with an outer diameter into a pipe with approximately the same inner diameter. For residual stress measurement, rings were cut-off from a number of compound pipes of different diameters. The width of the rings was 16 mm. Residual stresses were measured across the prepared cross-sections in three different locations at 120 degrees to each other with a subsequent averaging of the measurement results. Depending on the differences between the inner diameter D_1 of the outer pipe and the outer

diameter D2 of the inner pipe, the measurements were made in 3 to 5 points along the radius. The distribution of residual stresses as measured across the wall thickness of the compound pipe is presented in Figure 8.

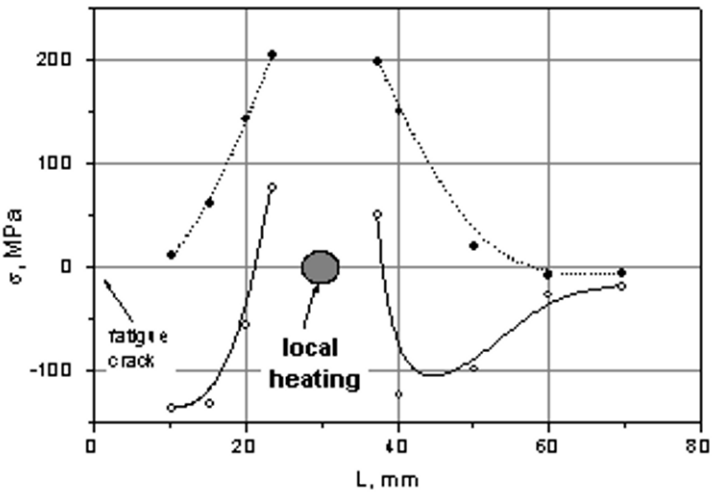

Figure 7. Distribution of residual stresses induced by local heating in a specimen made of an aluminum alloy with a fatigue crack: L – distance from the center of specimen [10]

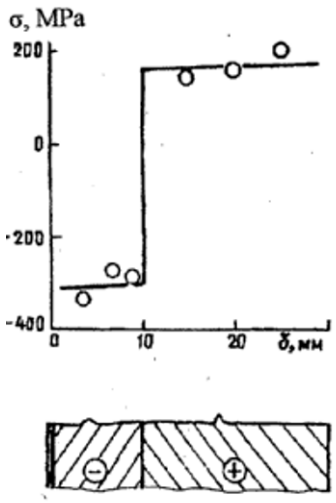

Figure 8. Residual stress distribution in a compound ring with the following dimensions [10]: inner ring: D_1 = 160mm and D_2 = 180mm; outer ring: D_1 = 180mm and D_2 = 220mm (D_1- inner diameter, D_2- outer diameter)

The results of the residual stress measurement by using ultrasonic method in rings cut-off from the pipes with inner surfacing are presented in Figure 9.

2.3.3. Measurement of Residual Stresses in Welded Samples

The residual stresses were measured in a specimen measuring 1000x500x36 mm, representing a butt-welded element of a wind tunnel. The distribution of biaxial residual stresses was investigated in X (along the weld) and Y directions after welding and in the process of cyclic loading of the specimen [7]. Figure 10 represents the distribution of longitudinal (along the weld) and transverse components of residual stresses along the weld toe. Both components of the residual stress reached their maximum levels in the central part of the specimen: longitudinal - 195 MPa, transverse - 110 MPa.

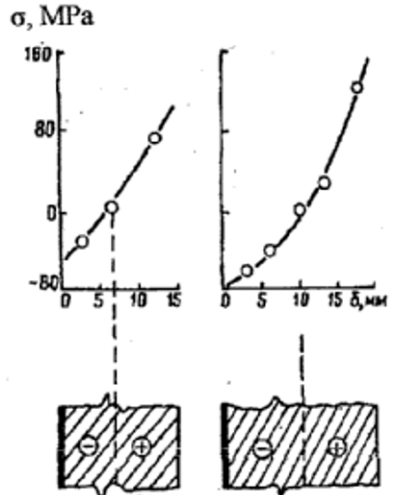

a) b)

Figure 9. Residual stress distribution in rings with inner surfacing [10]: a) ring with D_1 = 150mm and D_2 = 180mm; b) ring with D_1 = 180mm and D_2 = 220mm (D_1- inner diameter, D_2- outer diameter, width of the rings - 16 mm)

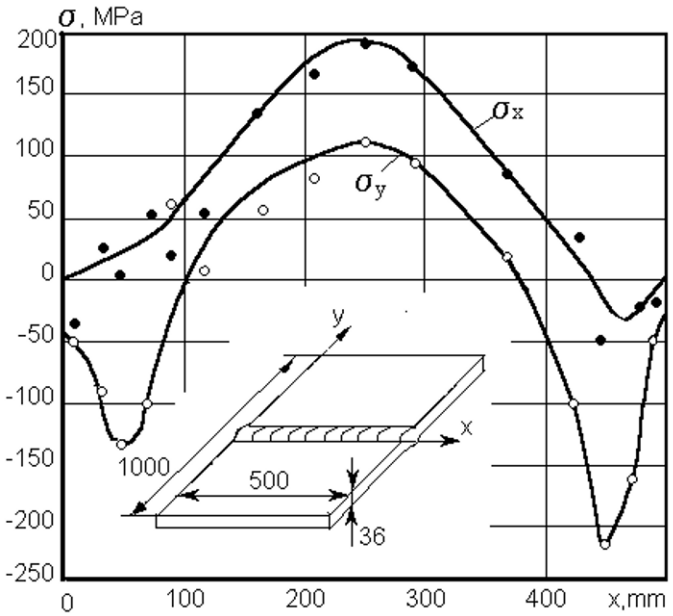

Figure 10. Distribution of longitudinal (along the weld) and transverse components of residual stresses along the butt weld toe [7]

The ultrasonic method was applied also for residual stress measurement in a specimen measuring 900x140x70 mm and made of low-alloyed steel, representing the butt weld of a structure [8]. The distribution of residual stress components in X_3 (along the weld) and X_2 (perpendicular to the weld) directions as well as through the thickness of the specimen near the weld (X_1direction) are presented on Figure 11.

2.3.4. Measurement of Residual Stresses in Welded Structures

The developed ultrasonic equipment could be used for RS measurement for both laboratory/factory and field conditions.

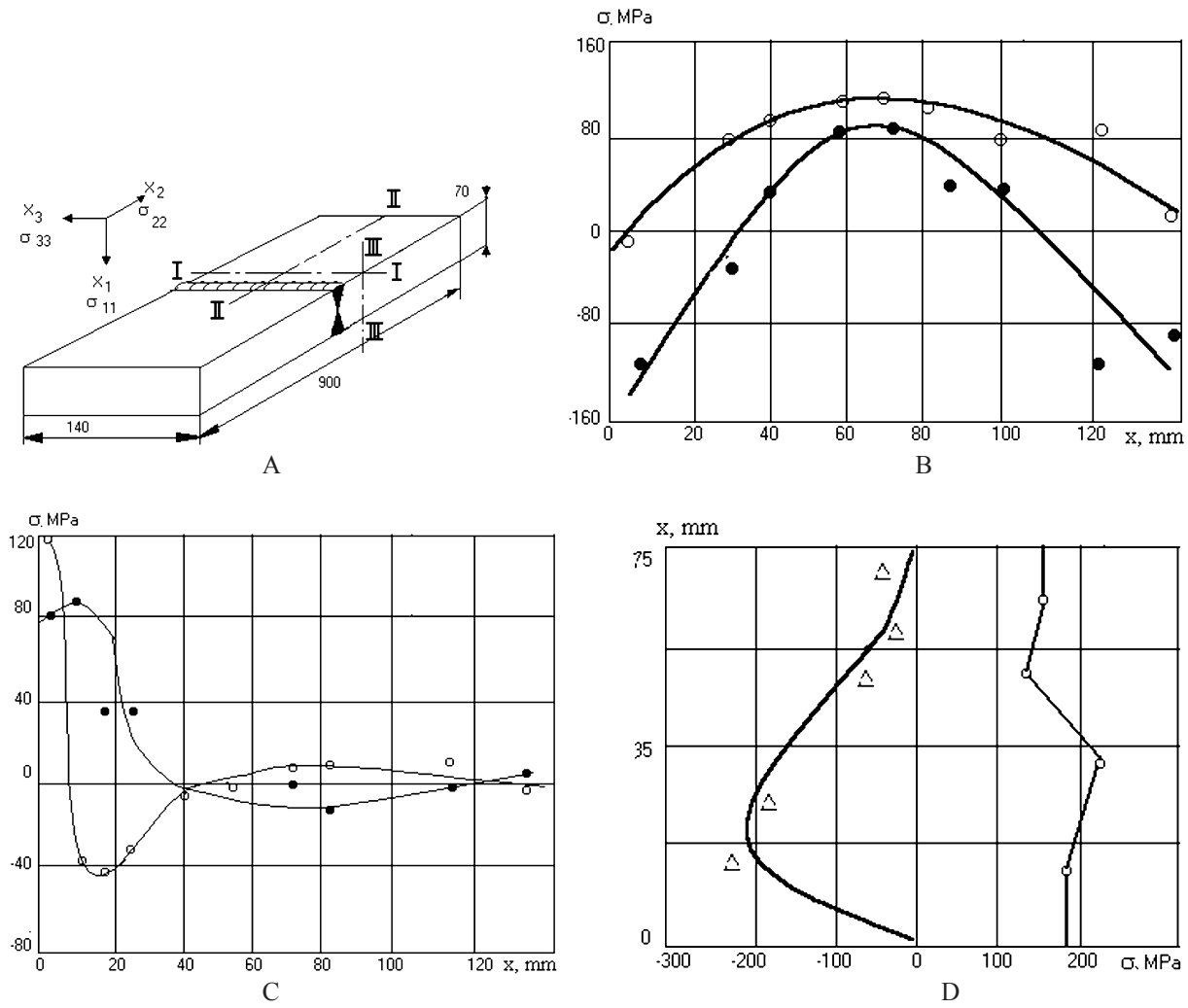

Figure 11. Welded specimen (A) and distribution of the residual stresses along the butt weld I-I (B), perpendicular to the weld II-II (C) and through the thickness near the weld III-III (D) [8]: ● – σ_{22} ; ○ - σ_{33} ; Δ - σ_{11}.

The residual stresses were measured by the ultrasonic method in large-scale welded panels in as-welded condition and during the fatigue loading of the panels [11]. The objectives of the study were to identify the residual stress distribution and relaxation in specimens with welded longitudinal attachment and welded panel that represent large scale models of ship structural detail, and compare the results of experimental and numerical analyses. During the fatigue testing the residual stresses were measured after 1, 2, 10 and 2010 cycles of loading. Figure 12 shows the process of residual stress measurement after certain number of cycles of loading. Figure 13 illustrates the distributions of the residual stress in large-scale welded panel near the weld that is critical from the fatigue point of view in as-welded condition and after 2010 cycles of loading.

The process and some of the results of ultrasonic measurement of residual stresses in welded elements of a bridge are shown in Figures 14 and 15. The residual stresses were measured by ultrasonic method in the main wall of the bridge span near the end of one of welded vertical attachments. In the vicinity of the weld the measured levels of harmful tensile residual stresses reached 240 MPa. Such high tensile residual stresses are the result of thermo-plastic deformations during the welding process and are one of the main factors leading to the origination and propagation of the fatigue cracks in welded elements.

Figure 12. Measurement of residual stresses using UltraMARS system in large-scale welded panel in as-welded condition and during the fatigue loading of the panel

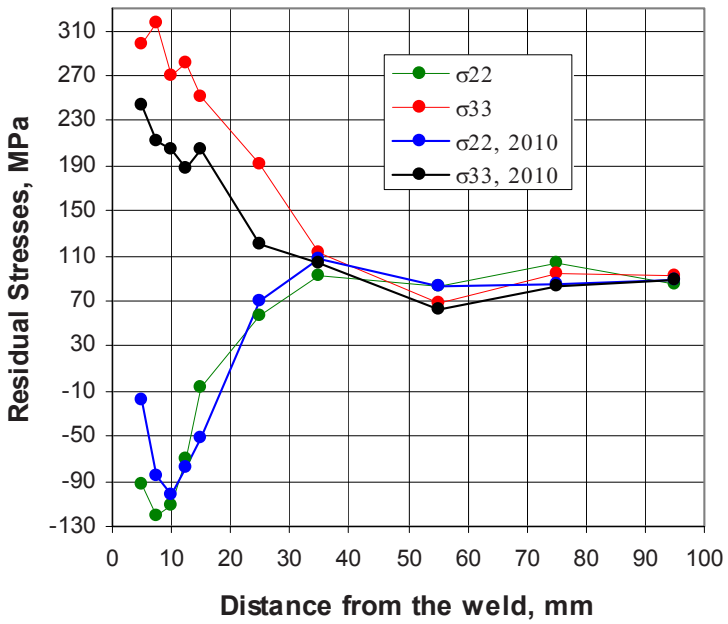

Figure 13. The distributions of residual stress in large-scale welded panel near the weld that is critical from the fatigue point of view in as-welded condition and after 2010 cycles of loading [11]

Based on the ultrasonic method the stresses were measured in the bridge both in conditions of no traffic on the bridge as well as in condition when a few heavy loaded trucks were put in certain locations to determine the total stress.

Figure 14. Process of measurement of residual stresses in a welded bridge

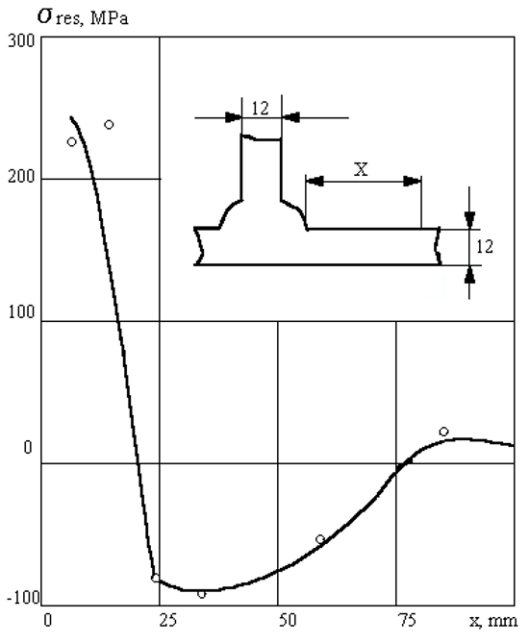

Figure 15. Distribution of longitudinal (oriented along the weld) residual stresses near the fillet weld in bridge span: x – distance from the weld toe

SUMMARY

1. Residual stresses play an important role in operating performance of materials, parts and structural elements. Their effect on the engineering properties of materials such as fatigue and fracture, corrosion resistance and dimensional stability can be considerable. The residual stresses, therefore, should be taken into account during design, fatigue assessment and manufacturing of parts and welded elements.

2. Certain progress has been achieved during the past few years in improvement of traditional techniques and development of new methods for residual stress measurement. The developed advanced ultrasonic method, based on it portable instrument and the supporting software can be used for non-destructive measurement of applied and residual stresses in laboratory samples and real parts and structural elements in many applications for a wide range of materials. The developed ultrasonic technique was successfully applied in construction industry, shipbuilding, railway and highway bridges, nuclear reactors, aerospace industry, oil and gas engineering and in other areas during manufacturing, in service inspection and repair of welded elements and structures.

REFERENCES

[1]. Handbook on Residual Stress. *Volume 1. Edited by Jian Lu. Society for Experimental Mechanics. 2005. 417 p.*

[2]. V. Trufyakov, P. Mikheev and Y. Kudryavtsev. Fatigue Strength of Welded Structures. Residual Stresses and Improvement Treatments. *Harwood Academic Publishers GmbH. London. 1995. 100 p.*

[3]. Y. Kudryavtsev and J. Kleiman. Fatigue Improvement of Welded Elements and Structures by Ultrasonic Impact Treatment (UIT/UP). *International Institute of Welding. IIW Document XIII-2276-09. 2009.*

[4]. Y. Kudryavtsev. Residual Stress. *Springer Handbook on Experimental Solid Mechanics. Springer – SEM. 2008. P. 371-387.*

[5]. Y. Kudryavtsev and J. Kleiman. Residual Stress Management: Measurement, Fatigue Analysis and Beneficial Redistribution. *X International Congress and Exposition on Experimental and Applied Mechanics. Costa Mesa, California USA, June 7-10, 2004. pp. 1-8.*

[6]. Handbook of Measurement of Residual Stresses. *Society for Experimental Mechanics. Edited by J. Lu. 1996. 238 p.*

[7]. Y. Kudryavtsev. Application of the ultrasonic method for residual stress measurement. *Development of fracture toughness requirement for weld joints in steel structures for arctic service. VTT-MET. B-89. Espoo. Finland. 1985. p.62-76.*

[8]. Y. Kudryavtsev, J. Kleiman and O. Gushcha. Residual Stress Measurement in Welded Elements by Ultrasonic Method. *IX International Congress on Experimental Mechanics. Orlando. Florida. USA, June 5-8, 2000. p. 954-957.*

[9]. Y. Kudryavtsev, J. Kleiman and O. Gushcha. Ultrasonic Measurement of Residual Stresses in Welded Railway Bridge. *Structural Materials Technology: An NDT Conference. Atlantic City. NJ. February 28-March 3, 2000. p. 213-218.*

[10]. Y. Kudryavtsev, J. Kleiman, O. Gushcha, V. Smilenko and V. Brodovy. Ultrasonic Technique and Device for Residual Stress Measurement. *X International Congress and Exposition on Experimental and Applied Mechanics. Costa Mesa, California USA, June 7-10, 2004. pp. 1-7.*

[11]. H. Polezhayeva, J. Kang, J. Lee, Y. Yang and Y. Kudryavtsev. A Study on Residual Stress Distribution and Relaxation in Welded Components. *Proceedings of the 20th International Offshore (Ocean) and Polar Engineering Conference ISOPE-2010, June 20−26, 2010, Beijing, China.*

Benchmark measurement of residual stresses in a 7449 aluminium alloy using deep-hole and incremental centre-hole drilling methods

Sayeed Hossain, Chris Truman, David Smith
Department of Mechanical Engineering, University of Bristol, Bristol BS8 1TR, UK

ABSTRACT
Residual stress measurements using non-destructive techniques including neutron diffraction and X-ray diffraction are dependent on assumptions made in the analysis. For example, the different stress free reference sample and the presence of precipitates in a material can influence the measured results. Previous residual stress measurement using neutron diffraction technique in a quenched aluminium block revealed that the result can be influenced by the choice of the stress free reference sample. A benchmark method is therefore essential to validate the different measurement techniques.

In this paper, the deep-hole drilling technique was used first as a benchmark technique to validate (1) the measured residual stresses in a water quenched 7449 aluminium alloy block using the neutron diffraction technique, and (2) residual stresses measured using the layer removal technique in a 7449 aluminium plate which was water quenched followed by stretching. Second, the incremental centre-hole drilling technique was used to validate the near surface residual stresses in an aluminium strip measured using the X-ray diffraction technique. The excellent correlations with the benchmark measurement methods validated the different results.

KEYWORDS: residual stress, 7449 aluminium alloy, distortion, quenching, forging, machining stress

1. INTRODUCTION

Measurements of residual stresses may be carried out using non-destructive techniques such as the X-ray diffraction (XRD) and the neutron diffraction (ND) or using semi-destructive techniques such as the incremental centre-hole drilling (ICHD) and the deep-hole drilling (DHD) techniques. The XRD and ICHD measurements are limited to only the subsurface whereas the ND and DHD methods can measure deep into components. The ND technique is not readily available and is not portable. Although the ND technique has a penetrative depth limit of about 60mm in most steels, the depth of penetration in aluminium alloys is far greater. However, the presence of strong texture in aluminium alloys can complicate data interpretation [1].

In contrast the DHD technique [2] is portable and can measure residual stresses deep into metal parts, e.g., 430mm deep into steels [3]. Like all other mechanical strain relief techniques, the DHD technique works by measuring distortions when part of the component is machined away. The underlying assumption is that such displacement changes result from elastic unloading. Furthermore, unlike in the ND technique where good result depends on an accurate design of a stress-free reference sample, the DHD technique does not require a stress-free reference sample. However, in components containing high levels of residual stress, elastic-plastic unloading may well occur during material removal, particularly when the residual stresses are highly triaxial. A modification is made to the existing conventional DHD procedure which accounts for the additional change in diametral distortions during the elastic-plastic unloading steps [4].

In this paper, these measurement methods are applied to a 7449 aluminium alloy. This alloy is used for aerospace applications owing to its high strength, stress-corrosion-cracking resistance and toughness. The quenching process is typically used to create high strength in aluminium alloys, but also introduces high residual stresses. These stresses cannot be relieved by thermal relaxation without diminishing the alloys' favourable mechanical properties. Alternatively, these stresses are relieved by applying a uniform plastic strain. Typically for rolled plate stress relief involves stretching in the rolling direction to strains of 1.5% to 3%. However, the residual stresses remaining after this stress relief process are sufficient to cause distortion during manufacture of aircraft components. The subsequent corrections of the distorted parts to ensure correct fit-up of parts can cost the aircraft parts manufacturing industry tens of millions of Euros per annum [5]. An EU FP6 project called COMPACT consisting of metal producers, aircraft manufacturers and universities was involved in investigating effective ways of reducing and managing the part distortion that arises during component

T. Proulx (ed.), *Engineering Applications of Residual Stress, Volume 8*, Conference Proceedings of the Society for Experimental Mechanics Series 999, DOI 10.1007/978-1-4614-0225-1_9, © The Society for Experimental Mechanics, Inc. 2011

manufacture [6]. An accurate characterisation of the residual stress field present in the stress relief alloy was a key step towards establishing a relationship between the stress field and the part distortion resulting from machining.

As part of the COMPACT project University of Bristol was involved in validating residual stresses by benchmarking measurement techniques such as the DHD and the ICHD methods. The samples used in the study are described in the next section followed by a brief description of the residual stress measurement methods. Results are then provided and discussed. Conclusions are drawn about the importance of accurate characterisation and validation of the residual stress present in aluminium alloys.

2. MATERIAL AND TEST SPECIMENS

Three specimens manufactured from 7449 aluminium alloy were used in the present study. The specification composition of 7449 is given in Table 1. The first sample consisted of a rectilinear forging of dimensions 432mm (L) × 156mm (LT) × 123mm (ST), where L=longitudinal, LT=long-transverse and ST=short-transverse, solution heat treated at 470±5 °C for 5 h followed by immersion quenching into agitated water at less than 20°C. This block, along with two others [7] were forged as a single unit from a 400mm × 145mm × 700mm rectilinear cast slab of 7449 aluminium alloy provided by Alcan, Issoire, France.

Si	Fe	Cu	Mn	Mg	Cr	Ni	Zn	Ti	Zr
0.12	0.15	1.4-2.1	0.20	1.8-2.7	-	-	7.5-8.7	-	0.25*

Table 1 Specification alloy composition of the aluminium alloy 7449 (Al balance, wt%). * Zr + Ti

The second specimen consisted of two notionally identical rolled plates of dimensions 76mm (ST) × 1000mm (L) × 1380mm (LT). The orientations were referenced to the original mother plate from which these plates were sectioned. The mother plate was water quenched to obtain high strength. This was followed by stretching in the rolling direction to 4.4% plastic strain to relieve the quench residual stresses.

The third specimen, also manufactured from 7449 aluminium alloy, consisted of two identical thin (2mm) metal strips of approximate dimensions 400mm × 44mm. These strips were used to study the influence of different machining parameters (cutting speed, feed per tooth, width of cut, depth of cut) on the subsequent part distortions due to the relaxation of residual stresses.

3. RESIDUAL STRESS ANALYSES

Table 2 summarises the different residual stress measurement methods used on the specimens. A total of five samples with six different residual stress measurement techniques were covered in the present study.

	Specimen 1	Specimen 2		Specimen 3	
Specimen description	Forged quenched block	Plate 1 (198856B-1)	Plate 2 (198856BB)	Strip 1	Strip 2
Residual stress measurement	Neutron diffraction, Incremental deep-hole drilling	Layer removal technique	Standard deep-hole drilling	X-ray diffraction	Incremental centre-hole drilling

Table 2 Summary of the specimens and the residual stress measurement methods.

3.1 NEUTRON DIFFRACTION

Residual stress measurement deep inside the forged block was carried out using the ENGIN-X instrument at ISIS, Rutherford Appleton Laboratory in Oxford, UK following standard guidelines [8, 9]. Fig. 1 shows the measurement locations. As ENGIN-X utilises a spallation neutron source, it is a time-of-flight facility and multiple diffraction peaks were acquired simultaneously. This enabled the lattice spacing a to be obtained directly using a Pawley-Rietveld refinement [10] of a time-of-flight profile encompassing the {111}, {200}, {220}, {311} and {222} matrix peaks. A gauge volume of 4mm × 4mm × 4mm allowed measurements to be completed within the allocated time. The specimen was positioned to permit determination of stresses in the three primary working orthogonal directions of the forging which were assumed to be the principal stress directions. Stress-free measurements (a_0) were performed on a small cube sample cut from the corner of a 10mm thick slice which was cut from an end of the block prior to ND measurement. The measured lattice spacing was converted to residual strain, $\varepsilon=(a-a_0)/a_0$. Residual stresses were determined [11] by using Hooke's law.

$$\sigma_{xx} = \frac{E}{1+\nu}\left[\varepsilon_{xx} + \left(\frac{\nu}{1-2\nu}\right)\left(\varepsilon_{xx} + \varepsilon_{yy} + \varepsilon_{zz}\right)\right] \quad \text{... (1)}$$

As shown in Fig. 1, the x direction corresponds to the LT direction, y to the L, and z to the ST. The bulk elastic modulus *E* for 7449 aluminium alloy was assumed to be 70 GPa with a Poisson's ratio ν = 0.3.

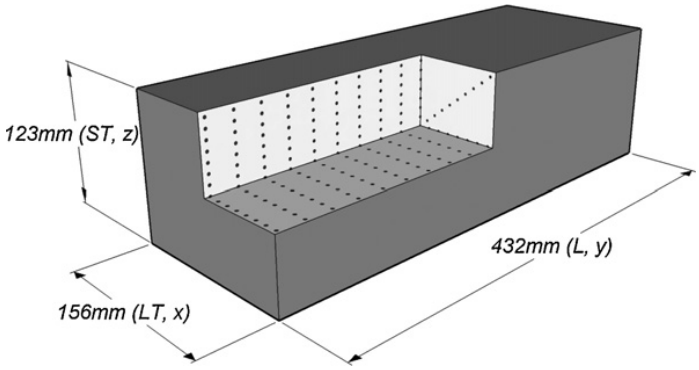

Figure 1 Neutron diffraction measurement locations denoted by dots in the octant.

3.2 STANDARD DEEP-HOLE DRILLING TECHNIQUE

The DHD method determines the through-thickness residual stress distribution in a component by measuring the change in diameter of a reference hole that occurs when a core of material containing the hole is removed by trepanning [2]. The steps (Fig. 2) include: (1) A reference hole gun-drilled through the component, (2) Accurate measurements of the initial reference hole diameter taken at a number *N*, of angles θ around the reference hole axis and at several increments in depth *z*, giving *d*(θ, *z*), (3) A core of material containing the reference hole trepanned free of the rest of the component using a plunge electric discharge machine, (4) After core removal, the reference hole diameter re-measured to give *d'*(θ, *z*).

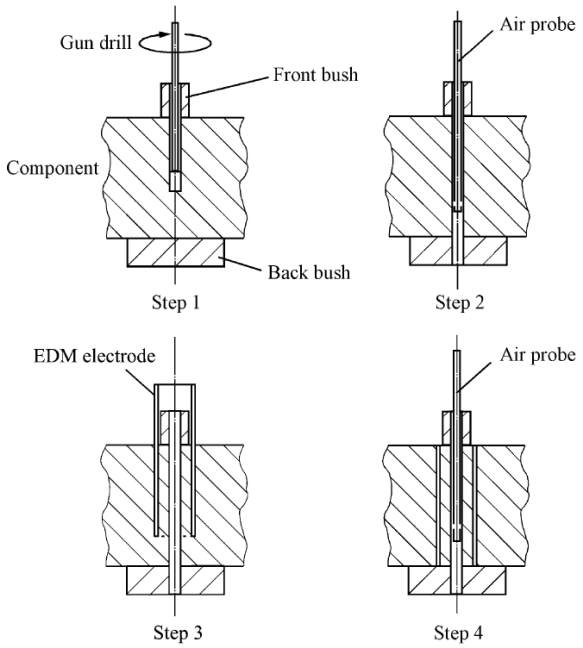

Figure 2 Schematic illustration of DHD method.

The normalised distortions $u_{rr} = (d'-d)/d$ are related to the residual stress components $\sigma_{xx}(z)$, $\sigma_{yy}(z)$ and $\sigma_{xy}(z)$ in the plane normal to the reference hole axis. Elasticity relates the deformations occurring at a hole in a finite-thickness planar-infinite plate subjected to remote planar stress components assumed to be constant through the plate thickness. The unknown stress components are calculated from the measured normalised reference hole distortions using a least squares analysis:

$$\{\sigma(z_i)\} = -E\left(M^T M\right)^{-1} M^T u_{rr} \quad \text{... (2)}$$

where,

$$M = \begin{bmatrix} 1+2\cos 2\theta & 1-2\cos 2\theta & -4\sin 2\theta & -\nu \\ \vdots & \vdots & \vdots & \vdots \\ 1+2\cos 2\theta_N & 1-2\cos 2\theta_N & -4\sin 2\theta_N & -\nu \\ -\nu & -\nu & 0 & 1 \end{bmatrix}$$

The standard DHD method was used to measure the through-thickness residual stresses in Plate 2 (COMPACT reference 198856BB). The measurement was carried out across the ST direction (Fig. 3). The in-plane longitudinal (σ_L), long-transverse (σ_{LT}) and shear ($\sigma_{L\text{-}LT}$) residual stress components were obtained. This measurement was used to benchmark the layer removal technique described below that was applied to measure residual stresses in Plate 1 (198856B-1).

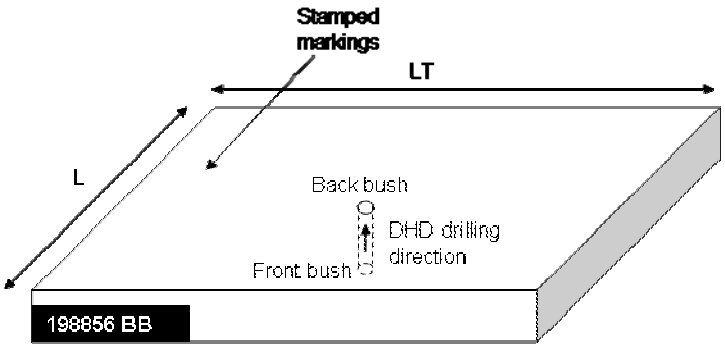

Figure 3 Schematic of Plate 2 used in DHD measurement with the measurement direction indicated.

3.3 INCREMENTAL DEEP-HOLE DRILLING TECHNIQUE

The recently developed iDHD technique [4] provides an approximate solution to measurements of near yield residual stresses by considering the effects of plasticity during trepanning. The incremental technique relies on obtaining measurements of hole distortions progressively for increments of trepanning depth giving diameters d'_j where j is the number of interrupted trepanning steps. The changes in diameter are normalised to give normalised distortions $u_{rrj} = (d' - d'_j)/d'_j$ at the j^{th} trepan increment. Only a limited set of measurements along the reference hole axis, corresponding to the trepan increments, can be obtained. At each trepan increment the measured hole distortions are introduced into the standard DHD analysis procedure, Eq. 2, to provide stress components at each trepan increment, j, $\{\sigma_j(z_i)\}$ and are then compared and combined to create the finalised, discrete measurement results.

The iDHD technique was used to measure the highly triaxial residual stresses in the forged quenched block along the ST direction. This measurement was carried out following the neutron diffraction measurement, and was used to benchmark the ND measurement.

3.4 LAYER REMOVAL TECHNIQUE

The layer removal (LR) technique determines the through-thickness residual stress distribution in a component by measuring the change in strain that occurs when layers of material are removed from the component, Fig. 4. Full details can be found in [12], and only an outline of the procedure is given here [13].

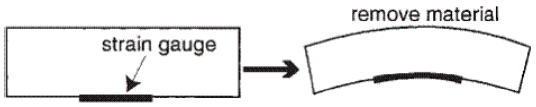

Figure 4 Illustration of the layer removal technique. A strain gauge was used to measure the change in curvature due to successive removal of material layers.

The residual stresses in Plate 1 (198856B-1) were measured using the LR technique. Fig. 5 shows the schematic of the plate with direction of the measurement. Assuming that residual stress were only in the longitudinal (L) and long-

transverse (LT) directions as functions of position in thickness, two rectilinear blocks in L and LT directions were removed. Removal of the two blocks modified the stress field in the plate. Typical dimensions of the blocks included the original plate thickness (76mm), width of 25mm and length which was 5 times the thickness (380mm). In each block the residual stresses were assumed to be unidirectional.

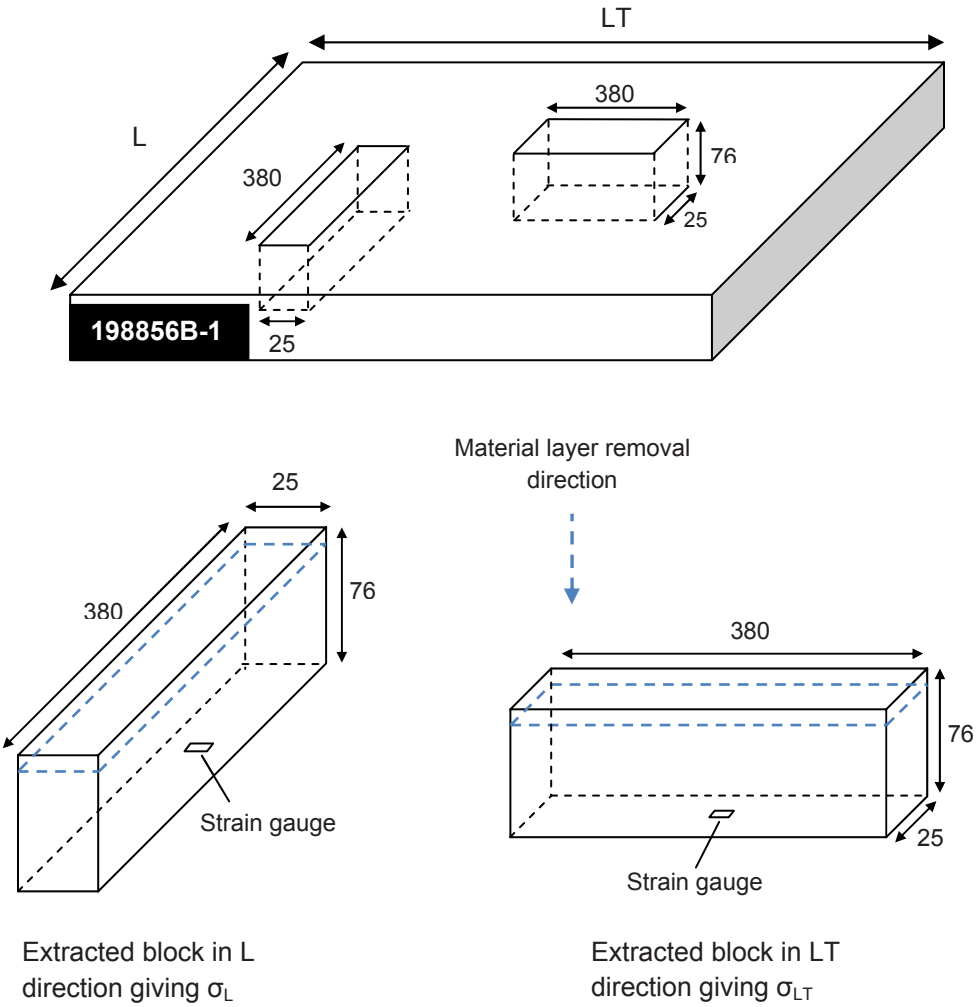

Figure 5 Schematic of Plate 1 sample with the measurement direction indicated.

When layers are removed from one side of each of the extracted flat blocks the stresses become unbalanced and the block bends as in Fig. 4. The curvature depends on the original stress distribution present in the layer that has been removed and on the elastic properties of the remainder of the block. By carrying out a series of curvature measurements after successive layer removals the distribution of stress in the original block can be determined. Curvature can be measured using contact methods (e.g. profilometry, strain gauges) or without direct contact (e.g. video, laser scanning, grids, double crystal diffraction topology), allowing curvatures down to about 0.1 mm^{-1} to be routinely characterised. Finally the stress field in each block is correlated back to the stress field that was in the original plate from which the blocks were extracted.

3.5 X-RAY DIFFRACTION TECHNIQUE

X-ray diffraction is a non-destructive method for measuring near surface residual stresses to depths of up to 0.025mm through measurement of a material's inter-atomic spacing. X-rays have wavelengths on the order of a few angstroms (Å), the same as typical inter-atomic distances in crystalline solids. During measurement the component is irradiated with x-rays that penetrate the surface, the crystal planes within the component diffract some of these x-rays according to Bragg's law. A detector is moved around the component to detect the angular positions where diffracted x-rays are located and records their intensity. The positions of the peaks enable the user to evaluate the stresses within the component.

The near surface residual stresses present in Specimen 3 Strip 1 were measured using the X-ray diffraction technique. The stresses were calculated using the $\sin^2\psi$ method. Electro-polishing was used to measure the residual stresses up to a depth of 0.20mm.

3.6 INCREMENTAL CENTRE-HOLE DRILLING TECHNIQUE

The ICHD method [14] was used to measure the near surface residual stress in Specimen 3 Strip 2. Strip 2 was notionally identical to Strip 1 so that the ICHD measured residual stresses could be used to benchmark the XRD measured residual stresses in Strip 1. A strain gauge rosette with an external diameter of 5.13mm was used in conjunction with a hole of diameter 1.8 mm. Measurements were made at non-uniform drill increments starting at fine increment of 0.016 mm, with the released strain on each of the three gauges in the rosette being recorded at each increment. From the relaxed strains the residual stresses were calculated using the integral method and cumulative influence functions derived by Schajer [15]. Following a procedure proposed by Zuccarello [16], the interpolation of Schajer's cumulative functions was made.

4. RESULTS AND DISCUSSION

The measurement results are shown in Figs. 6 to 8. Fig. 6 compares the iDHD measured residual stresses with the ND measured in the forged quenched aluminium block along ST direction. Similar trends are shown with compressive residual stresses on the surface and tensile stresses in the interior. As expected, the longitudinal stress component (σ_{yy}) was higher than the long-transverse stress (σ_{xx}) for both measurement techniques. The iDHD measured stress distributions to some extent were symmetric about the x-y face (Fig. 1). This justified the ND measurements limited to an octant. It was assumed that the stresses were symmetric about x-y, y-z and x-z planes. However, the iDHD measurements were significantly more tensile in the interior than the σ_{xx} and σ_{yy} neutron diffraction data (Fig. 6a). This difference is attributed to the choice of stress-free sample used [7]. Re-analysing the ND data, utilising the iDHD core as a stress-free sample, a much improved correlation was obtained as shown in Fig. 6(b).

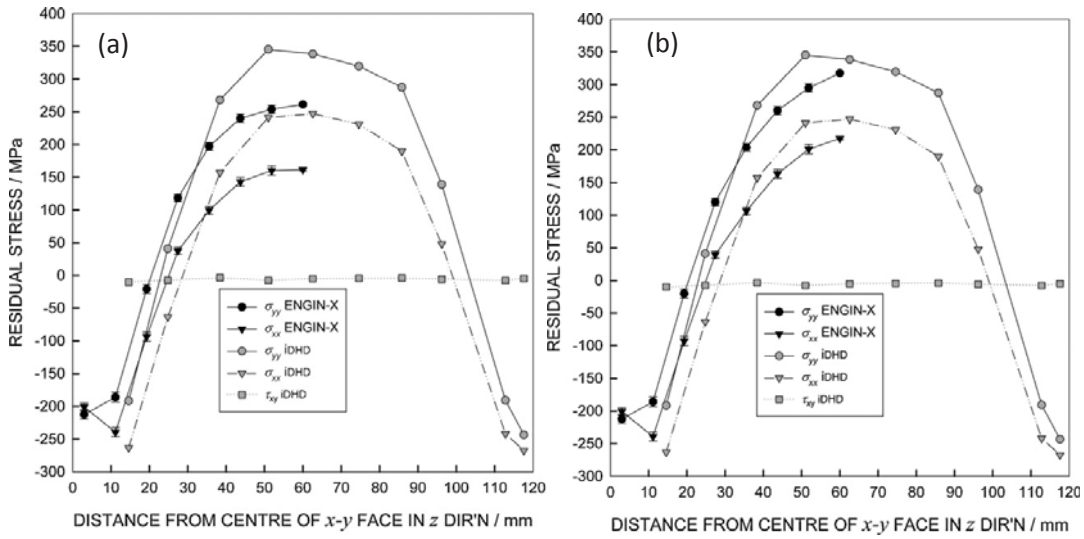

Figure 6 Comparison of iDHD and ND measured residual stresses along ST (z) direction of the forged quenched block (a) corner cube stress-free sample, (b) DHD core stress-free sample.

A comparison is made between the results obtained from the DHD and LR measurement methods in Fig. 7. For clarity, the longitudinal (L) and long transverse (LT) components of the residual stress distribution are shown separately in Figs. 7 (a) and (b) respectively. An excellent correlation exists between the two measurement methods. This close correlation first, validated the LR technique data using the DHD method and second, confirmed the existence of a uniform residual stress distribution across the thickness in the original mother plate from which these smaller plate samples were machined out.

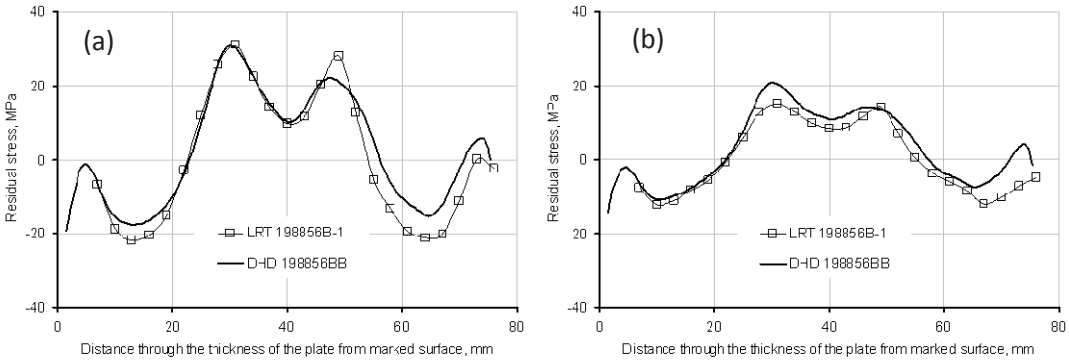

Figure 7 Comparison of the (a) longitudinal and (b) transverse residual stress distribution in plate samples 198856B-1 and 198856BB, using the layer removal and deep-hole drilling techniques.

Figure 8 compares the near-surface XRD measured residual stresses with those obtained from the application of the ICHD method. Both the trend and the magnitudes of stresses are in excellent agreement. The ICHD stress value at zero depth was erroneous. The stress profile is complemented by the XRD data closer to the surface. The compressive stresses due to machining of the surfaces were measured by both the XRD and the ICHD techniques.

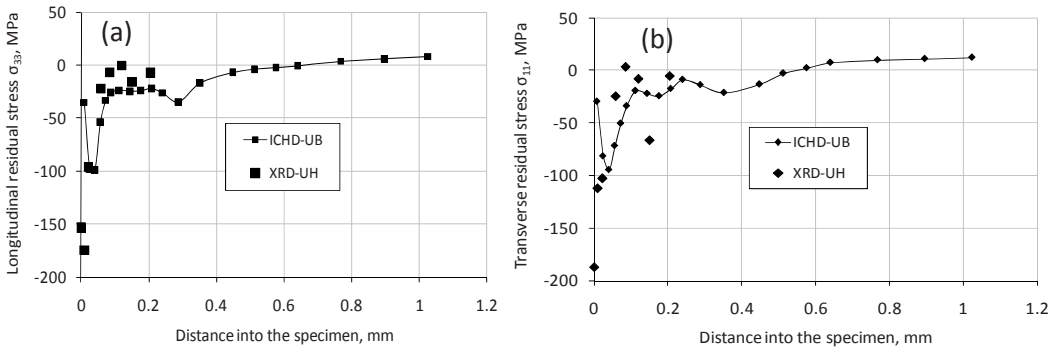

Figure 8 Comparison of near-surface (a) longitudinal and (b) transverse residual stresses in machined strips using the XRD and ICHD techniques.

5. CONCLUSIONS

This study showed the usefulness of the DHD and the ICHD techniques in validating the ND, the XRD and the LR techniques in samples ranging from a metal strip to forged block, from machining induced residual stresses to water quenched residual stresses. Deep-hole drilling is a relatively robust technique whereas the accuracy of the ND measured result is dependent on the correct choice of stress-free sample. The study showed that the DHD core can be used as a stress-free sample and accounted for the change in lattice parameter across the measurement direction. Fig. 6 illustrated how selecting the correct stress-free sample can improve the accuracy of the measurement.

The close correlation between the DHD and the LR techniques not only validated the LR measured stresses but also the assumptions made in the LR technique. Similarly the ICHD measured stresses validated the XRD data. Fig. 8 also illustrates the complementary nature of the two techniques.

ACKNOWLEDGEMENT

This work was carried out with the financial support of EU FP6 COMPACT project.

REFERENCES

1. Fitzpatrick ME (ed) (2003) Analysis of residual stress by diffraction using neutron and synchrotron radiation. Taylor and Francis, London.
2. George D., Kingston E., Smith D.J., Measurement of through-thickness stresses using small holes, J. Strain Analysis, 37(2), pp. 125-139, 2002.
3. Kingston, E.J., Stefanescu, D., Mahmoudi, A.H., Truman, C.E., Smith, D.J., Novel applications of the deep-hole drilling technique for measuring through-thickness residual stress distributions, Journal of ASTM International, April 2006, Vol. 3, No.3.

4. A.H. Mahmoudi, S. Hossain, C.E. Truman, D.J. Smith, M.J. Pavier, A new procedure to measure near yield residual stresses using the deep hole drilling technique, Experimental Mechanics, 49 (4): 595-604, 2009.
5. Lequeu P, Lassince P, Warner T, Raynaud GM. Aircraft Engg Aerospace Tech. 73, 147 (2001).
6. Wei-Ming Sim, Challenges of residual stress and part distortion in the civil airframe industry, 2nd International Conference on Distortion Engineering 2008.
7. J.S. Robinson, S. Hossain, C.E. Truman, A.M. Paradowska, D.J. Hughes, R.C. Wimpory, M.E. Fox, Residual stress in 7449 aluminium alloy forgings, Materials Science and Engineering A 527 (2010) 2603-2612.
8. ISO/TTA3, Technology Trends Assessment, International Standardisation Organisation, 2001.
9. D.C.I.T. 21432, Non-destructive Testing. Standard Test Method for Determining of Residual Stresses by Neutron Diffraction, British Standards Institute, 2005.
10. Pawley GS. Unit-cell refinement frompowder diffraction scan. J Appl Crystallogr 1981;14:357–61
11. M.T. Hutchings, P.J. Withers, T.M. Holden, T. Lorentzen, Introduction to the Characterisation of Residual Stress by Neutron Diffraction, CRC Press, Boca Raton, FL, USA, 2005, p. 131.
12. R.G. Treuting and W.T. Read, Jr., A Mechanical Determination of Biaxial Residual Stress in Sheet Materials, Journal of Applied Physics, Volume 22, Number 2, pp 130-134, 1951.
13. P. J. Withers and H. K. D. H. Bhadeshia, Residual stress: Part 1 – Measurement techniques, Materials Science and Technology, Vol. 17, pp 355-365, 2001.
14. Grant PV, Lord PD, Whitehead PS. The measurement of residual stresses by the incremental hole drilling technique. Measurement Good Practice Guide 53, National Physical Laboratory, UK, 2002.
15. Schajer GS. Measurement of non-uniform residual stresses using the hole drilling method. Journal of Engineering Materials and Technology 1998; 110(4): Part I, 338–43; Part II, 344–49.
16. Zuccarello B. Optimal calculation steps for the evaluation of residual stress by the incremental hole drilling method. Experimental Mechanics 1999;39(2):117–24.

A New Procedure for Measuring Residual Stresses in Electron Beam Welds Using the Deep Hole Drilling Technique

Gang Zheng, DJ Smith,
Department of Mechanical Engineering, University of Bristol, UK
P Hurrell, Rolls Royce, plc, Derby, UK
D. Goudar, E. Kingston, Veqter Ltd, UK

ABSTRACT

Residual stress measurements in a thick cylindrical steel electron beam (EB) welded sample are described. This is a particularly challenging problem because the residual stresses are distributed in a very narrow region, in and adjacent to the EB weld, when compared to more conventional welding methods. Several variations of the deep hole drilling (DHD) method were applied, including the original conventional method, an incremental approach and a newly developed over-coring method. It is demonstrated that the over-coring method can be used just as effectively as the more difficult incremental method.

KEY WORDS

Residual stress, Deep hole drilling, Plasticity, Over-coring

NOTATION

DHD	deep hole drilling
OD	outer diameter
Øo	diameter of the reference hole after gun-drill
Ø	diameter of the reference hole after 5mm core extraction
Ø'	diameter of the reference hole after 40mm core extraction
$Ø_1$~$Ø_{10}$	diameter of the reference hole after each trepan step
σ_{xx}	direct stress component in x direction
σ_{yy}	direct stress component in y direction
σ_{xy}	shear stress component
$\overline{u_{rr}(\theta)}$	normalised distortion at angle θ
E	Young's Modulus
EDM	electric discharge machining

1 INTRODUCTION

Electron beam welding (EBW), created in 1950's, is a fusion welding method where a beam of high energy electrons are applied to heat the metal weld joint. No additional weld filler metal is introduced and the resulting fusion area is narrow relative to other welding processes. EB welding is preferred as a manufacturing process for high-value welds in the nuclear energy and aerospace industries [1]

T. Proulx (ed.), *Engineering Applications of Residual Stress, Volume 8*, Conference Proceedings of the Society for Experimental Mechanics Series 999, DOI 10.1007/978-1-4614-0225-1_10,

because there is very little distortion of the component. In order to create a narrow weld joint the process is often carried out in a vacuum to prevent dispersion of the electron beam. The requirement of the vacuum presents a practical issue for welding large components due to the operational cost and sizes of vacuum chamber available. Recent developments by the Welding Institute (TWI), in creating a moveable seal and vacuum system, have opened up the use of EBW on large, practical engineering components.

The determination of the residual stresses introduced by this novel welding technique remains important in determining the structural integrity of the component. However, the narrow weld region is highly constrained and consequently, it has been shown [2] that there are highly localised residual stresses in excess of the yield strength. Also the magnitude and distribution of residual stresses in thick cylindrical components only allows a few measurement methods to be applied and in this paper attention is directed to the development and application of the deep hole drilling method. First, the basic principles of the original method are described. This is followed an explanation of its application to an EB welded stainless steel cylinder. Finally, the results are reported and discussed.

2 MEASUREMENT TECHNIQUE

The deep hole drilling (DHD) is a semi-destructive, mechanical strain relaxation method that relies on the measurement of the distortion of a reference hole drilled through the component. The distortions between the stressed and unstressed states of the specimen are used to calculate the stress distribution, and initially the strain relaxation is assumed to be elastic. Leggatt et al [3] initially developed an analysis method for converting the measured distortions to residual stresses. Later, Granada-Garcia et al [4] and Kingston et al [5] advanced the method to include more precise measurement procedures and refined analyses.

Recent work showed that when residual stresses are close to the yield stress the assumption of entirely elastic relaxation of strains breaks down and plastic deformation occurs. To account for this an incremental deep hole drilling [6] method was developed. However, the technique currently provides only limited data and is time consuming. Alternatively, it has been shown [7] that by initially relaxing the residual stresses away from the yield surface it is possible to continue to use the conventional DHD method. In this paper, the initial step of reducing the residual stresses is undertaken by using a new over-coring method.

Irrespective of whether conventional, incremental or over-coring variations of the DHD technique are applied the conversion of the measured distortion to residual stresses remains the same.

The conventional DHD procedure involves 4 steps as illustrated in **Figure 1**. In the experiments, described later in the paper, the procedure was applied to a fully circumferential EB weld in a cylinder. For brevity the steps in the method were as follows.

1) Prior to gun-drilling two bushes were attached to the outer and inner surfaces of cylinder. A reference hole was gun-drilled through the component and reference bushes. A gun-drill is a

special type of drill with a self-aligning tip. It is suitable for drilling long holes where a high degree of straightness is required. In these experiments a 1.5 mm diameter drill was used.

2) The internal diameter, Øo, of the reference hole was measured accurately at locations inside the reference hole through the entire thickness of the component and reference bushes. Diametral measurements were taken at 0.2mm increments along the reference hole and at angles of 22.5° increments using an air probe.
3) A cylinder, with a diameter of 5mm and with the reference hole as its axis, was trepanned free of the remainder of the component using electric discharge machining (EDM).
4) Finally, the internal diameter, Ø, of the reference hole was re-measured at the same locations as in step 2.

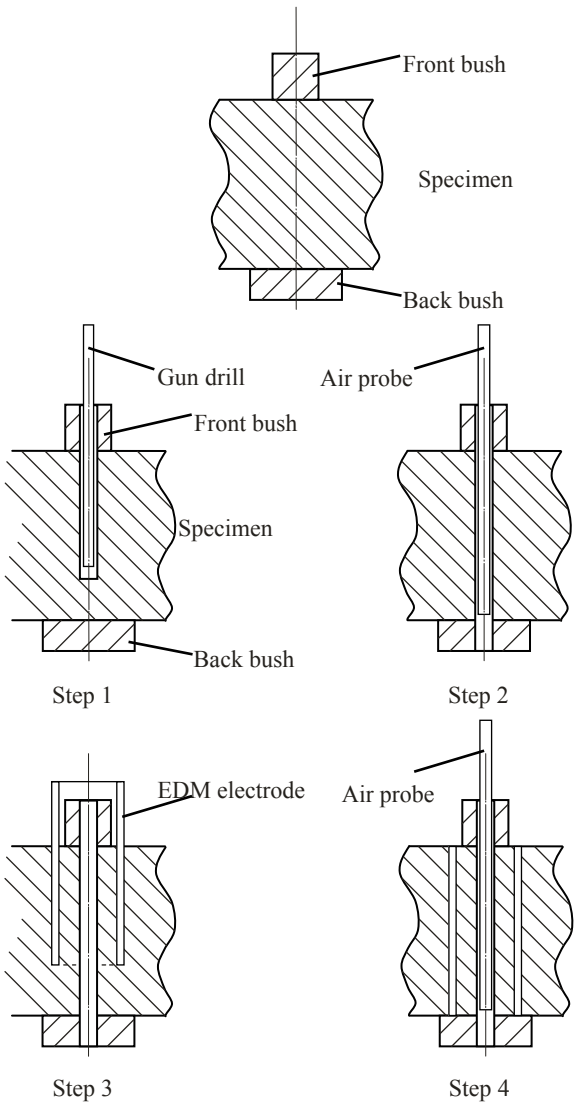

Figure 1 An illustration of the procedures in standard DHD technique: step 1: drilling a reference hole; step 2: measurement of reference hole diameter; step 3: core trepanning and step 4: re-measurement of hole diameter

The diameter, $Ø_0$, of the reference hole measured in Stage 2 is the diameter when stresses are present. During Stage 3 the stresses are relieved, hence the diameter, Ø, of the reference hole measured in Stage 4 is the diameter when stresses are not present. The differences between the measured diameters in Stages 2 and 4 enable the original residual stresses to be calculated.

In general, only the in-plane distortions (the plane normal to the reference hole axis) of the reference hole are measured throughout the DHD technique and only in-plane residual stresses are calculated. The normalised distortions of the reference hole are related to the residual stress components in the plane normal to the reference hole axis, σ_{xx}, σ_{yy} and σ_{xy}. To calculate residual stresses that vary with depth, it is assumed that the trepanned core is composed of a stack of annular slices, which act independently of one another and behave in a manner predicted by the constant remote stress analysis [4]. The measured distortions are related to the stresses using

$$\overline{u_{rr}} = -\frac{1}{E}\left[M_{2D}\right] \bullet \sigma \,, \qquad (1)$$

where

$$\overline{u_{rr}} = \begin{bmatrix} \overline{u_{rr}(\theta_1)} \\ \overline{u_{rr}(\theta_2)} \\ \vdots \\ \overline{u_{rr}(\theta_N)} \end{bmatrix}, \quad \sigma = \begin{bmatrix} \sigma_{xx} \\ \sigma_{yy} \\ \sigma_{xy} \end{bmatrix} \text{ and}$$

$$\left[M_{2D}\right] = \begin{bmatrix} f(\theta_1) & g(\theta_1) & h(\theta_1) \\ f(\theta_2) & g(\theta_2) & h(\theta_2) \\ \vdots & \vdots & \vdots \\ f(\theta_N) & g(\theta_N) & h(\theta_N) \end{bmatrix}$$

where $\overline{u_{rr}(\theta)}$ is the normalised distortion at angle θ, E is Young's Modulus, $f(\theta)$, $g(\theta)$ and $h(\theta)$ are given by Bonner [8] and Garcia-Granada et al [4]. By determining the inverse of equation 1 the residual stresses σ_{xx}, σ_{yy} and σ_{xy} can be calculated.

If the component contains high magnitude, tri-axial residual stress, it is has been shown [6] that plastic relaxation occurs during trepanning. Like all mechanical strain relief techniques, the DHD technique is based on the assumption of elastic relaxation. Hence the distortion of the reference hole, on completion of trepanning through the thickness, can not represent the original residual stress field when plastic deformation occurs. Nevertheless, as shown by Mahmoudi et al [6], if the core is extracted in incremental steps and the diameter of the reference hole is measured between each increment then the residual stresses can be determined using the measured distortions and inverting equation 1. Since the

incremental technique divides the trepan step into many stages, this technique can provide only limited depth resolution and is time consuming.

To avoid plasticity during trepanning, recent work by Hossain et al [7] demonstrated that removal of a section of material containing the region of interest allowed the initial high stresses to relax elastically away from the yield surface. In this paper, rather than only remove one cylinder (i.e. core) of material containing the reference hole along its axis, trepanning is carried out in two steps. First, a 40mm diameter core concentric to the reference hole is extracted followed by re-measurement of the reference hole. The difference between the diameters before (Øo) and after (Ø') extraction permits us to determine the partially relaxed residual stresses. Finally, a 5mm core is removed from the 40mm core to completely relax the stresses in the 40mm core followed by re-measurement of the reference hole (Ø). The difference between the diameters before core extraction (Øo) and after 5mm core extraction (Ø) allows us to calculate the initial residual stresses.

3 SPECIMEN AND MEASUREMENTS

The EB welded pipe investigated in this work was supplied through Rolls-Royce (RR), UK and manufactured by TWI Ltd. The specimen comprised of two cylinders, with an outer diameter of 356mm, inner diameter of 286mm and 235mm high. The cylinders were butt welded together through the thickness by using a reduced pressure electron beam welding method. A schematic of the cross-section of the sample is shown in **Figure 2**, together with photographs of the outside of the pipe at the locations of the measurements. Both cylinders were manufactured from type 304 stainless steel and, due to the nature of EB weld, no additional material was deposited. The axial length of the weld cap was approximately 5mm.

The sample was measured in the as-welded condition. An angular position of 0º was marked on the sample and coincided with the EB weld start and stop positions. Two measurements were conducted through the weld centre line from the outer surface and made with respect to the 0° location. With reference to **Figure 2**, an incremental DHD measurement was performed at 180° while the new over-coring method was applied at 90°.

The incremental DHD technique was carried out with the extraction of 5mm diameter core containing a 1.5mm diameter reference hole. In total 10 trepanning increments were conducted and the diameter of the reference hole was re-measured after each increment, ($\phi_1, \phi_2 \ldots\ldots \phi_{10}$). Then the diameters were compared against each other to calculate the original residual stresses by inverting equation 1.

In the over-coring method a 40mm diameter core, concentric to the reference hole, was first extracted. This was followed by re-measurement of the reference hole diameter. Then a 5mm diameter core containing the reference hole was extracted and the hole was re-measured again. The residual stresses at each stage were then calculated by inverting equation 1.

4 RESULTS AND DISCUSSION

The residual stresses obtained at 180° are shown in **Figure 3**. Two sets of results are shown, one from the application of conventional DHD method and a second from the incremental technique. In both cases only the hoop and axial stresses are shown. The axial-hoop shear stresses were relatively low (less than 50MPa) compared to the principal stresses and have been omitted for clarity. Due to the depth resolution, the incremental DHD technique did not measure the first few millimetres through the weld from either side of the weld surface.

The conventional method initially measured tensile near surface residual stresses, but at greater depths the measured residual stresses remained relatively low. In contrast, the incremental technique revealed increasingly more tensile stresses in the hoop direction with increasing depth. These results are similar to those shown by Mahmoudi et al [6] for measurement of residual stresses in a quenched cylinder. Their results are reproduced in **Figure 4** and illustrated that the significant plastic relaxation of the residual stresses took place during trepanning. In contrast, the incremental method was shown to provide results in the quenched cylinder that agreed well with neutron diffraction results.

There are no comparable finite element results available for the EB welded stainless steel cylinder but the results obtained from the incremental DHD measurements, shown in **Figure 3**, also revealed the presence of high tensile residual stresses. When the results obtained via the over-coring method are compared with incremental results (as shown in **Figure 5**) it is evident that similar trends were produced. The hoop and axial stresses followed the same trend, with the hoop stresses always larger than the axial stresses in the tensile stress region while the axial stresses were larger than the hoop stresses in the compressive region.

Although not shown here there was also an intermediate step in the over-coring method that was able to provide additional data. The results from these are being examined in further work but clearly show that relaxation of residual stresses in multiple steps provides supplementary information about the state of the residual stresses on the periphery of the over-core.

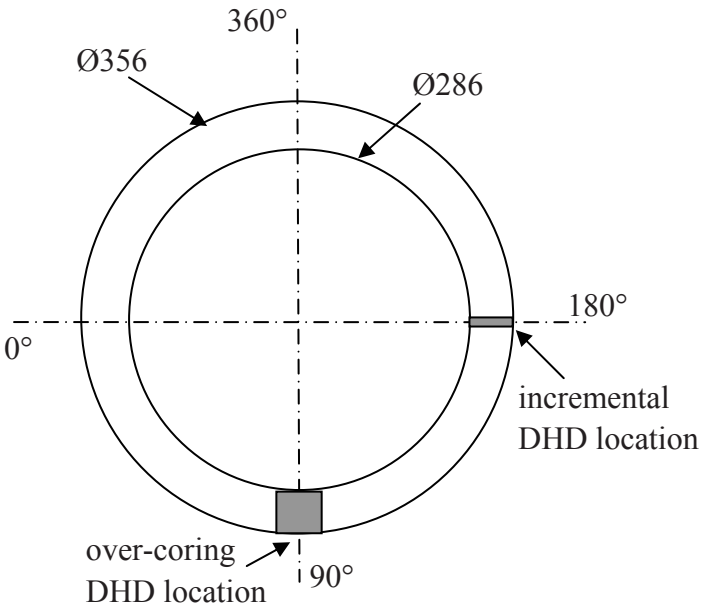

(a)

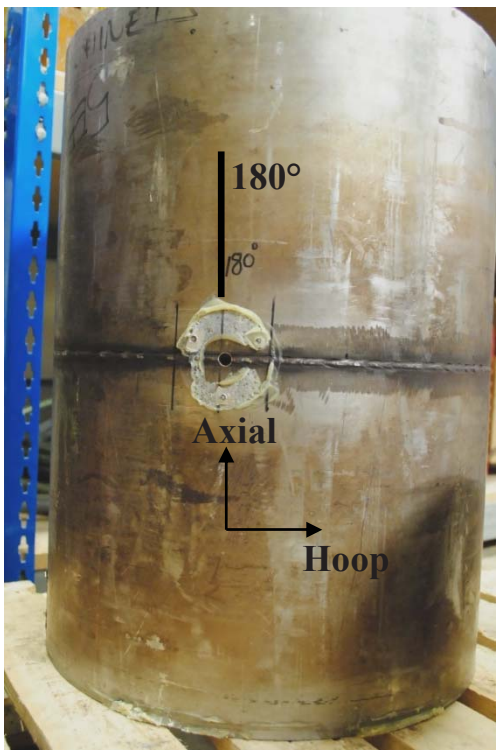

(b)

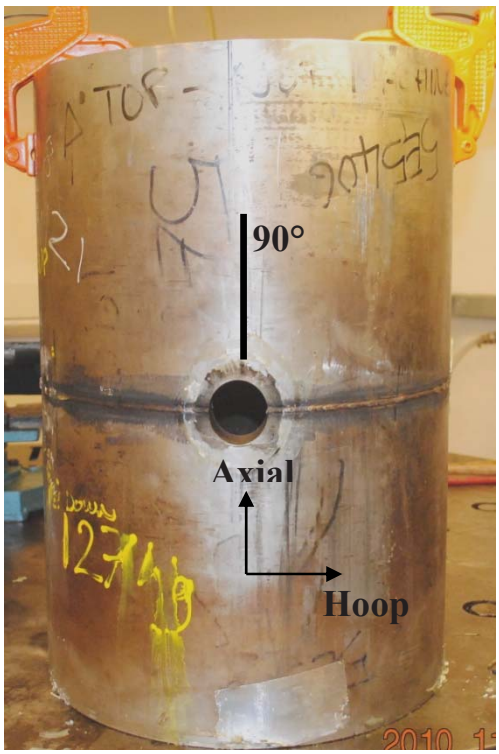

(c)

Figure 2 Electron beam weld pipe sample: (a) Schematic drawing of the EB weld pipe showing the top view with measurement locations; (b) Photograph of sample after incremental DHD measurement at 180°; (c) Photograph of sample after over-coring DHD at 90°

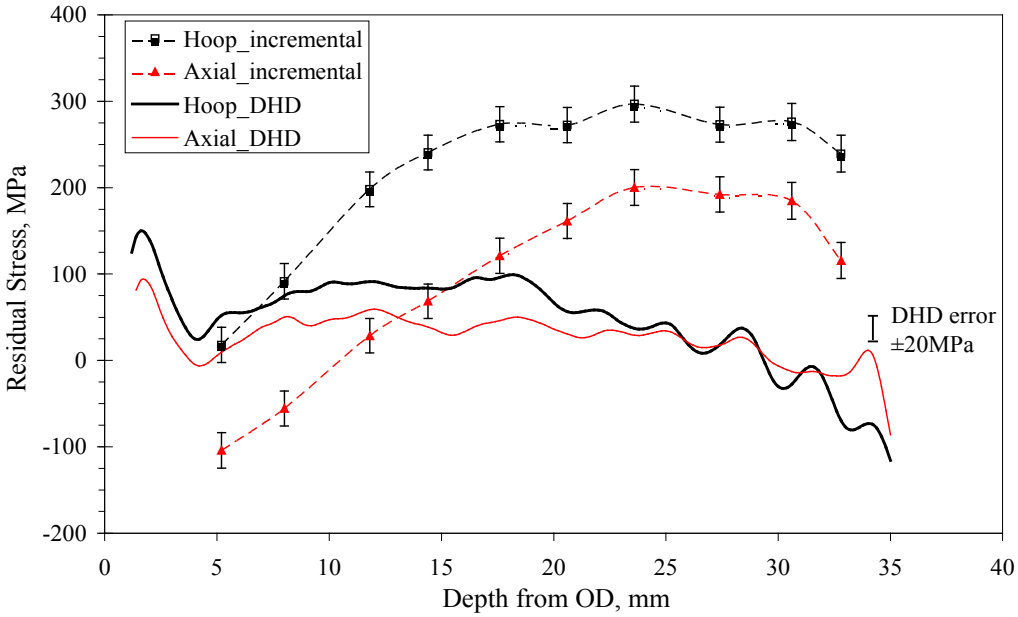

Figure 3 Residual stresses obtained from the conventional DHD and incremental DHD techniques at the 180° location of the EB welded stainless steel pipe

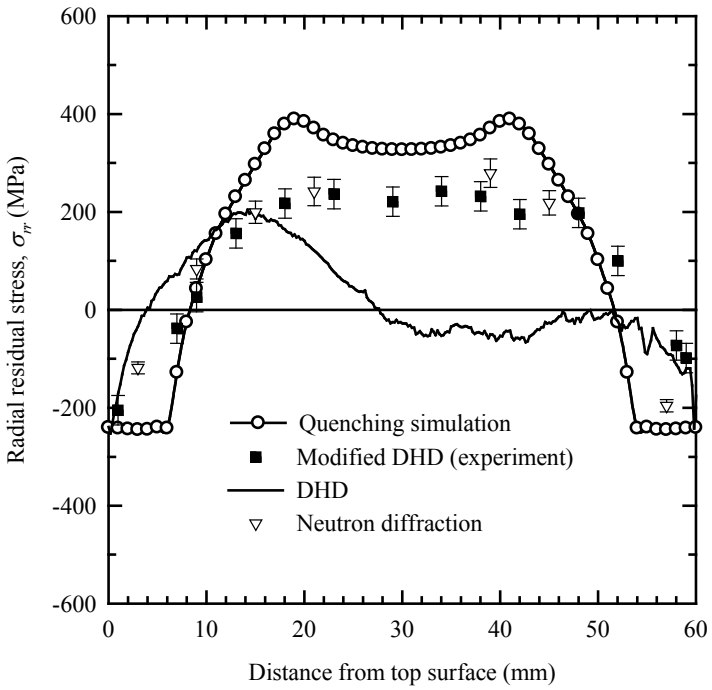

Figure 4. Measured residual stresses using conventional and modified DHD method and comparison with finite element predictions for quenching in a stainless steel cylinder

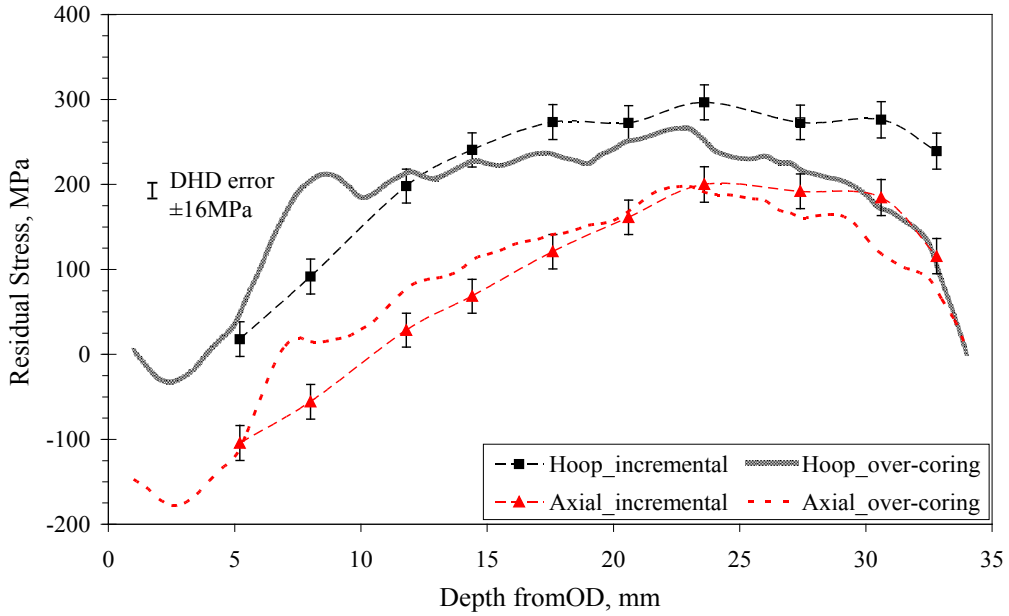

Figure 5 Comparison of the residual stresses obtained from the incremental and over-coring DHD methods

5 CONLUDING REMARKS

Several DHD techniques were carried out on a 304 stainless steel electron beam (EB) weld pipe. Two of the techniques, incremental and over-coring showed good repeatability, with a general trend of compressive residual stress near the outer diameter surface and increasing to high tensile residual stress within at mid-thickness of the cylinder wall. The conventional DHD method was not able to measure the residual stress because of plastic relaxation as found in earlier work [6]. The maximum tensile stress of 296 MPa was obtained by incremental DHD technique at a depth of 24mm from the outside diameter, while the maximum compressive stress of 177MPa was found via the over-coring method at the depth of 2.5mm. Finally, the newly developed over-coring method appears to improve significantly the depth resolution of residual stress measurement and retains the simplicity of the DHD technique compared to the incremental method.

REFERENCE

1. Thomas, G., V. Ramachndra, R. Ganeshan, and R. Vasudevan, *Effect of pre- and post-weld heat treatments on the mechanical prperties of electron beam welded Ti-6Al-4V alloy [J]*. J mater Sci, 1993. **28**(18): p. 4892-4899.
2. Kingston, E., D.J. Smith, G. Zheng, C. Gill, and P. Hurrell. *MEASUREMENT OF RESIDUAL STRESSES IN THICK SECTION STEEL ELECTRON BEAM WELDS*. in *Proceedings of the ASME 2010 Pressure Vessels and Piping Division Conference*. 2010. Bellevue, Washington, USA: Proceedings of the ASME 2010 Pressure Vessels and Piping Division Conference.
3. Leggatt, R.H., D.J. Smith, and F. S and Faure, *Development and experimental validation of the deep hole method for residual stress measurement.* Journal of Strain Analysis for Engineering Design, 1996. **31**(No 3): p. 177-186.

4. Granada-Garcia, A.A., D. George, and D.J. Smith. *Assessment of Distortions in the Deep Hole Technique for Measuring Residual Stresses*. in *11th Exp Mech Conference*. 1998. Oxford, UK.
5. Kingston, E.K., D. Stefanescu, A.E. Mahmoudi, C.E. Truman, and D.J. Smith, *Novel applications of the deep-hole drilling technique for measuring through-thickness residual stress distributions.* Journal of ASTM International, 2006. **3**(4): p. Paper ID JAI12568.
6. Mahmoudi, A.H., S. Hossain, C.E. Truman, D.J. Smith, and M.J. Pavier, *A new procedure to measure near yield residual stresses using the deep hole drilling technique.* Experimental Mechanics, 2009. **49**: p. 595-604.
7. Hossain, S., E. Kingston, C. Truman, and D. Smith. *Finite element validation of the over-coring deep-hole drilling technique*. in *The 2011 International Conference on Advances in Experimental Mechanics: Integrating Simulation and Experimentation for Validation (ISEV)*. 2011.
8. Bonner, N.W., *Measurement of Residual Stresses in Thick Section Welds*, in *Mechanical Engineering*. 1996, University of Bristol: Bristol, UK.

The Incremental Core Drilling Method to Determine In-Situ Stresses in Concrete

Christopher A. Trautner
Simpson, Gumpertz, and Heger, Inc.
41 Seyon St.
Waltham, MA 02453

Michael J. McGinnis
University of Texas at Tyler
3900 University Blvd.
Tyler, Texas 75799

Stephen P. Pessiki
Lehigh University
13. E. Packer Avenue
Bethlehem, PA 18015

ABSTRACT

The incremental core-drilling method (ICDM) is a nondestructive technique to assess in-situ stresses in concrete. In contrast to other available methods of in-situ stress measurement in concrete, the ICDM can quantify stresses that vary through the thickness of the concrete member under investigation, such as those due to bending or eccentric prestressing. In this method, a core is drilled into a concrete structure in discrete increments. The displacements which occur locally around the perimeter of the core at each increment are measured and related to the in-situ stresses by an elastic calculation process known as the influence function method. This paper presents the analytical and numerical techniques necessary for practical use of the ICDM, as well as results from experimental tests in which simple concrete beams were subjected to controlled loads and in-situ stresses measured via the ICDM were compared to known stress distributions. The ability of the technique to accurately measure a variety of different stress distributions is demonstrated, and practical considerations for an ICDM investigation are discussed.

T. Proulx (ed.), *Engineering Applications of Residual Stress, Volume 8*, Conference Proceedings of the Society for Experimental Mechanics Series 999, DOI 10.1007/978-1-4614-0225-1_11,

INTRODUCTION

Reliable information about the in-situ state of stress in the concrete of an existing structure can be critical to an evaluation of that structure. This evaluation may be performed as part of a load rating determination, or it may be performed to determine whether repair or replacement of the structure is necessary. Often, as in the case of a beam subjected to bending or eccentric prestressing, the stresses of interest vary through the thickness of the member. For example, the bending stress in a simple beam varies as a function of the through-thickness position z, as shown in Figure 1.

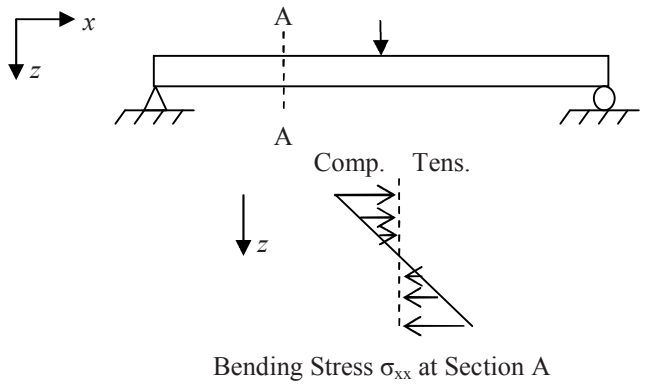

Figure 1: Example of Stress Variation Through the Thickness of a Beam

The ICDM is an attractive method of in-situ stress determination because it is more general than existing methods (which cannot be used in cases when the stress varies as a function of depth [1, 2, 3]), requires access only to the top or bottom of the member under investigation, and is non-destructive (i.e. it allows the structure to still perform its intended purpose). This paper describes four steps taken in the development of this method: analytical formulation, finite-element models used to calibrate the method, numerical simulations used to verify accuracy and robustness, and a series of experiments in posttensioned concrete beams designed to demonstrate the accuracy and repeatability of the technique.

ANALYTICAL FORMULATION

The influence function (IF) method has been developed over the past two decades as a method of relating non-uniform residual stresses in steel structures to strains acquired at the surface in the ASTM hole-drilling method [4,5,6,7]. The ICDM is an extension of the IF method, except that the basis for the ICDM is displacement measurement instead of strain. Because it is extension of the IF method, the ICDM is subject to several of the same assumptions made in the ASTM hole-drilling method. Specifically, it is assumed that the following conditions are satisfied for the member under investigation [9]:

1. The material under investigation can be idealized as a linear-elastic, homogeneous continuum.
2. Plane stress conditions exist.
3. The stresses under investigation vary only with respect to the through-thickness position z (i.e. they do not vary within the plane of the object).

Some experimental and analytical work has been performed to justify that these assumptions are appropriate for typical concrete structures [1, 9].

Displacements for use in the ICDM are acquired along a “measurement circle” – an imaginary circle offset from the outer edge of the core hole drilled into the concrete. The measurement circle used for this work is shown in Figure 2:

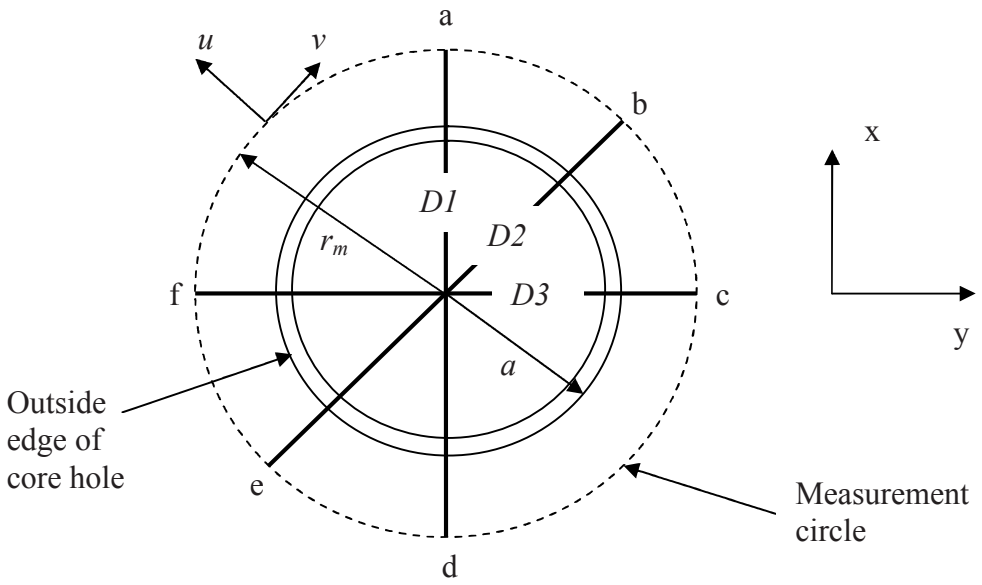

Figure 2: Measurement Circle

A Cartesian reference frame is defined at the center of the core hole of outside radius a, with the x-axis typically aligned with the longitudinal axis of the member under investigation. The measurement circle is defined by radius r_m, which is typically on the order of 25 mm larger than the outside core-hole radius a [1, 2]. For simulation and calibration of the core-drilling technique, a is typically taken as 75 mm and the core hole width t_b is taken as 5 mm, reflecting the radius and blade thickness of commonly-available coring bits for concrete [9, 10]. For convenience, displacements along the circle are measured in terms of their radial (u) and tangential (v) components. Although many different measurement configurations are possible [8], the current work is based radial displacements at the six points labeled a through f in Figure 2. To make the IFs for the ICDM as general as possible and to reduce the number of units in calculations, it is convenient to measure through-thickness position in terms of normalized depth H, where $H=z/r_m$.

The ICDM is formulated in terms of mean or equibiaxial stress P, deviatoric stress Q, and shear stress component τ, because any two dimensional plane stress distribution can be expressed in terms of these components. In the ICDM, each of these components is considered separately and is assumed to be a function of through-thickness depth H. The following notation is used to denote this in terms of Cartesian stresses:

$$P(H) = \frac{\sigma_{xx}(H) + \sigma_{yy}(H)}{2}$$

$$Q(H) = \frac{\sigma_{xx}(H) - \sigma_{yy}(H)}{2}$$

$$\tau_{XY}(H) = \tau_{XY}(H)$$

Once these functions are known, any general stress distribution can be represented by superimposing these components. The variation through depth can be fit as a linear or higher-order function, although most problems of interest are best fit as either a constant or linear variation [9, 10]. If a linear variation is assumed, the variation of stress with depth is referred to as the stress gradient.

Influence functions (IFs) provide the solution for these stress functions by correlating displacements found during the coring procedure to in-situ stresses. A complete description of the influence function method as applied to the ICDM is available [8, 9, 10]; only the basic concepts are described here.

Within an infinitesimally small increment at H, the IF G_A provides the relieved radial displacement that would occur under a unit equibiaxial (P=1) stress field if the core depth is h:

$$uR(h,H) = \frac{1}{E} G_A(h,H) \quad (1)$$

The core hole depth h is also normalized to the measurement circle radius. As the core hole is drilled in successively deeper increments, the total relieved displacement is due not only to the relieved displacement in that increment, but also in previous increments. Therefore, the total displacement at a particular hole depth is the summation or integral over all the increments up to that point. Displacement and stress are then related by the integral of the IF. This can be written as:

$$uR(h,H) = \frac{1}{E} \int_0^h G_A(h,H) P(H) dH$$

IFs for relating both deviatoric stress Q and shear stress τ_{xy} to radial displacement can be developed in a similar manner. However, because deviatoric stress and shear stress in a core hole are not axisymmetric, the displacement patterns they produce are not constant around the measurement circle but are sinusoidal functions of angular position around the measurement circle:

$$uR(h,H,\theta) = \frac{1}{E} \int_0^h G_B(h,H) Q(H) \cos(2\theta) dH$$

where θ is the angular position of the point being measured, measured from the x-axis and G_B is the influence function. An IF relating tangential displacement to deviatoric and shear stress can also be formulated [8, 9], but was not used in the current work. Because the IFs do not lend themselves to analytical formulation, it is convenient to use a matrix of IF coefficients so that the value of the IF at a particular core depth can be determined. This can be represented by a double-power expansion. For example, the mean stress radial displacement IF G_A is:

$$G_A = \sum_{k=1}^{n} \sum_{l=1}^{m} \alpha_{kl} h^{i-1} H^{j-1}$$

where α is a matrix of influence function coefficients with row and column indexes k and l. The IF for radial displacement due to deviatoric and shear stresses G_B can be similarly represented.

DETERMINATION OF IF COEFFICIENTS BY FINITE ELEMENT SIMULATION

The first step in the ICDM process is to determine these matrices of IF coefficients relating mean stress to radial displacement (α) and shear and deviatoric stress to radial displacement (β). This is accomplished by finite element analyses in which the core drilling process is simulated by removing layers of elements in a simulated structure. These analyses are described in detail in [10]. In the analyses, the core hole is loaded from the inside, resulting in displacement at the measurement circle. The displacements vary as the core-hole depth and loading depth change, and the influence function coefficients are calibrated from these displacements. The influence function coefficients calculated in this manner can then be used in the reverse process: the calculation of in-situ stresses from known displacements.

To produce the matrix of relieved radial displacements due to mean stress *uRp*, an axisymmetric finite element model was employed. 25 partial core depths were simulated, with a maximum core depth of 150 mm. To produce the matrix of relieved radial displacements due to deviatoric stress *uRq* and the matrix of relieved tangential displacements due to deviatoric stress *vRq*, an analogous 3D finite element model was employed. To determine the IF coefficients, the stress within each layer of elements is set to unity. The relieved displacement at the measurement circle due to unit loading can be expressed as:

$$uRp_{ij} = \frac{1}{E} \sum_{k=1}^{n} \sum_{l=1}^{m} \frac{\alpha_{kl}}{k} h_i^{l-1} h_j^k$$

$$uRq_{ij} = \frac{1}{E} \sum_{k=1}^{n} \sum_{l=1}^{m} \frac{\beta_{kl}}{k} h_i^{l-1} h_j^k \cos(2\theta)$$

These two equations are solved for the matrices of IF coefficients α and β based on the matrices of displacements calculated by FE analysis *uRp* and *uRq* . As shown by the presence of the elastic modulus E in the previous equations, the IF matrices developed using models with one elastic modulus can be adapted for use on a concrete structure with any elastic modulus by simple scaling. Another consequence of this formulation is that accuracy of the calculated in-situ stresses is directly related to the accuracy to which the elastic modulus of the structure can be estimated.

NUMERICAL VERIFICATION

A number of measures have been used to verify the numerical accuracy of the IF solution [9,10], but the method is best tested by using displacements acquired from FE simulations of a core-drilling procedure in which calculated stresses can be compared to applied stresses. To do this, a 3D FE model similar to that used to calibrate the IF matrix β was used. Two examples are presented here: one with a linearly-varying stress in the x-direction only (σ_{yy}, $\tau xy=0$), and one with a linearly-varying stress in the x-direction and a constant stress in the y-direction ($\tau_{xy}=0$). These models are representative of beams or plates under simultaneous bending and prestressing in one or two directions.

At minimum, a set of three displacements must be acquired at each coring depth, so that each of the unknown stress components (*P, Q,* and τ_{xy}) can be computed. For both of these examples, a set of three radial displacements at θ =0º, 45º, and 90º were acquired along a measurement circle of r_m=100 mm at non-dimensional core depths of 0.75 and 1.5. The stresses calculated from these displacements and the applied stresses are shown in Figure 3:

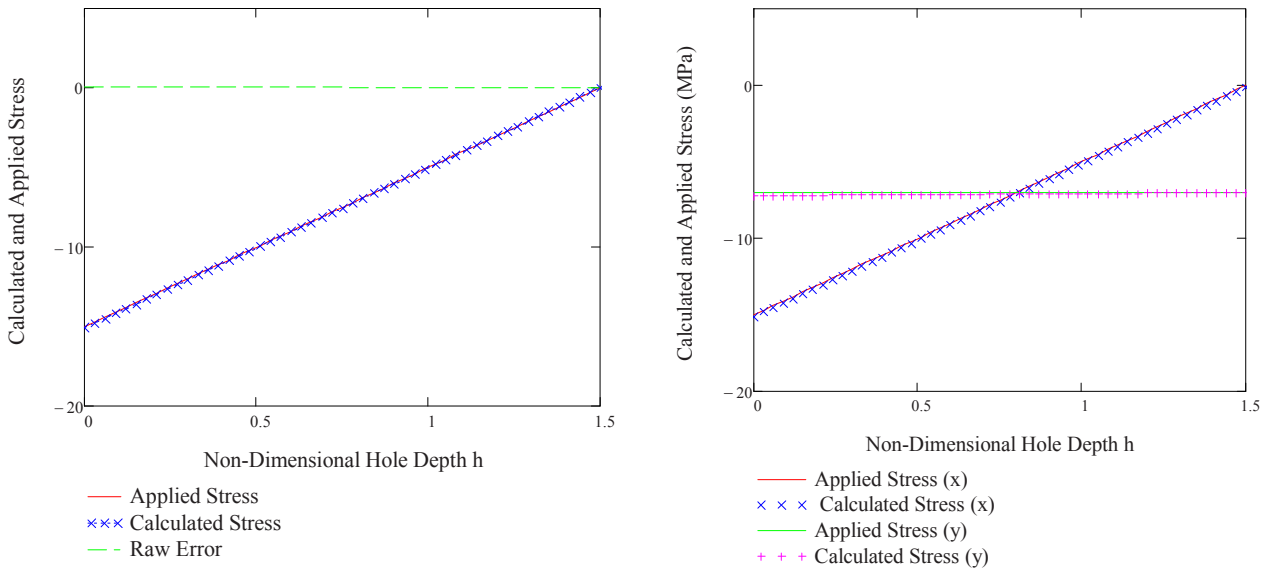

Figure 3: (a) Uniaxial Stress σ_{xx} *(b) Biaxial Stresses* σ_{xx} *and* σ_{yy}

The maximum error in the calculation of any of these stresses is less than 3% when compared to the average stress in that direction. These verification examples indicate that the IF solution is capable of highly accurate prediction of both uniaxial and biaxial stresses with constant and linear distributions.

EXPERIMENTAL VERIFICATION

To verify that the ICDM can be used to calculate in-situ stresses in real concrete structures, a total of nine tests were conducted on three experimental specimens. The experimental program is described in detail in [17]. Each specimen was an unreinforced concrete beam approximately 488 cm in length, loaded by eccentric post-tensioning bars, as shown in Figure 4:

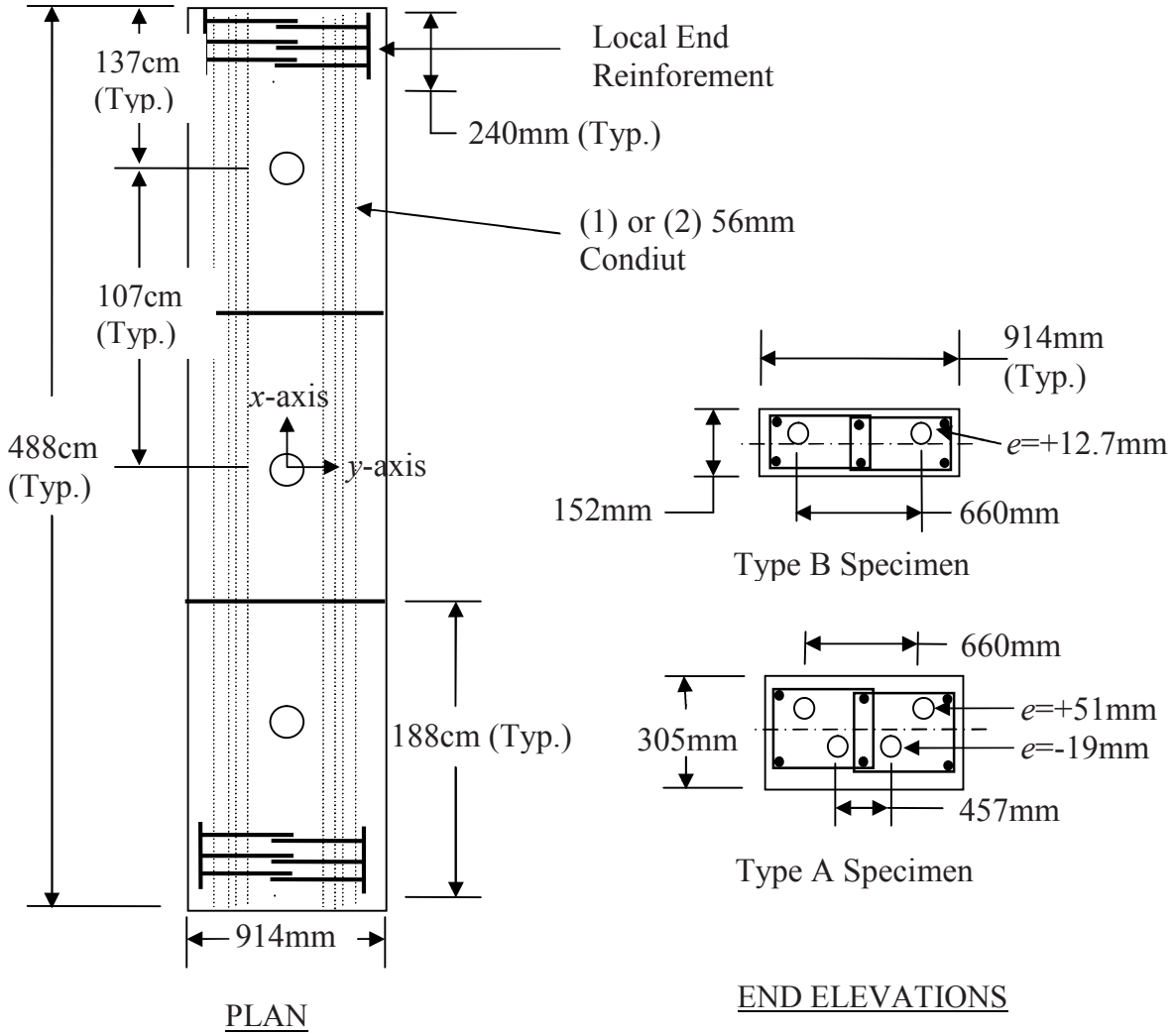

NOTE: 1) 1mm is approximately 0.039 in. 2) e = nominal eccentricity

Figure 4: Specimen Details

The objective of the testing was to measure the stress in the top fiber of the beam and the variation of stress through the depth of the beam. The variation of stress with depth was assumed to be linear, and the variation of stress was referred to as the stress gradient. Two Type B specimens and one Type A specimen were tested to determine whether a single set of IF coefficients would produce accurate results, or whether calibration of the coefficients to the particular thickness of the member under investigation is required.

Because displacements due to core-drilling water and shrinkage can create "apparent" stresses that affect the accuracy of the technique [15, 16], the specimens were kept saturated from the time of casting to immediately before testing. In a practical application of the technique, the effect of core drilling water and shrinkage would need to be compensated for either by saturating the member under investigation prior to testing, or by quantifying and removing the apparent stresses from the solution by accounting for the concrete volume change due to water movement. Simulating the change in concrete volume by FE simulation and removing the calculated displacements from the measured displacements is one method for removing apparent stresses [16].

Specimens were cast using a concrete mix with a water/cement ratio of 0.41 and a 28-day design strength of 45MPa (6500psi). The specimens were cast on top of a double layer of plastic sheeting to ensure that the beams were not restrained by the form base. The tops of the specimens were screeded flat using the top of the forms and then given a smooth steel-

trowel finish in order to facilitate application of the stochastic spray-paint pattern required for digital DIC was used as the primary measurement tool for the experimental procedure – i.e. it wa displacements that occur locally around the core hole, which are used in the ICDM to calculate the accomplished by taking images before the coring procedure is started and after each increme displacements which occur at each increment were measured by comparing the image taken at tha taken before the coring procedure is started. Although the ICDM can be carried out with more cc measurement techniques, DIC provides nearly full-field displacement measurement that adds to the a and does not require mounting of instrumentation in the core area which could be damaged during th was also used to measure the strain on the top surface of the specimens during loading. This inform output from load cells mounted in-line with the prestressing jacks and the modulus of elasticity of th tests was used to calculate the "applied" stress distribution to which the stress distribution m compared.

The holes were cored in between three and eight increments of between 12 mm and 50 mm. Alth increments would likely not be practical in a field application of the technique, the large amou allowed for parametric study of accuracy versus number of increments used in the solution proce study, displacements from a variety of different increment combinations was used and averaged to ca

The displacements were captured using the ARAMIS suite of DIC software [11]. Negative radial d as displacement toward the core hole, and 0 and 180 degrees are measurement points aligned with th to the experimental program, an FE model of the specimens was created and the loads from the post A comparison of the observed and predicted displacements is shown in Figure 5:

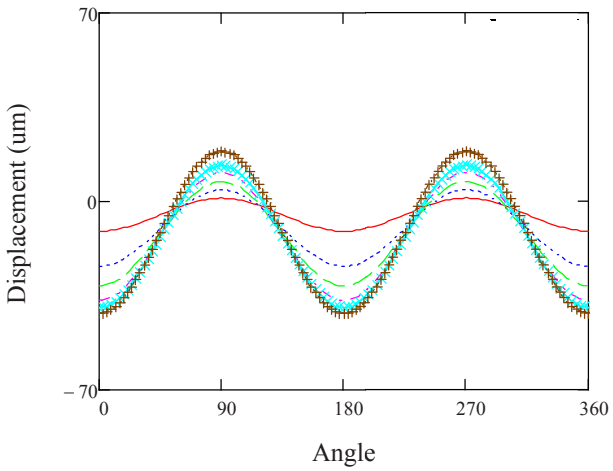

Figure 5: Typical Predicted and Measured Radial Displacement Pattern

As can be seen in the figure, the general magnitude and pattern of the displacements is consistent v FE analysis, but there is significant noise present in the data. The experimental displacement data noise than that of previous researchers [1, 2], possibly due to the relatively large black dots that were the stochastic pattern. The radial displacements at each increment were combined into displacemer and D3 (as shown in Figure 1), and the IF solution was applied at each 1° increment around the mea the data becomes redundant after a 180° rotation, a total of 180 separate solutions was obtained ar the measured stress gradient. Due to the high level of noise in the data, there was substantial variati 1° rotation, but in general, the solution clustered around the applied stresses, as shown in Figure 5:

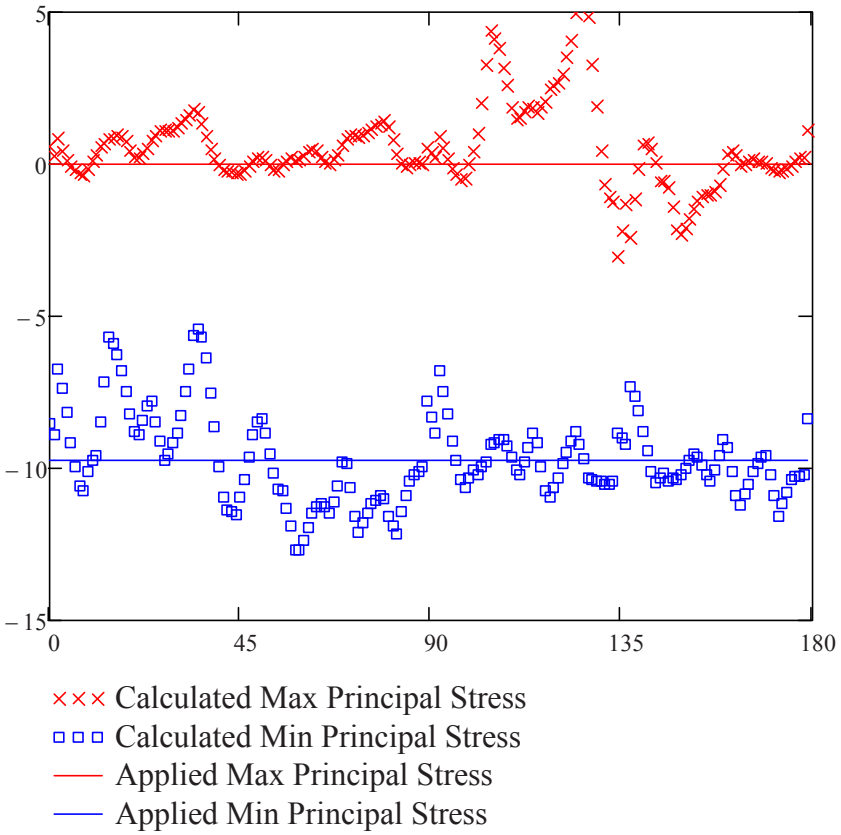

Figure 6: Typical Calculated and Applied Stress at the Top Fiber

Calculated stress gradients showed a similar clustering [17]. The 180 solutions were averaged for each of the nine tests and compared to the applied stresses. The results are summarized in Table 1:

Table 1: Summary of Calculated and Applied Stresses

Core	Applied Top Fiber Stress σ_1 (MPa)	Measured Top Fiber Stress σ_1 (MPa)	Error (%)	Applied Gradient (MPa/h_{max})	Measured Gradient (MPa/h_{max})	Error (MPa/h_{max})
1	-14.05	-12.43	11.5%	6.87	7.55	0.67
2	-15.04	-13.90	7.5%	8.21	10.16	1.95
3	-16.08	-15.29	4.9%	9.61	11.17	1.56
4	-10.22	-9.08	11.2%	3.79	2.90	0.88
5	-9.74	-9.06	6.9%	3.18	2.81	0.36
6*	--	--	--	--	--	--
7	-8.87	-8.28	6.6%	2.92	2.01	0.91
8	-4.53	-3.66	19.2%	-0.08	-1.86	1.79
9	-8.83	-7.76	12.2%	2.90	2.83	0.08
		Average:	10.0%	4.68	4.70	1.03
			Top Fiber		Gradient	
		Total Average Error:	10.0%		21.8%	

* omitted from averages

NOTE: 1 MPa equals about 0.145 ksi

The Stage 1 image for Core 6 was mistakenly overwritten, so measurement of relieved displacements and calculation of in-situ stresses was not possible. Error in top fiber stress was taken as the absolute difference between the applied and measured top fiber stress divided by the applied top fiber stress. Total average error for the top fiber stress was taken as the average of the percent error for each test. In each of the tests performed, the measured top fiber stress was less than the applied top fiber stress. This type of error is consistent with underestimation of the in-situ elastic modulus.

The accuracy of the measured stress gradient was generally lower than that of the top fiber stress. However, the numerical value of the stress gradients were relatively small in the specimens tested (essentially 0 for test 8). The total average error in the stress gradient (taken as the average error divided by the average applied stress gradient) is 22%. However, the average applied gradient and the average measured gradient agree to within 1%. This suggests that the measured stress gradient in a single test would be expected to be accurate to within about 20%, but that the average of multiple tests would be significantly more accurate. No significant improvement in accuracy was found using IF coefficients calibrated to the geometry of the Type A specimen.

SUMMARY AND CONCLUSIONS

The ICDM calculates in-situ stresses in concrete from measured displacements based on the well-established influence function method. The proposed influence function coefficients can accurately calculate in-situ stresses based on displacements from finite element simulations of a core drilled incrementally into a concrete structure. The ICDM can accurately determine in-situ stresses in simple concrete structures. The calculated accuracy is about 10% for the stress at the surface of the concrete and about 20% for the variation of stress with depth.

REFERENCES

1. McGinnis, M. J., “Experimental and Numerical Development of the Core-Drilling Method for the Nondestructive Evaluation of In-situ Stresses in Concrete Structures,” Dissertation, Lehigh University, 2006, 366 pp.
2. McGinnis, M. J., Pessiki, S., Turker, H., “Application of 3D Digital Image Correlation to the Core-Drilling Method,” *Experimental Mechanics*, V. 45, No. 4, 2005, pp. 359-367.
3. Buchner, S.H., “Full-Scale Testing of Prestressed Concrete Structures,” Doctoral Thesis, University of Surrey, Guildford, Great Britain, 1989, 303 pp.
4. Schajer, G.S., “Measurement of Non-uniform Residual Stresses Using the Hole-Drilling Method, Part I,” *Transactions of ASME*, V. 110, No. 4, 1988, pp. 338-343.

5. Schajer, G.S., "Measurement of Non-uniform Residual Stresses using the Hole-Drilling Method, Part II," *Transactions of ASME*, V. 110, No. 4, 1988, pp. 344-349.
6. Beghini, M. and Bertini, L., "Recent Advances in the Hole-Drilling Method for Residual Stress Measurement," *Journal of Materials Engineering and Performance*, V. 7, No. 2, 1998, pp. 163-172.
7. Beghini, M., "Analytical Expression of the Influence Functions for Accuracy and Versatility Improvement in the Hole-Drilling Method," *Journal of Strain Analysis*, V. 35, No. 2, 2000, pp. 125-135.
8. Turker, H., "Theoretical Development of the Core-Drilling Method for Nondestructive Evaluation of Stresses in Concrete Structures," Dissertation, Lehigh University 2003, 336 pp.
9. Trautner, C., "Development of the Incremental Core Drilling Method for Non-Destructive Investigation of Stresses in Concrete Structures," Master's Degree Thesis, Lehigh University, 2008, 342 pp.
10. Trautner, C., McGinnis, M., and Pessiki, S., "Analytical and Numerical Development of the Incremental Core Drilling Method of Nondestructive Determination of In-Situ Stresses In Concrete Structures," The Journal of Strain Analysis for Engineering Design, Volume 45, pg. 647-658.
11. GOM International AG, ARAMIS User's Manual, Bremgarterstrasse 89B CH-8967 Widen, Switzerland, 2007.
12. McGinnis, M.J., Pessiki, S., Turker, H., "Application of 3D Digital Image Correlation to the Core-Drilling Method," *Experimental Mechanics*, V. 45, No. 4, 2005, pp. 359-367.
13. Buchner, S.H., "Full-Scale Testing of Prestressed Concrete Structures," Doctoral Thesis, University of Surrey, Guildford, Great Britain, 1989, 303 pp.
14. Mehrkar-Asl, S. "Concrete Stress Relief Coring: Theory and Practice," Proceedings of the FIP First Symposium on Post Tensioned Concrete Structures, London, pp. 569-576.
15. McGinnis, M.J., Pessiki, S., "Differential Shrinkage Effects in the Core-Drilling Method," *Magazine of Concrete Research*, V. 59, No. 3, 2007, pp. 155-164.
16. McGinnis, M.J., Pessiki, S., "Water Induced Swelling Displacements in the Core-Drilling Method," *ACI Materials Journal*, V. 104, No. 1, 2007, pp. 13-22.
17. Trautner, C., McGinnis, M., and Pessiki, S., "Application of the Incremental Core Drilling Method to Determine In-Situ Stresses in Concrete," Accepted by the Materials Journal of the American Concrete Institute, August 2010.

Influence of Drilling Parameters on the Accuracy of Hole-drilling Residual Stress Measurements

D. Upshaw[1,2], M. Steinzig[2], and J. Rasty[1]
[1]Texas Tech University, Mechanical Engineering Department, 7th and Boston, Lubbock, TX 79409
[2]Los Alamos National Laboratory, P.O Box 1663, Los Alamos, NM 87545

Abstract
The objective of this research is to define drill speeds that produce acceptable results when using the hole-drilling technique for measuring residual stress. For this study, three common engineering materials; alloy 6061-T651 aluminum, 304 stainless steel, and A36 carbon steel were used. This was achieved by performing ESPI/hole-drilling stress measurement of a known applied stress in discrete rpm intervals ranging from 2-40K rpm for each material. To produce a known state of stress specimens were bent elastically in a four-point bend fixture. Stress measurements were taken using single-axis electronic speckle-pattern interferometry (ESPI). It was found that for 6061-T6 aluminum, accurate and repeatable results can be achieved between speeds of 2-40K rpm. For 304 stainless steel, result accuracy diminishes when drill speeds go below 6K rpm. The A36 steel had a large as-received stress gradient across the longitudinal dimension and was therefore removed from this study.

Introduction
Residual Stress (RS) is locked in stress that is induced due to non-uniform treatment of materials and exists in the absence of applied loads. RS is usually unwanted, unavoidable, and will promote premature failure of a part or assembly. RS is often purposely induced into a part or material, and is called "engineered stress". Shot and laser-peening, for instance, introduce compressive residual stresses to a surface layer of a part, significantly increasing its fatigue life [1]. Residual-stresses arising from metal forming and machining and the grounds for their induction have challenged the minds of engineers and scientists since the Industrial Revolution. Figure 1 shows a classic photograph of the spontaneity of residual stress effects, which highlights the significance of its presence.

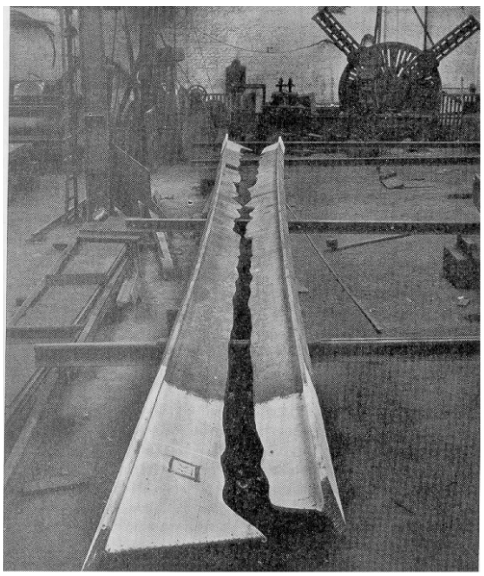

Fig. 1 Beam split from relaxation of residual stresses [2]

T. Proulx (ed.), *Engineering Applications of Residual Stress, Volume 8*, Conference Proceedings of the Society for Experimental Mechanics Series 999, DOI 10.1007/978-1-4614-0225-1_12, © The Society for Experimental Mechanics, Inc. 2011

When the science of residual-stress progressed to the point to where its actual measurement could be employed (1930s), an explosion of thought resulted in ways to increase accuracy and improve results. Fueled with the desire to more accurately reveal these undesired stresses, theories have been proposed and experiments performed.

The conclusion of a study conducted in the 1980s inferred that for hole-drilling residual-stress measurement, one should use the highest drill-speed attainable in order to minimize induced drilling stresses and ensure accurate data [3]. Since then, it has just been standard to use the highest speed attainable. Flaman's study of the effect of drill-speed on the accuracy of hole-drilling residual stress measurements is the only of its kind contained in the literature.

The aim of the current study is to obtain more data, which will give a better picture of what effects are taking place when varying drill-speeds are utilized. The previous study was conducted using an air-turbine spindle along with strain-gage rosettes, whereas, this study will use a state-of-the-art NSK electric spindle and controller combined with a laser speckle interferometer. Air turbines have variable speed as a function of load which very likely decreases by a significant amount under load. Therefore, air turbines are not particularly appropriate for studying drill-speed effects, which is why the electric drill and feedback controller have been employed. Additionally, using an ESPI system for strain measurement, rather than strain-gage rosettes, will enable the acquisition of many residual-stress measurements in a short period of time. While it has been shown that holes drilled at low speeds (~2K rpm) will produce larger strain readings than holes drilled at ultra-high speeds ~400K rpm, there is a huge data gap between these two extreme values. Taking many measurements between 2K and 40K rpm and using the data to find out where result accuracy actually begins to diminish is the primary purpose of this study. Any information gained with the ESPI system can be applied back to the hole-drilling/strain-gage technique.

Material Procurement

The .5" plate materials used in this study were all rolled plate stock and comprised of, 6061-T651 aluminum, A36 carbon-steel, and 304 stainless-steel. All materials were purchased from Reliance Steel & Aluminum Company in Albuquerque, NM.

Sample Preparation

Bar specimens, of dimensions 12"x1"x0.5" (304.8 x25.4 x12.7mm^3), were very carefully machined from each of their 16"x16"x0.5" (406.4 x406.4 x12.7mm^3) parent plates as to minimize induced machining stresses. The specimen plates were specified to be cut away from the edges of the parent plates in order to avoid the stress gradients close to the edges of large rolled plate [8]. The material properties were acquired from each material's certified test report. Each bar specimen was slow cut on a band saw with cutting lubrication/cooling fluid and then side-milled with a carbide tip, under flood coolant, to a final dimension of 12"x1"x.5". The specimens' longitudinal dimension runs parallel to the rolling direction. All machining processes were performed by Hand Precision Machining, Inc., of Los Alamos, NM.

Experimental Apparatus

ESPI/Hole-drilling Equipment

An electric high-speed machining spindle with a range of 2K-40K rpm and electronic feedback controller were used in conjunction with an American Stress Technologies, PRISM system [4,5,6,7]. The function of the ESPI system is based on the hole-drilling method of residual-stress measurement but uses holographic techniques, rather than strain gages, to measure strain due to stress relaxation. The laser is of wavelength 532nm and power 20mW. However, the laser is mounted, in this particular experiment, to 7.5mW and the beam is expanded to a 32mm diameter. This setup was chosen to reduce the laser intensity to adhere to workplace safety protocol. The ESPI/hole-drilling system is used to drill a hole into a surface which is illuminated by a speckle pattern. When the hole is drilled, if residual stress is present, deformation around the hole occurs, which changes the intensity of light at and around the hole. The change in intensity is found by subtracting before and after images of the speckle pattern. This intensity change is converted into the corresponding deformation along the sensitivity angle. The sensitivity angle is the bisector of the illumination and observation vectors. From the deformation, the stress state in the in-plane dimension is found.

The ESPI system is capable of using drill-bits of sizes ranging from 1/32" to 1/8" (0.79375 to 3.175mm). This range relies on the camera's ability to properly image the drilled hole. Proper adjustment of the camera is performed prior to drilling so that the hole diameter will comprise 1/8 to 1/4 of the on-screen image.

The choice of hole-depth is dependent on the chosen diameter of the hole. The depth to diameter ratio, 'D/d', usually does not exceed 0.6. There is a depth at which further drilling will not produce any response at the surface. The numerical models used with the ESPI system allow D/d ratios ranging from 0.1 to 0.6. Table 1 lists the most common depth-bit configurations.

Table 1 Depth to diameter, D/d, ratios for common bits

Depth/diameter ratio	0.1	0.2	0.3	0.4	0.5	0.6
Bit size	-	-	-	-	-	-
1/64 - 0.0156" *(0.397)*	0.0016" (0.040)	0.0031" (0.079)	0.0047" (0.119)	0.0063" (0.159)	0.0078" (0.198)	0.0094" (0.238)
1/32 - 0.03125" *(0.79)*	0.0031" (0.079)	0.0063" (0.159)	0.0094" (0.238)	0.0125" (0.318)	0.0156" (0.397)	0.0188" (0.476)
3/64 – 0.0469" *(1.19)*	0.0047" (0. 119)	0.0094" (0. 238)	0.0140" (0. 357)	0.0188" (0.476)	0.023" (0.595)	0.0281" (0.714)
1/16 - 0.0625" *(1.59)*	0.00625" (0.159)	0.0125" (0.318)	0.0188" (0.476)	0.0250" (0.635)	0.03125" (0.794)	0.0375" (0.953)
3/32 – 0.0938" *(2.38)*	0.0094" (0.238)	0.0188" (0.476)	0.0281" (0.714)	0.0375" (0.953)	0.0469" (1.191)	0.0563" (1.429)
1/8 - 0.125" *(3.18)*	0.0125" (0.318)	0.025" (0.635)	0.0375" (0.953)	0.050" (1.27)	0.0625" (1.588)	0.0750" (1.905)

Four-point Bend Fixture

In an effort to fulfill the need for a standard method of creating a sample with a non-uniform through-thickness stress distribution, a load fixture was developed [9]. This fixture was designed to help assess the accuracy of residual-stress measurement methods and is therefore used in this study. A schematic of the load fixture pin locations are displayed below in Fig. 2.

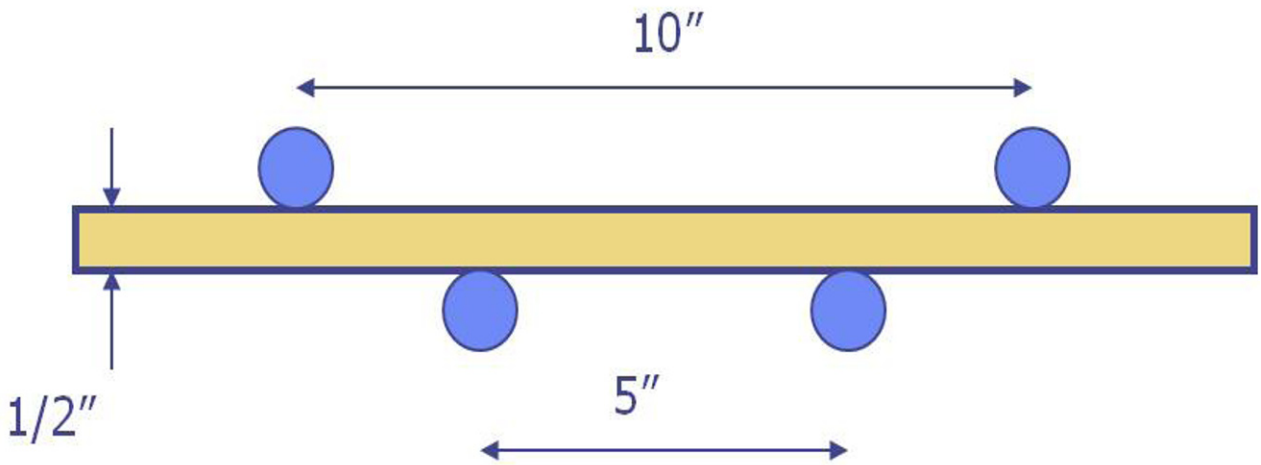

Fig. 2 Schematic of 4-point bend fixture, pin locations

The pins are designed to rotate during the bend process eliminating traction forces. Through integration of the moment equation for the fixture, one can find the centerline deflection to be expressed as:

$$y_{\max} = \frac{\sigma}{12Et}(4a^2 - 3l^2)$$

Where l is the distance between the outer supports (10"), a is the distance between the inner supports (2.5", 63.5mm), t is the thickness of the specimen (0.5", 12.7mm for specimens used in this study), σ is the desired surface stress between the inner supports, and E is the modulus of elasticity (Table 2). This equation is used to give a deflection value at which the desired stress is achieved in the surface of the beam. The centerline deflection of the specimen is measured using a dial-gage scaled in increments of .001" (Fig. 3).

Table 2 Material properties of 6061-T651 aluminum and 304 stainless steel

Material	Elastic Modulus	Poisson's Ratio	Yield Stress
6061-T651 Aluminum	10,300ksi (71.1 GPa)	0.344	41.8ksi (288 MPa)
304 Stainless Steel	27,600ksi (190.4 GPa)	0.305	39.6ksi (273 MPa)

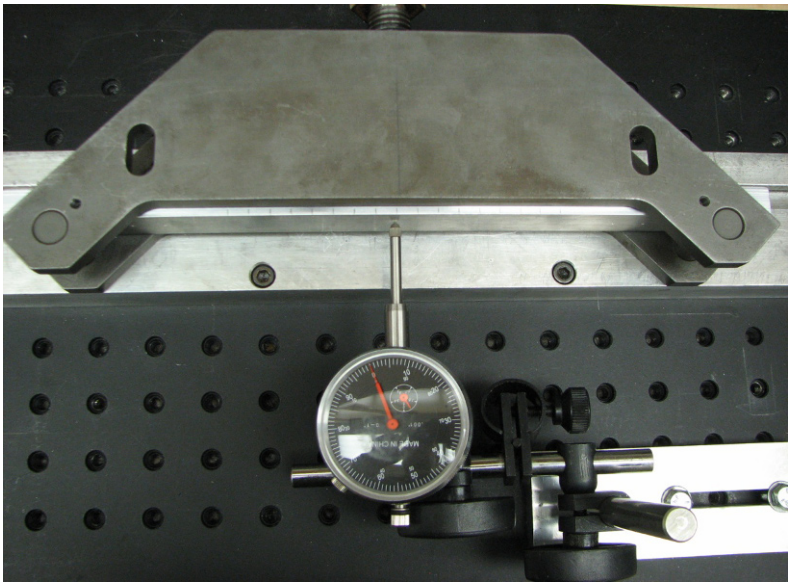

Fig. 3 Measurement of specimen centerline deflection with dial gage

Experimental Procedure

Quantifying As-Received State of Stress

Before any worthwhile experimental comparison on a series of materials can be performed, the initial conditions of each test specimen should be evaluated. For this particular test, in which we seek to compare stresses, the presence, location and orientation of the existing stresses should be determined. For clarity, the longitudinal axis is along the 12” dimension and the transverse along the 1”. All holes were drilled in the 12” x1” face of each specimen. In order to characterize the as-received state of stress, a row of four .0625” (1.59mm) diameter holes was drilled at a depth of .0125” (.318mm), on the face of each specimen along the longitudinal axis. The four holes were located at 2” and 2.5” from each end. Drill-bits were changed every 15 holes in the aluminum and every 8 holes in both steels for the as-received measurements. Using machinist clamps and an aluminum block, the bar specimen were secured for drilling (Fig. 4).

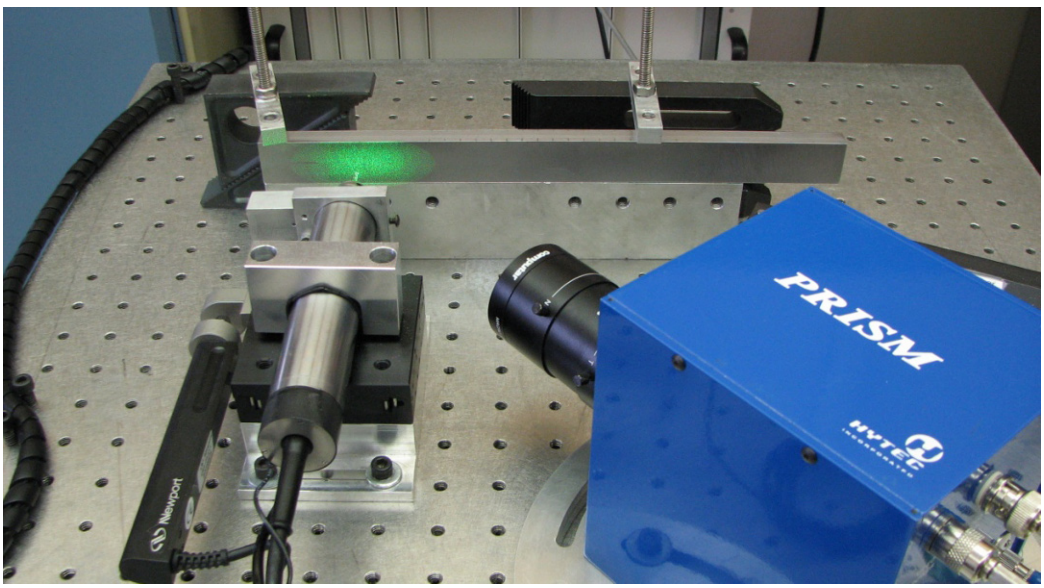

Fig. 4 Specimen fixture for as-received stress measurements

Parameter Variation

For all tests, two-flute carbide tipped end mills were used to drill the holes and were changed every 15 holes. Hole-centers were spaced at a distance of five hole-diameters to minimize the measurement results at one location being affected by the stress relief from a previously drilled hole. Each row was positioned .25" from the top and bottom edge of the specimens in order to minimize edge effects and still maintain enough distance in between the hole-centers in opposing rows. A .0625" (1.59mm) diameter drill-bit was used which gives, since two rows of measurements were taken and each hole center should be spaced at least 5 hole-diameters, 30 potential measurements on each bar specimen (Fig. 5). The parameters varied in this study are drill-speed, hole-depth/diameter ratio, and drill-bit size.

Drill-speed

After characterization of the as received surface stress, the aluminum and stainless steel specimens were elastically deformed in a four-point bending fixture to create a known surface stress equating to ~50% of the yield stress for each material ; 20 ksi (138 MPa) and 15.6 ksi (107.6 MPa) at the surface for 6061-T6 aluminum and 304 stainless steel respectively. These values were chosen in order to adhere to the 50% of yield-stress limit rule for hole-drilling/strain gage residual stress measurement accuracy [10]. It has been shown that errors in residual stress results are obtained when measuring stresses that are greater than 50% of the yield stress of the material [11]. This overestimate is caused by localized plasticity effects occurring at the periphery of the hole due to the stress concentration factor of the hole. The highest stress obtainable without inducing plasticity effects was desired so the measurement's error and uncertainty would have less weight on the overall accuracy of our measurements.

A total of thirty, .0625" diameter, holes were drilled in both, 6061-T6 aluminum specimen 1 (Al-1) and 304 stainless steel specimen 1 (SS-1) at a depth of .0125" (0.318mm). Holes 1 through 15 in these specimens were drilled at 40K rpm, 16-18 at 12K rpm, 19-21 at 10K rpm, 22-24 at 8K rpm, 25 and 26 at 6K rpm, 27 and 28 at 4K rpm, and 29 and 30 at 2K rpm. This gives a total of seven drill-speed increments for each specimen.

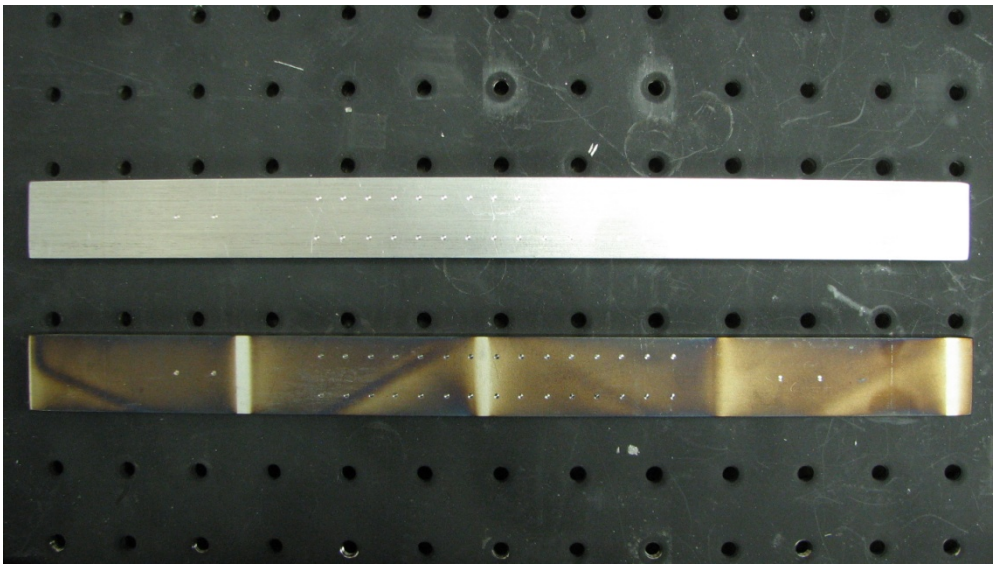

Fig. 5 Aluminum (top) and annealed stainless-steel (bottom)

In 6061-T6 aluminum specimen 2 (Al-2), five .0125" depth holes were drilled per drill-speed-increment in a series of thirty holes. This gives six speed increments, in descending order, at 40K, 30K, 20K, 14K, 8K, and 2K rpm.

The speed increments for stainless steel specimen 2 (SS-2) were chosen to be, in descending order, 40K, 20K, 10K, 8K, 6K, and 4K rpm.

Depth

While maintaining a speed of 40K rpm, the hole-depth/diameter ratio was varied from 0.2 to 0.6 to investigate any effect on measurement accuracy. Fifteen .0625" (0.318mm) diameter holes were drilled in both specimens Al-3 and SS-6. The fifteen-hole series began at one end of the bar and finished at the other. Holes 1 through 5 were produced at a depth of .0125"

(.318mm) (D/d = 0.2), 6-10 at .0250” (.635mm) (D/d = 0.4), and 11-15 at .0375” (.953mm) (D/d = 0.6). The procedure utilized for stainless steel specimen 6 (SS-6) was identical.

Bit-diameter

The final parameter variation investigated is that of drill-bit diameter. The drill-speed and D/d ratio were held constant at 40K rpm and 0.2 respectively. Specimens Al-3 and SS-6, also used for depth variation, will be flipped end on end and then used for the bit-variation tests. The first 5 holes from the depth variation test in each material (40K rpm, .0625” diameter, and .0125” depth) were used as a baseline comparison for the data from the other two bit sizes.

In aluminum specimen 3(Al-3), four holes (16-19) were drilled with a .03125” (0.79mm) diameter bit, at a depth of .0063” (0.159mm). Next, four holes (24-27) were drilled with a .125” (3.18mm) diameter bit at a depth of .025” (0.635mm).

In stainless steel specimen 6 (SS-6), eight holes (16-23) were drilled with a .03125” (0.79mm) diameter bit at depths of .0063” (0.159mm). Then, five holes (24-28) were drilled with a .125” (3.18mm) diameter bit at depths of .025” (0.635mm).

Results and Discussion

As-Received Stress Measurements

The aluminum exhibited a near-zero and near-uniform as-received surface stress throughout each of the twelve specimens. This is a very good result and exactly what we were looking for in specimen quality. Assuming that the stress distribution is relatively uniform across the longitudinal dimension, we will be able to attribute any change in stress to the parameter variation. Specimens Al-1, Al-2, and Al-3 were used for the parameter variation experiments (Fig. 6). The variation of the as-received stress state between each specimen is small (± 2ksi, ± 13.8 MPa) and will not be corrected for in the results. This follows for the stainless steel as well.

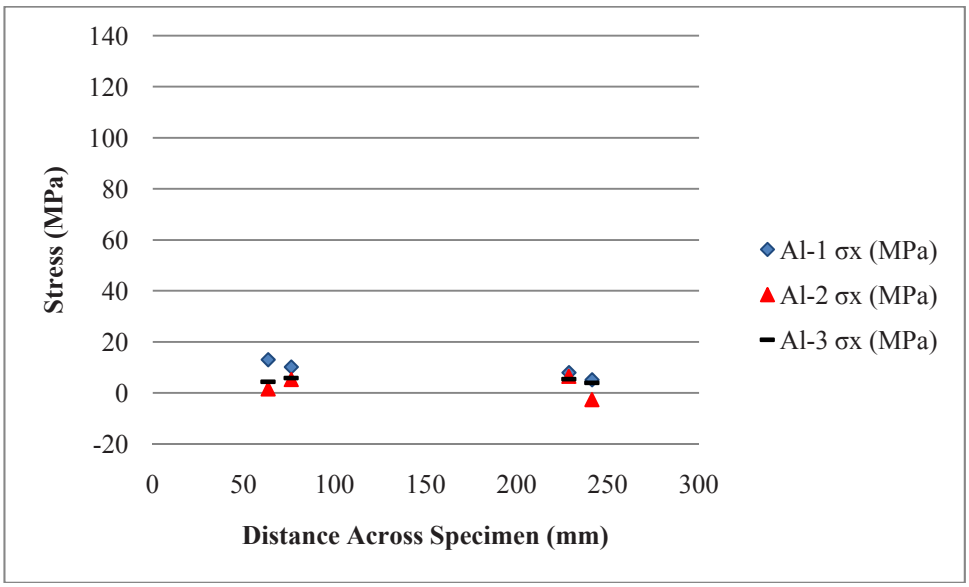

Fig. 6 As-received longitudinal residual stress distribution in aluminum specimens 1, 2, and 3

Unfortunately, the 304 stainless steel specimens were found to contain a large, non-uniform surface stress that would serve to corrupt any noticeable effects due to drilling-parameter variations (Fig. 7).

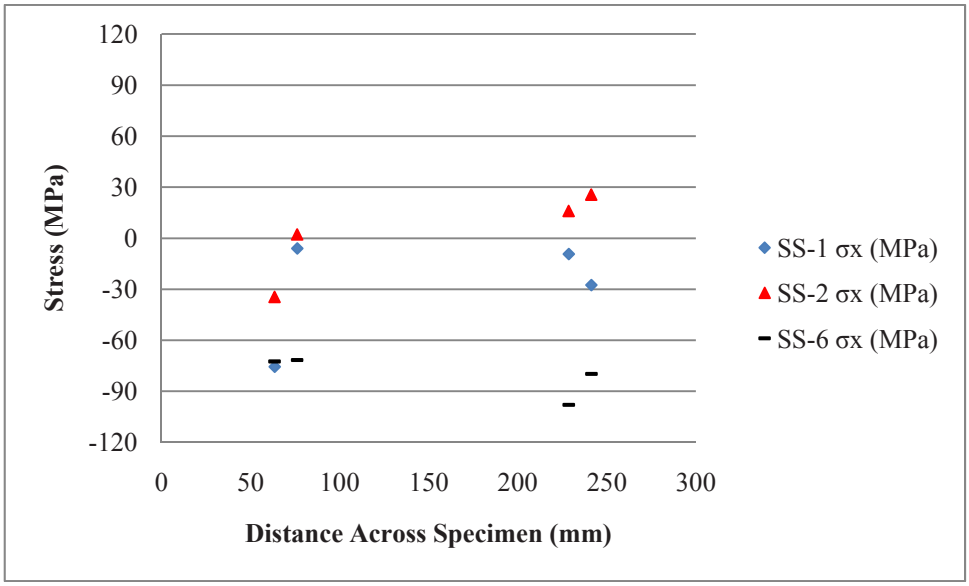

Fig. 7 As-received longitudinal residual stress distribution in stainless steel specimens 1, 2, and 6

Additionally, the A36 steel specimens had a small (< 0.01") layer of mill scale on the surface which flaked off during drilling and de-correlated the ESPI measurements, making the RS results inconsistent and inaccurate (Fig. 8).

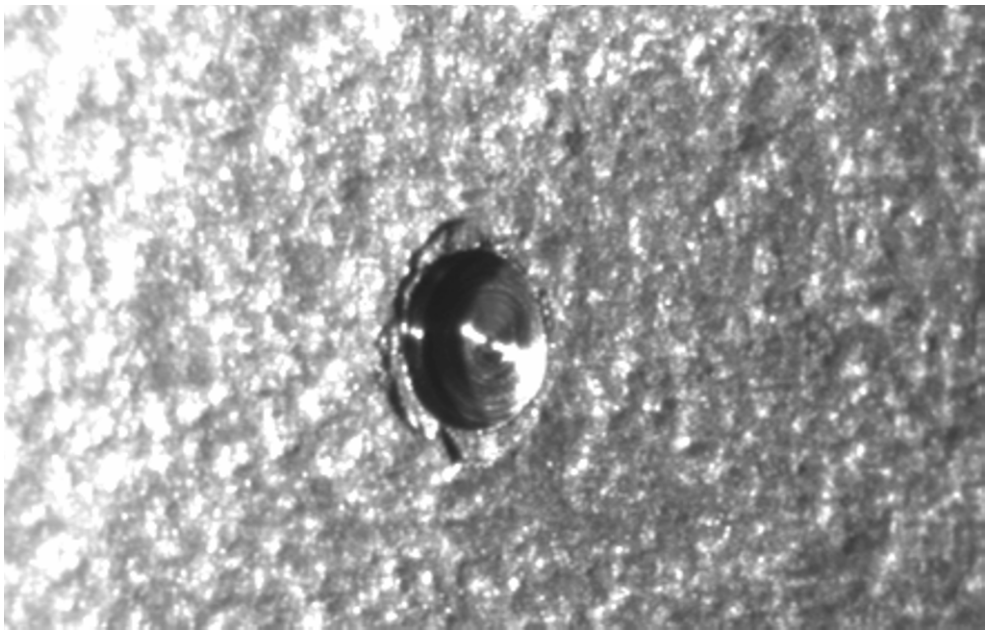

Fig. 8 Surface scale flaking off around perimeter of drilled holes

Annealing of Type 304 Stainless Steel

To remedy the large, non-uniform stress field in the 304 stainless steel, each of the specimens were fully annealed. The specimens were treated at 1050° C for 30 minutes, and then allowed to cool slowly in an argon-gas flow-chamber for 3 hours. Afterwards, four more holes were drilled in each of the stainless steel specimens, in the same pattern as the four prior holes, but on the opposite faces. The annealing was shown to both reduce the magnitude of surface stress in each of the specimens and increase uniformity of stress across the specimens' surfaces (Fig. 9). A thin layer of oxidation was left on the stainless steel specimens from the annealing procedure, but this did not affect the ESPI system's ability to image their surfaces.

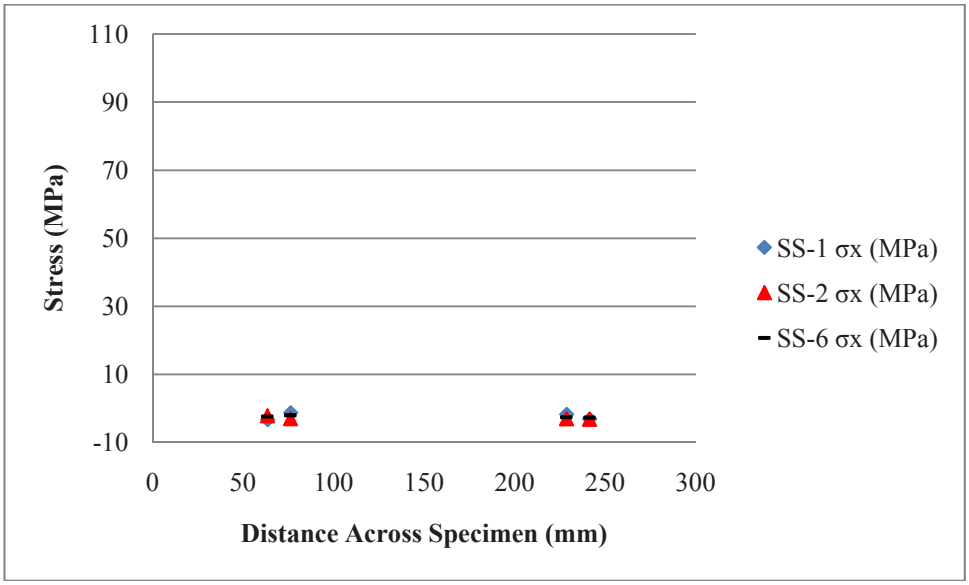

Fig. 9 Post-anneal longitudinal residual stress distribution in stainless steel specimens 1, 2, and 6

Shell-milling of A36 Steel

The plain carbon steel specimens were returned to the machine shop to remove the small layer of mill scale present at the surfaces. The faces of each specimen were shell-milled with a 1" carbide-tipped fly-cutter tool to a depth of .01". This reduced the nominal thickness of each carbon steel specimen from .5" to .48". After the milling procedure successfully removed the mill scale another attempt was made at characterizing the state of stress. To preserve the carbon steel specimens by preventing unnecessary drilling in specimens CS-3 through CS-6, the first bar was flipped to the untouched face and four holes were drilled in the same format as the opposite face (Holes 5-8). These measurements showed vast improvement in data quality due to the shell-milling, so the rest of the A36 steel specimens were tested for as-received residual stress. However, it was noticed later on that during the shell milling process, a pass was made with the carbide tool in the center of the longitudinal dimension in the transverse direction of each carbon steel specimen. To identify the effect of this change in milling direction, a set of 15 as-received stress measurements were taken in two A36 steel specimens across this zone. It was identified that for these specimens a large longitudinal stress gradient was present across the center 2" span of the longitudinal dimension (Fig. 10). Therefore, the A36 steel was chosen to be left out of the remaining tests.

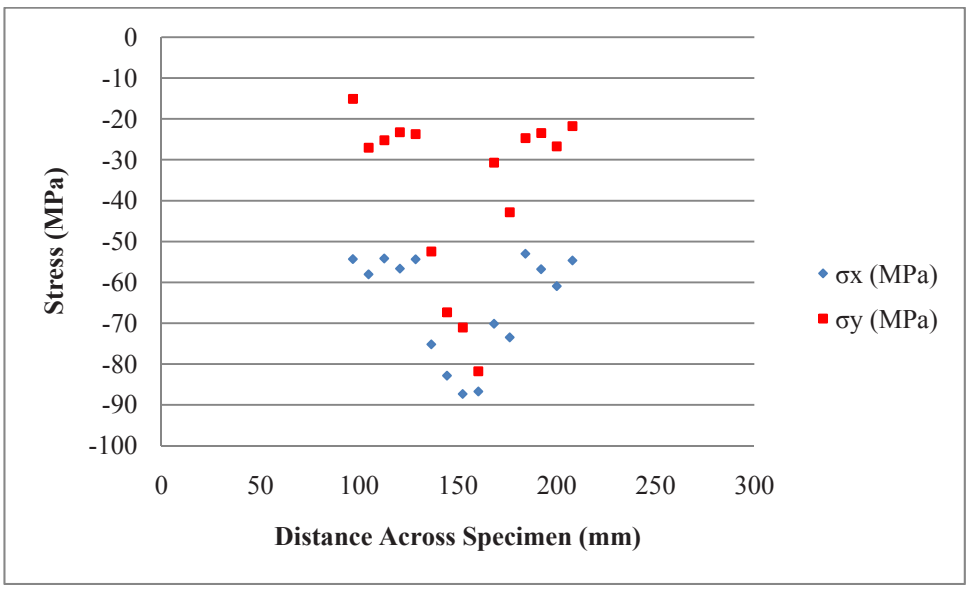

Fig. 10 Stress gradient across the longitudinal dimension of A36 steel specimen 3

Drill-Speed vs. Applied Stress

The aluminum samples were subjected to an applied surface stress of 20 ksi (138 MPa) (~48% of yield) corresponding to a .09167" (2.328mm) deflection in the 4-point bend fixture, while stress measurements were taken in various drill-speed intervals. An analysis of the data shows that reducing the drill-speed down to 2K rpm has no noticeable effect on the accuracy of the stress measurement in 6061-T651 aluminum (Figs. 11 and 12). The drilling of the holes gave little to no vibration or noise. The ejected chips at 40K rpm were so small and light that they momentarily hovered in the air. As the speed was decreased they became larger and fell to the table immediately after ejection. This was accompanied by a slight increase in noise during drilling. The measured stress values in aluminum specimen 1 are approximately 2ksi (13.8 MPa) higher than those in aluminum specimen 2 due to the higher as-received stress state. Visual comparison of holes produced in the aluminum at both 40K and 2K rpm show no noticeable difference. Figure 13 displays a hole of acceptable quality produced at 2K rpm.

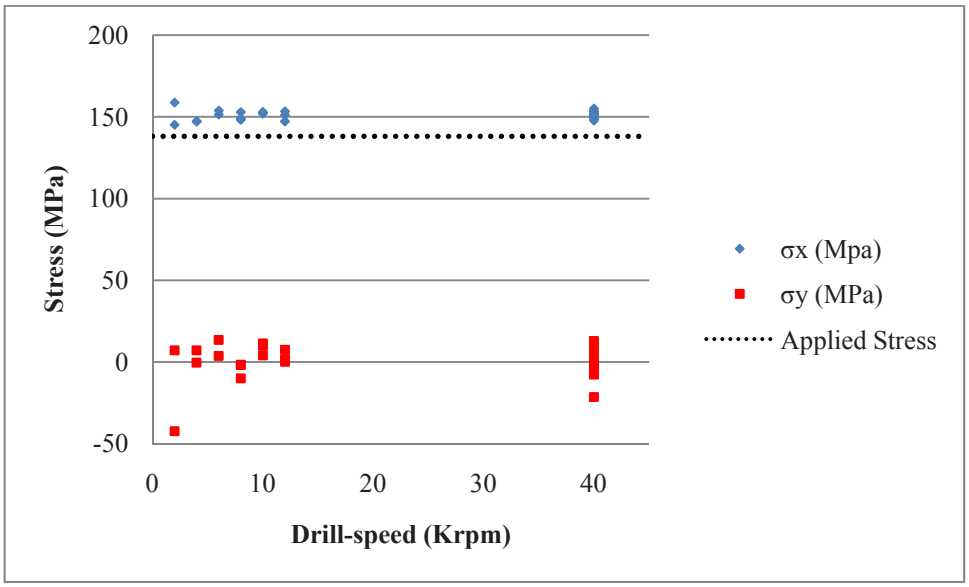

Fig. 11 Measured stress vs. drill-speed in aluminum specimen 1 with an applied surface stress of 138 MPa

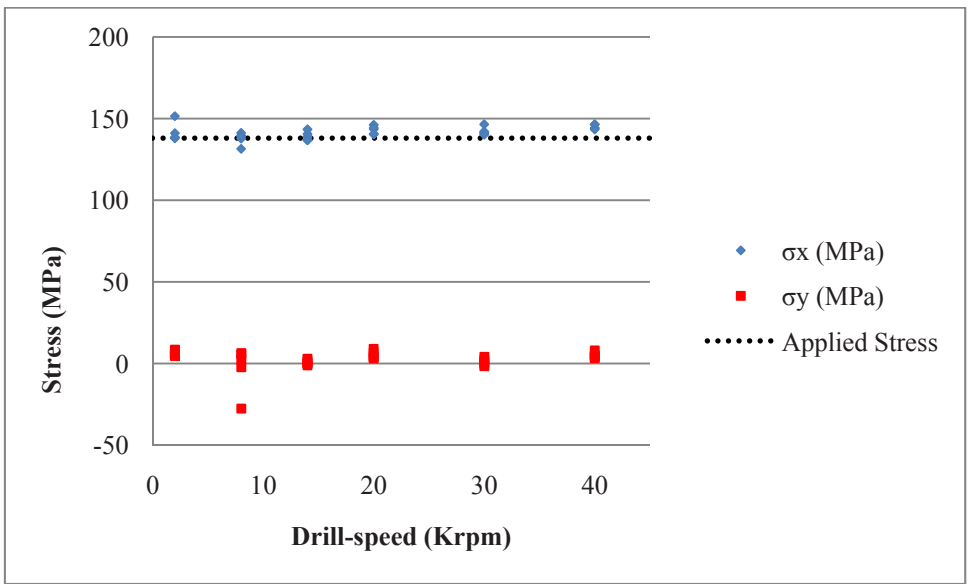

Fig. 12 Measured stress vs. drill-speed in aluminum specimen 2 with an applied surface stress of 138 MPa

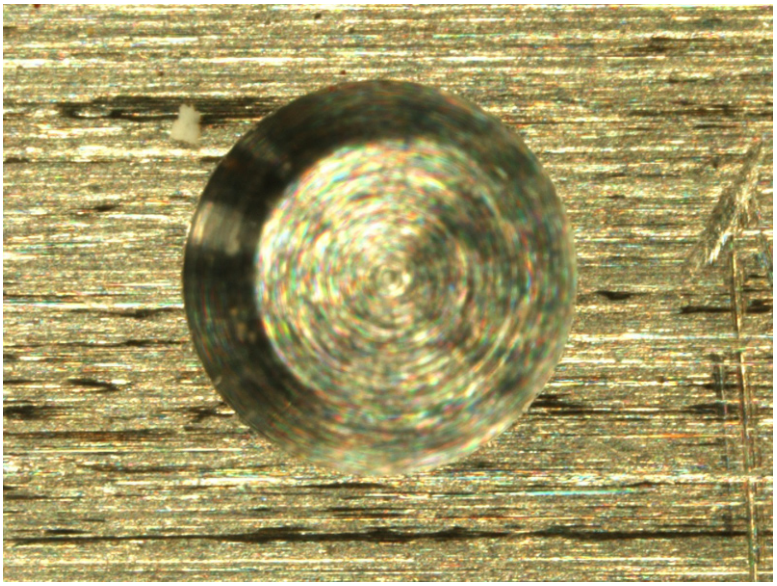

Fig. 13 Good quality hole drilled at 2K rpm in 6061-T651 aluminum specimen

The stainless steel specimens were elastically bent to achieve a centerline deflection of .02591" (0.6581mm), corresponding to a 15.6 ksi (107.6 MPa) (~40% of yield) surface stress. Stress measurement in stainless steel specimen 1showed a stress overestimation that began to occur at and below 6K rpm. Measurements were not obtainable at 2K rpm. Stainless steel is more difficult to machine and this trait manifested itself in the increased noise and vibration as the drill-speed was decreased. Chips ejected from the hole became longer with decreased drill-speed and the holes seemed to lose their quality. This was confirmed to be the case after visual inspection of the holes was performed with a high-resolution, Nikon digital stereoscope. Figure 14 displays holes drilled at speeds of 40K, 12K, 10K, 8K, 6K, 4K, and 2K rpm. The quality of the hole-perimeter begins to decrease at 8K rpm and the results follow suit beginning at 6K rpm. This decrease in hole quality has already been confirmed by Flaman in 1982, but only at 2K rpm. Seeing a side by side comparison of holes drilled at incrementally decreasing speeds gives a good idea of about where the quality begins to affect the results of a given measurement. The measured stress vs. drill-speed results in both stainless steel specimens are given in figures 15 and 16. The overestimation of the stress may very well be due to the reduced hole quality found at lower drill-speeds.

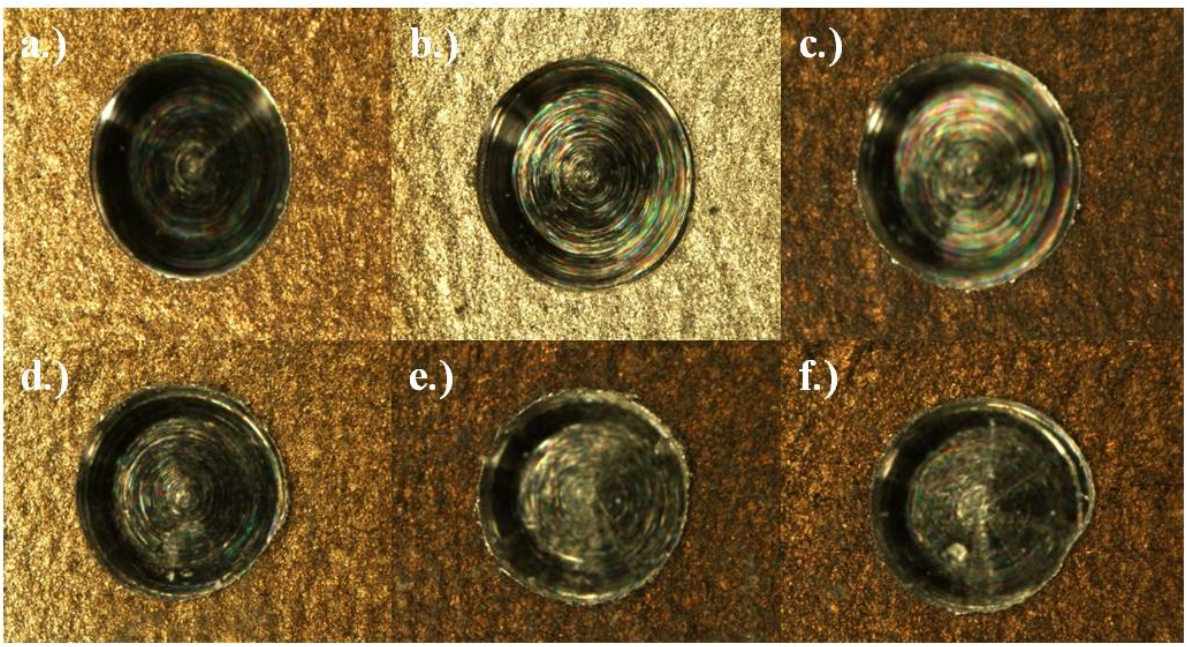

Fig. 14 Holes imaged with Nikon HR stereoscope at speeds of a.) 40K, b.) 10K, c.) 8K, d.) 6K, e.) 4K, and f.) 2K rpm

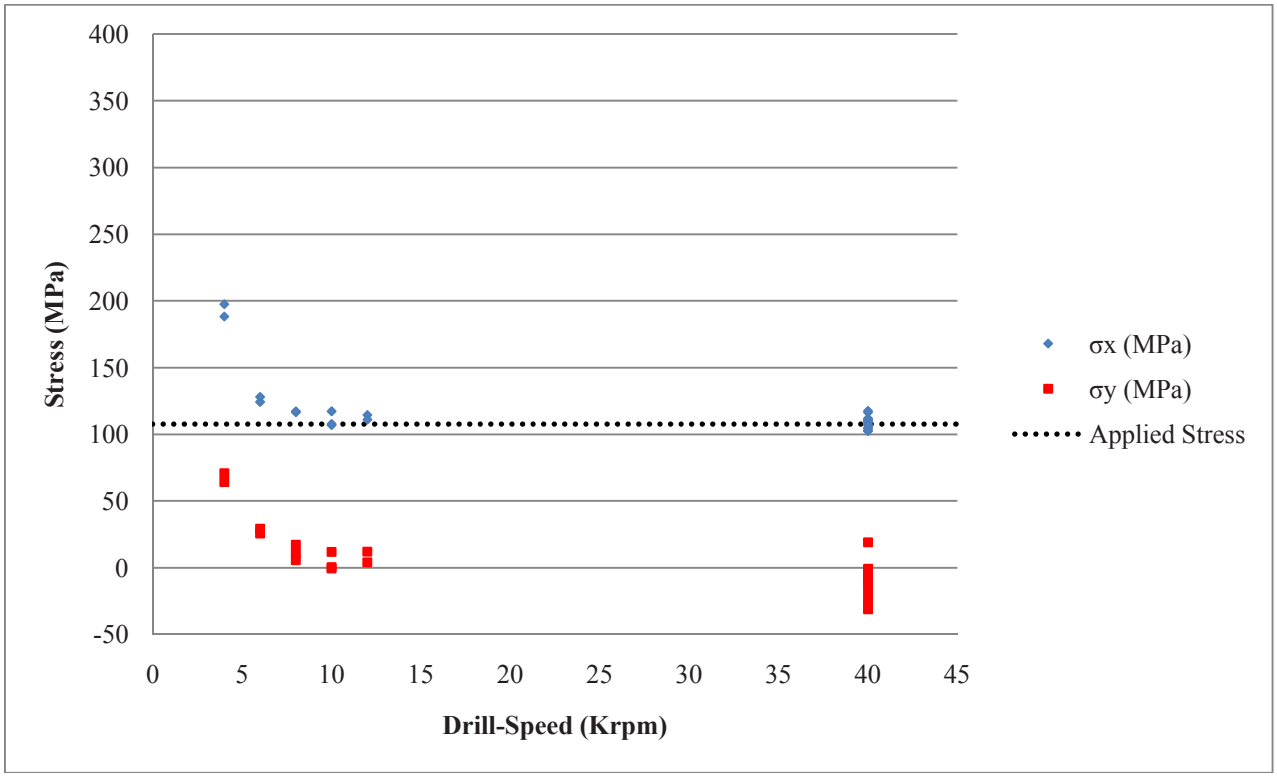

Fig. 15 Measured stress vs. drill-speed in stainless steel specimen 1 with an applied surface stress of 107.6 MPa

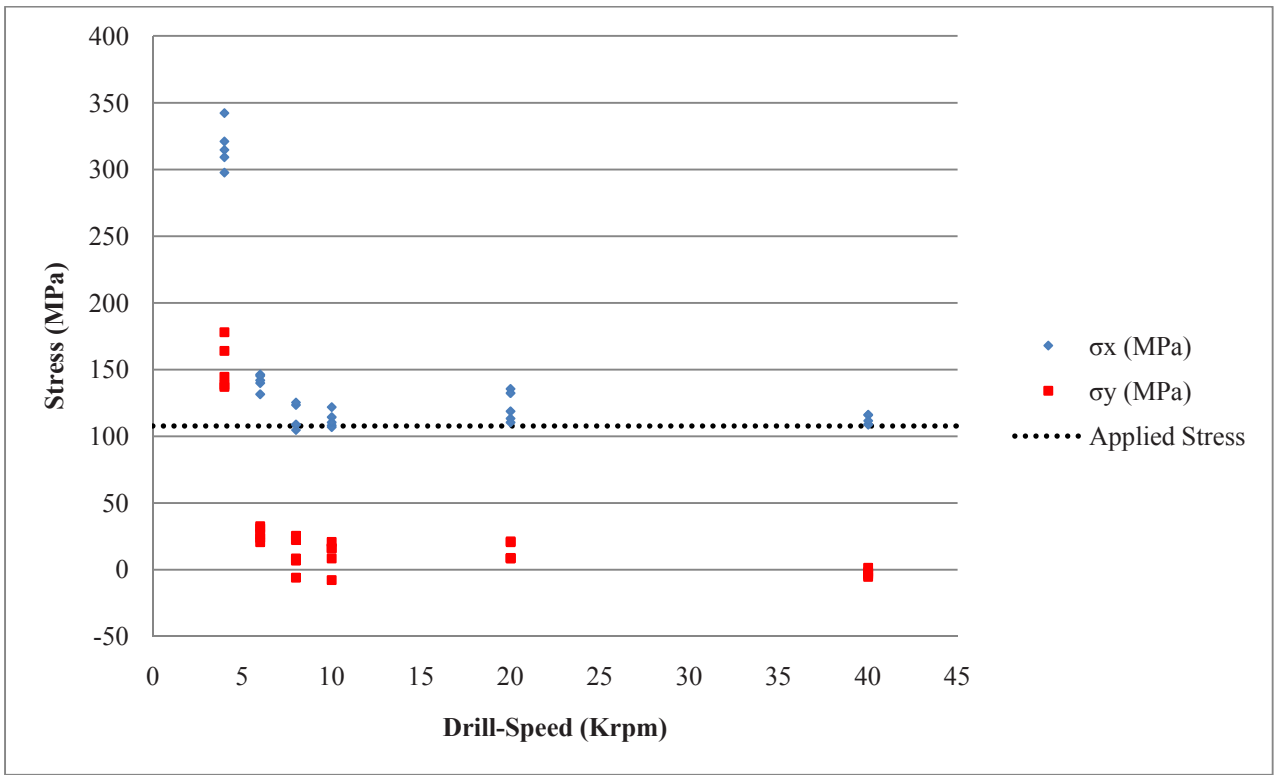

Fig. 16 Measured stress vs. drill-speed in stainless steel specimen 2 with an applied surface stress of 107.6 MPa

Depth/Diameter ratio vs. Applied Stress

This series of tests was performed to identify any adverse effects to accuracy caused by altering the hole-depth. Specimens were loaded to surface stresses of 20ksi and 15.6ksi for aluminum and stainless steel, respectively. While holding the drill-speed (40K rpm) and bit-diameter (.0625") constant, holes were drilled at depths of .0125" (.318mm), .025" (.635mm), and .0375" (.953mm), corresponding to D/d ratios of 0.2, 0.4, and 0.6 respectively.

Good results were achieved at all depths for both the aluminum and the stainless steel. The results for the depth variation are given in figures 17 and 18.

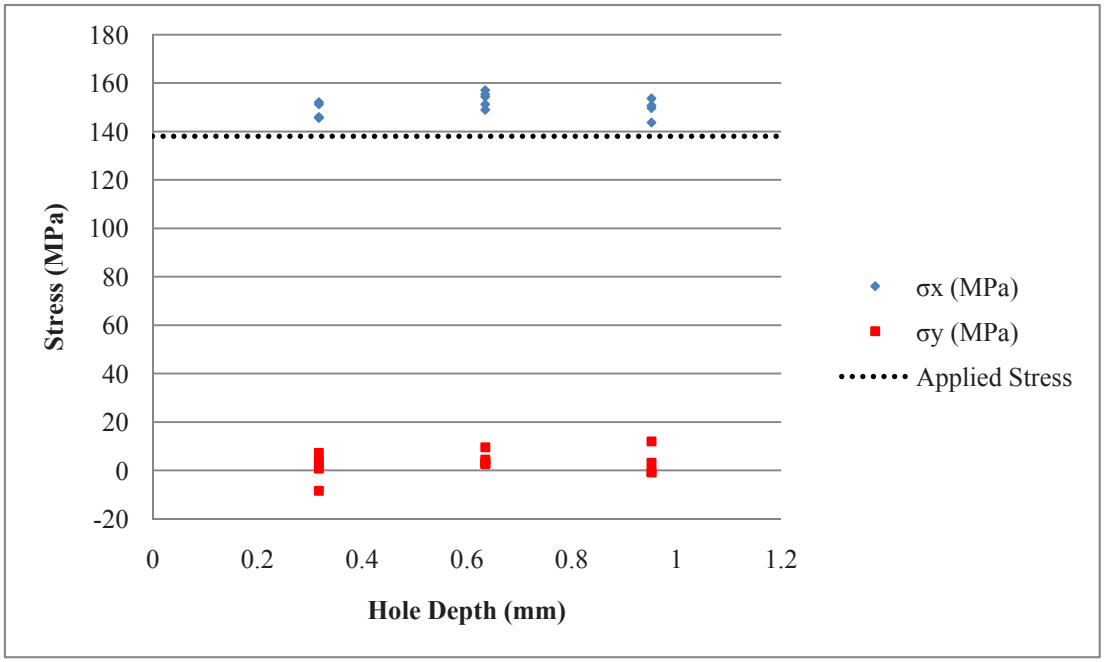

Fig. 17 Stress Measured stress vs. hole-depth in aluminum specimen 3 with an applied surface stress of 138 MPa

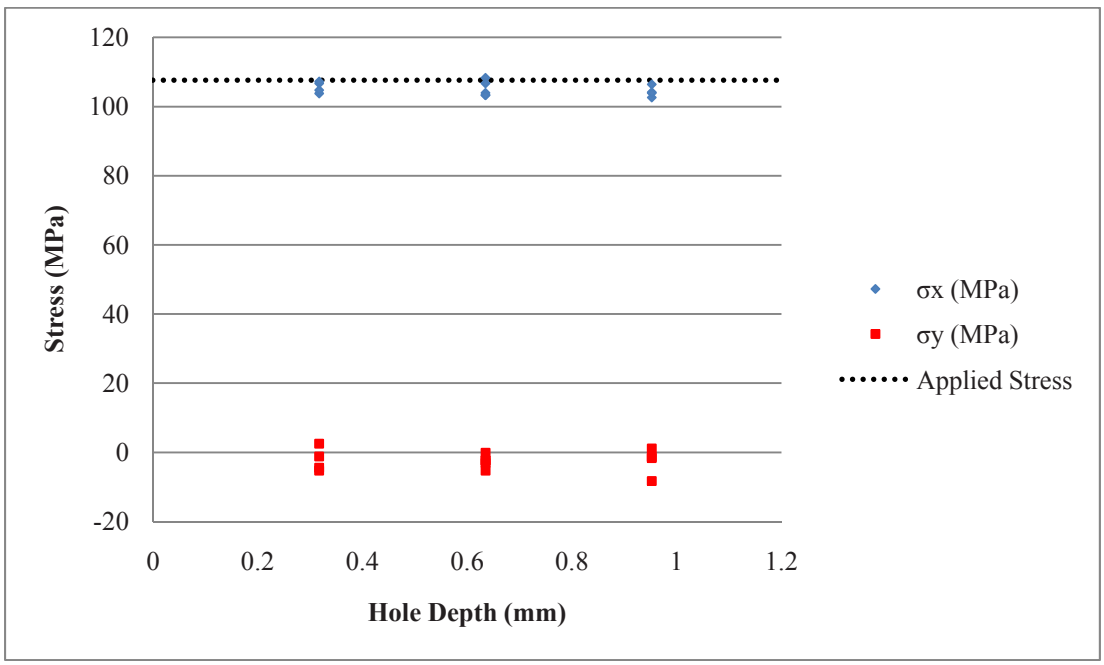

Fig. 18 Measured stress vs. hole-depth in stainless steel specimen 6 with an applied surface stress of 107.6 MPa

Drill-Bit Diameter vs. Applied Stress

Drill-bit diameter was varied while the D/d ratio and drill-speed was held constant at 0.2 and 40K rpm, respectively. Aluminum gives good results for all three bit sizes. One issue with the stainless steel exposed itself when drilling with the smaller, .03125" diameter bit. The results for this series of holes were very scattered ranging from 20 to 50ksi (138 to 345 MPa) for the longitudinal component and from 3 to 40ksi (20.7 to 276 MPa) for the transverse component. These results don't seem to be due to any operator error or data corruption. Since the aluminum results behaved well when a .03125" bit was used, this points to the problem being caused by a characteristic of the stainless steel. Since the elastic modulus is much higher in stainless steel, there may not be enough surface displacement when using the .03125" bit. The test results are given in figures 19 and 20.

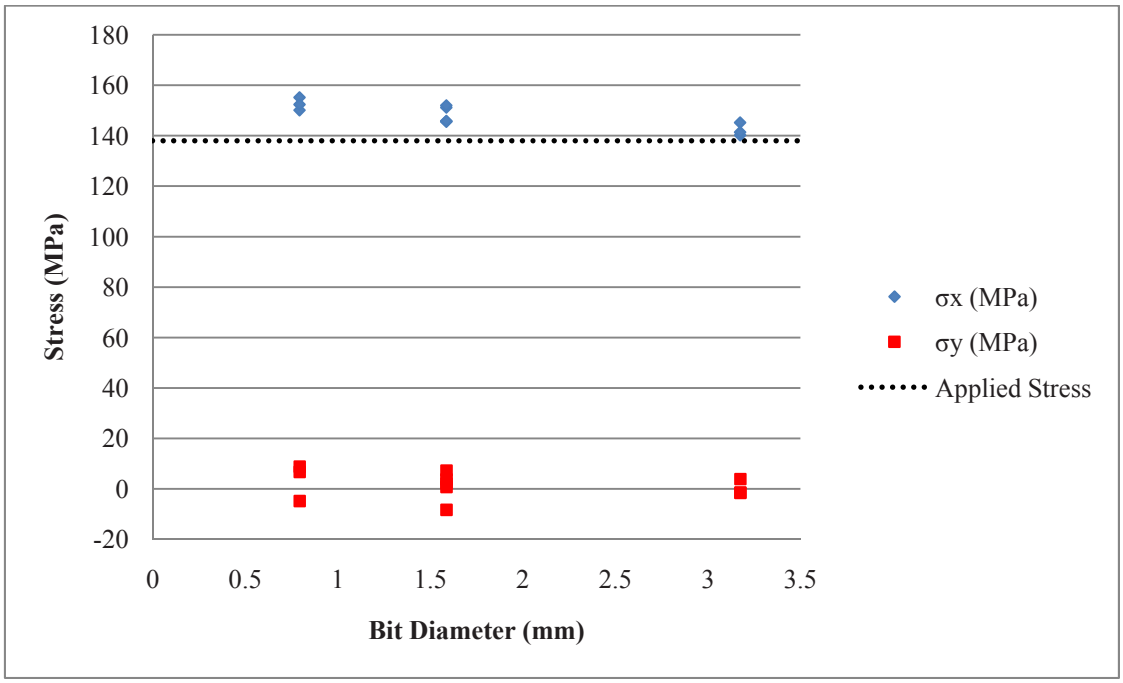

Fig. 19 Measured stress vs. bit-diameter in aluminum specimen 3 with an applied surface stress of 138 MPa

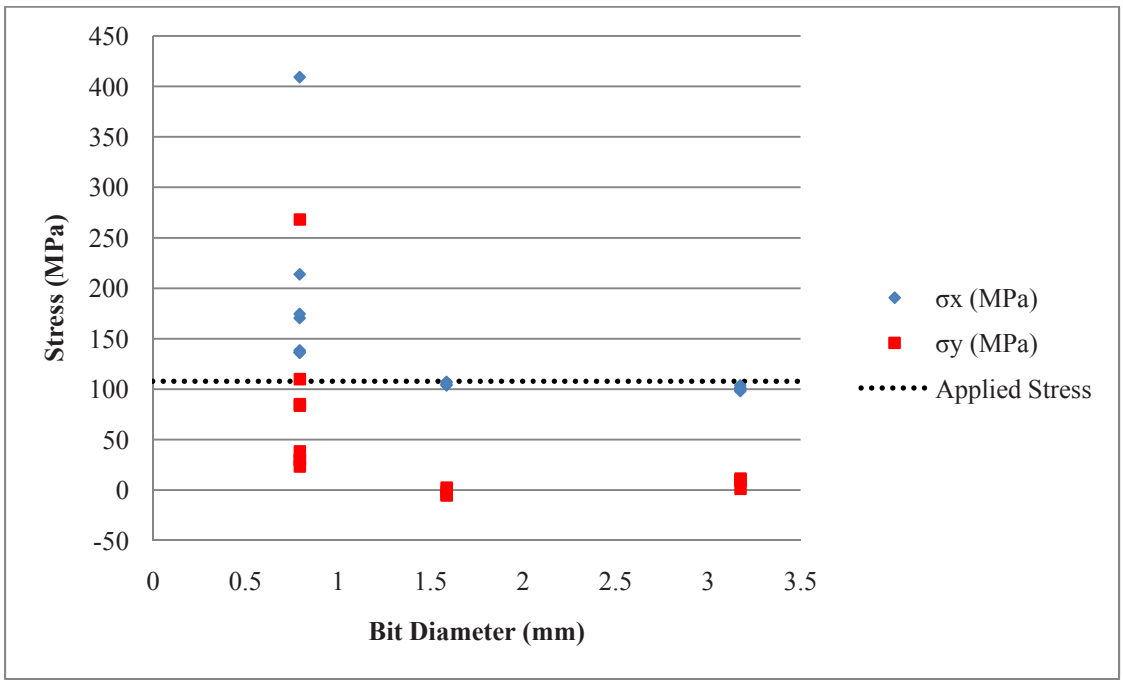

Fig. 20 Measured stress vs. bit-diameter in stainless steel specimen 6 with an applied surface stress of 107.6 MPa

Conclusions

Good results are possible at speeds between 2K and 40K rpm for 6061-T651 aluminum. Visual inspection shows no noticeable drop in hole-quality with reduction in drill-speed. Good measurements were obtained for all tests in the aluminum specimens with all measured values within ±3 ksi (±20.7 MPa) of the calculated values. This is within the error and uncertainty of the ESPI/hole-drilling instrument.

Good results are obtainable between speeds of 8K and 40K rpm for 304 stainless steel. While reducing drill-speed in the 304 stainless specimens, a noticeable decrease in machining quality was observed. These ill effects, including very intense noise and vibration along with reduction in hole-quality, may be the mechanism by which the stress is being overestimated in holes produced at speeds ≤ 6K rpm.

Good results in both 6061-T651 aluminum and 304 stainless steel are maintained even as hole-depth is varied.
No change in measurement quality is observed when vary bit-size in the 6061-T651 aluminum. Inaccurate and inconsistent measurements obtained in the stainless steel when using a .03125” diameter bit may be caused by a lack of deformation due to the high modulus combined with the reduction in removed material. This acts to decrease the signal to noise ratio and render the data useless.

Future Suggested Work

More testing should be conducted to see at exactly what drill-speed residual stress measurement accuracy and repeatability begins to decrease for a broader range of commonly used engineering materials. This will help aid the residual stress community in choosing the proper parameters and tools for a given material.

References

[1] Luong, H, M R Hill. "The Effects of Laser Peening and Shot Peening on High Cycle Fatigue in 7050-T7451 Aluminum Alloy." *Materials Science and Engineering A*, Vol. 527, 2010, pp. 699-707

[2] Campus, F. "Effects of Residual Stresses on the Behavior of Structures." *Residual Stresses in Metals and Metal Construction*, W.R. Osgood, Ed., Reinhold Publishing Co., 1954, pp.1-21

[3] Flaman, M T. "Brief Investigation of Induced Drilling Stresses in the Center-hole Method of Residual-stress Measurement." *Experimental Mechanics*, Vol. 22, No. 1, pp. 26-30, 1982

[4] Steinzig, M, E Ponslet. "Residual Stress Measurement Using the Hole Drilling Method and Laser Speckle Interferometry: Part I." *Experimental Techniques*, May/June 2003, pp. 43-46

[5] Ponslet, E, M Steinzig. "Residual Stress Measurement Using the Hole Drilling Method and Laser Speckle Interferometry Part II: Analysis Technique." *Experimental Techniques*, July/August 2003, pp. 1-5

[6] Ponslet, E, M Steinzig. "Residual Stress Measurement Using the Hole Drilling Method and Laser Speckle Interferometry Part III: Analysis Technique." *Experimental Techniques*, September/October 2003, pp. 45-48

[7] Steinzig, M, T Takahashi. "Residual Stress Measurement Using the Hole Drilling Method and Laser Speckle Interferometry Part IV: Measurement Accuracy." *Experimental Techniques*, November/December 2003, pp. 59-63

[8] Dong, P, P Cahill, Z Yang, X L Chen, and N J Mattel. "Plate Residual Stress Effects on Dimensional Accuracy in Thermal Cutting." *Journal of Ship Production*, Vol. 20, No. 4, pp. 245-255, November 2004

[9] Yerman, J A, W C Kroenke, W H Long. "Accuracy Evaluation of Residual Stress Measurements." *Proceedings of Fourth European Conference on Residual Stresses*, June 4-6, 1996

[10] ASTM Standard Test Method E837–08. "Determining Residual Stresses by the Hole-drilling Strain-gage Method." *American Society for Testing and Materials,* 2008.

[11] Lin, Y C, C P Chou. "Error Induced by Local Yielding around Hole in Hole Drilling Method for Measuring Residual Stress of Materials." *Materials Science Technology*, Vol. 11, pp. 600-604, 1995

RESIDUAL STRESS ON Ti6Al4V HYBRID AND LASER WELDED JOINTS

C. Casavola, C. Pappalettere, F. Tursi

Politecnico di Bari, Dipartimento di Ingegneria Meccanica e Gestionale, Viale Japigia, 182 – 70126 Bari, e-mail: casavola@poliba.it

ABSTRACT - Ti6Al4V alloy combines mechanical strength, deformability, excellent fatigue and corrosion resistance and high strength to weight ratio. Furthermore, the mechanical behavior remains excellent at high temperature. Such characteristics make this material attractive for numerous applications (structural, aerospace and naval) because of recent improvements in welding techniques (laser, hybrid laser/MIG) that allow realizing high quality titanium welded joints. However some problems related to the welding, as deteriorated material properties, residual stresses and distortions, need further investigations.

This paper presents a detailed study on residual stresses of Ti6Al4V butt plates welded by laser or hybrid laser/MIG process. Residual stresses were measured by hole drilling method using electrical strain gage rosettes bonded at different position, in order to evaluate magnitude and distribution of residual stresses along the cord. Residual stresses curves obtained for each type of joint and each welding technique are presented and discussed in terms of transversal residual stresses. Residual stresses were also measured at surface by means of X-ray diffractometer.

The aim of this work is to present experimental data related to welding processes in order to confirm the validity of currently procedures or improve them.

INTRODUCTION

Ti6Al4V is a biocompatible material that can be used in different applications such as chemical, aerospace, naval and biomedical engineering.

Welding technology is widely used to assemble metal parts because of high productivity and flexibility [1]. One of the concerns associated with welding Ti-based alloys results from their poor thermal conductivity, which leads to the creation of a steep thermal gradient across the weld region, and hence results in high residual stresses. Ti-based alloys are also susceptible to the formation of porosity and inclusions (e.g. hard alpha) when welded in the presence of hydrogen, oxygen, nitrogen, or carbon contamination, which results in reduced mechanical properties. Accordingly, in fusion welding processes, argon shielding is customarily used to avoid any contamination [2]. Because of its high level of specific power and the limited area involved, laser technology appears to be a promising solution. The laser beam sources of the new generation are capable of producing deep and narrow seams. However, the laser welding process leads to a non-uniform temperature distribution and associated thermal strains, which generate residual stresses due to melting and subsequent cooling of the weld and surrounding material [3].

Steen [4] showed that an addition of electric arc to the laser beam used for welding and cutting could decrease the needed power of laser with respect to the case when only laser is used for welding. This technique combines the best characteristics of both laser and arc welding processes, acting simultaneously in the same process zone [5]. Subsequently, the laser-based hybrid welding technology development was initiated not only at the academic level but also at industrial level, from shipbuilding to automotive production. The advantages of the hybrid welding technique compared to pure laser welding or arc-welding are well known and include an increase in (a) the welding speed, (b) the weldable material thickness, (c) the gap bridging ability, and (d) the welding process stability and efficiency [6]. In particular, laser-arc hybrid welding offers many advantages for heavy industrial applications involving thick-walled materials as it enables full penetration weld of thick plates without the need of multiple passes and at that reduces welding after works such as cutting for adjustment and

T. Proulx (ed.), *Engineering Applications of Residual Stress, Volume 8*, Conference Proceedings of the Society for Experimental Mechanics Series 999, DOI 10.1007/978-1-4614-0225-1_13, © The Society for Experimental Mechanics, Inc. 2011

fairing at the assembly stage. Hybrid welding improves productivity by two to four times as compared to the conventional arc welding [5]. In addition, in the fusion zone of hybrid laser-arc welding, equiaxed grains exist, whose sizes are smaller than that obtained from arc welding but larger than those from laser beam welding. Welding process unavoidably involves a stage of residual stress in the welded structure that could lead to some problems in terms of dimensional stability and structural integrity. Because of the variety of factors involved in welded parts, it is very difficult to predict and control residual stresses caused by welding. Tensile stresses, such as welding residual stresses, may have a significant effect on corrosion, fracture resistance and fatigue performance, so that a reduction of these stresses is generally desirable [7]. As the welded part of a component is often the least resistant to fatigue, stress-corrosion and fracture, numerous experimental methods have been developed and applied to research in the field of residual stresses caused by welding [3].
In view of these aspects, the aim of this research is relating residual stresses to welding technique and type of joint. In this paper, we report experimental hole drilling method measurements on Ti6Al4V butt plates produced by means of laser or hybrid laser/MIG welding process. Electrical strain-gage rosettes have been bonded at different position, in order to evaluate magnitude and distribution of residual stresses along the cord. The focus is on the value of residual stresses normal to the weld cord. Residual stresses were also measured at surface by means of X-ray diffractometer in order to discuss these concentrated values of stress with data obtained by HDM.

MATERIALS AND WELDED JOINTS PREPARATION

Titanium alloys can be classified as α alloys (hexagonal crystal structure), β alloys (body centered cubic structure) and α–β alloys. Alpha alloys (titanium grade 2) are characterized by satisfactory strength, toughness and weldability, but are less forgeable than β alloys. Properties of α–β alloys (titanium grade 5) can be controlled through heat treatment. Ti6Al4V is a α–β alloy where aluminum is a α – stabilizing element and vanadium is a β – stabilizing element. The final microstructure and mechanical properties depend on the initial temperature of heat treatment and on cooling time [8]. Table 1 reports the chemical composition of tested material. Table 2 summarizes some mechanical and physical properties of titanium with respect to comparable steel, as indicated in data sheet of manufacturers (tensile ultimate strength σ_u, yield strength σ_y, modulus of Young E). Density, coefficient of thermal linear expansion (CTE) and thermal conductivity in titanium are quite low with respect to steel [9].
Four types of welded plates have been considered as indicated in Table 3.

	Ti	N	C	Fe	O	Al	Sn	Zr	Mo	V
Ti6Al4V	90	0.05	0.1	0.3	0.2	6	-	-	-	4

Table 1 - Chemical composition

	σ_y [MPa]	σ_u [MPa]	E [GPa]	Hardness Vickers	Density [g/cc]	CTE [µm/m-.°C]	Thermal conductivity [W/m.K]
Ti6Al4V	1100	1200	114	396	4.43	8.6	6.7
AISI 4340	862	1282	205	384	7.85	12	44.5

Table 2 - Mechanical and physical properties

	Thickness [mm]	Length x Width L[mm] x W[mm]	Welding technique	Type of joint
Plate 1 (Ti236)	3	400 x 450	Hybrid	butt
Plate 2 (Ti239)	3	400 x 450	Hybrid	butt
Plate 3 (Ti233)	3	400 x 450	Laser	butt
Plate 4 [9]	3	400 x 380	Laser	butt

Table 3 - Welded plates tested

Before welding, titanium plates are subject to heat treatments and subsequent cooling in air. Titanium plates are accurately lapped and edges are chemically etched. Then, both laser welding (LBW) and hybrid laser/MIG (HYB) are executed without gap between the welded plates. Nd–YAG laser and CO2 laser are utilized respectively. During welding operations, all plates are constrained in 3 points in order to avoid the opening of the junction. Weld traces are then crossed out by the next welding passage. Both in HYB and LBW, the molten welded metal area has been shielded with a specific device and inert gas until 700°C in order to avoid contamination from the air and absorption of impurities.

Welding type	**LASER**
Equipment	Laser ND-YAG -HAAS HL 2006D
Focal lens [mm]	f=100
Device for Gas for plasma suppression	standard nozzle f=6mm; special nozzle: Scarpeta TINEA
Gas for plasma suppression	Elio 4.8, delivery capacity 25 Nl/min
Gas for protection	Ar 5.0
Edge preparation	right (gap 0)
Power of laser beam [W]	1600
Feed velocity [m/min]	3

Table 4 – Process parameters of the laser welded plates

Welding type	**HYBRID (LASER+MIG)**
Laser CO_2 power [W]	3000
MIG power [W]	7200
Distance laser-MIG [mm]	0
Welding velocity [m/min]	2
Wire velocity [m/min]	4
Gas for plasma suppression	He
Gas for protection	Ar

Table 5 – Process parameters of the hybrid laser –MIG welded plates

TEST METHOD

The Hole Drilling Method (HDM) is the most widely used technique for residual stress measurement. The principle involves introduction of a small hole (1.8 mm diameter and up to about 1.0 mm depth) at the location where residual stress is measured. Due to drilling of the hole, residual stresses are relieved and the corresponding strains on the surface are measured using strain gauges bonded around the hole. From these measured strains, residual stresses are calculated using appropriate calibration constants derived for the particular type of strain gauge rosette used. The procedure for residual stress measurement using hole drilling is described in ASTM standards with designation E837-08 [10]. In most practical cases, the residual stresses are not uniform with depth. The incremental hole drilling method is an improvement on the basic hole drilling method, which involves carrying out the drilling in a series of small steps, which improves the versatility of the method and enables stress profiles and gradients to be measured. A high-speed air turbine and carbide cutters are used to drill the hole without introducing any further machining stresses and thereby modifying the existing stress system. The strain data at pre-determined depths are precisely acquired. Different stress calculation methods are used to arrive at the residual stress system from the measured strains. The major techniques in vogue are uniform stress, power series and integral methods. In any case, a meticulous measurement practice is crucial to obtaining good quality strain data and the application of the correct analysis method to the relieved strain data can provide accurate assessment of the residual stress field. In this case, in order to consider the variation of the residual stresses measured through the thickness, the power series method has been used.

The X-ray diffractometer method (XRD) is the most common non-destructive method to determine the surface residual stress in crystalline materials. XRD is accurate, but it is limited by the fact that only information is obtained about a relatively thin surface layer.

The XRD-sin2ψ technique was developed from the theories of crystallography and solid mechanics [11]. Given the limited penetration of X-rays in solid surfaces, what the XRD-sin2ψ technique measures is the surface residual stress in a depth of up to a few micrometers.
The XRD-sin2ψ stress measurement starts from XRD scans at a series of fixed incident angles and over a predefined diffraction angle. In each obtained scan, the chosen diffraction peak position has to be accurately determined, i.e. the 2θ value has to be measured from a very broad and sometimes irregularly shaped peak (Fig. 1). The obtained 2θ values are then used to perform the linear regression in order to obtain the slope and intercept values to be used for the stress calculation.
The accuracy of the XRD-sin2ψ residual stress measurement depends on the minimization of various measurement errors derived from several sources, e.g. the material to be measured, the instrument setup and the data processing. In terms of the tested materials, it is often the case that the surfaces to be measured are not ideally flat, may contain coarse crystalline grains, strong texture, high density of lattice defects and an in-depth stress gradient. Consequently, the diffraction peaks obtained in such materials have different scales of broadening, roughening and asymmetry.
Figure 3 shows the in-plane stress σ_ϕ with respect to the two principal stress components σ_1 and σ_2. When a X-ray beam hits the sample surface at an incident angle Ω, those grains, with their (hkl) lattice planes meeting the Bragg diffraction condition and having an off-axis angle ψ with respect to the sample surface normal, emit a diffraction X-ray beam at a diffraction angle 2θ. Then the d-spacing $d_{\phi\psi}$ of the (hkl) lattice plane is measured. The principal formula for the XRD-sin2ψ stress measurement can be written as:

$$(d_{\phi\psi}-d_0)/d_0=(1+\nu)/E \cdot \sigma_\phi \cdot \sin^2(\psi) - \nu/E \cdot (\sigma_1 + \sigma_2) \quad (1)$$

where d_0 is the unstressed lattice parameter, E and ν are the Young's modulus and the Poisson's ratio normal to the (hkl) orientation of the material respectively, and ψ is the angle between the diffraction vector and the normal to the surface.
Assuming $\sigma_\phi=\sigma_1=\sigma_2$ when the in-plane stress σ_ϕ is independent of the orientation (for a state of equi-biaxial stress) the equation describing the stress dependence of the lattice parameter, $d_{\phi\psi}$ is related by the equation:

$$d_{\phi\psi} =[(1 + \nu)/E \cdot \sin^2(\psi) - 2\nu/E] \cdot \sigma \cdot d_0 + d_0 \quad (2)$$

Then Eq. (2) can be treated as a linear function Y=a·X+b where:

$$Y = d_{\phi\psi} = \lambda/(2\cdot\sin(\theta)); \quad X = [(1 + \nu)/E \cdot \sin^2(\psi) - 2\nu/E] \quad (3)$$

Therefore after making a series of XRD scans covering a known Bragg 2θ at fixed glancing angles Ω_i (for i=1, 2, 3, etc.), the Bragg diffraction half angle θi can be measured in each diffraction peak and the associated off-axis angle ψ_i is calculated according to the relation $\psi_i=\theta_i - \Omega_i$. The obtained θ_i and ψ_i are subsequently used to calculate the data group {Xi, Yi} according to Eq. (3), from which a linear regression processing of Eq. (2) is used to obtain the value of the constants a and b. Finally the in-plane stress σ, as well as the strain free lattice d-spacing d_0, can be obtained from the relations d_0=b and σ=a/d0 respectively.

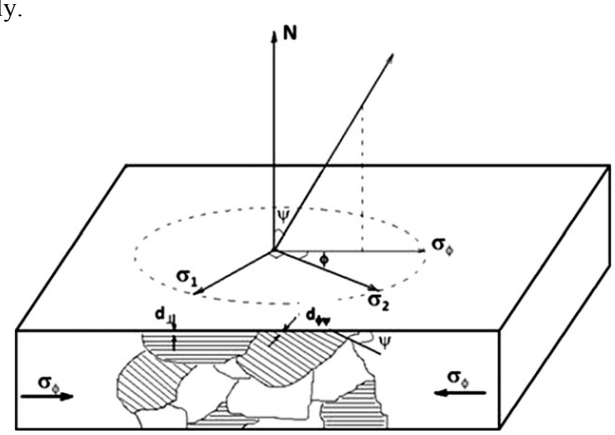

Fig. 1 - A schematic diagram showing the set-up of the XRD-sin2ψ in-plane stress measurement [12]

The $\sin^2\psi$ method of XRD has utilized to measure the residual stress of welded plates by XSTRESS 3000 equipment [11], in which TiKα radiation (λ = 2.2909 Å) is used as X-ray source. Fig. 2 shows schematic of X-ray diffractometer.

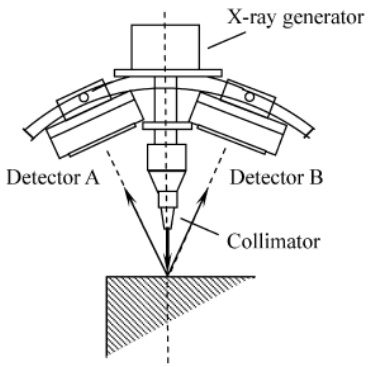

Fig. 2 - Schematic of X-ray diffractometer.

Residual stress measurement has been performed on the transversal direction to the weld cord of butt welded plates. The collimator with 1 mm illuminated spot size has been used and the exposure time has been set at 90 sec to ensure the adequate intensity. The operation voltage and current were 30 kV and 6.7 mA. The 110-diffraction of titanium with the diffraction angle of 137.4° has been analyzed. During the stress measurement, ψ of 0°, 19.3°, 27.9° and 35° have been selected to plot d–$\sin^2$ ψ curves on both positive and negative ψ range. Considering the texture effect on the stress measurement, a ψ oscillation with ±3° has been used during the measurement. Indeed, to give reliable values of residual stress, measurements have been replicated on the same points.

The experimental investigation is focused on residual stress measurements. Residual stress and distortion are unavoidable in welding and their effects on global strength of structures cannot be disregarded [13]. Welded plates studied in this work present a very slight misalignment: about 0.03° for LBW and about 0.33° for HYB. The extension of heat-affected zone could give indication on the severity of welding thermal cycle. Typically, LBW has a very narrow heat affected zone (0.5 mm for plates 3 and 4) with respect to HYB plates (2 mm for plates 1 and 2) [9].

Geometry of welded plates and locations of residual stress measurements are shown in figures 3-4.

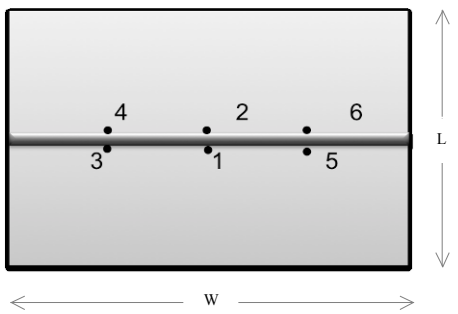

Fig. 3 - Geometry of welded plates and location of drilled holes in HDM

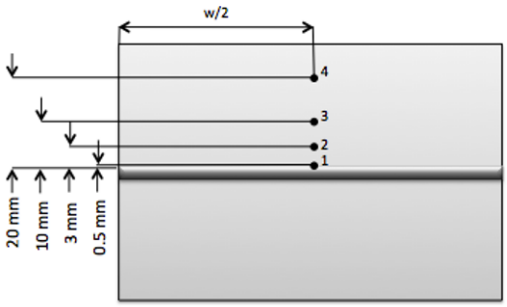

Fig. 4 – Geometry of welded plates and location of XRD measurements

Test plan is summarized in Table 6: residual stress on both hybrid and laser welded plates are measured by means of HDM and XRD. Location of measurement points is indicated in fig. 3 and 4. Strain gage rosettes are bonded very close to the weld cord, with the hole at 1 mm from the weld line.

	Welding technique	Residual stress measurement	Location of residual stress measurement
Plate 1 (Ti236)	Hybrid	HDM	As indicated in Fig. 3
Plate 2 (Ti239)	Hybrid	XRD	As indicated in Fig. 4
Plate 3 (Ti233)	Laser	XRD	As indicated in Fig. 4
Plate 4 [9]	Laser	HDM	As indicated in Fig. 3

Table 6 – Test plan

EXPERIMENTAL RESULTS

Figures 5 and 6 show calculated residual stress in the transversal directions with respect to the weld cord. Stresses are plotted against the hole depth h. Plotted residual stresses are calculated by power series method. Some "strange" values have been measured at the first drilling steps probably produced during the surface preparation for strain gage bonding. Experimental data show a more regular residual stress trend at higher depth. Residual stress value in the direction normal to the cord and at location 1 (same location of XRD measurements) is about 90 MPa (0.8 mm depth) in case of laser plates and 15 MPa in case of hybrid ones.

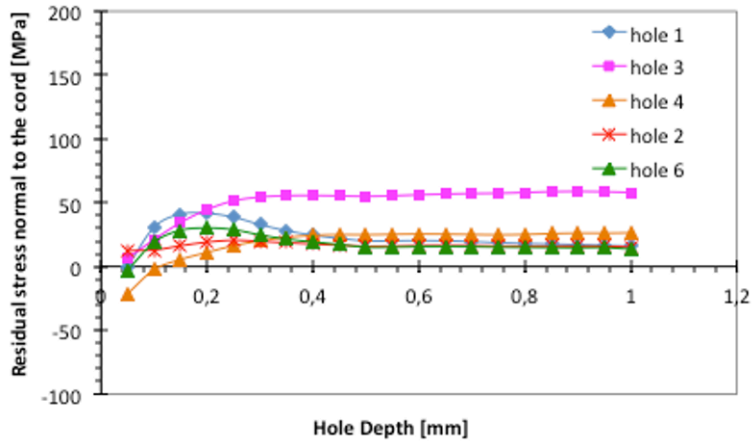

Fig. 5 – Calculated residual stresses transversal to the cord on hybrid welded plate (residual stress on location 1 and at 0.8 mm depth is about 15 MPa)

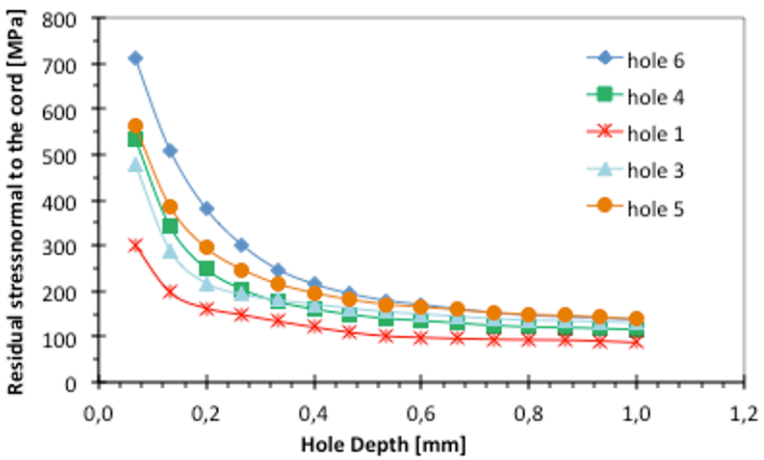

Fig. 6 – Calculated residual stresses transversal to the cord on laser welded plate (residual stress on location 1 and at 0.8 mm depth is about 90 MPa)

Residual stress measured by means of HDM gives the average stress related to the area (the hole diameter range between 1.8 and 2.0 mm) where the material is drilled. Moreover, this value of stress is usually read at a hole depth of about 1 mm, that is where the strain gage signal is steady and stress values are stabilized.

Figure 7 and 8 show values of residual stress normal to the weld cord in the case of XRD measurements. In this case, locations of measurements have been chosen at progressive distance from the weld cord. XRD values are commonly referred to the surface of specimen and indicate local concentrated residual stress.

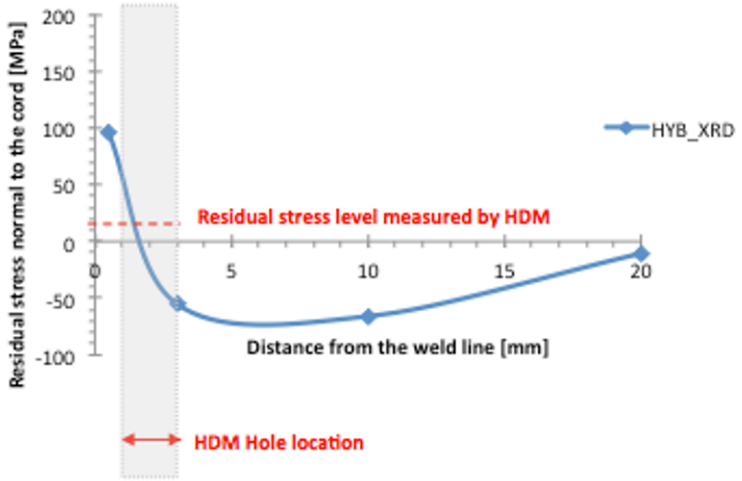

Fig. 7 – Residual stress values measured by means of XRD in different position on the HYB plate

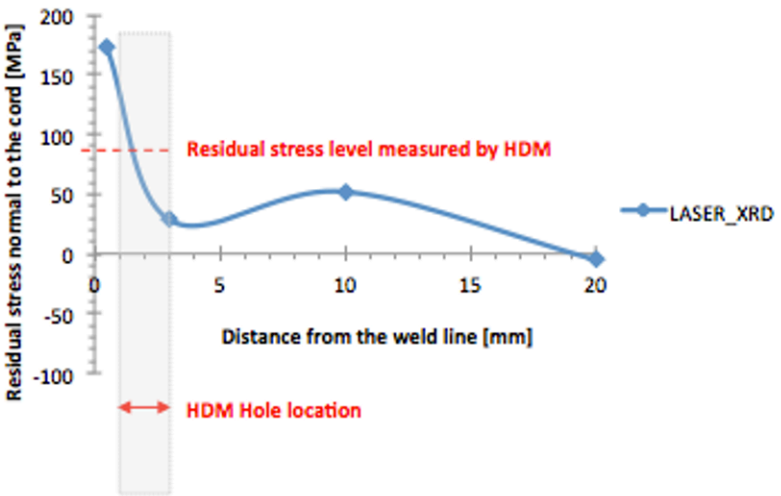

Fig. 8 - Residual stress values measured by means of XRD in different position on the LASER plate

Experimental data show that residual stresses on laser welded plates are higher than on hybrid plates, both in case of XRD and HDM measurements, that is both on surface of specimen and in depth. This result should be correlated to the extension of heat affected zone: it seems that hybrid plates, having a larger heat affected zone and larger distortions, allow thermal stresses to distribute on a larger area, so reducing the stress level restrained in the material at the end of welding thermal process.
The area corresponding to the hole drilled by HDM is marked in Fig. 7-8. It can be observed that the XRD measurements no. 1 and 2 are localized at 0.5 and 3 mm from the weld line, while HDM hole cover the area between 1 and 3 mm from the cord, due to the inherent limitation laying in the size of

strain gage rosette. Residual stress levels given by HDM, corresponding to 0.8 mm depth, seem to be an intermediate value.

CONCLUSION

Titanium alloy Ti6Al4V can be used in different fields ranging from chemical, aerospace, naval and biomedical engineering. Recently, welding technology has been improved and it is possible to assemble titanium parts. However, an important drawback associated with welding of Ti-based alloys results from their poor thermal conductivity, which leads to the generation of a steep thermal gradient across the weld region, and hence results in high residual stresses. Two different welding techniques have been considered in this work: laser and hybrid (laser/MIG).
Residual stress measurements have been executed by means of hole drilling method and X-ray diffractometer, which gives a concentrated localized value of stress. Measured points are located along the weld cord and along a direction transversal to the cord.
Analysis of residual stresses measured values suggests the following considerations:

- HDM measurements show that residual stress value in the direction normal to the cord, in the center of the welded plate (location 1) is about 90 MPa (0.8 mm depth) in case of laser plates and 15 MPa in case of hybrid ones.
- XRD measurements confirmed that residual stresses are higher in the case of laser welded plates (175 MPa with respect of 95 MPa of hybrid plates at 0.5 mm from the weld line).
- These different magnitude of residual stresses should be correlated to the different level of energy involved during welding process, that affects also the extension of heat affected zone and distortions of welded plates.

REFERENCES

[1] Denga D., Kiyoshima S., *Numerical simulation of residual stresses induced by laser beam welding in a SUS316 stainless steel pipe with considering initial residual stress influences*, Elsevier, Nuclear Engineering and Design 240, pp. 688–696, 2010.
[2] Romero J., Attallah M. M., Preuss M., Karadge M., Bray S. E., *Effect of the forging pressure on the microstructure and residual stress development in Ti–6Al–4V linear friction welds*, Elsevier, Acta Materialia 57, pp. 5582–5592, 2009.
[3] Ya M., Marquette P., Belahcene F., Lu J., *Residual stresses in laser welded aluminium plate by use of ultrasonic and optical methods*, Elsevier, Materials Science and Engineering A 382, pp. 257–264, 2004.
[4] Eboo M, Steen WM, Clarke J., *Arc-augmented laser welding,* Proc. of 4th International conference on advances in welding processes, Harrogate, UK, 1978.
[5] Bang Hee Seon, Bang Han Sur, Kim You Chul, Oh Ik Hyun, *A study on mechanical and microstructure characteristics of the STS304L butt joints using hybrid CO2 laser-gas metal arc welding*, Elsevier, Materials and Design 32, pp. 2328–2333, 2011.
[6] Kong F., Kovacevic R., *3D finite element modeling of the thermally induced residual stress in the hybrid laser/arc welding of lap joint*, Elsevier, Journal of Materials Processing Technology 210, pp. 941–950, 2010.
[7] Buschenhenkea F., Hofmannb M., Seefelda T., Vollertsena F., *Distortion and residual stresses in laser beam weld shaft-hub joint*, Elsevier, Physics Procedia 5, pp. 89-98, 2010.
[8] Casavola C., Pappalettere C., Tattoli F., *Experimental and numerical study of static and fatigue properties of titanium alloy welded joints*, Elsevier, Mechanics of Materials 41, pp. 231–243, 2009
[9] Casavola C., Pappalettere C., *Residual stress on titanium alloy welded joints*, Experimental Analysis of Nano and Engineering Materials and Structures, Editor E.E. Gdoutos, Springer (Netherlands), 2007.
[10] ASTM E 837 *Standard method for determining residual stresses by the hole-drilling strain gage method*, Annual Book of ASTM Standards, 2008.
[11] Stresstech group, *X-ray Diffraction*,The method for residual stress testing, ASW 15 Sep. 2003.
[12] Luo Q., Jones A.H., *High-precision determination of residual stress of polycrystalline coatings using optimised XRD-sin2ψ technique*, Surface & Coatings Technology 205, pp. 1403–1408, 2010.
[13] Casavola C., Pappalettere C., *Residual stresses and fatigue strength of butt welded components* – 2004 SEM International Conference and Exposition on Experimental and Applied Mechanics, Costa Mesa (USA), June 6-10, 2004.

Residual Stresses Management: Measurements, Fatigue Analysis and Beneficial Redistribution

Y. Kudryavtsev
Structural Integrity Technologies Inc. (SINTEC), Markham, Canada
E-mail: ykudryavtsev@sintec.ca

Abstract

Residual stresses (RS) can significantly affect engineering properties of materials and structural components, notably fatigue life, distortion, dimensional stability, corrosion resistance. RS play an exceptionally significant role in fatigue of welded elements. The influence of RS on the multi-cycle fatigue life of butt and fillet welds can be compared with the effects of stress concentration. Even more significant are the effects of RS on the fatigue life of welded elements in the case of relieving harmful tensile RS and introducing beneficial compressive RS in the weld toe zones. The results of fatigue testing of welded specimens in as-welded condition and after application of ultrasonic peening showed that in case of non-load caring fillet welded joint in high strength steel, the redistribution of RS resulted in approximately two-fold increase in the limit stress range. A concept of residual stress management (RSM) and a number of engineering tools were proposed recently that address major aspects of RS in welds and welded structures. According to the concept, three major stages, i.e. RS determination, RS analysis and RS redistribution are considered and evaluated, either experimentally or theoretically to achieve the optimum performance of welded elements and structures. The main stages of RSM are considered in this paper. A number of new engineering tools such as ultrasonic computerized complex for RS measurement, software for analysis of the effect of RS on the fatigue life of welded elements as well as a new technology and, based on it, compact system for beneficial redistribution of RS by ultrasonic peening are introduced. Examples of industrial applications of the developed engineering tools for RS analysis and fatigue life improvement of welded elements and structures are discussed.

1. Introduction

Residual stresses (RS) can significantly affect engineering properties of materials and structural components, notably fatigue life, distortion, dimensional stability, corrosion resistance, brittle fracture [1]. Such effects usually lead to considerable expenditures in repairs and restoration of parts, equipment and structures. For that reason, the RS analysis is a compulsory stage in the design of parts and structural elements and in the estimation of their reliability under real service conditions.

Systematic studies had shown that, for instance, welding RS might lead to a drastic reduction in fatigue strength of welded elements. In multi-cycle fatigue ($N>10^6$ cycles of loading), the effect of RS can be compared with the effect of stress concentration [2]. Figure 1 illustrates one of the results of these studies. The butt joints in low-carbon steel were tested at symmetric cycle of loading (stress ratio R=-1). There were three types of welded specimens. The relatively small specimens (420x80x10 mm) were cut from a large welded plate. Measurements of RS revealed that in this case the specimens after cutting had a minimum level of RS. Additional longitudinal weld beads on both sides in specimens of second type created at the central part of these specimens tensile RS close to the yield strength of material. These beads did not change the stress concentration of the considered butt weld in the direction of loading. In the specimens of third type longitudinal beads were deposited and then the specimens were bisected and welded again. Due to the small length of this butt weld the RS in these specimens were very small (approximately the same as those within the specimens of first type) [2].

Tests showed that the fatigue strength of specimens of first and third types (without RS) is practically the same with the limit stress range 240 MPa at $N=2\cdot10^6$ cycles of loading. The limit stress range of specimens with high tensile RS (second type) was only 150 MPa. In all specimens the fatigue cracks originated near the transverse butt joint. The reduction of the fatigue strength in this case can be explained only by the effect of welding RS. These experimental studies showed also that at the level of maximum cyclic stresses close to the yield strength of base material the fatigue life of specimens with and without

T. Proulx (ed.), *Engineering Applications of Residual Stress, Volume 8*, Conference Proceedings of the Society for Experimental Mechanics Series 999, DOI 10.1007/978-1-4614-0225-1_14,

high tensile RS was practically identical. With the decrease of the stress range there is corresponding increase of the influence of the welding RS on the fatigue life of welded joint.

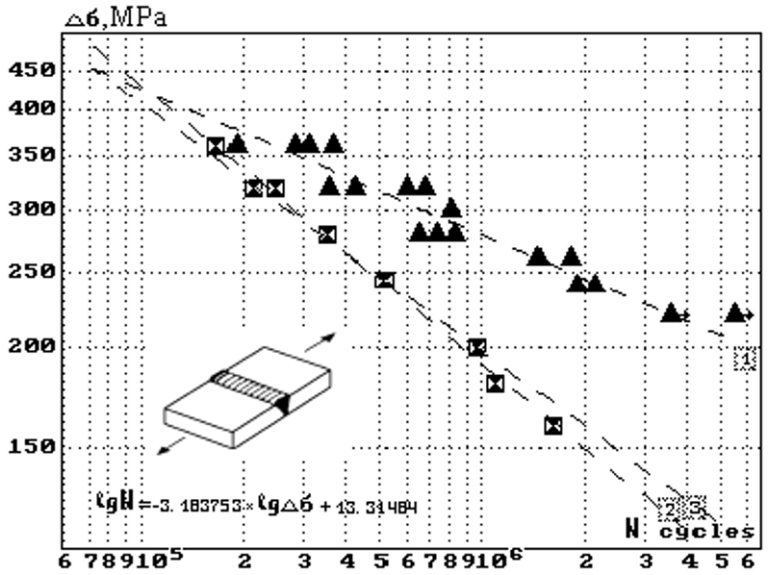

Figure 1. Fatigue curves of butt welded joint in low-carbon steel [2]:
1 - without residual stresses; 2,3 - with high tensile residual stresses (fatigue testing and computation)

The effect of RS on the fatigue life of welded elements is more significant in the case of relieving of harmful tensile RS and introducing of beneficial compressive RS in the weld toe zones. The beneficial compressive RS with the level close to the yield strength of material are introduced at the weld toe zones by, for instance, the ultrasonic peening (UP) [1,3]. The results of fatigue testing of welded specimens in as-welded condition and after application of UP are presented on Figure 2. The fatigue curve of welded element in as-welded condition (with high tensile RS) was used also as initial fatigue data for computation of the effect of the UP. In case of non-load caring fillet welded joint in high strength steel (σ_y = 864 MPa, σ_u = 897 MPa), the redistribution of RS resulted in approximately two times increase in limit stress range and over 10 times increase in the fatigue life of the welded elements [3].

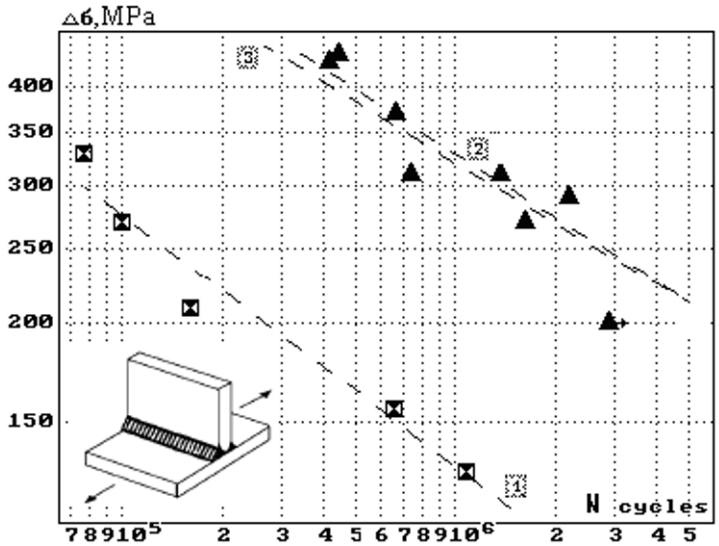

Figure 2. Fatigue curves of non-load caring fillet welded joint in high strength steel [3]:
1 - in as welded condition; 2,3 - after application of ultrasonic peening (fatigue testing and computation)

The RS, therefore, are one of the main factors determining the engineering properties of materials, parts and welded elements and this factor should be taken into account during the design and manufacturing of different products. Despite the fact that the RS have a significant effect on the strength and reliability of parts and welded elements, their influence is not sufficiently reflected in corresponding codes and regulations. This is, mainly, because the influence of RS on the fatigue life of parts and structural elements depends greatly not only on the level or RS, but also on the mechanical properties of materials used, the type of welded joints, the parameters of cyclic loading and other factors [1-3]. Presently elaborate, time- and labor-consuming fatigue tests of large-scale specimens are required for this type of analysis.

Generally, in modern standards and codes on fatigue design of welded elements the presented data correspond to the fatigue strength of real welded joints including the effects of welding technology, type of welded element and welding RS [4]. Nevertheless, in many cases there is a need to consider the influence of welding RS on the fatigue life of structural components in greater details. These cases include use of the results of fatigue testing of relatively small welded specimens without high tensile RS, analysis of effects of such factors as overloading, spectra loading and application of the improvement treatments.

Residual Stress Management: Measurement, Fatigue Analysis and Beneficial Redistribution

The efficient approach to the problem of RS includes, at least, stages of determination, analysis and beneficial redistribution of residual stresses. The combined consideration of the above-mentioned stages of the RS analysis and modification gives rise to so called Residual Stress Management (RSM) concept approach [5]. The RSM concept includes the following main stages:

Stage 1. Residual Stress Determination:
- Measurement: Destructive, Non-destructive
- Computation

Stage 2. Analysis of the Residual Stress Effects:
- Experimental Studies
- Computation

Stage 3. Residual Stress Modification (if required):
- Changes in Technology of Manufacturing/Assembly
- Application of Stress-Relieving Techniques

The main stages of RSM are briefly considered in this paper with the emphasis on examples of practical application of new engineering tools for RSM that include the ultrasonic complex for RS measurement and a technology and, based on it, compact system for redistribution of RS by ultrasonic peening.

2. Measurement of Residual Stresses

Over the last few decades, various quantitative and qualitative methods of RS analysis have been developed [6]. In general, a distinction is usually made between destructive and non-destructive techniques for RS measurement. The first series of methods is based on destruction of the state of equilibrium of the RS after sectioning of the specimen, machining, layer removal or hole drilling. The most common destructive methods are:
- the hole drilling method,
- the ring core technique,
- the bending deflection method,
- the sectioning method, etc.

The application of the destructive or so-called partially-destructive techniques is limited mostly to laboratory samples. The second series of methods of RS measurement is based on the relationship between the physical and the crystallographic parameters and the RS and does not require the destruction of the part or structural elements and could be used for field measurement. The most developed non-destructive methods are:
- the X-ray and neutron diffraction methods,
- the ultrasonic techniques,
- the magnetic methods.

Ultrasonic Method and Equipment for Residual Stress Measurement

Ultrasonic stress measurement techniques are based on the acoustic-elasticity effect, according to which the velocity of elastic wave propagation in solids is dependent on the mechanical stress [7-9]. Some of the advantages of the ultrasonic technique are associated with the facts that the instrumentation is convenient to use, quick to set up, portable, inexpensive and free of radiation hazards. In the proposed in [7-9] technique, the velocities of longitudinal ultrasonic wave and shear waves of orthogonal polarization are measured at a considered point to determine the uni- and biaxial RS. The bulk waves in this approach are used to determine the stresses averaged over the thickness of the investigated elements. Surface waves are used to determine the uni- and biaxial stresses at the surface of the material. The mechanical properties of the material are represented by the proportionality coefficients, which can be calculated or determined experimentally under an external loading of a sample of considered material.

The Ultrasonic Computerized Complex (UCC) for residual stress analysis includes a measurement unit with supporting software and a laptop (optional item) with an advanced database on RS and an expert system for analysis of the influence of residual stresses on the fatigue life of welded components. The developed device with gages/transducers for ultrasonic RS measurement is presented in Figure 3.

Figure 3. The Ultrasonic Computerized Complex for measurement of residual and applied stresses

The developed equipment allows one to determine the magnitudes and signs of uni- and biaxial residual and applied stresses for a wide range of materials as well as stress, strain and force in various size fasteners. The sensors, using quartz plates measuring from 3×3 mm to 10×10 mm as ultrasonic transducers, are attached to the object of investigation by special clamping straps (Figure 3) and/or electromagnets. The main technical characteristics of the measurement unit:

- stress can be measured in materials with thickness 2 - 150 mm;
- error of stress determination (from external load): 5 - 10 MPa;
- error of residual stress determination: 0.1 σ_Y (yield strength) MPa;
- stress, strain and force measurement in fasteners (pins) 25-1000 mm long;
- independent power supply (accumulator battery 12 V);
- overall dimensions of measurement device: 300x200x150 mm;
- weight of unit with sensors: 7 kg.

The developed ultrasonic equipment could be used for RS measurement for both laboratory and field conditions [7-10]. For instance, the RS were measured in 1000x500x36 mm specimen, representing a butt-welded element of a large transonic wind tunnel. The distribution of biaxial RS was investigated in X (along the weld) and Y directions after welding and in the process of fatigue testing of a specimen [9]. Figure 4 represents the distribution of longitudinal (along the weld) and transverse components of RS along the weld toe before fatigue testing. Both components of RS reached their maximum levels in the central part of a specimen: longitudinal - 195 MPa, transverse - 110 MPa.

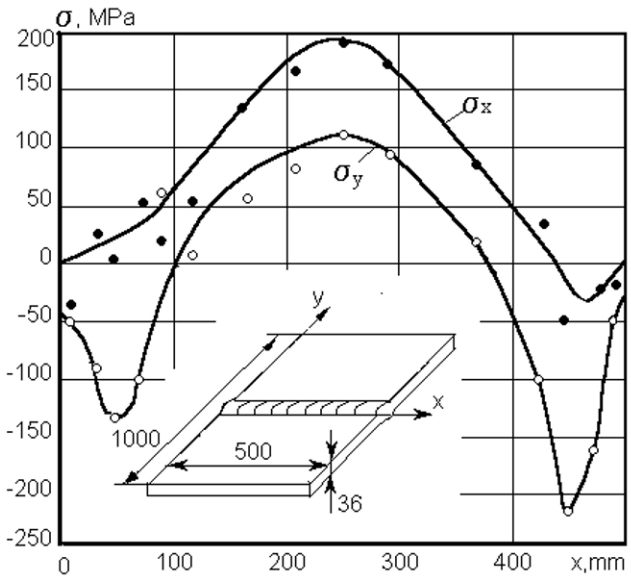

Figure 4. Distribution of longitudinal (along the weld) and transverse components of residual stresses along the butt weld toe [9]

Figures 5 and 6 show the process and some of the results of ultrasonic measurement of residual stresses in welded elements of bridge. The residual stresses were measured by ultrasonic method in the main wall of the bridge span near the end of one of welded vertical attachments [8]. In the vicinity of the weld the measured levels of harmful tensile residual stresses reached 240 MPa. Such high tensile residual stresses are the results of thermo-plastic deformations during the welding process and are one of the main factors leading to the origination and propagation of the fatigue cracks in welded elements.

Figure 5. Measurement of residual stresses in a welded bridge

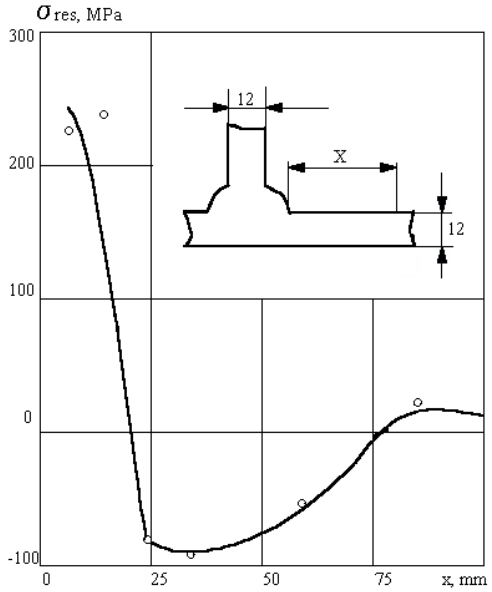

Figure 6. Distribution of longitudinal (oriented along the weld) residual stresses near the fillet weld in bridge span: x – distance from the weld toe

3. Residual Stress in Fatigue Analysis

The effect of RS on fatigue behavior of welded element could be analyzed based on experimental studies and/or computation (Figures 1 and 2). One of the examples of computation of the effect of RS on fatigue life of welded elements is presented in Figure 7. These data show how the redistribution of residual stresses will affect the fatigue performance of welded joint. The calculated fatigue curves for the transverse loaded butt weld at R=0 with different levels of the initial RS are shown. The fatigue curve of the welded element will be located between lines 1 and 2 in case of partial relieve of harmful tensile RS (line 3 and line 4). The decrease of the tensile RS from initial high level to 100 MPa causes, in this case, an increase of the limit stress range at $N=2\times10^6$ cycles from 100 MPa to 126 MPa.

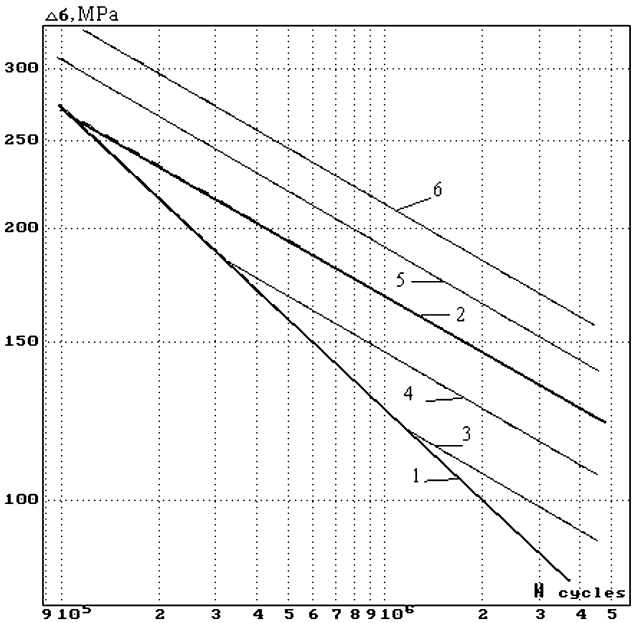

Figure 7. Fatigue curves of transverse loaded butt weld at R=0: 1 - with high tensile residual stresses; 2, 3, 4, 5 and 6 - with residual stresses equal to 0 MPa, 200 MPa, 100 MPa,-100 MPa and -200 MPa

The relieving of the RS in welded element to the level of 100 MPa could be achieved, for example, by heat treatment or overloading of this welded element at a level of external stresses equal to $0.52\sigma_y$. As a result, this originally fatigue class FAT 100 welded element could be considered after relieve of RS as the fatigue class FAT 125 element in the multi-cycle region ($N>10^6$ cycles of loading) [4]. After modification of welding RS, the considered welded element will have an enhanced fatigue performance and, in principle, can be used instead of transverse loaded butt weld ground flush to plate (Structural Detail No. 211) or longitudinal butt weld (Structural Details No. 312 and 313) [4]. Introducing of the compressive RS in the weld toe zone can increase the fatigue strength of welded elements even to a larger extend (line 5 and line 6 in Figure 7).

The results of computation presented in Figure 8 show the effect of the redistribution of RS by the UP on the fatigue life of welded joints in steels of different strength. The data of fatigue testing of non-load-carrying fillet weld specimens in as-welded condition (with high tensile RS) were used as initial fatigue data for calculating the effect of the UP. The fatigue strength of certain welded element in steels of different strength in as-welded condition is represented by a universal fatigue curve [2,4].

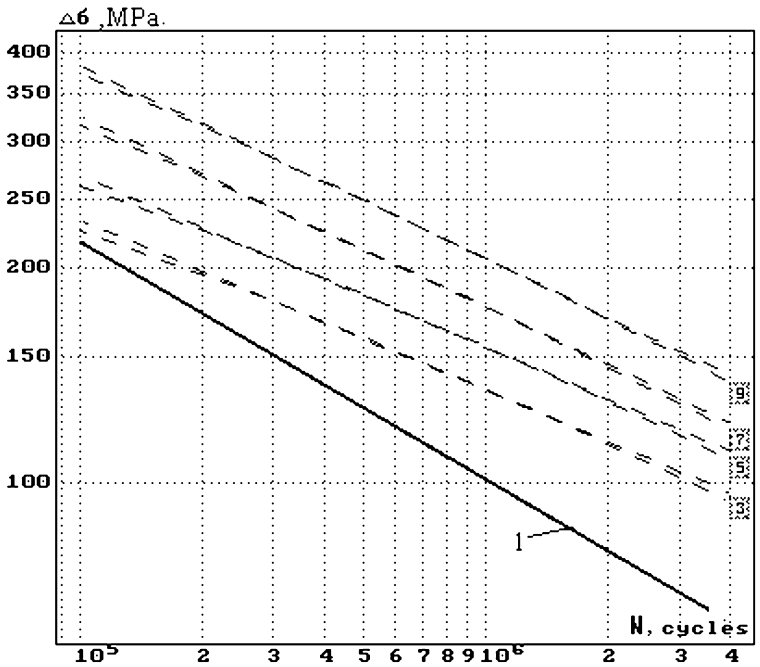

Figure 8. Fatigue curves of non-load-carrying fillet welded joint: 1 - in as-welded condition for all types of steel; 3, 5, 7 and 9 - after application of the UP to Steel 1,Steel 2, Steel 3, and Steel 4

Four types of steels were considered for fatigue analysis: Steel 1 - (σ_y = 270 MPa, σ_u = 410 MPa); Steel 2 - (σ_y = 370 MPa, σ_u = 470 MPa); Steel 3 - (σ_y = 615 MPa, σ_u = 747 MPa) and Steel 4 - (σ_y = 864 MPa, σ_u = 897 MPa). Line 1 in Figure 8 is the universal fatigue curve of considered welded joint for all types of steel in as-welded condition, determined experimentally. Lines 3, 5, 7 and 9 are the calculated fatigue curves for the welded joint after application of the UP for Steel 1, Steel 2, Steel 3 and Steel 4, respectively.

As can be seen from Figure 8, the higher the mechanical properties of the material - the higher the fatigue strength of welded joints after application of the UP. The increase in the limit stress range at $N=2\times10^6$ cycles under the influence of UP for welded joint in Steel 1 is 42%, for Steel 2 - 64%, for Steel 3 - 83% and for Steel 4 - 112%. These results show a strong tendency of increasing the fatigue strength of welded elements after application of UP with the increase in mechanical properties of the material used.

4. Residual Stress Modification. Ultrasonic Peening

One of the new and promising processes for effective redistribution of RS is Ultrasonic Peening (UP) [1, 6, 11-13]. During the different stages of its development the UP process was also known as ultrasonic impact treatment (UIT) [14-16] and ultrasonic impact peening (UIP) [17-18]. The beneficial effect of UP is achieved mainly by relieving of harmful tensile RS and introducing of compressive RS into surface layers of metals and alloys, decreasing of stress concentration in weld toe zones and enhancement of mechanical properties of the surface layers of the material. The fatigue testing of welded specimens showed that the UP is the most efficient improvement treatment as compared with traditional techniques such as grinding, TIG-dressing, heat treatment, hammer peening, shot peening etc. [2, 11-13].

The UP technique is based on the combined effect of high frequency impacts of special strikers and ultrasonic oscillations in treated material. The developed system for UP treatment (total weight ~11 kg) includes an ultrasonic transducer, a generator and a laptop (optional item) with software for UP optimum application - maximum possible increase in fatigue life of parts and welded elements with minimum cost, labor and power consumption. In general, the basic UP system shown in Figure 9 could be used for treatment of weld toe or welds and larger surface areas if necessary.

Figure 9. Basic UP-600 system for fatigue life improvement of parts and welded elements

Figure 10 shows the basic set of working heads for different applications of UP. The working head could be easily replaced, if necessary. Six different working heads are provided with the standard UP package:

- one four-pin working head with the pin's diameter of 3 mm,
- one three-pin working head with the pin's diameter of 4 mm,
- one "zig-zag" four-pin head with the pin's diameter of 4 mm,
- one single-pin working head with the pin's diameter of 4 mm,
- one seven-pin working head with the pin's diameter 5 mm,
- one two-pin working head with the pin's diameter of 3 mm.

The UP could be effectively applied for fatigue life improvement during manufacturing, rehabilitation and repair of welded elements and structures [11-13]. The results of fatigue testing of large-scale welded samples imitating the transverse non-load-carrying attachments where the UP was applied to specimens in as-welded condition and also after 50% of expected fatigue life are presented on Figure 11. The UP caused a significant increase in fatigue strength of the considered welded element for both series of UP treated samples. The increase in limit stress range (at $N=2\cdot10^6$ cycles) of welded samples is 49% (from 119 MPa to 177 MPa) for UP treated samples before fatigue loading and is 66% (from 119 MPa to 197 MPa) for UP treated samples after fatigue loading, with the number of cycles corresponding to 50% of the expected fatigue life of the samples in as-welded condition. The higher increase of fatigue life of UP treated welded elements for fatigue curve #3 could

be explained by a more beneficial redistribution of RS and/or “healing” of fatigue damaged material by UP in comparison with the fatigue curve #2.

Figure 10**.** Basic set of the changeable working heads

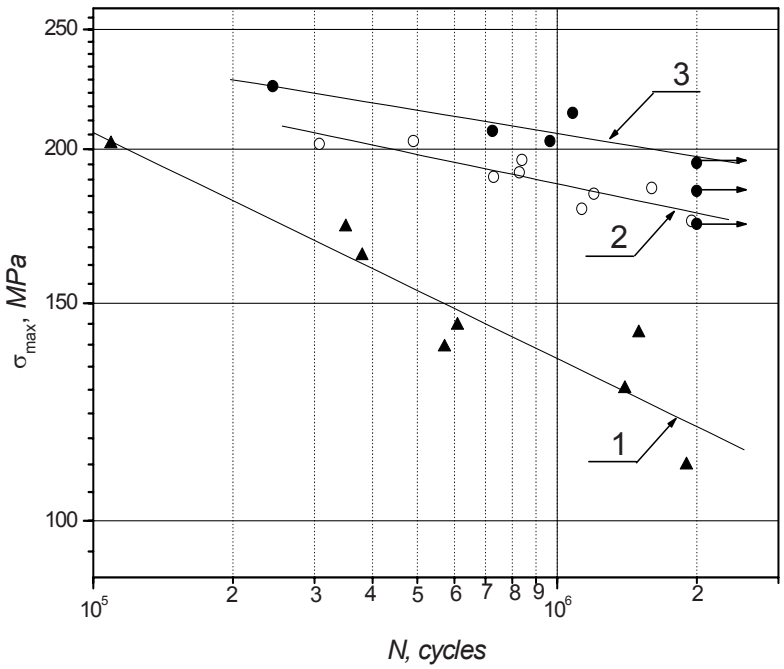

Figure 11. Fatigue curves of welded elements (transverse non-load-carrying attachment): 1 – in as welded condition, 2 – UP was applied before fatigue testing, 3 – UP was applied after fatigue loading with the number of cycles corresponding to 50% of expected fatigue life of samples in as-welded condition.

The developed computerized complex for UP was successfully applied in different applications for increasing of the fatigue life of welded elements, elimination of distortions caused by welding and other technological processes, residual stress relieving, increasing of the hardness of the surface of materials and surface nanocrystallization. The areas/industries where the UP was applied successfully include: Railway and Highway Bridges, Construction Equipment, Shipbuilding, Mining, Automotive and Aerospace.

5. Summary

1. Residual stresses play an important role in operating performance of materials, parts and welded elements. Their effect on the engineering properties of materials such as fatigue and fracture, corrosion resistance and dimensional stability can be considerable. The influence of residual stresses on the multi-cycle fatigue life of welded elements can be compared with the effects of stress concentration. The residual stresses, therefore, should be taken into account during design, fatigue assessment, manufacturing and repair of welded elements and structures.

2. Certain progress has been achieved during the past few years in improvement of traditional techniques and development of new methods for residual stress management. A number of new engineering tools for residual stress management such as ultrasonic computerized complex for residual stress measurement, technology and equipment for ultrasonic penning and software for analysis of the effect of residual stresses on the fatigue life of welded elements and structures were recently developed and verified for different industrial applications.

3. The beneficial redistribution of the residual stresses is one of the efficient ways of fatigue improvement of welded elements. The ultrasonic peening is the most effective and economical technique for increasing of the fatigue strength of welded elements in materials of different strength. The higher the mechanical properties of treated materials - the higher the efficiency of ultrasonic peening application. It allows using to a greater degree the advantages of the high strength material application in parts and welded elements, subjected to fatigue loading.

6. References

1. Handbook on Residual Stress. *Volume 1. Edited by Jian Lu. Society for Experimental Mechanics. 2005. 417 p.*

2. V. Trufyakov, P. Mikheev and Y. Kudryavtsev. Fatigue Strength of Welded Structures. Residual Stresses and Improvement Treatments. *Harwood Academic Publishers GmbH. London. 1995. 100 p.*

3. Y. Kudryavtsev, J. Kleiman et al. Ultrasonic Peening of Weldments: Experimental Studies and Computation. *IX International Congress on Experimental Mechanics. Orlando. Florida. USA, June 5-8, 2000. p. 504-507.*

4. Recommendations for Fatigue Design of Welded Joints and Components. *IIW Doc. XIII-1823-07. International Institute of Welding. 2008. 144 p.*

5. Y. Kudryavtsev and J. Kleiman. Residual Stress Management: Measurement, Fatigue Analysis and Beneficial Redistribution. *X International Congress and Exposition on Experimental and Applied Mechanics. Costa Mesa, California USA, June 7-10, 2004. pp. 1-8.*

6. Y. Kudryavtsev. Residual Stress. *Springer Handbook on Experimental Solid Mechanics. Springer – SEM. 2008. P. 371-387.*

7. Y. Kudryavtsev, J. Kleiman, O. Gushcha, V. Smilenko and V. Brodovy. Ultrasonic Technique and Device for Residual Stress Measurement. *X International Congress and Exposition on Experimental and Applied Mechanics. Costa Mesa, California USA, June 7-10, 2004. pp. 1-7.*

8. Y. Kudryavtsev, J. Kleiman and O. Gushcha. Ultrasonic Measurement of Residual Stresses in Welded Railway Bridge. *Structural Materials Technology: An NDT Conference. Atlantic City. NJ. February 28-March 3, 2000. p. 213-218.*

9. Y. Kudryavtsev. Application of the ultrasonic method for residual stress measurement. *Development of fracture toughness requirement for weld joints in steel structures for arctic service. VTT-MET. B-89. Espoo. Finland. 1985. p.62-76.*

10. H. Polezhayeva, J. Kang, J. Lee, Y. Yang and Y. Kudryavtsev. A Study on Residual Stress Distribution and Relaxation in Welded Components. *Proceedings of the 20th International Offshore (Ocean) and Polar Engineering Conference ISOPE-2010, June 20−26, 2010, Beijing, China.*

11. Y. Kudryavtsev and J. Kleiman. Fatigue Improvement of Welded Elements and Structures by Ultrasonic Impact Treatment (UIT/UP). *International Institute of Welding. IIW Document XIII-2276-09. 2009.*

12. Y. Kudryavtsev, J. Kleiman and Y. Iwamura. Fatigue Improvement of HSS Welded Elements by Ultrasonic Peening. *Proceedings of the International Conference on High Strength Steels for Hydropower Plants, July 20-22, 2009. Takasaki, Japan.*

13. Y. Kudryavtsev, J. Kleiman and V. Knysh. Fatigue Strength of Structural Elements with Cracks Repaired by Welding. *International Institute of Welding. IIW Document XIII-2236-08. 2008. 7 p.*

14. Y. Kudryavtsev, V. Korshun and A. Kuzmenko. Improvement of fatigue life of welded joints by the ultrasonic impact treatment. *Paton Welding Journal. 1989. No. 7. p. 24-28.*

15. Y. Kudryavtsev, P. Mikheev and V. Korshun. Influence of plastic deformation and residual stresses, created by ultrasonic impact treatment, on the fatigue strength of welded joints. *Paton Welding Journal. 1995. No. 12. p. 3-7.*

16. V. Trufiakov, P. Mikheev, Y. Kudryavtsev and E. Statnikov. Ultrasonic Impact Treatment of Welded Joints. *International Institute of Welding. IIW Document XIII-1609-95. 1995.*

17. V. Trufyakov, P. Mikheev, Y. Kudryavtsev and D. Reznik. Ultrasonic Impact Peening Treatment of Welds and Its Effect on Fatigue Resistance in Air and Seawater. *Proceedings of the Offshore Technology Conference. OTC 7280. 1993. p. 183-193.*

18. V. Trufyakov, P. Mikheev, Y. Kudryavtsev and D. Reznik. Fatigue Endurance of Welded Joints. Residual Stresses and Fatigue Improvement Treatments. *Ship Structure Symposium'93. Arlington, Virginia, USA. November 16-17, 1993. p. N1 - N14.*

ASSESSMENT OF EFFECTIVE PRESTRESS FORCE OF PCCV USINIG SI TECHNIQUE

Hong-Pyo Lee[a], Jung-Bum Jang[a], Kyeong-Min Hwang[a], Young-Chul Song[a]

[a] Nuclear Power Lab., KEPRI, 103-16 Munji-Dong, Yuseong-Gu, Daejeon, 305-380, Republic of Korea

E-mail : hplee@kepri.re.kr

ABSTRACT

Bonded tendons have been used in reactor buildings of heavy water reactors and the light water reactors of some nuclear power plants operating in Korea. The assessment of prestressed forces on those bonded tendons is becoming an important issue in assuring their continuous operation beyond their design life. In order to assess the effective prestressed force on the bonded tendon, indirect assessment techniques have been applying to the test beams which were manufactured on construction time.

Therefore, this research mainly forced to establish the assessment methodology to measure directly the effective prestressed force on the bonded tendon of containment buildings using System Identification (SI) technique. To accomplish this purpose, simple SI method was proposed and adapted three dimensional finite element analysis of the 1:4 scale prestressed concrete containment vessel (PCCV) tested by Sandia nation Laboratory in 2000.

1. PCCV MODEL

1.1 General Description

The PCCV test model uniformly scaled at 1:4 represents the containment building of an actual pressurized water reactor (PWR) plant OHI unit 3 in Japan. The objectives of the internal pressurization tests were to obtain measurement data on the structural response of the model to pressure loading beyond design basis accident in order to validate analytical modeling, find pressure capacity of the model and observe its failure mechanisms.

The schematic of the test model is shown in Fig. 1 and the design pressure is 0.39 MPa. The pressure at which the local analysis computed liner strains that reached the failure limits was 3.2 times the design pressure which is 1.27 MPa and the catastrophic rupture occurred at 3.6 Pd during the SFMT (Structural Failure Mode Test)

T. Proulx (ed.), *Engineering Applications of Residual Stress, Volume 8*, Conference Proceedings of the Society for Experimental Mechanics Series 999, DOI 10.1007/978-1-4614-0225-1_15, © The Society for Experimental Mechanics, Inc. 2011

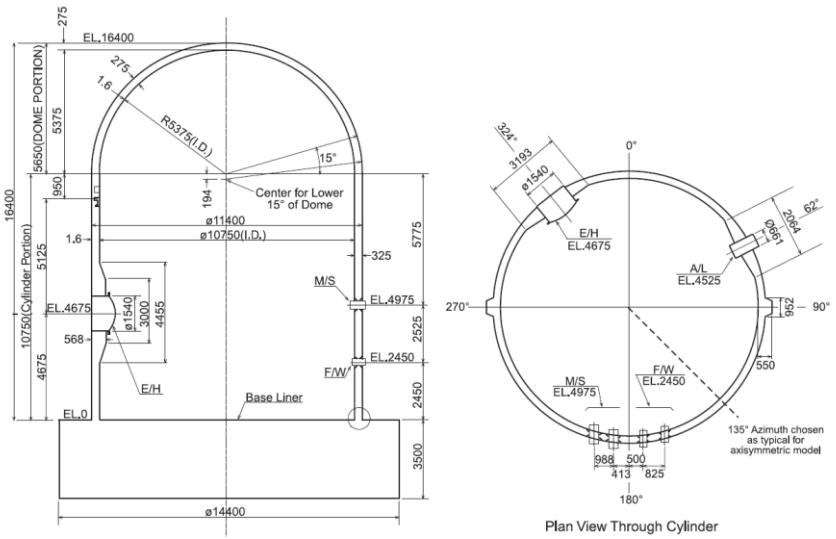

Fig. 1 1:4 scale PCCV model geometry (mm)

1.2 Material Properties

The material properties for concrete, steel rebar, post-tensioned tendons and steel liner are prepared by using the experiment data provide by Sandia National Laboratories (SNL).

1.2.1 Concrete

Two Type of concrete such as a normal strength concrete and a high strength concrete were used to construct the SNL PCCV test model. In the present finite analysis, the material property data for the trial mix concrete based on a field curing are used. The material properties adopted in the finite element analysis are described in Table 1.

Table 1. Material data for trial mix concrete (MPa)

Material / Item	f_c'=29.42 (basemat)		f_c'=44.13 (dome & wall)	
	Standard curing	Field curing	Standard curing	Field curing
Compressive strength	51.39	41.68	60.21	48.84
Tensile strength	3.93	3.37	4.21	3.45
Flexural strength	5.37	4.00	5.58	5.51
Young's modulus	29,030	27,950	31,970	26,970
Poisson's ratio	0.20	0.18	0.20	0.18
Density (ton/m^3)	2.25	2.21	2.26	2.19

1.2.2 Steel rebar

The material properties for each type of rebar are selected from the test data. The material properties are

summarized in Table 2 and the test data for steel rebar is illustrated in Fig. 2. In the finite element analysis, we adopt the mean value for the material properties of rebar: (a) SD490 is used for the basematn part; (b) SD390 is used for the cylinder wall and dome parts.

- Elastic modulus : 1.86E5 MPa (basemat), 1.848E5 MPa (wall and dome)
- Yield stress : 512.2 MPa (basemat), 479.9 MPa (wall and dome)
- Ultimate stress : 709.7 MPa (basemat), 628.7 MPa (wall and dome)
- Poisson's ratio : 0.3
- Elongation(%) : 17.8 MPa (basemat), 21.32 MPa (wall and dome)

Table 2. rebar material properties (unit:MPa)

Material / Item	D10 (SD390)	D13 (SD390)	D16 (SD390)	D19 (SD390)	D22 (SD390)	D19 (SD490)
Elastic modulus	1.83E5	1.83E5	1.83E5	1.84E5	1.91E5	1.86E5
Poisson's ratio	0.3	0.3	0.3	0.3	0.3	0.3
Yield stress	482.0	490.1	476.6	491.9	459.0	512.2
Ultimate stress	613.6	640.4	606.2	630.4	653.2	709.7
Elongation (%)	20.5	24.2	22.1	21.1	18.7	17.8

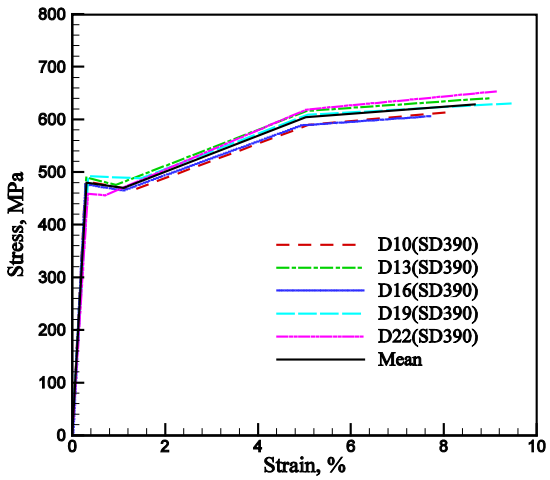

Fig. 2 Stress-strain relationship for steel rebar

1.2.3 Prestressing tendon

TAISE performed the calibration test of six samples of a three-strain tendon assembly. The stress-strain data are calculated by the division of the measured forces by the initial cross section area (339mm^2) as shown in Fig. 3. The ultimate stress and strain test data are summarized in Table 3.

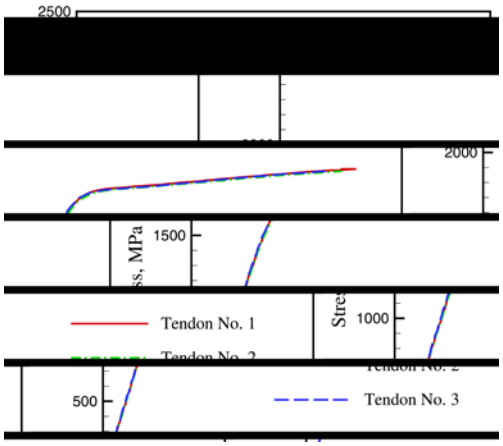

Fig. 3 Stress-strain relationship for tendons

Table 3. Tendon material data

Test specimen	Ultimate stress (MPa)	Failure strain (%)
Specimen 1	1,924	3.32
Specimen 2	1,912	3.51
Specimen 3	1,932	3.36
Specimen 4	1,921	No strain gages
Specimen 5	1,934	No strain gages
Specimen 6	1,924	3.3
Mean	1,924.5	3.3

* Estimate based on surviving strain gages

1.2.4 Steel liner plate

Two sets off material samples for the steel liner plate were tested to evaluate their material properties. The stress-strain data is illustrated in Fig. 4.

2. FINITE ELEMENT MODEL

Fig. 4 shows the finite element mesh of concrete, steel rebar and tendon. The mesh for concrete wall and dome are use lower order solid elements (ABAQUS elements C3D8, lagranginan formulation). The steel rebar and prestressing tendon is modeled with truss elements as displayed in Fig. 5 (T3D2). The truss element are coupled with the mother element, that is solid element, of the concrete with the *EMBEDDED ELEMENT function of ABAQUS. In this function, the nodes of a truss element are kinematically constrained to the nodes of the solid element in which it is located. It means that the displacement of the node of truss element is average value of the displacement of the neighboring nodes of the solid element in which the truss element is embedded. The mesh

for steel liner plate are used 4-node membrane element (M3D4).

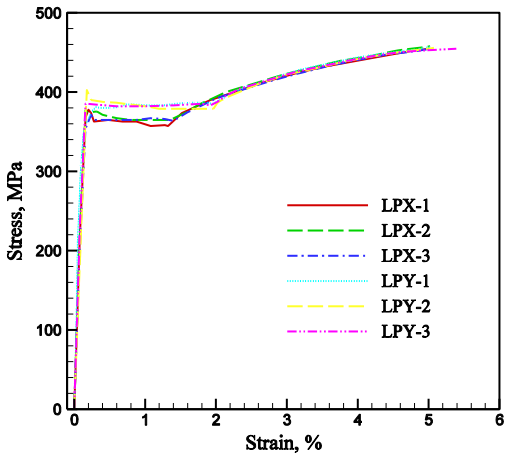

Fig. 4 Stress-strain relationship for steel liner

The prestressing force for tendon is represented by the *INITIAL CONDITION opting in ABAQUS. The tendons are assumed to remain rigidly bonded to the concrete. Therefore, the slippage of a tendon within the tendon sheath cannot be considered in the present finite element analysis model. The boundary condition for the bottom of the basemat is assumed to be fixed and this model also cannot simulate the possible vertical uplift internal pressurization.

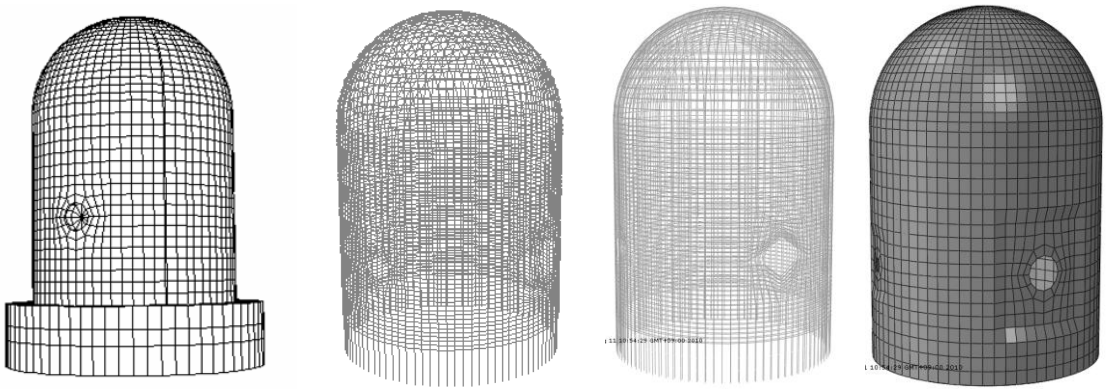

(a) concrete (b) tendon (c) reinforcement (d) liner

Fig. 5 Finite element models for PCCV

3. SI TECHNIQE

SI (System Identification) technique si defined as a type of inverse problems to estimate stiffness parameters of structure from the results such as displacement, stress at el., between measured responses and calculated responses with finite element method. To find a optimized solution, iterative works may be performed several

times. Fig. 6 shows the SI technique with ABAQUS finite element program.

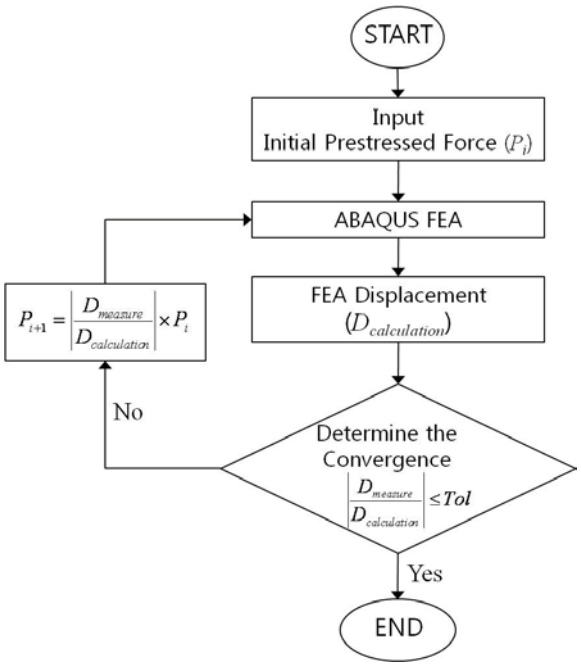

Fig. 6 SI technique procedure

4. FEA AND SI RESULTS

To verify the three dimension finite element model as mentioned section 2, nonlinear finite element analysis was employed. Fig. 7 shows the result of finite element analysis for 1:4 scale prestressed concrete containment vessel. The sampling point of the displacement is the mid-height of the wall which is elevation 10.73 m. The finite element analysis and experiment result curves are very well matched. Accordingly, finite element mesh is well-formed.

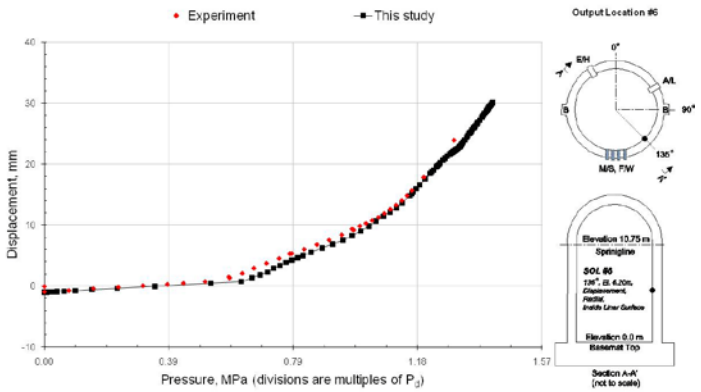

Fig. 7 Finite element analysis result

Using the proposed SI technique, iterative analysis was performed to find out the experimental measured displacement value at mid-height of the PCCV. In this case, because the true prestressed force of the tendon was known, initial prestressed force (P_i) was inputted the 0.1 times value of the real prestressed force at the first step. And then second prestressed force ($P_{i+1}i$) was calculated with respect to the SI procedures in Fig. 6.

Fig. 8 ~ Fig.10 show the results for displacement, effective prestressed force and error rate derived by proposed SI technique in this paper. Convergence rate is very fast as shown in these figures.

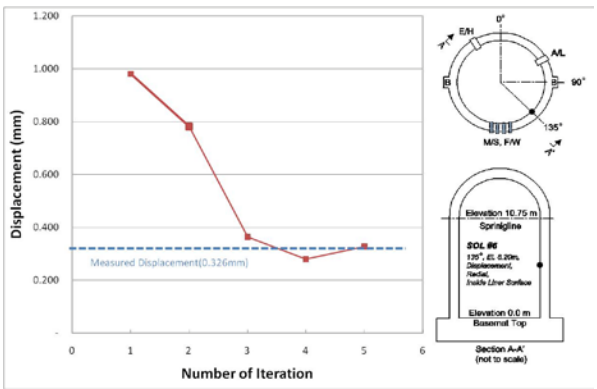

Fig. 8 Displacement and number of iteration relationship

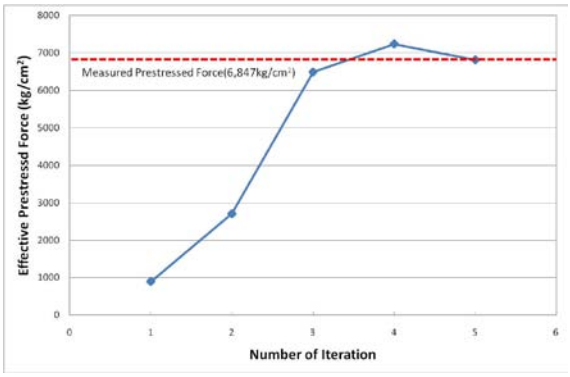

Fig. 9 Assessment result of tendon force

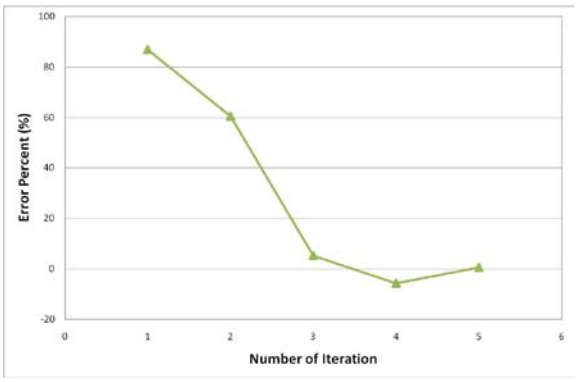

Fig. 10 Convergence process of SI technique

5. CONCLUSION

This paper describes SI technique to predict the effective prestressed force of nuclear containment building. And simple SI technique was proposed. To verify the proposed SI technique with finite element method, three dimension finite element analysis was employed at the 1:4 scale prestressed concrete containment vessel tested by SNL. From the analysis results, the proposed SI technique is useful to estimate effective prestressed force of containment building.

ACKNOWLEDGEMENT

This paper was conducted as a nuclear power technology innovation project with the generous support of the Korean ministry of Knowledge Economy. We greatly appreciate their support.

REFERENCES

[1] D.J. Naus, et. Al., Report on Aging of Nuclear Power plant Reinforced Concrete Structures, NUREG/CR-6424, 1996.
[2] Simulia Inc., Abaqus Ver.6.9-1 users manual, 2009.